SMART APPROACHES TO PREDICT URBAN FLOODING: CURRENT ADVANCES AND CHALLENGES

EDITED BY: Mingfu Guan, Qiuhua Liang and Jingming Hou
PUBLISHED IN: Frontiers in Earth Science

frontiers Research Topics

ISSN 1664-8714
ISBN 978-2-88966-842-7
DOI 10.3389/978-2-88966-842-7

About Frontiers

Frontiers is more than just an open-access publisher of scholarly articles: it is a pioneering approach to the world of academia, radically improving the way scholarly research is managed. The grand vision of Frontiers is a world where all people have an equal opportunity to seek, share and generate knowledge. Frontiers provides immediate and permanent online open access to all its publications, but this alone is not enough to realize our grand goals.

Frontiers Journal Series

The Frontiers Journal Series is a multi-tier and interdisciplinary set of open-access, online journals, promising a paradigm shift from the current review, selection and dissemination processes in academic publishing. All Frontiers journals are driven by researchers for researchers; therefore, they constitute a service to the scholarly community. At the same time, the Frontiers Journal Series operates on a revolutionary invention, the tiered publishing system, initially addressing specific communities of scholars, and gradually climbing up to broader public understanding, thus serving the interests of the lay society, too.

Dedication to Quality

Each Frontiers article is a landmark of the highest quality, thanks to genuinely collaborative interactions between authors and review editors, who include some of the world's best academicians. Research must be certified by peers before entering a stream of knowledge that may eventually reach the public - and shape society; therefore, Frontiers only applies the most rigorous and unbiased reviews.
Frontiers revolutionizes research publishing by freely delivering the most outstanding research, evaluated with no bias from both the academic and social point of view. By applying the most advanced information technologies, Frontiers is catapulting scholarly publishing into a new generation.

What are Frontiers Research Topics?

Frontiers Research Topics are very popular trademarks of the Frontiers Journals Series: they are collections of at least ten articles, all centered on a particular subject. With their unique mix of varied contributions from Original Research to Review Articles, Frontiers Research Topics unify the most influential researchers, the latest key findings and historical advances in a hot research area! Find out more on how to host your own Frontiers Research Topic or contribute to one as an author by contacting the Frontiers Editorial Office: frontiersin.org/about/contact

SMART APPROACHES TO PREDICT URBAN FLOODING: CURRENT ADVANCES AND CHALLENGES

Topic Editors:
Mingfu Guan, The University of Hong Kong, SAR China
Qiuhua Liang, Loughborough University, United Kingdom
Jingming Hou, Xi'an University of Technology, China

Citation: Guan, M., Liang, Q., Hou, J., eds. (2021). Smart Approaches to Predict Urban Flooding: Current Advances and Challenges. Lausanne: Frontiers Media SA. doi: 10.3389/978-2-88966-842-7

Table of Contents

frontiers in Earth Science

EDITORIAL
published: 20 April 2021
doi: 10.3389/feart.2021.681751

Editorial: Smart Approaches to Predict Urban Flooding: Current Advances and Challenges

Mingfu Guan[1]*, *Qiuhua Liang*[2] and *Jingming Hou*[3]

[1] Department of Civil Engineering, University of Hong Kong, Pokfulam, Hong Kong, [2] School of Architecture, Building and Civil Engineering, Loughborough University, Loughborough, United Kingdom, [3] State Key Laboratory of Eco-Hydraulics in Northwest Arid Region of China, Xi'an University of Technology, Xi'an, China

Keywords: urban flooding, stormwater runoff, flood modeling, pollutant transport, data-driven

Editorial on the Research Topic

Smart Approaches to Predict Urban Flooding : Current Advances and Challenges

Urban flooding induced by cloudburst has caused widespread disruption, damages, and environmental impact worldwide. In the context of climate change and rapid urbanization, it is expected that urban flooding will increase in both severity and frequency in the future (IPCC, 2013). In urban areas, concentration of populations, dense properties, key infrastructure systems, and businesses make flood impact be particularly severe, including both direct damage and indirect consequences such as loss of productivity and business opportunities. In addition, the potential risk to public health associated with exposure to contaminants due to urban flooding has also been increasingly recognized worldwide (Van der Vliet et al., 2014; Sales-Ortells and Medema, 2015). Urban flooding and their complex interaction with social and engineering systems impose great challenges on the conventional approaches both to short-term forecasting for emergency response and long-term planning for climate adaptation. There are clear technical challenges and knowledge gaps in understanding and predicting rainfall-induced urban flooding and the associated processes, e.g., pollutant transport.

This Research Topic compiles 11 contributions covering topics related to enhancing capability for urban flood modeling, the importance of data support in urban flood modeling, as well as the improved understanding of the fundamental urban runoff dynamics and associated processes. The papers report new approaches and demonstrate how urban flooding and associated runoff quality issues can be reasonably modeled and understood.

ENHANCEMENT OF URBAN FLOOD MODELING

Urban flood models solving the Shallow Water Equations (SWEs) have demonstrated their robustness in predicting detailed flood hydrodynamics in urban areas. Using a two-dimensional SWE model, Wang et al. simulates the inundation process due to dam-break in the downstream areas of Minzhi Reservoir in Shenzhen, China. Therein, urban structures are represented by using a refined grid with an unstructured mesh of triangular cells constrained by building walls. Currently, urban flood models are mostly two-dimensional, whereas Yu et al.develops a three-dimensional hydrodynamic model to look into the dam-break-induced flood dynamics and its interaction with buildings. The study exerts a simpler and more efficient algebraic Volume of Fluid method for free surface tracking. Alternatively, La Rocca et al. attempts the Discrete Boltzmann Equation (DBE) which

OPEN ACCESS

Edited and reviewed by:
Nick Van De Giesen,
Delft University of Technology,
Netherlands

***Correspondence:**
Mingfu Guan
mfguan@hku.hk

Specialty section:
This article was submitted to Hydrosphere, a section of the journal Frontiers in Earth Science

Received: *17 March 2021*
Accepted: *22 March 2021*
Published: *20 April 2021*

Citation:
Guan M, Liang Q and Hou J (2021) Editorial: Smart Approaches to Predict Urban Flooding: Current Advances and Challenges. Front. Earth Sci. 9:681751. doi: 10.3389/feart.2021.681751

consists of linear advection equations, to reproduce urban inundation processes. The study indicates that the DBE can be used to efficiently solve the SWEs for flood modeling and the resulting DBE model is validated against an idealized urban flood test case. Quantification of drainage capability in an urban flood model is crucial for accurate simulation of urban inundation, particularly at local scale. For this, Li et al. proposes an inlet-drainage approach to consider the drainage effects by subtracting the mass of water into drainage systems in particular parts of the domain, e.g., the areas with gullies or drainage inlets, providing a simple way to simulate the coupled rainfall-runoff-drainage-inundation processes.

Moreover, recent development has also been focused on the application of deep/machine learning approaches to support flood prediction. For example, Kabir et al. (2020) has recently developed a deep convolutional neural network (CNN) method for rapid prediction of flood inundation at a large scale. In this specific topic, Lin et al. also attempts to develop an Artificial neural network (ANN) for directly producing high-resolution inundation maps from multiple discharge inputs. Testing against historic flood events, it is shown that the ANN model is capable of predicting the maximum inundation extents reasonably well. The prediction quality may be further improved by introducing clustering for preprocessing discharge curves before model training.

DATA AND URBAN FLOOD MODELING

Data is crucial for urban flood prediction in real-world applications, but data to support high-resolution simulations is still largely scarce for urban areas. Despite the high recurrence frequency of urban floods, field observations during urban flooding are rarely available for model calibration and validation. Petersson et al. integrates data acquisition with survey design and quality assurance based on community mapping into flood model development and prediction. The study indicates that citizen science data from community mapping is affordable, comprehensible, quality assured and open source, making it applicable to support flood prediction in resource-strained contexts. Moreover, to evaluate the influence of data precision and generalization on urban flood modeling in real-world events, Xu et al. also applies a combined modeling approach to an urban area in Beijing through multi-mode surface data generalization and detailed urban flood modeling with pipe networks. When high-quality monitored data is lacking, modeling may provide valuable support for design flood estimation in urban environments. To verify this, Ball et al. presents an analysis of continuous and event-based modeling undertaken for design flood estimation in an urban catchment located in Sydney, Australia. It is shown that frequency analysis of the predicted flows from the continuous modeling resembles the frequency analysis of the recorded data more closely.

RUNOFF QUALITY ASSOCIATED WITH URBAN FLOODING

Urbanization generally creates significant changes to land surface, and anthropogenic activities and may cause remarkable changes in urban stormwater quality and quantity (Guan et al., 2015a). Stormwater runoff pollution commonly occurs before or after an urban flood event, and it is considered as the primary form of pollutant transport in urban environments. For example, Pan et al. analyses the migration characteristics of stormwater runoff pollutants based on field data in five different underlying surfaces of Guangzhou. It is verified that stormwater runoff causes urban non-point source pollution that increasingly introduces contaminants to urban water bodies and impedes sustainable development. On the stormwater quality issue, Zhang et al. proposes a 2D coupled model of flow and pollutant transport to reproduce the urban stormwater dynamics and associated pollutant transport process. It is shown that buildings may slow down pollutant transport, especially when the buildings are staggered.

Blue-green infrastructure (BGI) or sponge city has become increasingly considered as an effective option for managing urban flooding and runoff quality in urbanized landscapes (Guan et al., 2015b; Golden and Hoghooghi, 2018; Ahilan et al., 2019). In order to verify the effects of sponge city measures on soil moisture and water quality, Jia et al. conducts comprehensive analysis on land use change processes, the temporal and spatial soil water content change, as well as water quality change with different measures during a rainfall event in Guyang, China. It is found that the development of sponge city could improve urban ecological environment and hydrological conditions in the Loess Plateau and increase potential utilization of urban rainwater resources.

AUTHOR CONTRIBUTIONS

MG wrote the draft of the manuscript. QL and JH edited and commented on the draft. All authors approved the manuscript for publication.

FUNDING

This work was funded by the Early Career Scheme Grant from Hong Kong Research Grant Council (No. 27202419).

ACKNOWLEDGMENTS

We thank all the reviewers for reviewing the papers in the Research Topic.

REFERENCES

Ahilan, S., Guan, M., Wright, N., Sleigh, A., Allen, D., Arthur, S., et al. (2019). Modelling the long-term suspended sedimentological effects on stormwater pond performance in an urban catchment. *J. Hydrol.* 571, 805–818. doi: 10.1016/j.jhydrol.2019.02.002

Golden, H. E., and Hoghooghi, N. (2018). Green infrastructure and its catchment-scale effects: an emerging science. *Wiley Interdisc. Rev. Water* 5:e1254. doi: 10.1002/wat2.1254

Guan, M., Sillanpää, N., and Koivusalo, H. (2015a). Modelling and assessment of hydrological changes in a developing urban catchment. *Hydrol. Process.* 29, 2880–2894. doi: 10.1002/hyp.10410

Guan, M., Sillanpää, N., and Koivusalo, H. (2015b). Assessment of LID practices for restoring pre-development runoff regime in an urbanized catchment in southern Finland. *Water Sci. Technol.* 71, 1485–1491. doi: 10.2166/wst.2015.129

IPCC (2013) *Climate Change 2013: Synthesis Report*. Valencia.

Kabir, S., Patidar, S., Xia, X., Liang, Q., Neal, J., and Pender, G. (2020). A deep convolutional neural network model for rapid prediction of fluvial flood inundation. *J. Hydrol.* 590:125481. doi: 10.1016/j.jhydrol.2020.125481

Sales-Ortells, H., and Medema, G. (2015). Microbial health risks associated with exposure to stormwater in a water plaza. *Water Res.* 74, 34–46. doi: 10.1016/j.watres.2015.01.044

Van der Vliet, J. C., Van Knapen, F., and de Roda Husman, A. M. (2014). Quantitative assessment of infection risk from exposure to waterborne pathogens in urban floodwater. *Water Res.* 48, 90–99. doi: 10.1016/j.watres.2013.09.022

Conflict of Interest: The authors declare that the research was conducted in the absence of any commercial or financial relationships that could be construed as a potential conflict of interest.

frontiers in Earth Science

ORIGINAL RESEARCH
published: 24 April 2020
doi: 10.3389/feart.2020.00125

Effects of Sponge City Development on Soil Moisture and Water Quality in a Typical City in the Loess Plateau in China

Lu Jia[1], Guoce Xu[1], Miansong Huang[2], Zhanbin Li[1], Peng Li[3], Zhenxi Zhang[3], Bin Wang[3], Yixin Zhang[3], Jiaxin Zhang[3] and Yuting Cheng[3]*

[1] State Key Laboratory of Eco-hydraulics in Northwest Arid Region of China, Xi'an University of Technology, Xi'an, China, [2] Ningxia Capital Sponge City Construction & Development Company Limited, Guyuan, China, [3] Key Laboratory of National Forestry Administration on Ecological Hydrology and Disaster Prevention in Arid Regions, Xi'an University of Technology, Xi'an, China

OPEN ACCESS

Edited by:
Qiuhua Liang, Loughborough University, United Kingdom

Reviewed by:
Jiahong Liu, China Institute of Water Resources and Hydropower Research, China
Kaibo Wang, Institute of Earth Environment (CAS), China
Zhengchao Zhou, Shaanxi Normal University, China
Ming Xiao Zhang, China Institute of Water Resources and Hydropower Research, China

***Correspondence:**
Guoce Xu
xuguoce_x@163.com

Specialty section:
This article was submitted to Hydrosphere, a section of the journal Frontiers in Earth Science

Received: *05 October 2019*
Accepted: *01 April 2020*
Published: *24 April 2020*

Citation:
Jia L, Xu G, Huang M, Li Z, Li P, Zhang Z, Wang B, Zhang Y, Zhang J and Cheng Y (2020) Effects of Sponge City Development on Soil Moisture and Water Quality in a Typical City in the Loess Plateau in China. Front. Earth Sci. 8:125. doi: 10.3389/feart.2020.00125

Changes in soil moisture following the establishment of sponge cities play a key role in the regulation of the relationship between surface runoff and rain resources in arid and semi-arid regions of the Loess Plateau. Based on soil moisture and rainfall monitoring data obtained at the fine-scale (per 10-cm depth and hourly), temporal and spatial variation in soil moisture under different sponge measures and their responses to rain events were analyzed, in addition to water quality changes were investigated by water sampling. The results showed, from 2000 to 2018, the area of farmland greatly decreased from 56.88 to 5.02% in Guyuan, while the area of construction land increased from 29.24 to 45.96%. The area of changes in Guyuan accounted for 63.68% of the total area. Precipitation in July and August was large, and accounted for 19.11 and 23.24% of the multi-year average precipitation, respectively. The grasslands and sunken green spaces exhibited good water retention effects, with average soil moisture of 14.40 and 13.77% during the study period, and 18.48 and 15.52% during the rain event, respectively. During the rain event, the total nitrogen (TN), ammonia nitrogen (NH^3-N), available phosphorus (AP), and total phosphorus (TP) can be effectively reduced by the sunken green spaces, with average concentrations of 0.79, 0.28, 0.03, and 0.05 mg/L, respectively. The development of sponge measures could improve the urban ecological environment and hydrological conditions in the Loess Plateau, and increase the potential utilization of urban rainwater resources.

Keywords: soil moisture, water quality, rain event, sponge city, the Loess Plateau

INTRODUCTION

With the implementation of the reform and opening up policy in China, remarkable social and economic developments have been observed, and urbanization rate increased from 17.55% in 1977 to 57.35% in 2016 (Chen, 2007; Liu and Luk, 2009; Wang et al., 2017a). Urbanization has altered urban hydrological conditions and floods in urban spaces have become widespread in China (Zheng et al., 2013; Hu et al., 2015, Lyu et al., 2017, 2018a,b; He et al., 2018). Heavy rains and floods hit

about 200 cities annually in China (Yin et al., 2015; Sang and Yang, 2017; Lyu et al., 2018c). On July 21 2012, in Beijing, 79 people died following heavy rains (Yu and Liu, 2015). Wuhan in China often has substantial losses following inundation in the rainy season (Lyu et al., 2018a). Therefore, the construction of a sponge city was proposed in 2012, and the concept of low impact development was adhered to in the development of sponge cities in China (Xia et al., 2017; Yuan et al., 2017; Wang et al., 2017b). Regulating urban hydrological processes and increasing the storage capacity of urban rainwater are key goals in the development of sponge cities, and since 2015, a pilot sponge city is being constructed in China (Sang and Yang, 2017; Xia et al., 2017).

Sponge city measures include planting grasslands, establishing grass ditches and sunken green spaces, and other measures (Shafique and Kim, 2015). By adopting sponge measures, sources of flood runoff could be controlled, and the hydrological characteristic of the city surface was changed by regulating soil moisture using different sponge measures (Wang et al., 2009, 2017a). Water could also be accumulated and redistributed, which was as a way of regulating urban hydrological processes, to reduce floods and to improve urban water cycling. Therefore, it is critical to investigate the changes in soil hydrological characteristics that occur following the construction of sponge cities.

The water collected and stored in the soil is the result of the combined effects of precipitation infiltration, redistribution, evaporation, and water uptake by plant roots (Heathman et al., 2009; Chaney et al., 2015; Hou et al., 2015; Xu et al., 2017; Xiao et al., 2019). Soil water content influences penetration strongly, and the depth of penetrating decreases dramatically with increasing of water content (Njoku and Rague, 1996). At present, in order to explore the impact of low-impact development measures on hydrological process, numerous studies have been carried out to analyze the changing characteristics of soil moisture and to explore the impact of low-impact development strategies on water quality. Xu et al. (2016) have shown that soil depth influences the spatial and temporal distribution of soil water content significantly. Studies by Davis et al. (2009) have shown that bioretention measures such as rainwater gardens reduce runoff and flood peaks considerably, while storing rain. De Busk and Wynn (2011) observed that bioretention could reduce 97 to 99% of surface runoff, and Ahiablame and Shakya (2016) observed that different sponge measures reduced urban flooding significantly. In addition, Liu et al. (2016) and others have shown that the stable infiltration rate of a sunken greens spaces ranged between 0.5 and 2.3 mm/min. Furthermore, Wang et al. (2012) showed the runoff that can be accommodated by the water grass ditches is 2.16 times that of the hard road. The above studies have reported some effects of sponge measures on runoff and hydrological processes. However, only few studies have explored spatial and temporal variation of soil moisture and water quality under different sponge measures, particularly in the course of rain events. Therefore, it is necessary to study the hydrological characteristics of soil water and water quality under different sponge measures, and the responses during rain events.

As the largest and deepest loess deposit in the world, the Loess Plateau covers an area of 640,000 km^2 (Fu et al., 2017). Most of the plateau is located in semi-arid zone with low precipitation. The Loess Plateau is an area associated with soil erosion and drought, and its ecological environment is very fragile. In recent years, urbanization activities in the Loess Plateau have increased, accompanied by the frequent extreme precipitation events. Due to the collapsible characteristics of the Loess Plateau, the damage caused by urban flood is more severe than in other areas. In April 2016, Guyuan city located in the western part of China's Loess Plateau became the second pilot city among the 16 declared sponge cities in China. Assessing the impact of sponge city construction on soil moisture and water quality in cities in the Loess Plateau could reveal some rules that could facilitate the improvement of the ecological environment in the Loess Plateau.

Therefore, the present study analyzed the effects of sponge city measures in Guyuan city on the Loess Plateau, on soil moisture changes and water quality changes. The purpose of the present study is to: (1) analyze land-use change processes in the course of urbanization in Guyuan city; (2) quantitatively analyze the temporal and spatial changes of soil water content in the soil profile under different sponge measures and the response to rain events; and (3) evaluate impacts of different sponge measures during a rain event on water quality.

MATERIALS AND METHODS

Study Area

Guyuan city is located on the bank of Qingshui River to the north of Liupan Mountain on the Loess Plateau (**Figure 1**). The terrain is high in the south and low in the north. The coordinates are 36°00′N∼106°16′E and the altitude is 1753 m. It falls under the warm temperate semi-arid climate zone. It has drought and little precipitation, and the climate is a typical mid-temperate continental climate. The multi-year average temperature is 5°C and the multi-year average precipitation is 438.5 mm. The annual precipitation varied greatly among years, and mainly concentrated in June to September, accounting for 79.37% of the multi-year average precipitation. The rain events are short, water resources are scarce. The soil in the Loess Plateau is collapsible. The vegetation is dominated by *Larix principis-rupprechtii* and *Hippophae salicifolia*. The study site is located in the Rose Garden Community in the western part of Yuanzhou district of Guyuan city. The sponges in the study area are covered with water grass ditches, sunken green spaces, and grasslands.

Rainfall and Soil Moisture Monitoring

Three soil moisture monitoring tubes (ET100-Pro, Insentek, Beijing, China) were installed in the middle of the three different sponge measures, including water grass ditches, grasslands, and sunken green spaces, to monitor changes in soil moisture content. Volumetric soil moisture was obtained at 10-cm intervals to a depth of 60 cm using each moisture monitoring tube from August 30, 2018, to August 29, 2019. The soil layer from the top to the bottom was divided into six layers at equal intervals, and soil moisture content at each layer was measured every hour.

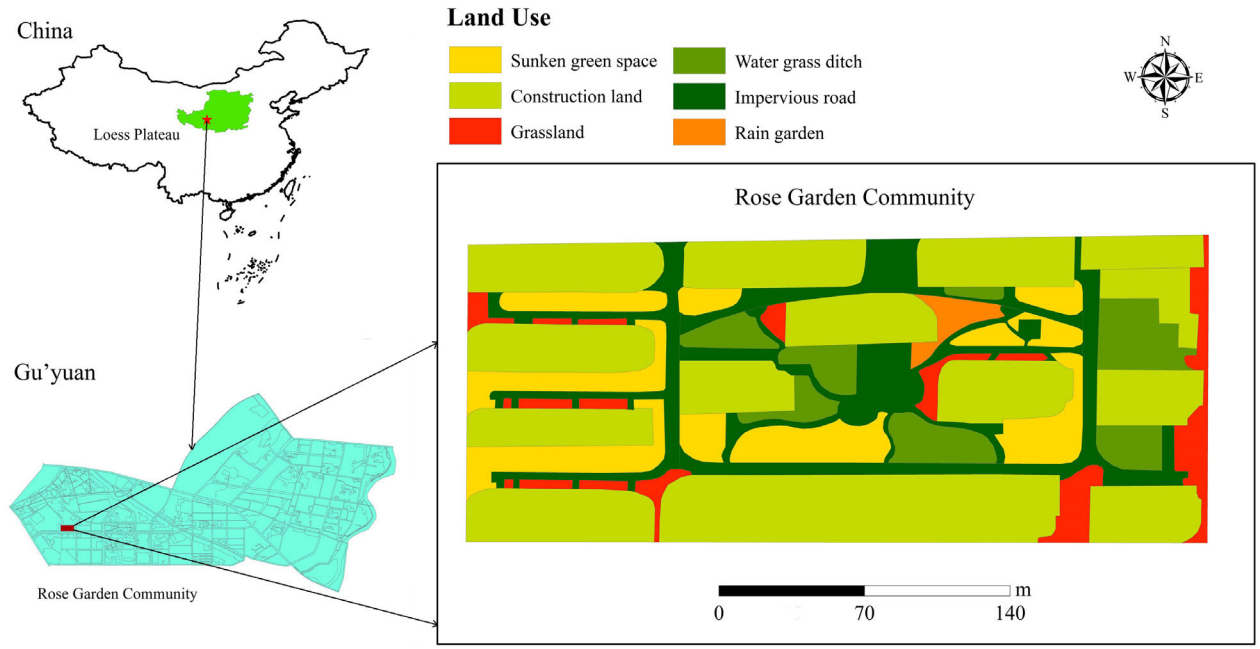

FIGURE 1 | Location of the study area.

Since the precipitation in Guyuan was concentrated in July and August, the present study monitored the rain events from 00:00 on July 16, 2019, to 24:00 on August 29, 2019. In addition, rain event was monitored from 10:00 on July 21, 2019, to 22:00 on July 21, 2019, and the rainfall data were recorded every 5 min. Rainfall data were obtained from the Guyuan weather station.

Water Quality Analysis

The total nitrogen (TN) content, ammonia nitrogen (NH^3-N) content, nitrate-nitrogen (NN) content, total phosphorus (TP) content, and available phosphorus (AP) content of the water samples were determined using an automatic Kjeldahl apparatus (Kjeltec 8400, FOSS Analytical, Hillerød, Denmark).

Water samples were collected from the three sponge measures at 21 time points during a rain event from 10:00 on July 21, 2019, to 22:00 on July 21, 2019 (**Figure 2**). The time distribution of sampling points is relatively uniform, and changes in water quality during rain event can be captured. The first sample was obtained at 12:45 on July 21, 2019, and the last sample at 18:30 on July 21, 2019. During the sample collection, three replicates were collected for each sample, and water quality indicators such as TN, TP, NH^3-H, NN, and AP were tested in each sample.

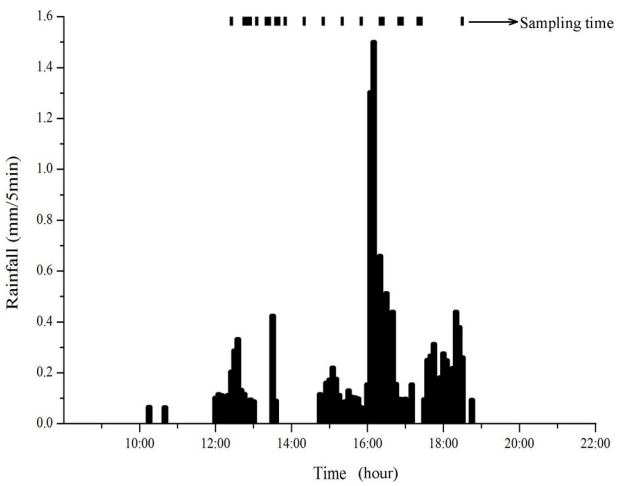

FIGURE 2 | Rain event process and water sampling time every 5 min on July 21, 2019.

RESULTS

Land-Use Change

In 2000, 2010, and 2018, there were mainly seven land-use in Guyuan city, including road, construction land, forestland, farmland, grassland, water system land, and unutilized land, as shown in **Figures 3A–C**. Construction land, farmland, and forestland were the main types of land-use in Guyuan in 2000, 2010, and 2018. The proportion of construction land in Guyuan increased from 29.24% in 2000 to 45.96% in 2018, increasing by 0.93% per year. The proportion of farmland decreased from 56.88% in 2000 to 5.02% in 2018, which was mainly observed in the central and northern parts of Guyuan city. Similarly, the area of water system land decreased slightly, and the areas of the other land-use exhibited increasing trends.

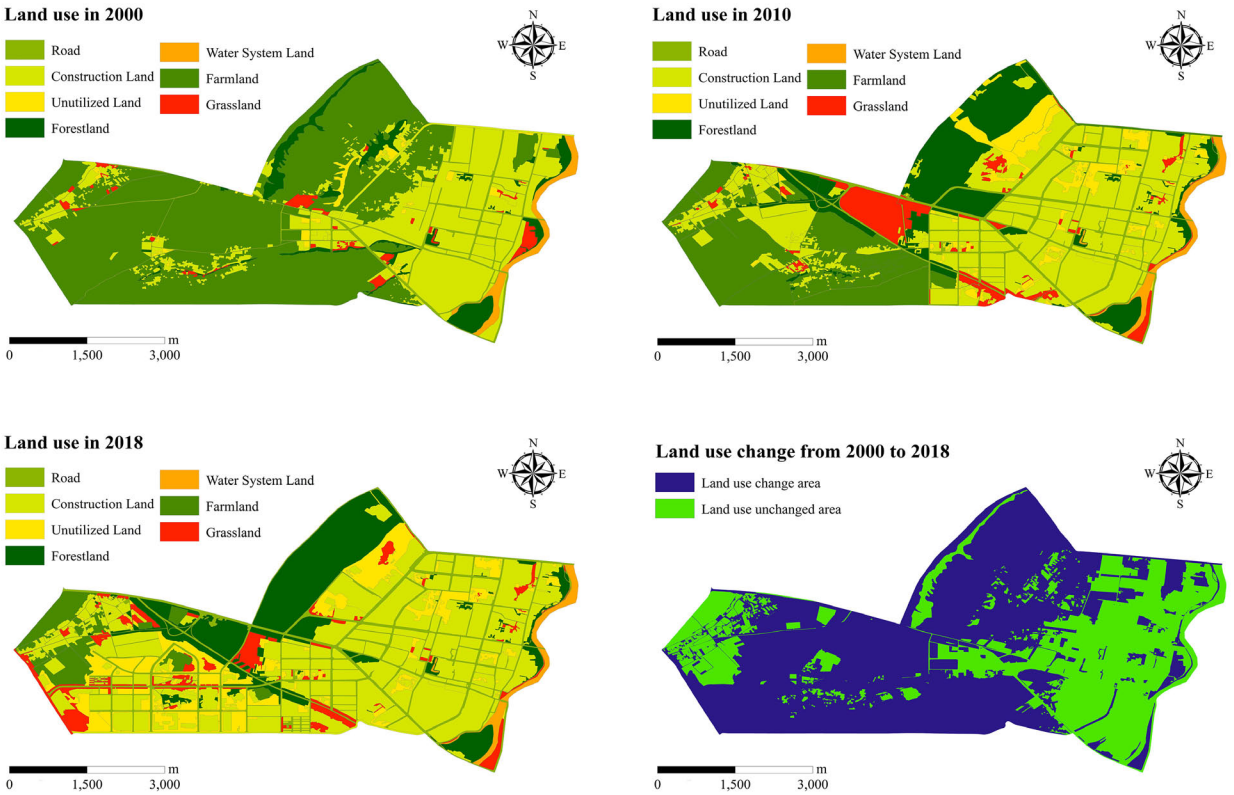

FIGURE 3 | Spatial distribution of land-use change in Guyuan City from 2000 to 2018.

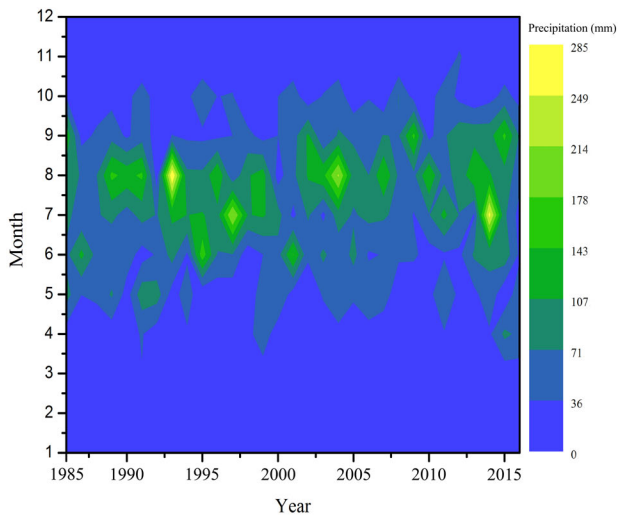

FIGURE 4 | Monthly precipitation changes in Guyuan City from 1985 to 2015.

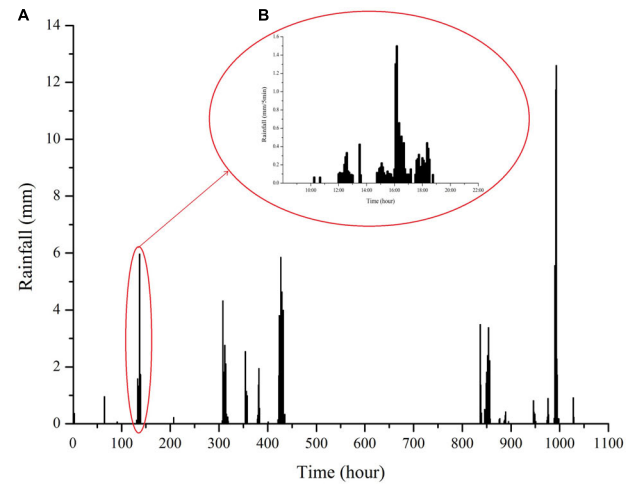

FIGURE 5 | Hourly rainfall from 1:00 on July 16, 2019 to 24:00 on August 29, 2019 in Guyuan City **(A)**; From 10:00 to 22:00 on July 21, 2019, every 5 min rainfall of the rain event in Guyuan City **(B)**.

The land use change area accounts for 63.68% of the total area, mainly in the central and northern regions from 2000 to 2018 (**Figure 3D**).

Variation in Precipitation and Rainfall

The monthly changes in precipitation in Guyuan city from 1985 to 2015 were shown in **Figure 4**. From 1985 to 2015, maximum

annual precipitation and minimum annual precipitation are 703.2 mm and 313.9 mm, respectively. And the average annual precipitation was 438.5 mm. The coefficient of variation of annual precipitation reaches 0.21, and the inter-annual variability of annual precipitation was weak. Rainfall is the main form of precipitation during the flood season from June to October. Maximum monthly rainfall and minimum monthly rainfall are 285 mm and 0 mm. And the proportion of rainfall in August and July of the total annual precipitation were the greatest, in the following proportion: 23.24 and 19.11%.

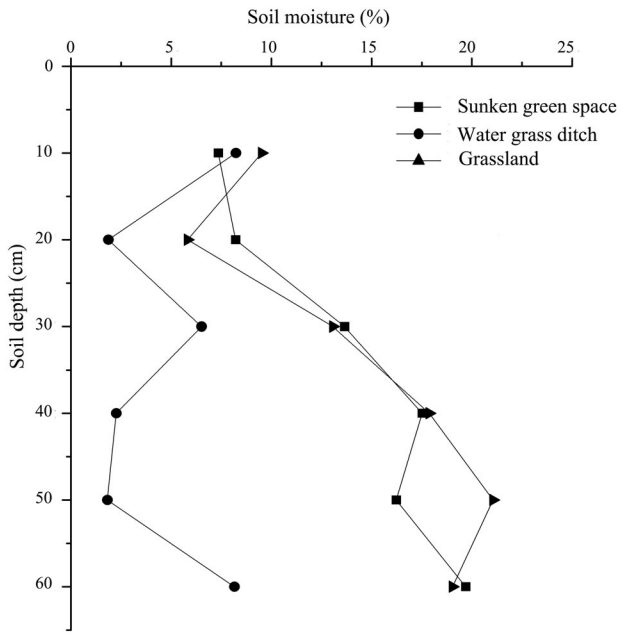

FIGURE 6 | Vertical changes of average soil moisture content under different sponge measures.

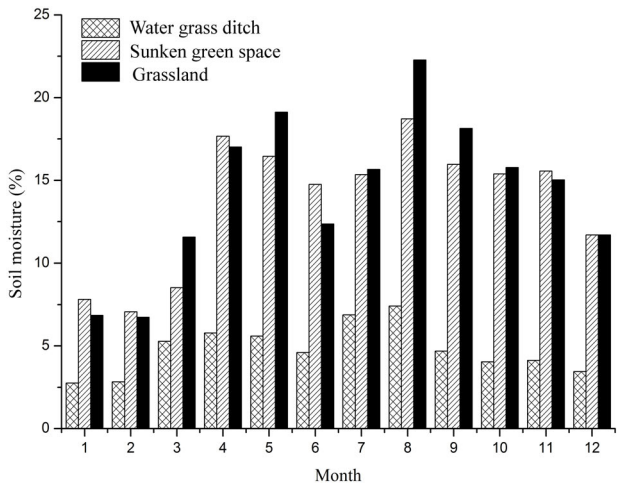

FIGURE 7 | Changes of average soil moisture content in different months under different sponge measures.

The hourly rainfall from 00:00 on July 16, 2019, to August 29, 2019 in Guyuan was shown in **Figure 5A**. The total rainfall was 133.87 mm, accounting for 30.53% of the multi-year average precipitation. The rain event from 10:00 on July 21, 2019 to 22:00 on July 21, 2019 were shown in **Figure 5B**. The rain event began falling at 10:15 on July 21, 2019, and ended at 18:45. It lasted for 510 min and lasted nearly 9 h. The total rainfall was 13.63 mm and the average rain intensity was 0.03 mm/min.

Temporal and Spatial Changes in Soil Moisture Under Different Sponge Measures

The changes in average soil moisture at different soil depths under three types of sponge measures, such as grasslands, sunken green spaces, and water grass ditches in Guyuan,

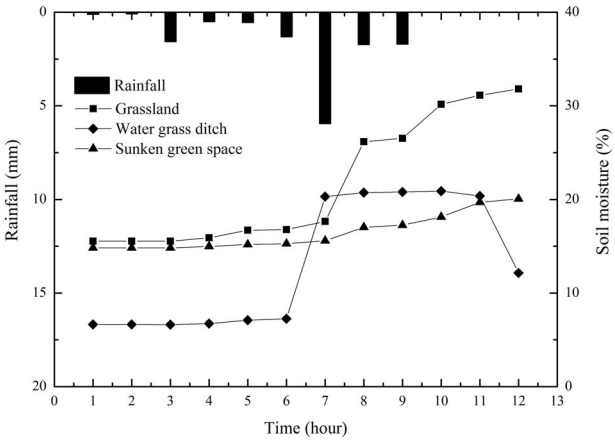

FIGURE 8 | Changes of average soil moisture content under different sponge measures during the rain event.

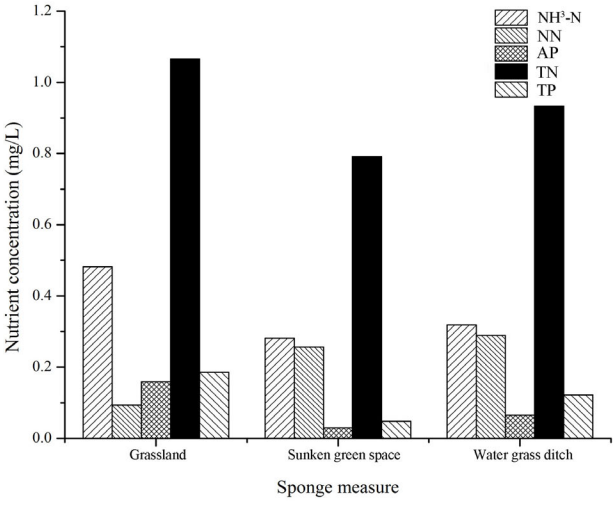

FIGURE 9 | Water quality changes under different sponge measures during the rain event.

as shown in **Figure 6**. During the monitoring period, the average soil moisture in water grass ditches varied with no clear pattern with an increase in soil depth, and the average value was stable at 4.80%. The average soil moisture in the grasslands and the sunken green spaces increased with an increase in soil depth, with average values of 14.40 and 13.77%, respectively.

The monthly average soil moisture under the three sponge measures over the 12-month monitoring period was shown in **Figure 7**. The average monthly soil moisture under the three sponge measures were 14.35, 4.78, and 13.74%, respectively. The monthly average soil moisture in the grasslands and sunken green spaces increased significantly from April to December. Compared with water grass ditches, average soil moisture in the grasslands and the sunken green spaces varied more greatly.

Figure 8 showed the variations in average soil moisture in grasslands, water grass ditches, and sunken green spaces on the process of the rain event. The average soil moisture under the three sponge measures exhibited increasing trends with an increase in rainfall duration. The rainfall peaked at the 7th hour, and the average soil moisture in the water grass ditches also increased significantly. However, the average soil moisture in the grassland and the sunken green space increased at the 8th hour, and the response to rainfall was delayed. When the rain event was end, the average soil moisture in the water grass ditches began to decrease, but the average soil moisture in the grassland and the sunken green space continued to increase. During the entire duration of rain event, the average soil water in the grassland, water grass ditches, and the sunken green space were 18.48, 11.43, and 15.52%, respectively.

Water Quality Change Under Different Sponge Measures

During the rain event, there were obvious differences in the five water quality indicators among the three sponge measures

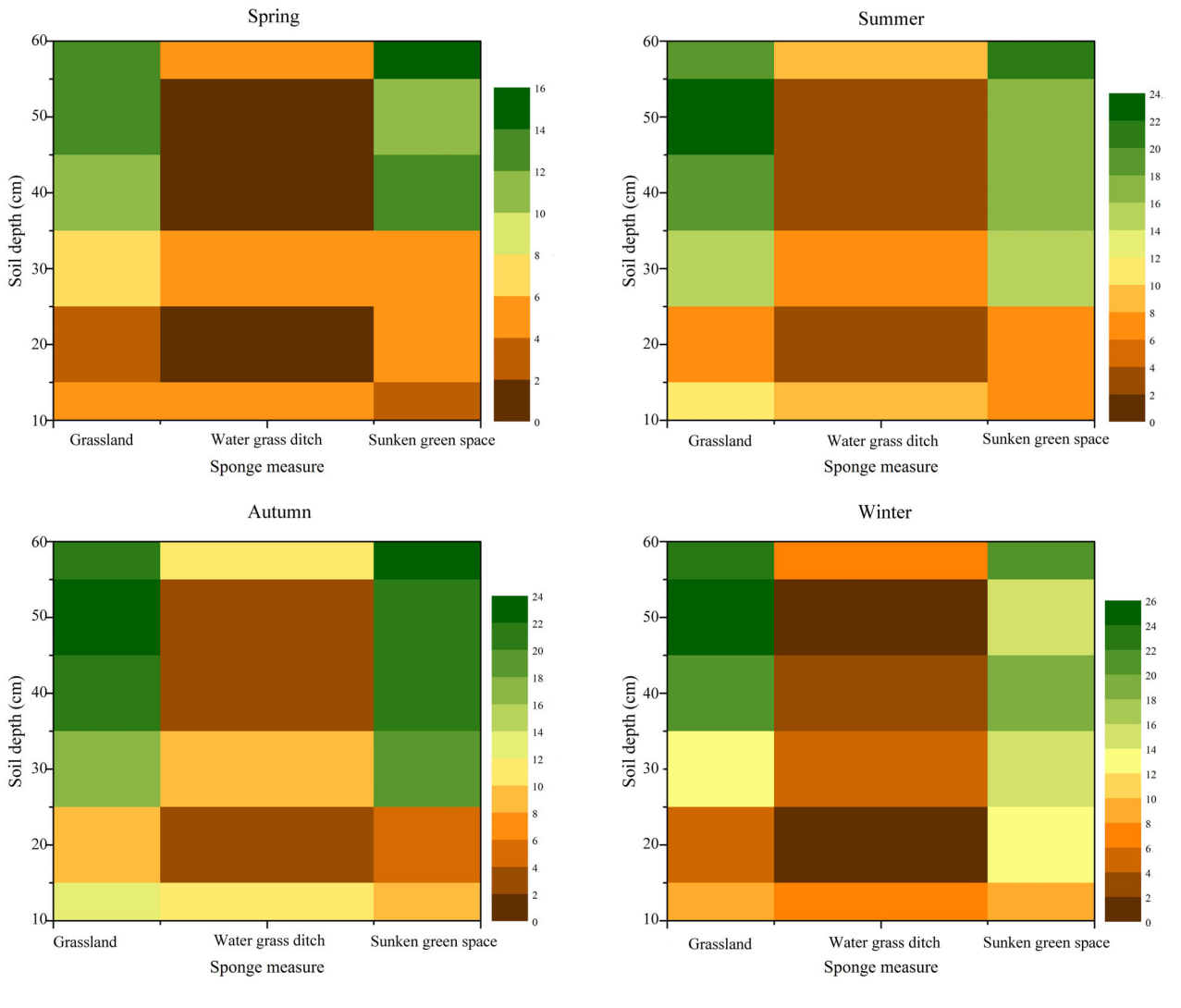

FIGURE 10 | Seasonal differences in soil moisture under different soil depths under different sponge measures.

(**Figure 9**). The average TN concentration in the water was the highest under three sponge measures, such as grassland, water grass ditch and sunken green space, reaching 1.07, 0.93, and 0.79 mg/L, respectively. Except for TN, compared with other three water quality indicators, the average concentration of NH^3-H was also higher. The average concentration of TN and NH^3-H in the water under the grassland were the highest, compared with the water grass ditch and sunken green space. Among the five water quality indicators, the average concentration of NN in the water under grassland was the lowest, and the average concentration of NN in the water under the water grass ditch and sunken green space was much higher than that of grassland. However, the average concentration of AP in the water was the lowest under the water grass ditch and sunken green space, but the average concentration of AP in the water in the grassland was higher. Compared with water grass ditch and grassland, the average concentration of TN, NH^3-H, AP, and TP in the water under the sunken green space was the lowest, with concentrations of 0.79, 0.28, 0.03, and 0.05 mg/L, respectively.

DISCUSSION

Temporal and Spatial Differences in Soil Moisture Content Under Different Sponge Measures

Increasing use of impermeable land-uses, such as building land and rural roads, would affect the spatial and temporal changes of soil hydrological processes. The construction of sponge measures

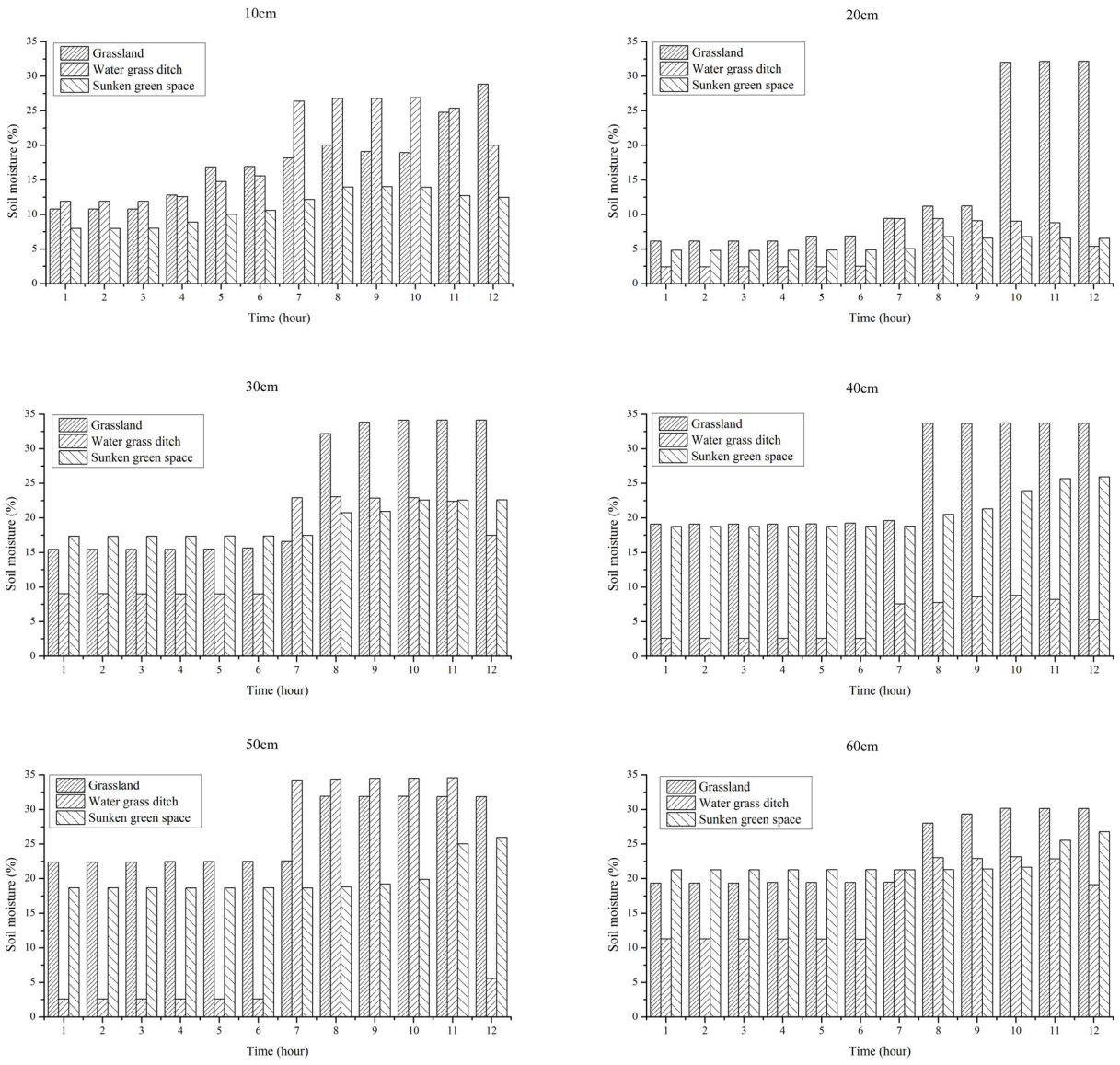

FIGURE 11 | Soil moisture at different soil depths under different sponge measures during the rain event.

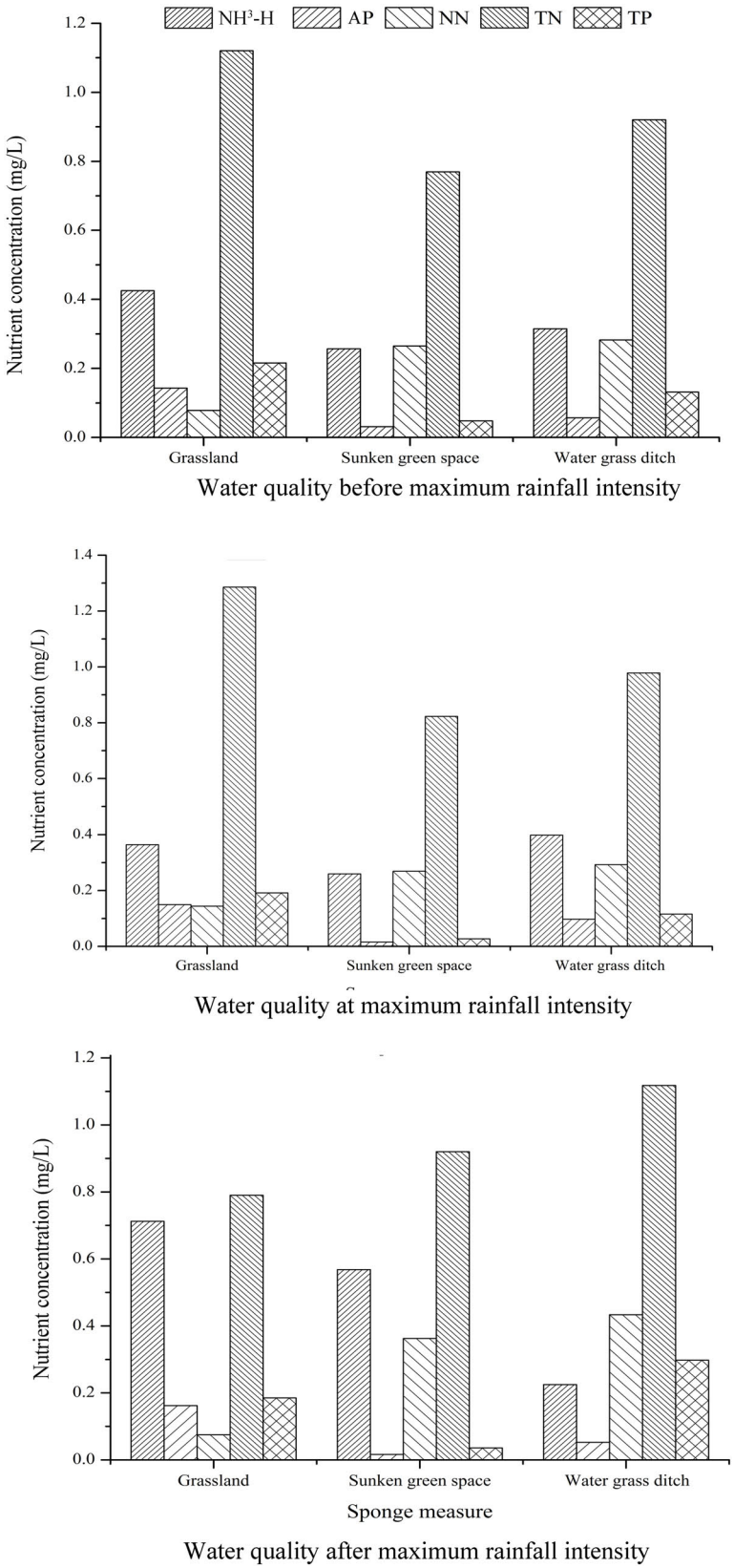

FIGURE 12 | Water quality changes in three stages during rain events.

can regulate soil hydrological processes. There were differences in soil moisture under different sponge measures (Rosenbaum et al., 2012). Soil moisture was higher in the three sponge measures in summer and autumn compared to spring and winter (**Figure 10**), and this may be affected by rainfall, which was similar to the results of previous studies (Liu and Shao, 2014; Wang et al., 2015; Liao et al., 2017; Xu et al., 2017). The soil moisture content in the water grassland ditches in the four seasons was not high and fluctuated with an increase in soil depth. The cause of the phenomenon was probably due to the better drainage of the water grassland ditches. Soil moisture in the sunken green spaces and grassland increased with an increase in soil depth, which was more pronounced in fall, which may be mainly because time changes in soil moisture were affected by climatic factors (such as precipitation and temperature; Entin et al., 2000; Koster et al., 2004).

At a depth of 10 cm, the soil moisture content under all the three sponge measures increased gradually with an increase in the duration of rain event (**Figure 11A**). Soil moisture was strongly affected by topographic factors (Lin et al., 2006). Root distribution had a strong influence on soil moisture of the top soil profile (Jia et al., 2017; Xu et al., 2017). When the rainfall peaked at the 7th hour, the soil moisture increased significantly under all the three sponge measures, and the changes in soil moisture in the grasslands were the most notable. This may be related to the vegetation cover of the grassland, because the grassland vegetation there was sparse and not high. At 30, 40, 50, and 60 cm soil depth, the soil moisture in the grasslands and sunken green spaces were very high, which may be because the deep soil moisture was relatively stable (He et al., 2012), which was also related to the magnitude of rain events, as shown in **Figures 11C–F** (Heisler-White et al., 2008).

Potential Uses of Rain Resources Following the Construction of a Sponge City in Guyuan

One of the main purposes of sponge city development was to control water quality and water recycling, to increase the potential of rainwater resources, and to make better use of rain resources (Matteo et al., 2019; Nguyen et al., 2019). During the construction of the sponge city in Guyuan, the implementation of different sponge measures had affected urban water resources considerably, particularly with regard to soil moisture and water quality in time and space. The implementation of different sponge measures had also influenced the distribution of soil moisture in space and time. The water-holding capacity of the sunken green spaces and the grasslands was significantly higher than that of the water grass ditches. The grassland was very sensitive to rainfall. Similarly, water quality was affected variably. The sunken green spaces reduced the TP and AP in the water significantly, as shown in **Figure 9**. The changes observed after the implementation of the sponge measures imply that the rainwater resources had different potential uses. A portion of the recovered rain resources could be used to alleviate water shortages in cities and to improve urban ecology (Su et al., 2019). **Figures 12A–C** showed the changes in water quality before maximum rainfall intensity, at maximum rainfall intensity, and after maximum rainfall intensity. At different stages of the rainfall event, the sunken green spaces could always decrease the TP and AP concentrations. Therefore, water purification could be achieved by establishing sunken green spaces in the city. In addition, the establishment of grasslands and sunken green spaces may facilitate water conservation, surface runoff reduction, and flood risk mitigation in case of heavy rain (Mehrabadi et al., 2013; Mahmoud et al., 2014; Karim et al., 2015).

CONCLUSION

With the increase in urbanization in Guyuan, the permeable surfaces in the form of farmland had been decreasing, and the construction land had been increasing. Due to the unique climatic conditions of the Loess Plateau of China, the precipitation during the year was concentrated in July and August, and the soil moisture in the soil layer increased significantly during the July-August rainy season. Grasslands, water grass ditches, and sunken green spaces had been established during the development of the sponge city. When rain events occurred, the grasslands and the sunken green spaces could conserve water, simultaneously, the sunken green spaces could purify the water. The development of sponge cities in the Loess Plateau in China could increase the value of rainwater resources and their potential applications.

DATA AVAILABILITY STATEMENT

All datasets generated for this study are included in the article/supplementary material.

AUTHOR CONTRIBUTIONS

LJ designed experiments, analyzed the results, and wrote manuscripts. GX, ZL, and PL providing experimental funding and equipment. MH, ZZ, BW, YZ, JZ, and YC conducted experiments.

FUNDING

This research was supported by the National Key Research and Development Program (2016YFC0402404), the National Natural Science Foundations of China (No. 51979219), Shaanxi Province Innovation Talent Promotion Plan Project Technology Innovation Team (No. 2018TD-037), and the Research Program for Key Technologies of Sponge City Construction and Management in Guyuan City (Grant NO. SCHM-2018-0103).

ACKNOWLEDGMENTS

In addition, we thank the reviewers for their useful comments and suggestions.

REFERENCES

Ahiablame, L., and Shakya, R. (2016). Modeling flood reduction effects of low impact development at a watershed scale. *J. Environ. Manage.* 171, 81–91. doi: 10.1016/j.jenvman.2016.01.036

Chaney, N. W., Roundy, J. K., Herrera-Estrada, J. E., and Wood, E. F. (2015). High-resolution modeling of the spatial heterogeneity of soil moisture: applications in network design. *Water Resour. Res.* 51, 619–638. doi: 10.1002/2013wr014964

Chen, J. (2007). *2008 Economic Blue Book on China's Economic Situation Analysis and Prediction*. Beijing: Social Sciences Documents Publishing House.

Davis, A. P., Hunt, W. F., Traver, R. G., and Clar, M. (2009). Bioretention technology: overview of current practice and future needs. *J. Environ. Eng.* 135, 109–117. doi: 10.1061/(asce)0733-9372(2009)135:3(109)

De Busk, K., and Wynn, T. (2011). Storm-water bioretention for runoff quality and quantity mitigation[J]. *J. Environ. Eng.* 137, 800–808. doi: 10.1061/(asce)ee.1943-7870.0000388

Entin, J. K., Robock, A., Vinnikov, K. Y., Hollinger, S. E., Liu, S., and Namkai, A. (2000). Temporal and spatial scales of observed soil moisture variations in the extratropics. *J. Geophys. Res.* 105, 865–877.

Fu, B. J., Wang, S., Liu, Y., Liu, J. B., Liang, W., and Miao, C. Y. (2017). Hydrogeomorphic ecosystem responses to natural and anthropogenic changes in the Loess Plateau of China. *Annu. Rev. Earth Planet. Sci.* 45, 223–243. doi: 10.1146/annurev-earth-063016-020552

He, B. S., Huang, X. L., Ma, M. H., Chang, Q. R., Tu, Y., Li, Q., et al. (2018). Analysis of flash flood disaster characteristics in China from 2011 to 2015. *Nat. Hazards* 90, 407–420. doi: 10.1007/s11069-017-3052-7

He, Z., Zhao, W., Liu, H., and Chang, X. (2012). The response of soil moisture to rainfall event size in subalpine grassland and meadows in a semi-arid mountain range: a case study in northwestern china's qilian mountains. *J. Hydrol.* 183–190. doi: 10.1016/j.jhydrol.2011.11.056

Heathman, G. C., Larose, M., Cosh, M. H., and Bindlish, R. (2009). Surface and profile soil moisture spatio-temporal analysis during an excessive rainfall period in the Southern Great Plains, USA. *Catena* 78, 159–169. doi: 10.1016/j.catena.2009.04.002

Heisler-White, J. L., Knapp, A. K., and Kelly, E. F. (2008). Increasing precipitation event size increases aboveground net primary productivity in a semi-arid grassland. *Oecologia* 158, 129–140. doi: 10.1007/s00442-008-1116-9

Hou, J., Liang, Q., Zhang, H., and Hinkelmann, R. (2015). An efficient unstructured MUSCL scheme for solving shallow water equations. *Environ. Model. Softw.* 66, 131–152. doi: 10.1016/j.envsoft.2014.12.007

Hu, S. L., Han, C. F., and Meng, L. P. (2015). A scenario planning approach for propositioning rescue centers for urban waterlog disasters. *Comput. Ind. Eng.* 87, 425–435. doi: 10.1016/j.cie.2015.05.036

Jia, X. X., Shao, M. A., Zhu, Y. J., and Luo, Y. (2017). Soil moisture decline due to afforestation across the Loess Plateau, China. *J. Hydrol.* 546, 113–122. doi: 10.1016/j.jhydrol.2017.01.011

Karim, M. R., Bashar, M. Z. I., and Imteaz, M. A. (2015). Reliability and economic analysis of urban rainwater harvesting in a megacity in Bangladesh. *Resour. Conserv. Recycle* 104(Part A), 61–67. doi: 10.1016/j.resconrec.2015.09.010

Koster, R. D., Dirmeyer, P. A., Guo, Z., Bonan, G., Chan, E., and Cox, P. (2004). Regions of strong coupling between soil moisture and precipitation. *Science* 305, 1138–1140. doi: 10.1126/science.1100217

Liao, K., Lai, X., Zhou, Z., and Zhu, Q. (2017). Applying fractal analysis to detect spatio-temporal variability of soil moisture content on two contrasting land use hillslopes. *CATENA* 157, 163–172. doi: 10.1016/j.catena.2017.05.022

Lin, H. S., Kogelmann, W., Walker, C., and Brunset, M. A. (2006). Soil moisture patterns in a forested catchment: a hydropedological perspective[J]. *Geoderma* 131, 345–368. doi: 10.1016/j.geoderma.2005.03.013

Liu, B. X., and Shao, M. A. (2014). Estimation of soil water storage using temporal stability in four land uses over 10 years on the Loess Plateau, China. *J. Hydrol.* 517, 974–984. doi: 10.1016/j.jhydrol.2014.06.003

Liu, C., Zhang, Y., Wang, Z., Wang, Y., and Bai, P. (2016). The LID pattern for maintaining virtuouswater cycle in urbanized area: a preliminary study of planning and techniques for sponge City. *J. Nat. Resour.* 31, 719–731.

Liu, W. M., and Luk, M. K. R. (2009). Reform and opening up: way to the sustainable and harmonious development of air transport in china. *Transp. Policy* 16, 220–223.

Lyu, H. M., Sun, W. J., Shen, S. L., and Arulrajah, A. (2018a). Flood risk assessment in metrosystems of mega-cities using a GIS-based modeling approach. *Sci. Total Environ.* 626, 1012–1025. doi: 10.1016/j.scitotenv.2018.01.138

Lyu, H. M., Xu, Y. S., Cheng, W. C., and Arulrajah, A. (2018b). Flooding hazards across southern China and prospective sustainability measures. *Sustainability* 10:1682. doi: 10.3390/su10051682

Lyu, H. M., Shen, S. L., and Arulrajah, A. (2018c). Assessment of geohazards and preventative countermeasures using AHP incorporated with GIS in Lanzhou China. *Sustainability* 10:304. doi: 10.3390/su10020304

Lyu, H. M., Wang, G. F., Cheng, W. C., and Shen, S. L. (2017). Tornado hazards on June 23rd in Jiangsu Province, China: preliminary investigation and analysis. *Nat. Hazards* 85, 597–604. doi: 10.1007/s11069-016-2588-2

Mahmoud, W. H., Elagib, N. A., Gaese, H., and Heinrich, J. (2014). Rainfall conditions and rainwater harvesting potential in the urban area of Khartoum. *Resour. Conserv. Recycle* 91, 89–99. doi: 10.1016/j.resconrec.2014.07.014

Matteo, R., Andrew, N., Yong, P., Jian-min, Z., Craig, L., Yan-peng, C., et al. (2019). Urban and river flooding: comparison of flood risk management approaches in the UK and China and an assessment of future knowledge needs. *Water Sci. Eng.* 12, 274–283. doi: 10.1016/j.wse.2019.12.004

Mehrabadi, M. H. R., Saghafian, B., and Fashi, F. H. (2013). Assessment of residential rainwater harvesting efficiency formeeting non-potablewater demands in three climate conditions. *Resour. Conserv. Recycle* 73, 86–93. doi: 10.1016/j.resconrec.2013.01.015

Nguyen, T. T., Ngo, H. H., Guo, W. S., Wang, X. C., Ren, N. Q., Li, G. B., et al. (2019). Implementation of a specific urban water management: sponge City. *Sci. Total Environ.* 652, 147–162. doi: 10.1016/j.scitotenv.2018.10.168

Njoku, E. G., and Rague, B. W. (1996). *Spatial and Temporal Trends in Land Surface Moisture and Temperature Observable using Data from the Nimbus-7 Microwave Radiometer. IGARSS 96 Remote Sensing for a Sustainable Future*. Pasadena, CA: CALTECH.

Rosenbaum, U., Bogena, H. R., Herbst, M., Huisman, J. A., and Vereecken, H. (2012). Seasonal and event dynamics of spatial soil moisture patterns at the small catchment scale. *Water Resour. Res.* 48, 3472–3476.

Sang, Y. F., and Yang, M. (2017). Urban waterlogs control in China: more effective strategies and actions are needed. *Nat. Hazards* 85, 1291–1294. doi: 10.1007/s11069-016-2614-4

Shafique, M., and Kim, R. (2015). Low impact development practices: a review of current research and recommendations for future directions. *Nephron Clin. Pract.* 22, 543–563. doi: 10.1515/eces-2015-0032

Su, D., Zhang, Q. H., Ngo, H. H., Dzakpasu, M., Guo, W. S., and Wang, X. C. (2019). Development of a water cycle management approach to Sponge City construction in Xi'an, China. *Sci. Total Environ.* 685, 490–496. doi: 10.1016/j.scitotenv.2019.05.382

Wang, H., Mei, C., and Liu, J. (2017a). Systematic construction pattern of the sponge city [J]. *J. Hydraul. Eng.* 49, 1009–1014.

Wang, Y. T., Sun, M. X., and Song, B. M. (2017b). Public perceptions of and willingness to pay for sponge city initiatives in China. *Resour. Conserv. Recycl.* 122, 11–20. doi: 10.1016/j.resconrec.2017.02.002

Wang, J.-L., Che, W., and Yi, H.-X. (2009). Low impact development for urban stormwater and flood control and utilization [J]. *China Water Wastewater* 25, 6–10.

Wang, Y., Zhang, X., Cheng, F., and Wang, X. (2012). Study on regulation effect of grass filter strip on city rainstorm runoff. *China Water Wastewater* 28, 61–63.

Wang, Y. Q., Hu, W., Zhu, Y. J., Shao, M. A., Xiao, S., and Zhang, C. C. (2015). Vertical distribution and temporal stability of soil water in 21-m profiles under different land uses on the Loess Plateau in China. *J. Hydrol.* 527, 543–554. doi: 10.1016/j.jhydrol.2015.05.010

Xia, J., Zhang, Y. Y., Xiong, L. H., He, S., Wang, L. F., and Yu, Z. B. (2017). Opportunities and challenges of Sponge City construction related to urban water issues in China. *Sci. China Earth Sci.* 60, 652–658. doi: 10.1007/s11430-016-0111-8

Xiao, L., Zhang, Y., Li, P., Xu, G. C., Shi, P., and Zhang, Y. (2019). Effects of freeze-thaw cycles on aggregate-associated organic carbon and glomalin-related soil

protein in natural-succession grassland and Chinese pine forest on the Loess Plateau. *Geoderma* 334, 1–8. doi: 10.1016/j.geoderma.2018.07.043

Xu, G., Ren, Z., Li, P., Li, Z., Yuan, S., Zhang, H., et al. (2016). Temporal persistence and stability of soil water storage after rainfall on terrace land. *Environ. Earth Sci.* 75:966.

Xu, G. C., Li, Z. B., Li, P., Zhang, T. G., Chang, E. H., Wang, F. C., et al. (2017). The spatial pattern and temporal stability of the soil water content of sloped forestland on the Loess Plateau, China. *Soil Sci. Soc. Am. J.* 81, 902–914. doi: 10.2136/sssaj2016.10.0331

Yin, J., Ye, M., Yin, Z., and Xu, S. (2015). A review of advances in urban flood risk analysis over China. *Stoch. Environ. Res. Risk Assess.* 29, 1063–1070. doi: 10.1007/s00477-014-0939-7

Yu, M., and Liu, Y. M. (2015). The possible impact of urbanization on a heavy rainfall event in Beijing. *J. Geophys. Res. Atmos.* 120, 8132–8143. doi: 10.1002/2015jd023336

Yuan, Y., Xu, Y. S., and Arulrajah, A. (2017). Sustainable measures for mitigation of flooding hazards: a case study in Shanghai, China. *Water* 9:310. doi: 10.3390/w9050310

Zheng, Z. P., Qi, S. Z., and Xu, Y. T. (2013). Questionable frequent occurrence of urban flood hazards in modern cities of China. *Nat. Hazards* 65, 1009–1010. doi: 10.1007/s11069-012-0397-9

Conflict of Interest: MH was employed by the company Ningxia Capital Sponge City Construction & Development Company Limited, Guyuan, China.

The remaining authors declare that the research was conducted in the absence of any commercial or financial relationships that could be construed as a potential conflict of interest.

frontiers in Earth Science

ORIGINAL RESEARCH
published: 28 April 2020
doi: 10.3389/feart.2020.00124

An Assessment of Continuous Modeling for Robust Design Flood Estimation in Urban Environments

*James E. Ball**

School of Civil and Environmental Engineering, University of Technology Sydney, Ultimo, NSW, Australia

Catchment management is a complex task that, over the past decade, has become increasingly important to urban communities. While there are many water related management issues, estimation of the magnitude and likelihood of flood events is one that remains a concern to many mangers of urban drainage systems. Data is an essential component of any approach for estimation of the magnitude and likelihood of design flood characteristics. This data can be obtained from catchment monitoring or catchment modeling with these data sources being complementary rather than competitive. However, the absence of monitored data in urban environments has resulted in the data being obtained predominantly from the use of catchment modeling. Numerous alternative approaches for catchment modeling have been developed; these approaches can be categorized as either single event or continuous models. The philosophical basis behind the use of a continuous modeling approach is the concept that the model predictions will replicate the data that would have been recorded if catchment monitoring were to be undertaken at that location and for the modeled catchment conditions. When using this philosophy, a modeler must determine when the predicted data suitably replicates the true data. Presented herein is an analysis of continuous and event modeling undertaken for design flood estimation in an urban catchment located in Sydney, Australia where monitored data is available to assess the utility of the catchment model. It will be shown that frequency analysis of the predicted flows from the continuous model more closely resemble the frequency analysis of the recorded data.

Keywords: floods, urban, SWMM, risk, model

OPEN ACCESS

Edited by:
Qiuhua Liang,
Loughborough University,
United Kingdom

Reviewed by:
Albert Chen,
University of Exeter, United Kingdom
Guy Jean-Pierre Schumann,
University of Bristol, United Kingdom

***Correspondence:**
James E. Ball
james.ball@uts.edu.au

Specialty section:
This article was submitted to Hydrosphere, a section of the journal Frontiers in Earth Science

Received: *14 January 2020*
Accepted: *01 April 2020*
Published: *28 April 2020*

Citation:
Ball JE (2020) An Assessment of Continuous Modeling for Robust Design Flood Estimation in Urban Environments. Front. Earth Sci. 8:124. doi: 10.3389/feart.2020.00124

INTRODUCTION

Catchment management is a complex task that, over the past decade, has become increasingly important to the community. This is particularly the case for urban environments. Of the many catchment management issues, estimation of the magnitude and likelihood of flood events is one that remains an issue in many urban environments. There are many different issues requiring design flood estimation; see, for example, Audisio and Turconi (2011), Hettiarachchi et al. (2018), and Andimuthu et al. (2019) who present different aspects of the need to estimate design floods in urban environments. As a consequence, design flood estimation remains a significant problem for management of many urban catchments.

While the flood characteristics important for management of a drainage system will vary between problems, Ball (2014) suggests that, typically, the flood characteristic of concern will be one of the following:

- Flood flow rate – the peak flow rate of the flood hydrograph is a common design flood hydrograph characteristic used, for example, to size drainage system components;
- Flood level – the peak flood level during a flood hydrograph is a common design flood hydrograph characteristic used, for example, in setting minimum floor levels;
- Flood rate of rise – this design flood characteristic is a concern when planning for evacuation;
- Flood volume – this design flood characteristic becomes a concern when storage of the design flood is being considered as part of a flood management system; or
- System failure – the usual design flood problem is located at a single point. There are numerous design problems, however, where the critical concern is prediction of system failure. Examples of these problems include urban drainage systems and transportation routes with multiple cross drainage structures.

In Australia, a risk management approach provides the foundation for flood management (Ball et al., 2016). When a risk management approach is used, it is necessary to estimate both the magnitude of the hazard and the likelihood of the hazard. In other words, there is a need to consider the relationship between the magnitude and the exceedance probability of a design flood characteristic. An example of this relationship is shown in **Figure 1**.

Arising from the need for predictions of the relationship between flood hazard and its likelihood, a number of alternative approaches have been developed. Smithers (2012), discusses these approaches and categorizes the approaches considered as being either "analysis of streamflow data" or "rainfall based"; herein, similar categories are used although they are referred to as "catchment monitoring approaches" and "catchment modeling approaches". In reviewing rainfall-based approaches, Smithers (2012) notes that continuous simulation approaches have been proposed to overcome inherent biases introduced through use of single event approaches.

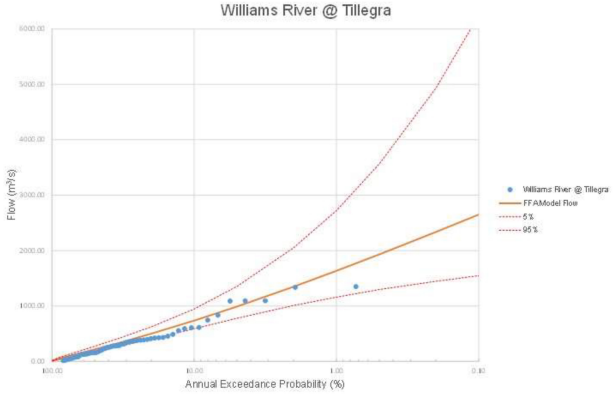

FIGURE 1 | Relationship between flood hazard and likelihood.

While estimation of the relationship between the magnitude and the likelihood, or probability, of a flood hazard can be achieved through alternative approaches, a fundamental need for all approaches is the availability of suitable data. This data can be obtained from catchment monitoring or catchment modeling. The aim of a catchment monitoring is the collection of data about the desired flood characteristics within the catchment over multiple storm events. Typically, the data obtained will include time-series data at various time scales and spatial data, during and post events, of differing resolutions. To obtain relevant information about the flood risk within the catchment, as explained by Ball (2018) this collected data is mined to extract relevant information about the relationship between the magnitude and the likelihood of the flood hazard.

The alternative approach to catchment monitoring is catchment modeling. Conceptually, the aim of catchment modeling is to generate data that would have been recorded if catchment monitoring had been in place for the event, or sequence of events, at the locations being considered. Hence, the generated data should have the same characteristics as the historical data that could have been monitored at the site or sites of interest. Where changes in catchment management, e.g., land-use, or changes in climatic conditions are to be considered, catchment modeling techniques are required; catchment monitoring approaches can be used only when a physical catchment exists. Finally, similar to data obtained from catchment monitoring, mining of the data obtained from catchment modeling is required to extract relevant information about the likelihood of a flood hazard.

As implied in the previous discussion, catchment modeling can be used to provide data at locations remote from monitoring locations. The converse is also valid; catchment monitoring can be used to validate predictions obtained from catchment modeling. Hence, effective flood management for a catchment requires data from both catchment monitoring and catchment modeling programs. Presented herein will be a discussion of the use of monitored and modeled data in the estimation of the flood risk in the Powells Creek catchment located in the inner west suburbs of Sydney, Australia. Of particular interest is the viability of predicting flood risk from analysis of data generated through continuous simulation of catchment processes.

POWELLS CREEK CATCHMENT

Catchment Description

The Powells Creek catchment, sometimes referred to as the Strathfield catchment, is an 841 ha catchment situated 10 km west of Sydney's central business district. The location of this catchment is shown in **Figure 2**. The catchment lies within the Sydney suburbs of Homebush West, North Strathfield, Rookwood and Strathfield, and is administered by the local government areas of Strathfield, Canada Bay and Auburn. The drainage network comprises a closed piped system that opens out to a lined channel and then into the Parramatta River. The

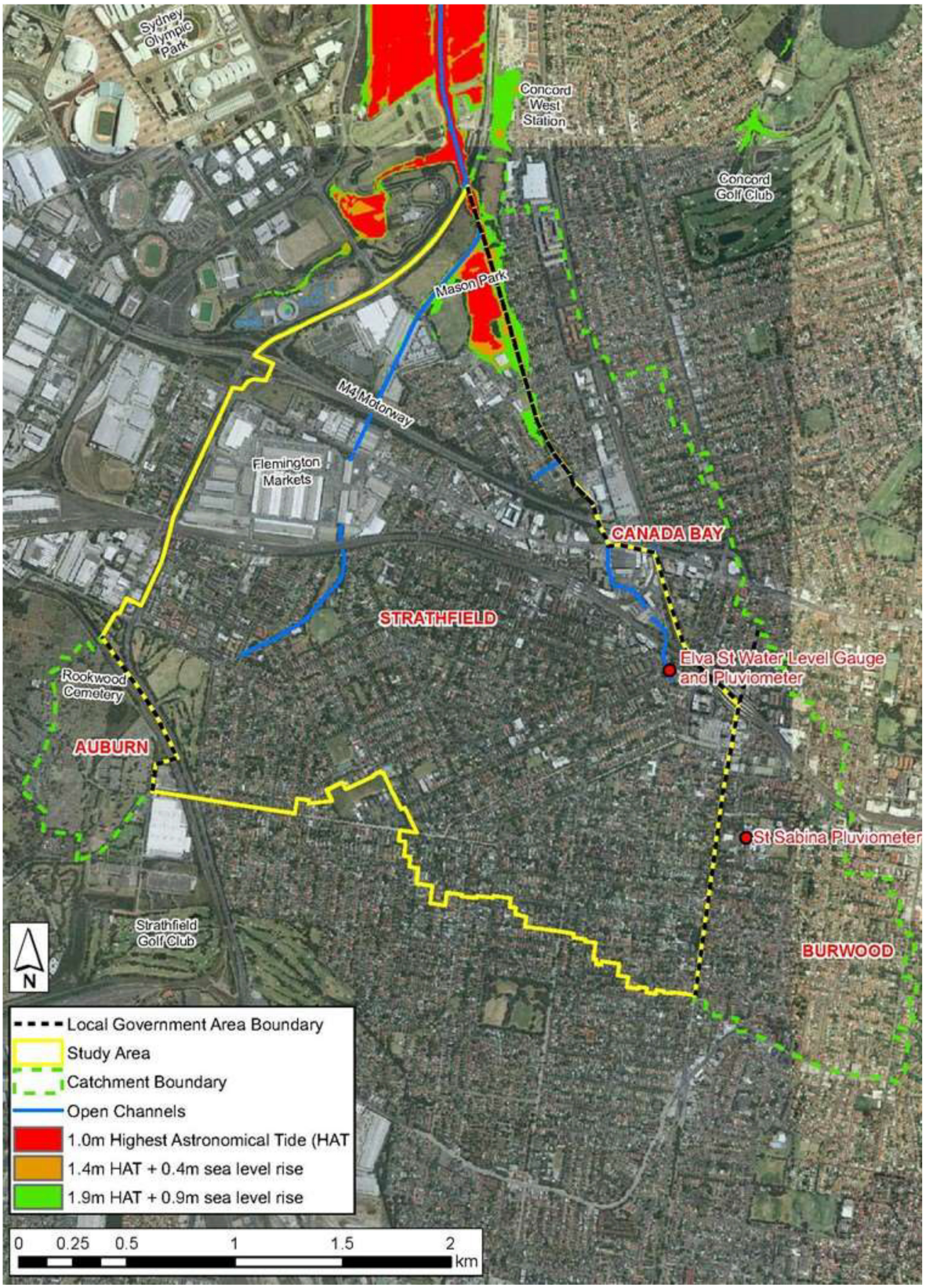

FIGURE 2 | Powells Creek catchment (after WMAwater, 2016).

TABLE 1 | Land use in the Powells Creek catchment (after Meutia, 2002).

Land use	Area (HA)	Proportion (%)
Residential	504.7	60.0
Industrial	40.5	4.8
Commercial	27.1	3.2
Open space	61.1	7.3
Special use	208.1	24.7

TABLE 2 | Calibration events.

Date	Rainfall (mm)	Flow (m^3/s)	Duration (hrs)	Rating table[1]	Approximately ARI[2] (years)
March 1990	55.2	22.94	5	Extrapolated	47
November 1984	179.5	21.16	90	Extrapolated	21
March 1995	57.2	12.24	25	Within	4.3
October 1985	16.2	11.89	3	Within	3.9
January 1997	52.2	6.871	32	Within	1.5
October 1997	46.0	5.706	9	Within	1.2

[1]Within – all recorded levels within the gauged portion of the rating table; Extrapolated – levels higher than gauged portion of the rating table, flows determined using extrapolated relationship. [2]Approximately ARI determined from Cunnane Plotting Position.

TABLE 3 | Parameter considered during model calibration.

Subcatchment parameter	Channel parameter
Subcatchment width	
Subcatchment slope	
Imperviousness	
Surface roughness (impervious and pervious)	Conduit roughness
Depression storage (impervious and pervious)	
Impervious area with no depression storage	
Infiltration parameters (maximum rate, minimum rate, infiltration decay, and infiltration recovery rate)	

main open channel was established in 1892 (Meutia, 2002) and the closed pipe system was established in the 1920s.

Shown in **Table 1** are the land-use classifications within the Powells Creek catchment as outlined by Meutia (2002). From a topographic perspective, the catchment is classified as having gentle slopes between 4 and 6% with a maximum elevation of 40 m AHD; the minimum elevation is governed by the tidal regime of the Parramatta River.

Available Data

The School of Civil and Environmental Engineering at The University of New South Wales operated a gauging station on the main Powells Creek Stormwater Channel during the period 1958 to 2005. The location of this gauging station is shown in **Figure 2**. The catchment area draining to this gauging station consists of 2.3 km^2 of the total 8.41 km^2 catchment area. Initially this gauging station monitored only the flow quantity but since the early 1990s monitored water quality parameters as well.

Numerous stream gaugings have been taken at this gauging station to define the rating curve for translation of level to recorded flows. There are 14 gaugings below 0.5 m and 14 gaugings between 0.5 and 1.0 m; the highest traditional gauging used in developing the rating curve was 1.35 m (13.8 m^3/s). Gauging data above 1.35 to 1.65 m used the technique presented by Tilley et al. (2000) for gauging in rapidly varying flows; no gauge data is available above 1.65 m to validate the rating curve for the peak flood flows.

In addition to the flow data, continuous rainfall data was collected at two locations within the gauged portion of the catchment; these locations were at the centroid of the gauged catchment and at the flow gauging station. While this rainfall data was collected for the same period as the flow data, only rainfall data for the period 1981 to 1998 from the flow gauging station was available for this study.

TABLE 4 | Powells Creek calibration metrics.

Event date	NSE best	NSE average	RMSE best	RMSE average	Peak Q best	Peak Q average
March 1990	0.91	0.82	0.069	0.099	0.000	0.071
November 1984	0.88	0.83	0.093	0.112	0.000	0.081
March 1995	0.93	0.86	0.033	0.047	0.000	0.086
October 1985	0.98	0.95	0.036	0.060	0.000	0.059
January 1997	0.87	0.79	0.101	0.127	0.146	0.337
October 1997	0.94	0.89	0.071	0.057	0.000	0.078

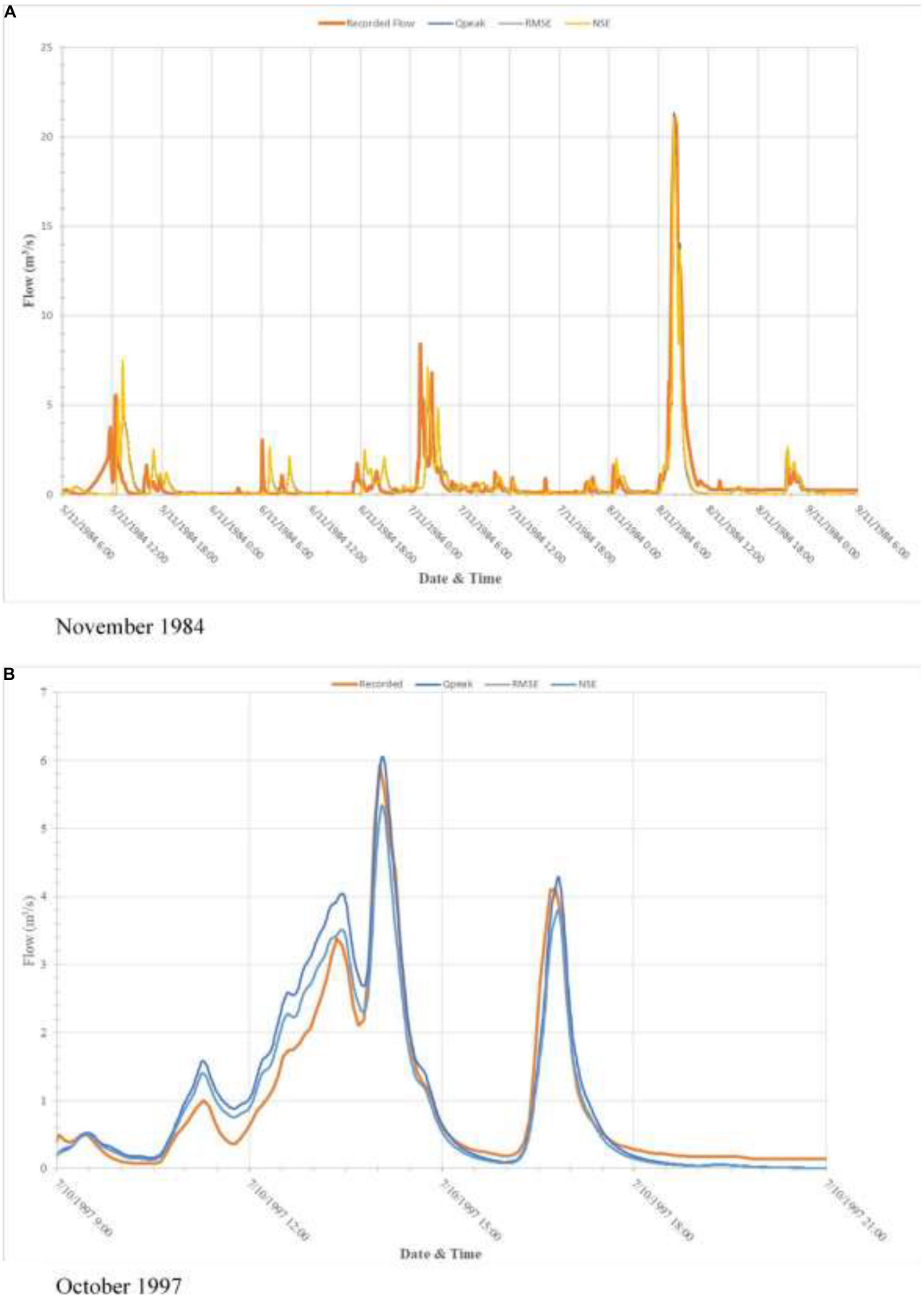

FIGURE 3 | Predicted hydrographs for selected calibration events, **(A)** November 1984, **(B)** October 1997.

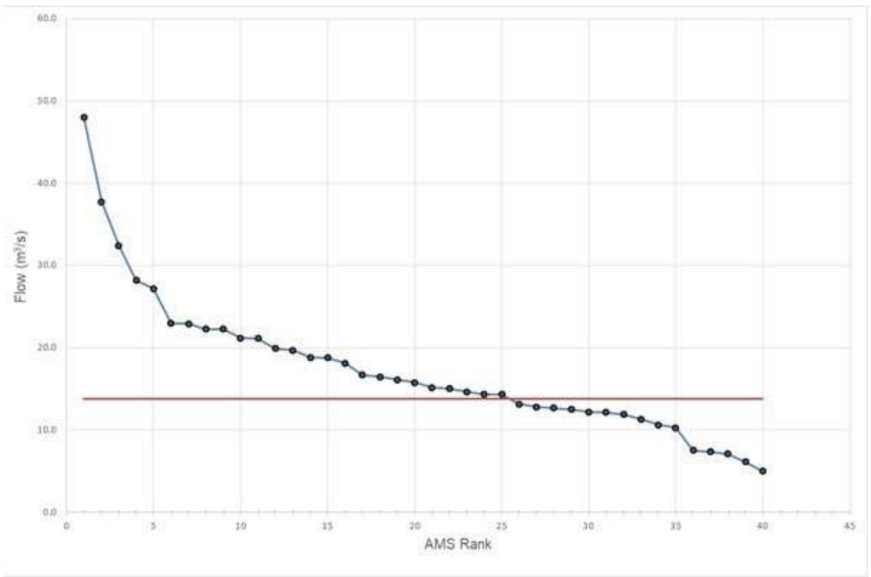

FIGURE 4 | Powells Creek ranked AMS.

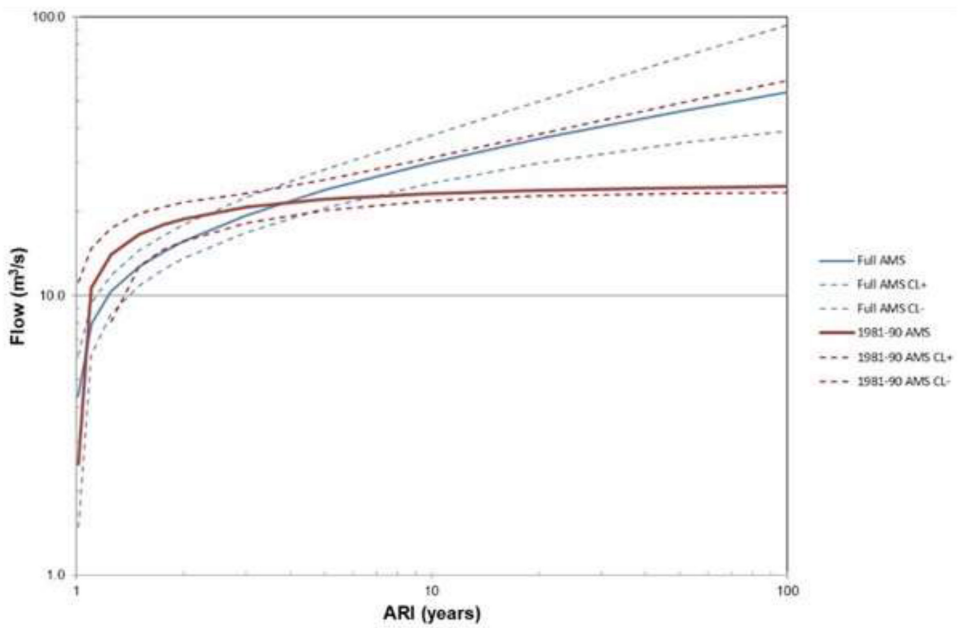

FIGURE 5 | Flood frequency for Powells Creek gauging station.

TABLE 5 | GEV parameters for annual maxima series of 40 and 10 years duration.

Parameter	40 Year AMS		10 YEAR AMS	
	Most probable value	*SD*	Most probable value	*SD*
Location	2.747	0.076	17.126	2.118
Log_e (Scale)	−0.731	0.113	1.686	0.363
Shape	−0.202	0.337	0.689	0.559

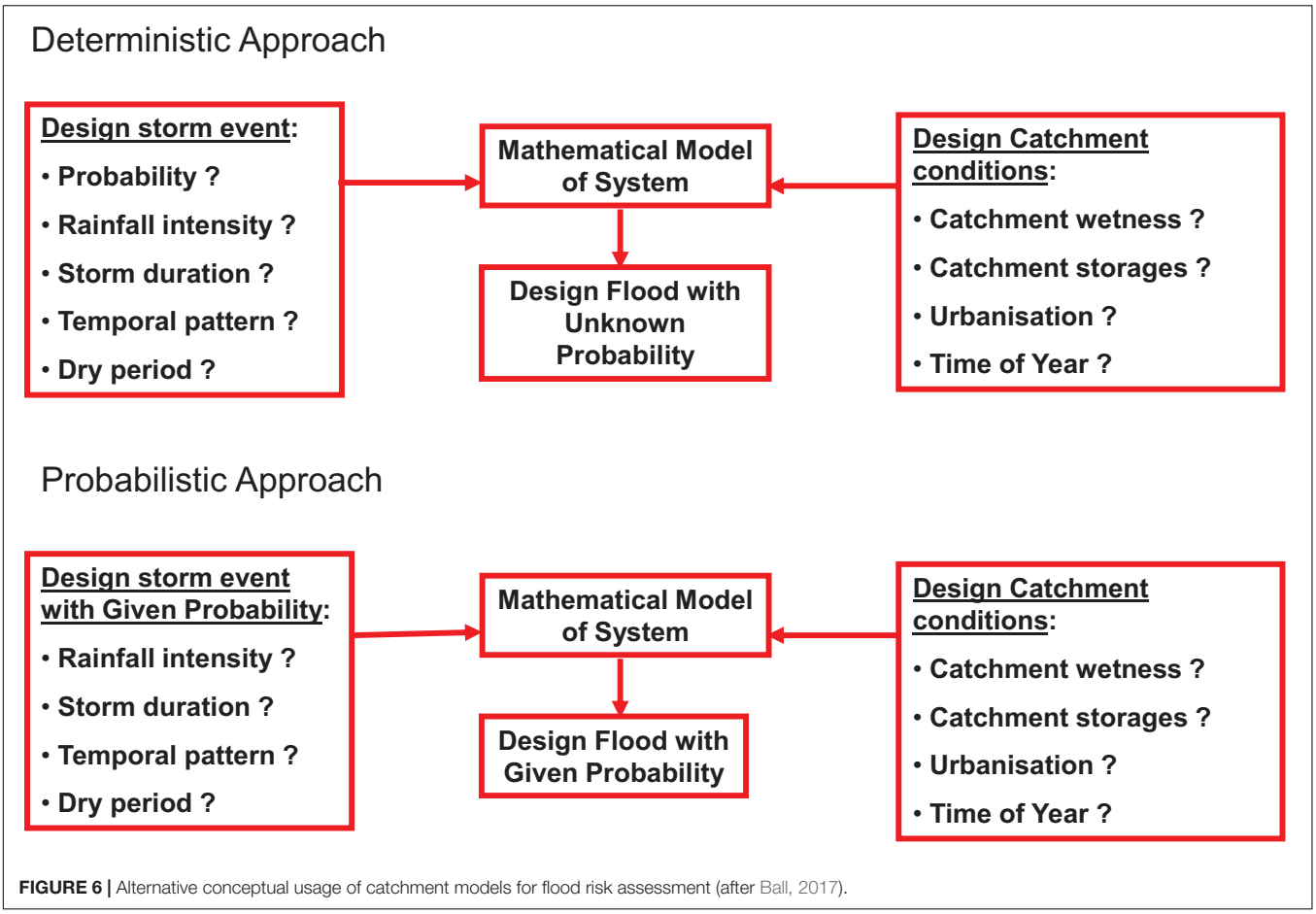

FIGURE 6 | Alternative conceptual usage of catchment models for flood risk assessment (after Ball, 2017).

Flow and rainfall data for individual events were extracted from this dataset for model calibration. Details of this data are presented in **Table 2**.

Catchment Model

There are numerous alternative software systems suitable for process-based modeling of existing and potential urban catchments. After considering these alternatives, the SWMM system (Rossman, 2005) was used herein for data generation. This model has received extensive application; see, for example, Leutnant et al. (2019) and Broekhuizen et al. (2020) for recent applications.

SWMM is a physically distributed catchment modeling system consistent with the conceptual components of a catchment modeling system proposed by Ball (1992); these components are:

- Generation – this component of the modeling system is concerned with spatial and temporal models necessary to convert point data into spatial-temporal data. An example is the conversion of point rainfall records into spatial rainfall models over the catchment at suitable resolution;
- Collection – the component of the model where those processes concerned with the generation of runoff are dominant. This is the hydrologic component of the modeling system;
- Transport – the component of the model where the processes concerned with the movement of water through the drainage system are dominant. This is the hydraulic component of the modeling system; and
- Disposal – the component of the modeling system concerned with the discharge of water from the drainage system into receiving waters.

For construction of the catchment model, the Powells Creek catchment was divided into 103 subcatchments and a similar number of channels. SWMM has the capacity for each subcatchment and channel to have unique parameter values. This capacity was utilized during calibration of the model.

There are many different parameters necessary for operation of a catchment modeling system; these parameters can be categorized arbitrarily into:

- Measured parameters. These are parameters that are physically measured such as pipe diameters, catchment areas, rainfall depth or rainfall intensity, etc.; and
- Inferred parameters. These are parameters that are not measured and are determined from the application of a model. Examples of inferred parameters are Manning's roughness for catchment surfaces or channels, depression storage, catchment or subcatchment imperviousness.

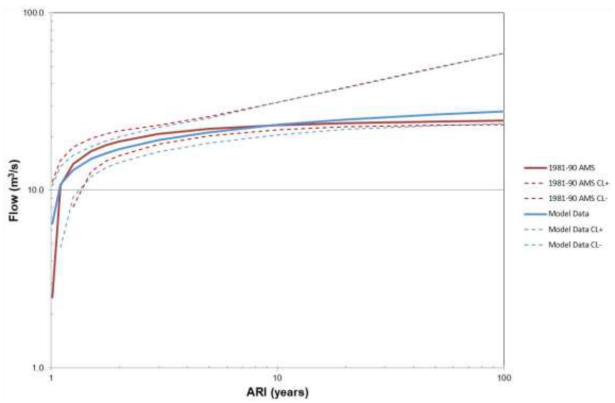

FIGURE 7 | Comparison of FFA from monitored and modeled data.

While the interface between these categories may appear as an absolute division, the interface between these categories is vague with parameters oscillating between the categories depending on the viewpoint of the user. For example, rainfall depth in the above discussion is defined as a measured parameter, but this measurement is only at the rainfall gauge itself with rainfall at other locations within the catchment (assuming the rain gauge is within the catchment) being inferred by application of a spatial rainfall model; see Ball and Luk (1998) for a discussion of the potential errors introduced through different inference models for the spatial distribution of rainfall over a catchment. Consideration of other parameters such as the catchment, or subcatchment, area also reveals a variability in measured parameters depending on, for example, the scale of the map from which the area was measured. In general, the values of inferred parameters are considered those that need to be adjusted during calibration, while measured parameters are assumed error free during the calibration process.

For the purposes of calibrating the Powells Creek model used in this study, the parameters considered are shown in **Table 3**. A previously calibrated model of Powells Creek was available from Meutia (2002). These parameter values were used as a search starting point for the most generic parameter values and their uncertainty. Initial feasible parameter values were defined as $\pm$ 50% of the values obtained by Meutia (2002); in other words, all parameter values tested were within $\pm$ 50% of the calibrated values obtained by Meutia (2002).

Previously Fang and Ball (2007) used a genetic algorithm (GA) to search the parameter space for feasible parameter sets within a GLUE framework; a similar approach was used herein with a GA population of 1000. More details of the GA are presented by Fang and Ball (2007) and, hence, are not presented herein.

There are numerous alternative metrics that can be used to assess the suitability of the calibration obtained. Shown in **Table 4** are the calibration metrics if Nash-Sutcliffe Efficiency (NSE), Root Mean Square Error (RMSE), and Peak Discharge (Q_{peak}) are used to assess the calibration. A visual comparison for some of the predicted hydrographs using the best parameter sets (i.e., the minimum error) for two events is shown in **Figure 3**. It should be noted that the best parameter set differed between events and between alternative calibration metrics.

ANALYSIS OF FIELD DATA

A common analysis approach for design flood estimation based on monitored data is the use of At-Site flood frequency analysis (FFA). While the period of record extended for 47 years, an annual maximum series (AMS) could be extracted only for a continuous 40 year period. Shown in **Figure 4** is the ranked AMS. As can be seen from consideration of this figure, the highest 25 recorded flows are in the extrapolation zone of the rating curve; in other words, 25 of the AMS data points are above the highest validated point on the rating curve. This means that the Mean Annual Flood (Median of the AMS) lies within the extrapolation zone of the rating curve; note that the Mean Annual Flood is important for estimation of the value of the location parameter for most three parameter statistical models of the relationship between flood magnitude and likelihood.

Undertaking an FFA for this site using the full 40 year AMS in accordance with guidance presented in Australian Rainfall and Runoff (Ball et al., 2016) results in the flood frequency shown in **Figure 5**. In this case, the three parameter GEV distribution was fitted to the 40 available data points. Shown in **Table 5** are the estimated values for these parameters together with their estimated variability.

Also shown in **Figure 5** and **Table 5** are the flood frequency predictions and the relevant statistical model parameters if the 10-year period, 1981–1990, were used in lieu of the full period of record. As can be seen in **Figure 4** and as suggested by the values presented in **Table 2**, there are considerable differences in the predicted relationships even though the shorter period AMS occurs within the period of the longer AMS. This highlights the need, when assessing flood frequency relationships, to ensure consistency of data sources and periods.

TABLE 6 | FFA parameters for 10 year AMS.

Parameter	Monitored data		Modeled data	
	Most probable value	SD	Most probable value	*SD*
Location	17.13	2.12	15.47	1.73
Log_e (Scale)	1.69	0.36	1.55	0.30
Shape	0.69	0.56	0.27	0.33

ANALYSIS OF MODELED DATA

As noted earlier, the aim of most physically based catchment models is the reproduction of the data that would have been recorded if monitoring were being undertaken at that location for the desired catchment conditions and climate state. While generation of both continuous and event specific data is feasible, for purposes of generating data for prediction of flood risk, techniques considering a single burst (or event) have been the more popular.

When catchment modeling using a single event or burst approach is employed, there are two alternative interpretations, namely AEP neutrality and event reproduction. These alternatives are shown in **Figure 6**.

Where the single burst approach has been implemented with the assumption that the frequency of the rainfall is transformed to the frequency of the resultant flood characteristic, it can be argued that the approach is a Regional Flood Frequency Estimation technique; in other words, the catchment model is used to provide a regression ensuring consideration of the main catchment factors. An example of this approach is provided by Hill et al. (1998) who developed a method of estimating loss model parameters that are likely to result in the frequency of the rainfall being transferred to the frequency of the design flood flow.

It is possible to use a single event or burst approach without the assumption of AEP neutrality. In these circumstances, the catchment model is used to analyze the catchment response to a design rainfall event with the probability of the resultant flood characteristics being unknown.

The alternative to simulation of single events is continuous simulation resulting in continuous time series data; to estimate the flood risk, it is necessary to analyze this data using Flood Frequency. Previously, the calibration of the SWMM model to individual events was discussed. Since the focus of the data generation is the estimation of the flood risk, successful prediction of higher flows and flow depths was required and lower flows that were not likely to influence the statistical analysis did not need similar prediction reliability. Hence, the parameter sets derived from the event calibration were employed in the generation of the continuous time series data.

The model generated time series data were analyzed in a similar manner to the field monitored data to develop a flood hazard magnitude likelihood relationship. Shown in **Figure 7** is a graphical representation of this relationship. Also shown in this figure is the same relationship developed from the field monitored data for the same period of record. Inspection of this figure suggests a visual similarity of the two relationships. This similarity of relationship is confirmed if the parameters for the GEV relationship, shown in **Table 6**, are considered.

CONCLUSION

Management of floods in urban catchments is a complex task. Data for this management task can come from a variety of sources, namely monitoring and modeling of the catchment. Catchment modeling here refers to modeling aimed at reproducing data that would have been recorded if field monitoring were undertaken at that location for that catchment condition and rainfall record; many catchment modeling approaches do not meet this definition as the models are used in a statistical context rather than a physical process context. Management of data from both sources requires definition of the metadata about the data to enable assessment of data uncertainty and to enable appropriate data mining to determine flood risk. Finally, using the Powells Creek catchment in Sydney, Australia as a case study, it was shown that design flood predictions from data mining of both field monitored and model generated data were similar provided consistent periods of record were utilized for the same catchment conditions; in other words, the rain records and catchment conditions were from the same period.

DATA AVAILABILITY STATEMENT

The datasets generated for this study are available on request to the corresponding author.

AUTHOR CONTRIBUTIONS

JB made substantial contributions to the conception, design of the work; drafted the work for important intellectual content; provided approval for publication of the content; and agrees to be accountable for all aspects of the work in ensuring that questions related to the accuracy or integrity of any part of the work are appropriately investigated and resolved.

REFERENCES

Andimuthu, R., Kandasamy, P., Mudgal, B. V., Jeganathan, A., Balu, A., and Sankar, G. (2019). Performance of urban storm drainage network under changing climate scenarios: flood mitigation in Indian coastal city. *Sci. Rep.* 9:7783. doi: 10.1038/s41598-019-43859-3

Audisio, C., and Turconi, L. (2011). Urban floods: a case study in the Savigliano area (North-Western Italy). *Nat. Hazards Earth Syst. Sci.* 11, 2951–2964. doi: 10.5194/nhess-11-2951-2011

Ball, J. E. (1992). *A Review of Numerical Models for Prediction of Catchment Water Quantity and Quality*. Research Report No. 180, Water Research Laboratory, Dept. of Water Engineering, School of Civil Engineering. Sydney: The University of New South Wales.

Ball, J. E. (2014). "Flood estimation under changing climates," in *Proeedings of the. 2014 IAHR-APD Congress*, Hanoi.

Ball, J. E. (2017). "Urban Flood Modelling – Process or Regression," in *Proceedings 37th IAHR World Congress*, Kuala Lumpur, Malaysia.

Ball, J. E. (2018). "A classic hydroinformatic problem - floods," in *Proceedings of the 2018 International Conference on Hydroinformatics*, Palermo.

Ball, J. E., and Luk, K. C. (1998). Modelling the spatial variability of rainfall over a catchment. *ASCE J. Hydrol. Eng.* 3, 122–130.

Ball, J. E., Babister, M., Nathan, R., Weeks, W., Weinmann, E., Retallick, M., et al. (2016). *Australian Rainfall and Runoff: A Guide to Flood Estimation*. Canberra: Commonwealth of Australia.

Broekhuizen, I., Leonhardt, G., Marsalek, J., and Viklander, M. (2020). Event selection and two-stage approach for calibrating models of green urban

drainage systems. *Hydrol. Earth Syst. Sci.* 24, 869–885. doi: 10.5194/hess-24-869-2020

Fang, T., and Ball, J. E. (2007). Evaluation of spatially variable control parameters in a complex catchment modelling system: a genetic algorithm application. *J. Hydroinform.* 9, 163–173. doi: 10.2166/hydro.2007.026

Hettiarachchi, S., Wasko, C., and Sharma, A. (2018). Increase in flood risk resulting from climate change in a developed urban watershed – the role of storm temporal patterns. *Hydrol. Earth Syst. Sci.* 22, 2041–2056. doi: 10.5194/hess-22-2041-2018

Hill, P. I., Mein, R. G., and Siriwardena, L. (1998). *How Much Rainfall Becomes Runoff? - Loss Modelling for Flood Estimation*. Industry Report 98/5, Cooperative Research Centre for Catchment Hydrology. Clayton: Monash University.

Leutnant, D., Döring, A., and Uhl, M. (2019). swmmr - an R package to interface SWMM. *Urban Water J.* 16, 68–76. doi: 10.1080/1573062X.2019.1611889

Meutia, E. Z. (2002). *Development of a Catchment Modelling System for the Powells Creek Catchment*. Unpublished Master of Engineering Science Report, The University of New South Wales, Sydney.

Rossman, L. A. (2005). *Storm Water Management Model - User's Manual, Version 5.0*. Report EPA/600/R-05/040. Cincinnati: U.S. Environmental Protection Agency.

Smithers, J. C. (2012). Methods for design flood estimation in South Africa. *Water SA* 38, 633–646. doi: 10.4314/wsa.v38i4.19

Tilley, J. H., Coates, A., Wojcik, A., Ball, J. E., and Abustan, I. (2000). Development of a stage-discharge relationship for rapidly varying flows in urban streams. *Austral. J. Water Resour.* 4, 139–145.

WMAwater. (2016). *Powells Creek and Saleyards Creek Revised Flood Study*. Unpublished Report. Sydney, Australia: Strathfield Municipal Council.

Conflict of Interest: The author declares that the research was conducted in the absence of any commercial or financial relationships that could be construed as a potential conflict of interest.

frontiers in Earth Science

ORIGINAL RESEARCH
published: 16 June 2020
doi: 10.3389/feart.2020.00159

An Efficient Method for Approximately Simulating Drainage Capability for Urban Flood

Donglai Li[1,2], *Jingming Hou*[1,2]*, *Junqiang Xia*[1]*, *Yu Tong*[2], *Dong Yang*[2], *Dawei Zhang*[3] and *Xujun Gao*[4]

[1] State Key Laboratory of Water Resources and Hydropower Engineering Science, Wuhan University, Wuhan, China, [2] State Key Laboratory of Eco-Hydraulics in Northwest Arid Region of China, Xi'an University of Technology, Xi'an, China, [3] Research Center on Flood & Drought Disaster Reduction of the Ministry of Water Resources, China Institute of Water Resources and Hydropower Research, Beijing, China, [4] Northwest Engineering Corporation Limited of the Power Construction Corporation of China, Xi'an, China

Assessing the performance and capability of drainage pipes is of significance for computing urban flooding. However, drainage-pipe data is not available for most urban areas, therefore raising the problem for computing the drainage capability in an approximate way. To resolve this problem, a new type of approach that improves on the existing approach, termed the inlet-drainage approach, is proposed by assuming the drainage effects as a mass subtracted in particular parts, e.g., the area with gullies or inlets. The proposed approach is incorporated into a 2D hydrodynamic model for surface flow to simulate the coupled rainfall-runoff-drainage-inundation processes. Through validation against the measured and modeled results in two test cases involving ideal and realistic urban catchments, it is demonstrated that the proposed new approach could provide fairly good modeled results for computing drainage effects. More importantly, the new approach is simple and easy to implement.

Keywords: urban flooding, numerical simulation, unavailable drainage pipe, inlet drainage, surface flow

OPEN ACCESS

Edited by:
Ke Zhang,
Hohai University, China

Reviewed by:
Juan Pablo Rodríguez Sánchez,
University of Los Andes, Colombia
Shuliang Zhang,
Nanjing Normal University, China

***Correspondence:**
Jingming Hou
jingming.hou@xaut.edu.cn
Junqiang Xia
xiajq@whu.edu.cn

Specialty section:
This article was submitted to Hydrosphere, a section of the journal Frontiers in Earth Science

Received: *07 January 2020*
Accepted: *28 April 2020*
Published: *16 June 2020*

Citation:
Li D, Hou J, Xia J, Tong Y, Yang D, Zhang D and Gao X (2020) An Efficient Method for Approximately Simulating Drainage Capability for Urban Flood. Front. Earth Sci. 8:159. doi: 10.3389/feart.2020.00159

INTRODUCTION

Rainfall frequency and intensity have increased due to the acceleration of urbanization, change in climate, and increase in extreme weather, which has directly led to an increase in the runoff coefficient and frequent urban flooding. Urban flooding, causing heavy losses, has been among the worst disasters in many cities in recent years (Ali et al., 2011; Hou et al., 2018a; Khaing et al., 2019; Lashford et al., 2019). It is difficult for the drainage-pipe capacity to cope with extreme rainfall of growing frequency and intensity (Jang et al., 2018). Then, with rapid runoff over impermeable surfaces covering large areas, a greater amount of urban flooding and inundation, impacting human society, will frequently arise under these conditions. It is essential to gain a better understanding of flooding and inundation processes so as to develop effective countermeasures against urban water disaster risk. In urban areas with high densities of buildings and underground pipes, the topography and the drainage-pipe system affect surface runoff propagation significantly (Hou et al., 2018b; Chao et al., 2019). Therefore, a modeling approach reflecting the impacts of these factors is required to assess the flooding and inundation dynamics in urban areas.

With the increasing accessibility of fine-scale terrain data, enhancement in computing performance, improvement of numerical methods, and demand of detailed simulation results in

some important areas, two-dimensional (2D) overland flow models have become a commonly used tool in recent years (Hou et al., 2015; Liang et al., 2016). Under storm conditions, the runoff should be conveyed by the essential infrastructure of drainage-pipe systems, which is put in place to alleviate flooding and inundation for modern urban areas. Hence, it is very significant to assess the performance and capability of drainage pipe with numerical models for emulating the processing of flooding events, especially to gain predictions of inundation depths and areas (Jang et al., 2018). However, drainage-pipe data is unavailable for many urban areas. The main reasons for this are either that the data was never well-documented in the beginning or that the data been lost over time because most drainage pipes were installed decades ago (Kratt et al., 2020). Sometimes, even though there is a drawing of the drainage network layout, it is inconsistent with the actual situation due to the impact of construction. Moreover, it is costly and difficult to measure the drainage network layout on site. Meanwhile, it is difficult to set up the model, especially when the area of research is large. More importantly, the data for such a complex layout are typically not made available to the public due to security concerns for key areas. In contrast, high-resolution image data and satellite data with a spatial resolution of <1 m, e.g., GF-2, WorldView-3, and Google Earth satellite imagery, can now be obtained (Malarvizhi et al., 2016; Zhang et al., 2019; Huang et al., 2020), and this can be used to discern the distribution of gullies and inlets of the drainage pipe network. To make use of this information, a new approach to clarify the drainage effects is required. Several models and methods have proposed a discounted rainfall or a fixed infiltration to consider the impact of drainage pipes in urban flood modeling. In the discounted rainfall approach, a corresponding discount is applied to the rainfall before input to the model to reflect drainage capacity in urban areas. As for the fixed infiltration approach, the drainage capacity is represented as additional infiltration rates in addition to the infiltration of the soil. The Environment Agency (2013) represented infiltration by reducing the rate of design rainfall in the beginning and then applying a further reduction in all areas to account for the effect of the drainage pipe. In addition, Yu and Coulthard (2015) assumed that the drainage system conveys water away at the maximum design capacity, and then the mass loss in the whole area is considered in the model to reflect the drainage system capability. Hou et al. (2018b) used constant infiltration over the whole study area to represent urban drainage network capacity when simulating flood inundation, and results similar to the measured effect were attained. Wang et al. (2018) used the constant infiltration method and the rainfall reduction method to represent urban drainage-pipe capacity. The results show that the constant infiltration method is better than the rainfall reduction method because the former can better describe the flood recession process. All of the abovementioned approaches assumed that the drainage process happens across the whole area, which differs from the drainage process in reality (here, the existing approach of reducing water over the whole area is called the all area-drainage approach; hereinafter, the existing approach). However, drainage pipe is commonly laid only on roads, and the water exchange processes take place at the inlets and manholes of the drainage pipe, so the above assumption may lead to misestimation. Aiming at solving these existing problems, a new approach of reducing the water in the inlets of roads, named the inlet-drainage approach (hereinafter, the new approach), is proposed for reflecting the urban drainage-pipe capacity when such information is unavailable.

Both the new approach and the existing approach are based on mass conservation, which reduces the mass mainly from the surface runoff. The complete urban rainfall-runoff process can be divided into the generation and confluence processes of surface runoff and drainage-pipe flow, which involve hydrological and hydrodynamic processes (Chang et al., 2015). The existing approach reduces water over the whole area, which happens in the process of runoff generation. However, during the hydrodynamic processes of the real rainfall-runoff process, the water is reduced through inlets after water flow to the inlets on the road (Chang et al., 2015; Jang et al., 2018; Wang et al., 2018). Therefore, the new approach reducing the water at the inlets of the road is proposed. Both of the approaches will be described in detail later. Although these approaches are different from one to another, they are both based on the same theory of reducing the mass. It is worth noting that the new approach is similar to the hydrodynamics of the real rainfall-runoff process (Jang et al., 2018; Martínez et al., 2018).

As the rainfall-runoff process in an urban catchment is a very complicated process, it is very important to choose a model that can completely simulate the generation and confluence processes of surface runoff and drainage-pipe flow to evaluate the existing approach and the new approach. In recent years, many hydrological models that couple the 2D surface runoff process and the one-dimensional (1D) drainage-pipe process have been developed to emulate the complete urban rainfall-runoff process (Russo et al., 2015; Fan et al., 2017; Jang et al., 2018; Li et al., 2020). These models can be divided into two main types based on different considerations of the rainfall-runoff process (Chang et al., 2015). One type allows the rainfall to flow directly into a drainage pipe system after deducting infiltration, evaporation, and interception at the surface. The flooding will overflow to the surface through manholes or inlets when the capacity of the sewer network is exceeded. Then, the flooding flow on the 2D surface (Leandro et al., 2009) is collected. For example, the Storm Water Management Model (SWMM), where the flooding is collected in nodes, is commonly used to simulate the rainfall-runoff process (Rossman, 2010). This method is inconsistent with the actual rainfall-runoff process because it does not first consider surface runoff dynamics, and it overestimates the drainage capacity of drainage pipes. In another type, rainfall is first simulated on the surface to generate surface runoff. Then, the rainfall discharges into the drainage pipe network through manholes and inlets and is simulated by the 1D sewer flow model (Chang et al., 2015; Chen et al., 2017). This method is closer to the actual physical process, and it is gradually becoming widely used with the development of computing power. For example, Fan et al. (2017) presented a coupled model based on the implicit method and tested it in real urban scenarios. Li et al. (2020) proposed a novel 1D-2D coupled model that can even simulate transient flows in drainage networks.

To simulate the drainage-pipe capacity, this study develops a coupled model that couples a 1D sewer flow model with a 2D overland flow model based on the latter method (hereinafter, the coupled model). The sewer flow model was developed on the basis of diffusion wave equations, and the overland flow model is based on dynamic wave equations. The interactions between surface runoff and drainage-pipe flow are also coupled by the inlets and manholes, and the water exchange between the pipe and the surface is calculated by the weir formula. Therefore, three approaches to calculating the drainage-pipe capacity are simulated in this work: the existing approach, the new approach, and the coupled model approach. The details of the three approaches will be described in the next section. The performance of the new approach is validated against two test cases, an idealized urban catchment and a realistic urban catchment, in the following section. Finally, conclusions are briefly drawn.

METHOD FOR COMPUTING THE CAPACITY OF PIPE NETWORK DRAINAGE

The hydrodynamic-based rainfall-runoff and inundation model solves the 2-D shallow water equations (SWEs). The SWEs are derived by depth-integrating the Navier-Stokes equations and assuming a hydrostatic pressure distribution (Hou et al., 2018a). The conservation law of the two-dimensional no-linear shallow water equations can be written in the vector form as follows (Liang and Marche, 2009; Xia et al., 2017) when the kinetic and wind stresses, turbulent viscous terms, and Coriolis effects are neglected.

$$\frac{\partial q}{\partial t} + \frac{\partial f}{\partial x} + \frac{\partial g}{\partial y} = S \tag{1}$$

$$q = \begin{bmatrix} h \\ q_x \\ q_y \end{bmatrix}, f = \begin{bmatrix} uh \\ uq_x + gh^2/2 \\ uq_y \end{bmatrix}, g = \begin{bmatrix} vh \\ vq_x \\ vq_y + gh^2/2 \end{bmatrix} \tag{2}$$

$$S = \begin{bmatrix} R \\ -\frac{gh\partial z_b}{\partial x} - C_f u\sqrt{u^2+v^2} \\ -\frac{gh\partial z_b}{\partial y} - C_f v\sqrt{u^2+v^2} \end{bmatrix} \tag{3}$$

where t represents the time; x and y represent the Cartesian coordinates; t denotes the vector of conserved flow variables consisting of h, q_x, and q_y, i.e., the water depth, unit-width discharges in the x- and y-directions, respectively; $q_x = uh$, $q_y = vh$, u, and v are depth-averaged velocities in the x- and y- directions; f and g are the flux vectors in the x- and y- directions; S is the source vector, which may be further subdivided into the slope source term S_b and friction source term S_f; Z_b represents the bed elevation; C_f is the bed roughness coefficient, which is generally computed by $gn^2/h^{1/3}$, with n being the Manning coefficient.

The R denotes the rainfall source term including rainfall, evaporation, infiltration, and the water exchange between the surface and the drainage pipe in the actual rainfall-runoff process, where the exchange accounts for most of the total loss in urban areas. The interception and evaporation are neglected in the hydrodynamic-based rainfall-runoff and inundation model. R can then be written as follows.

$$R = i - f \tag{4}$$

where i denotes the rainfall rate (mm/h) and f denotes the infiltration rate (mm/h).

The Coupled Model

The governing equations of the sewer flow model are 1D SWEs. When the inertia term is assumed to be negligible in the equation, the 1D SWEs can be simplified as the diffusion wave equation, which is written as in Equations (5) and (6).

$$\frac{\partial A_p}{\partial t} + \frac{\partial Q_p}{\partial s_p} = 0 \tag{5}$$

$$\frac{dQ_p}{dt} + gA_p\frac{dZ_p}{ds_p} + gA_pS_{fp} = 0 \tag{6}$$

where Q_p represents the discharge in the pipe; A_p are the discharge section area of the pipe; t denotes the time and is synchronized with the two-dimensional model; s_p represents the length of the pipe; Z_p is the water level of the sewer; g is the gravitational acceleration; S_{fp} is the friction slope of the pipe.

As for the water depth calculations at inlets, the continuity equation for an inlet or manhole is shown as Equation (7), which includes the flow interaction with the 2-D surface flow model.

$$\frac{\partial h_I}{\partial t} = \frac{\sum_j q_{pj} + q_{in} - q_{out}}{A_I} \tag{7}$$

where h_I is the water depth at the inlet; t denotes the time; q_{pj} is the discharge of the jth pipe connecting to the inlet, which is positive for entering flow and negative for exiting flow; q_{in} represents the discharge that flows into the inlet from the overland surface; q_{out} is the surcharge discharge leaving the drainage pipe to the overland surface; A_I is the area of the inlet.

When the water flows through an inlet, the water will enter the drainage-pipe system at the inlet. In contrast, when the water depth in an inlet reaches the surface elevation, overflow occurs so that the flow will move from the drainage-pipe system to the surface system. In this paper, the water exchange between the 2D surface flow model and the 1D sewer flow model is coupled through the inlet. When considering the surface water flow to the inlet, the model uses the weir formula to calculate the inflow from the ground surface, i.e.,

$$q_{in} = \varphi l_I h_s^{1.5} \tag{8}$$

where φ is the discharge coefficient, l_I is the perimeter of the inlet, and h_s represents the surface water depth at the inlet.

Overflow or backward flow occurs when the water depth in an inlet exceeds the surface water elevation, and then the water depth above the surface water elevation will be spread on the surface grid. The backward flow and overflow discharge in the coupled model are calculated by the maximum pressure of the

inlets. As for the water depth updates on the 2D surface, water exchange only happens on the grid connecting with the inlet, and the rainfall source term in these grids can be rewritten as Equation (9).

$$R = i - f - 3.6 \times 10^6 \frac{q_{in} - q_{out}}{A_s} \tag{9}$$

where i and f are in mm/s, q_{in} and q_{out} are in m^3/s, and A_s is the area of the surface grid (m^2);

The Existing Approach

The rainfall-runoff process can be divided into four main parts: soil infiltration, drainage-pipe discharge, surface runoff, and evaporation/transpiration (Zhang and Pan, 2014). According to the water conservation law, the amount of water discharged from the drainage pipe can be approximated by using the methods of subtracting mass and thus achieving a similar effect. In this work, the new approach based on the existing approach is proposed to compute the drainage-pipe discharge.

In the existing approach, as well as considering the basic soil infiltration, all areas additionally need to subtract a mass that corresponds to the drainage-pipe capacity (**Figure 1**). Equation (10) can then be obtained and applied to the existing approach.

$$R = i - f - \alpha_1 \tag{10}$$

where α_1 denotes the subtracted mass rate of the existing approach (mm/h).

The New Approach

The rainwater is subtracted through inlets in the actual rainfall-runoff process. The new approach subtracts mass only at the inlets (**Figure 2**), and the mass subtracted is calculated by the weir formula after correction, as shown in Equation (11). In contrast with the coupled model, the new approach ignores the hydrodynamic processes of the drainage pipe. The new approach is more in accordance with the actual physical processes of the flooding and inundation process. Meanwhile, in order to improve the accuracy of the new approach, a correction is applied in the formula for calculating the subtracted mass.

$$R = \begin{cases} i - f - \alpha_2, & \text{if flag} = \text{Inlet} \\ i - f, & \text{if flag} \neq \text{Inlet} \end{cases} \tag{11}$$

$$\alpha_2 = \frac{3.6 \times 10^6 q_{Inlet}}{A_S} \tag{12}$$

where α_2 represents the subtracted mass rate in the inlet of the new approach (mm/h); flag is the general land attribute term of the surface grids, Inlet denotes grids with the attribute term 'inlet'; q_{Inlet}, introduced later, is the correction of q_{in} that is calculated by Equation (8) (m^3/s), and A_S is the area of one surface grid.

It is necessary to correct q_{in} for better effect. If we do not correct the inflow, the mass subtracted will be larger than the actual condition. This is because of limited drainage-pipe capacity: the drainage pipe cannot discharge so much rainwater within a short period of time because of the restriction on the size of the drainage pipe. Hence, a correction of inflow based on the size of the drainage pipe is required. Firstly, the maximum discharge of the pipe, $Q_{P\max}$, is computed by Equations (13) and (14); both equations reference Code GB 50014-2006. Secondly, the total inflow, Q_i, of all of the q_I in the ith pipe is calculated, where i represents the id of the drainage pipe. Thirdly, the values of the maximum pipe flow $Q_{P\max}$ and the total inflow Q_i are compared, and the inlet inflow q_I must be corrected when $Q_i > Q_{p\max}$. A coefficient representing the ratio of Q_i and $Q_{P\max}$ is used to achieve the correction of inlet inflow q_{in}. The detailed equations are shown as follows.

$$Q_P = A_p v = A \frac{1}{n} R_p^{\frac{2}{3}} I_p^{\frac{1}{2}} \tag{13}$$

$$Q_{P\max} = \frac{1}{16n} \pi d_P^3 I_p^{\frac{1}{2}} \tag{14}$$

where Q_P represents the flow of the drainage pipe based on Code GB 50014-2006, and $Q_{P\max}$ is the status of full pipe flow; A_p is the discharge section area of the pipe; R_p is the hydraulic radius of the pipe; n is the Manning coefficient in the pipe; d_p is the diameter of the pipe; I_p is the slope of the pipe. The diameter of the pipe can be determined according to the design capability of drainage pipes and the relevant code (The Ministry of Housing and Urban-Rural Development of the People's Republic of China, 2006). The slope of the pipe can be obtained with reference to the terrain features (Liang and Cheng, 2018). The maximum discharge of the pipe network can also be calibrated according to actual inundation and flooding if we can get measured data.

$$Q_i = \sum_j^N q_{Ij} \tag{15}$$

$$q_{Inlet} = \begin{cases} q_I & Q_i \leq Q_{P\max i} \\ \frac{Q_{P\max i}}{Q_i} q_I & Q_i > Q_{P\max i} \end{cases} \tag{16}$$

where Q_i represents the total flow of all inlets to the ith pipe and the subscript j represents the id of the inlet. The symbol diagram of the computation process is shown in **Figure 3**.

A flow diagram of the methods for reflecting the capacity of pipe network drainage is shown in **Figure 4**. As a first step, the same basic data are provided to the different approaches, including the initial conditions, the Digital Elevation Model (DEM), and the land use. The rainfall and soil infiltration are then calculated. The third step is to modify the rainfall source term to reflect the capacity of the drainage pipe. It is reduced over the whole area with the existing approach, while only grids with the inlet type are reduced in the new approach. In the new approach, the inflow of the inlet is corrected when the total inflow exceeds the drainage capacity, which is based on the design standards and actual situation of the drainage pipe. Both the existing approach and the new approach correct the rainfall source term in the model to reflect the capacity of the drainage pipe network. Finally, the fluxes, slope source term, and friction source term calculations are the same for the different approaches.

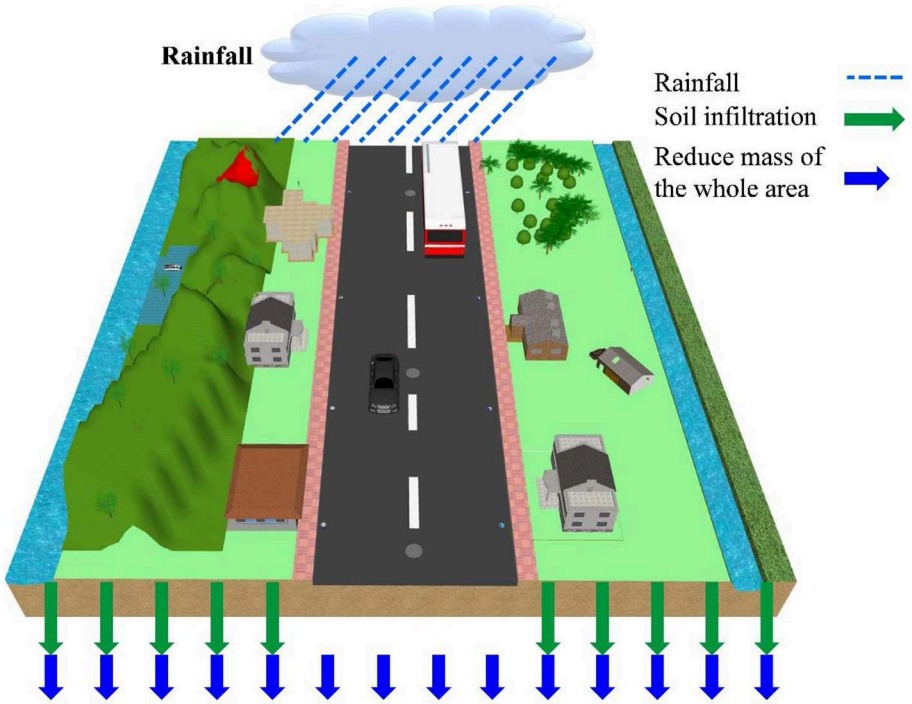

FIGURE 1 | Schematic diagram of the existing approach.

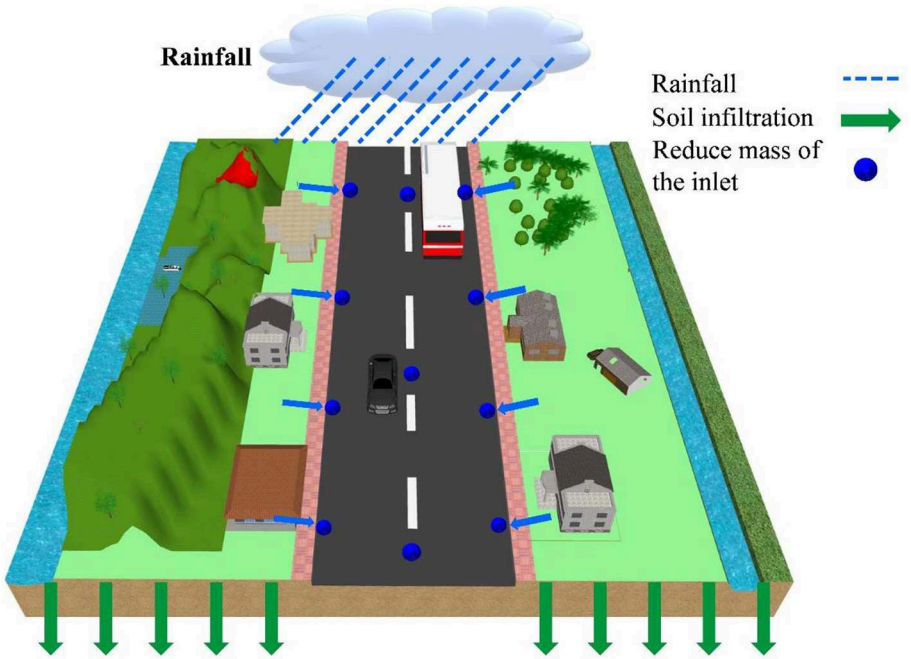

FIGURE 2 | Schematic diagram of the new approach.

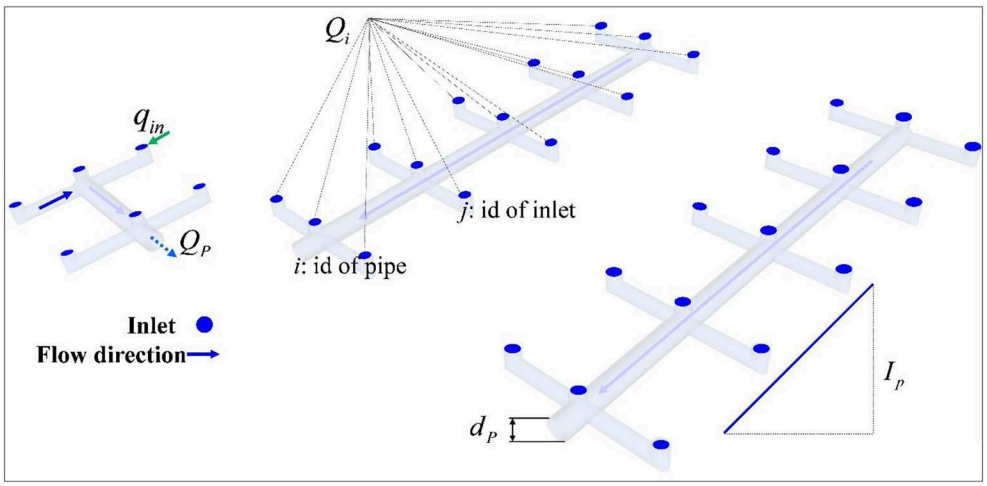

FIGURE 3 | Symbol diagram of the new approach.

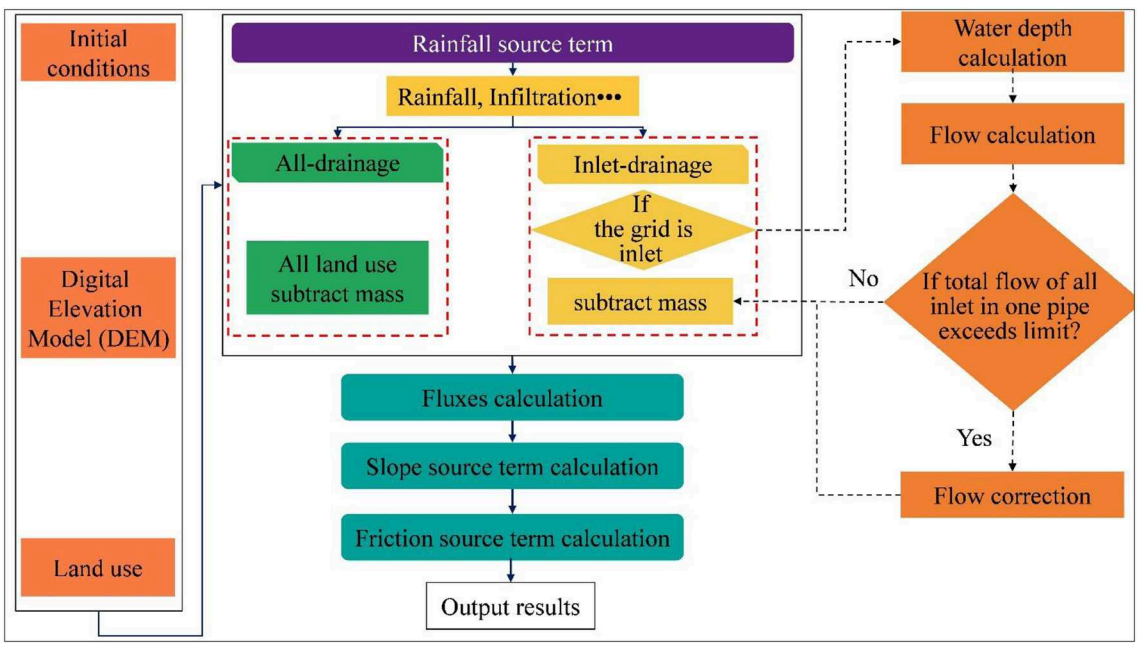

FIGURE 4 | Flow diagrams of the new approach and the existing approach.

TEST CASES

In order to investigate the effectiveness of the new approach and the existing approach in representing the capability of drainage pipe systems, the rainfall-runoff process is simulated in two cases: an idealized urban catchment and the Fengxi New City of the Xixian New Area urban catchment. Meanwhile, the coupled model is applied to quantitatively compute the amount of flooding to compare the effects of the two approaches. The subtracted mass rate of the existing approach in each case is first calibrated based on the results of the coupled model, and then the three different approaches are used to simulate the rainfall-runoff process under rainfall with different return periods.

Rainfall-Runoff Process in an Idealized Urban Catchment

To investigate the performance of the existing approach and the new inlet-drainage approach for the urban catchment, rainfall and runoff propagating over an idealized urban catchment are computed to demonstrate the performance of the three methods. In the test case, the idealized urban catchment is 240 m long

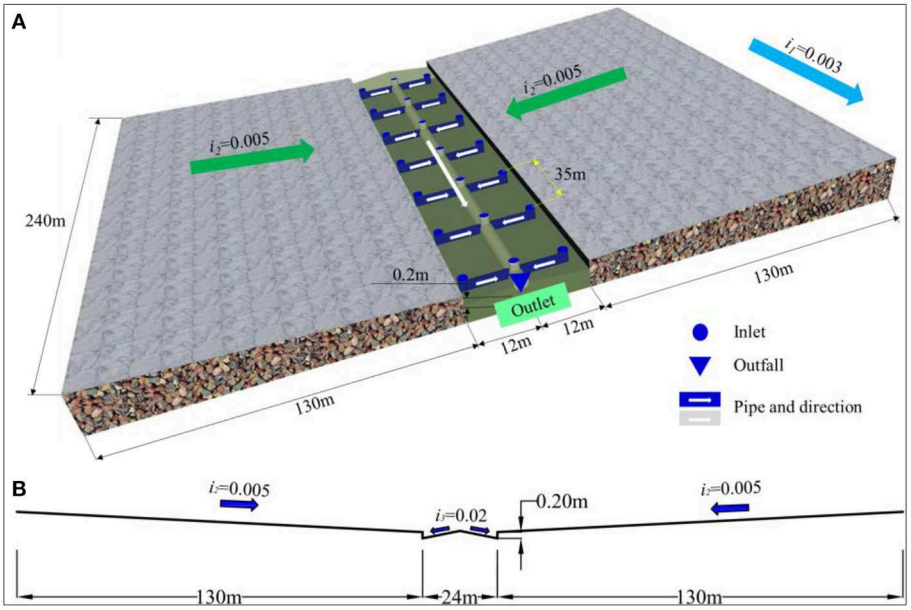

FIGURE 5 | Schematic diagram of the ideal urban catchment (**A**: Stereogram and drainage-pipe layout; **B**: cross-section diagram).

and 284 m wide, the cross-sectional width consists of a 130-m-wide confluence area on both sides and a 24-m-wide road, as shown in **Figure 5A**. The size of the idealized urban catchment is based on an actual urban catchment. According to the code for the design of outdoor wastewater engineering (The Ministry of Housing and Urban-Rural Development of the People's Republic of China, 2006) and some research (Van Dijk et al., 2014; Liang and Cheng, 2018), the vertical and horizontal slopes of the urban area are taken as $i_1 = 0.003$ and $i_2 = 0.005$, respectively. The road is 0.2 m lower than the sides, and there is a slope of $i_3 = 0.02$ from the middle of the road to the side of the road (**Figure 5B**).

The drainage-pipe layout is determined according to actual survey, combined with the code. The inlet is 0.7 m long and 0.4 m wide. Inlets are generally 25–50 m apart on the two sides of the road, considered to be 35 m for this study, and the main pipe is laid in the middle of the road. Therefore, there are 20 inlets, 1 outlet, and 20 pipes in the urban area. The drainage-pipe layout is shown in **Figure 5A**.

The rainwater design flow is calculated by using the following inference formula.

$$Q_S = \frac{\psi i F}{3600} \tag{17}$$

where Q_S is the rainwater design flow (m^3/s); i denotes the rainfall intensity (mm/h); ψ represents the runoff coefficient; F is the catchment area (m^2).

The design storm from Xi'an County, Shaanxi Province, with a return period of 1 year (the standard for the drainage-pipe design of the study area) and a duration of 2 h is employed as rainfall input data. The storm formula is expressed as follows (Bi et al., 2015):

$$i = \frac{795.913 \times (1 + 2.915 \times \lg p)}{(t + 21.933)^{0.974}} \tag{18}$$

where i denotes the rainfall intensity (mm/h); p is the return period, year; t denotes rainfall duration, min.

Finally, the pipe diameter is calculated according to Equation (19).

$$d = \sqrt{\frac{4Q_S}{\pi v}} \tag{19}$$

where v is the pipe flow velocity. According to the code, the minimum value is 0.6 m/s, and here it is 1 m/s. After calculation, the pipe diameter is 0.8 m.

Regarding the boundary condition, all boundaries are closed boundaries except for the outlet. The Manning value on both sides is 0.03, and that on the road is 0.014. The computational domain is discretized into a 1-m resolution DEM. The rainfall with a constant intensity of 60 mm/h and with a duration of 3,600 s was selected for calibration of the subtracted values of the existing approach and of the new approach; the simulation duration is 7,200 s. Under the above rainfall event, firstly, simulation with the coupled model without infiltration in the urban area is used to obtain the water discharge volumes at the outlet of the road. Secondly, the subtracted values in the existing approach are calibrated until the error of discharge volumes between the existing approach and coupled model at the 2nd h is <5%. Finally, a subtracted value of 16.5 mm/h is obtained for the existing approach. The related parameters in the new approach are consistent with the coupled model. A simulation without a

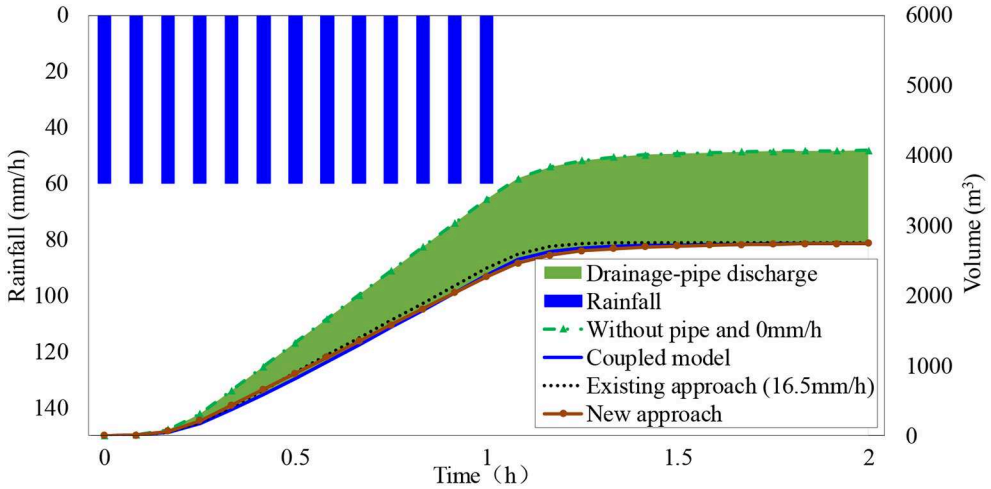

FIGURE 6 | Rainfall process diagram and volume process diagram under different scenarios.

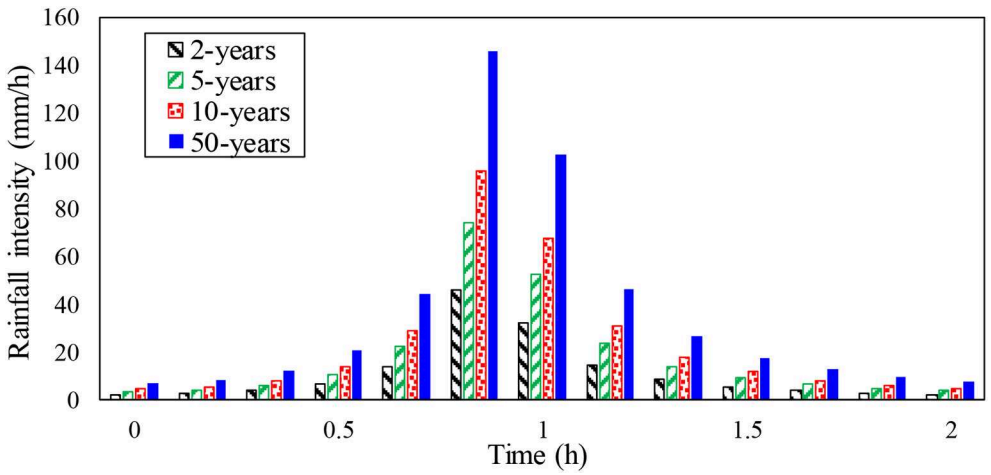

FIGURE 7 | Hyetography of design storms with different return periods.

drainage pipe and no infiltration over the whole area is performed to reflect the drainage effect of the pipe network. The process of the rainfall event and discharge volumes at the outlet under different scenarios are shown in **Figure 6**.

Simulations using the coupled model, the existing approach, and the new approach were then run for different return periods, and the effects of the existing approach and the new approach were evaluated based on the coupled model results. The design storms from Xi'an County, Shaanxi Province, with return periods of 2, 5, 10, and 50 years and a duration of 2 h are employed as rainfall input data (**Figure 7**). The storm formula is shown in Equation (18). The volumes processed at the outlet of the ideal urban catchment are presented in **Figure 8**. The results clearly demonstrate that the new approach is more effective than the existing approach, especially for the rainfall with a 2- and 5-years return period. Moreover, the runoff delay in the existing approach can be clearly observed in **Figure 8**. Compared with the coupled model, the runoff delay times in the existing approach are 1,200–1,500 s under rainfall events with different return periods, whereas there is almost no delay in the new approach.

The volumes at the outlet with different approaches and the error vs. the coupled model are listed in **Table 1**. The results clearly demonstrate that the new approach is very effective in assessing the capability of a drainage pipe compared to the coupled model. The error percentage between the coupled model and the existing approach is 13.89–57.34%, which decreases with an increase in the rainfall return period. The error between the coupled model and the new approach is only 0.14–6.66% and is much smaller than with the existing approach. Compared with the existing approach, the error with the new approach can reduce by 57.97, 27.89, 20.86, and 14.28% for rainfall events with the return periods of 2, 5, 10, and 50 years, respectively. In other words, the new approach is more similar to the coupled model than is the existing approach.

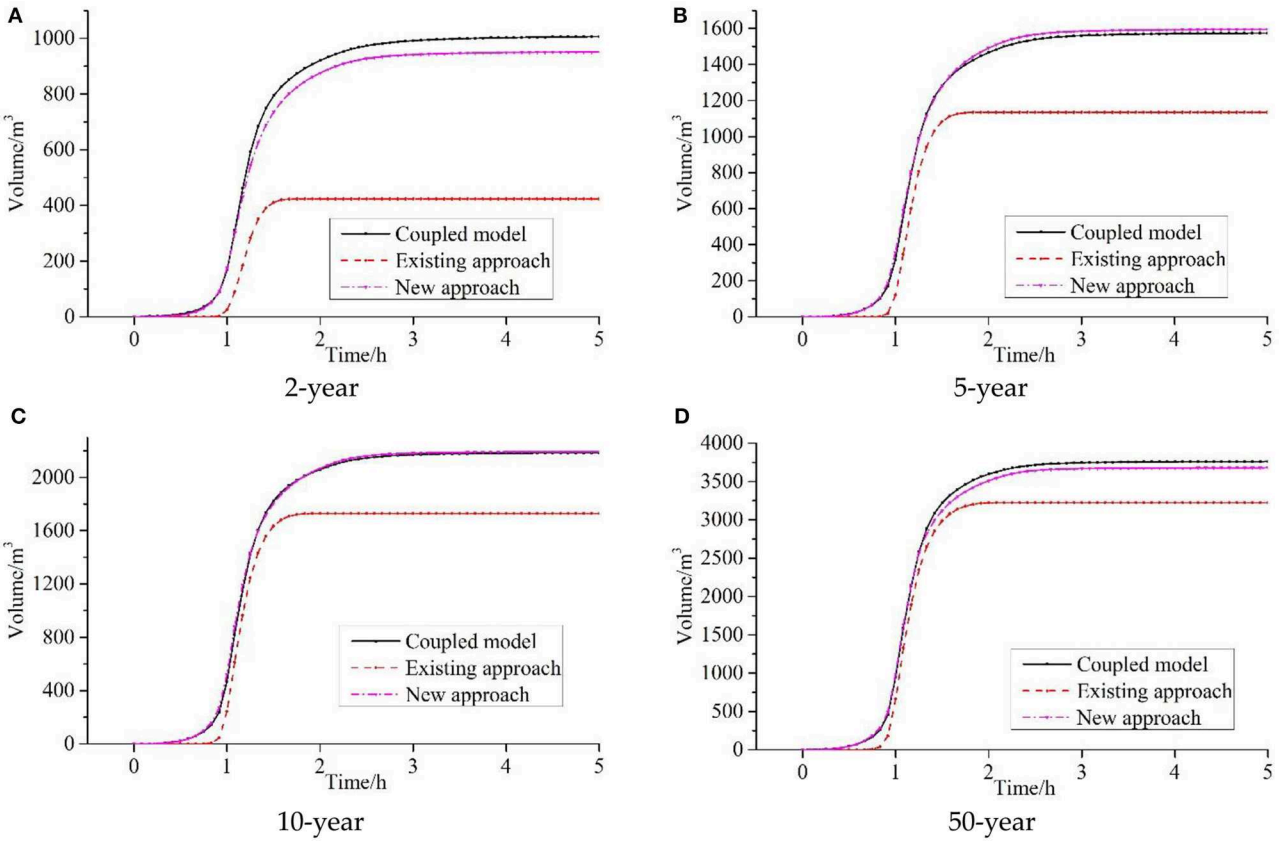

FIGURE 8 | Simulated volumes at the outlet of the road of the urban area for different approaches under **(A)** 2-year, **(B)** 5-year, **(C)** 10-year, and **(D)** 50-year rainfall events.

TABLE 1 | Comparison of volumes with different approaches and error vs. the coupled model (5th h).

Return period of rainfall	Volumes (m^3)			Error against the coupled model (%)	
	Coupled model	Existing approach	New approach	Existing approach	New approach
2	1006.2	422.9	939.2	57.97	6.66
5	1573.8	1134.8	1576.0	27.89	0.14
10	2184.3	1728.6	2168.7	20.86	0.71
50	3761.3	3225.4	3643.0	14.25	3.15

With regard to the computational efficiency, the new approach takes only an average of 493.92 s with 73,840 cells in the rainfall with different return periods, while simulation with the coupled model costs an average of 1,806.39 s, showing that the new approach can accelerate the computation by 3.77 times while generating the results with similar accuracy.

Rainfall-Runoff Process in Fengxi Urban Catchment

To investigate the effectiveness of the existing approach and the new approach for the rainfall-runoff process in a real catchment, the three approaches are implemented for the abovementioned conditions in Fengxi New City of Xixian New Area urban catchment, China.

The Fengxi New City urban catchment (**Figure 9**) is applied to calibrate the parameters of the reduction rate of the existing approach and the new approach in an actual catchment. It is a typical urban area with a catchment area of 47.35 hm^2. The catchment is located in Xixian New Area, Shaanxi Province, China. The regional climate is classified as monsoonal, and more than 50% of the rainfall falls from July to September. The input data to the model include the DEM with a resolution of 2 m (**Figure 9A**), infiltration rates, and Manning coefficients (**Table 2**). The soil infiltration rate of different land use types is based on actual measurement using double-ring

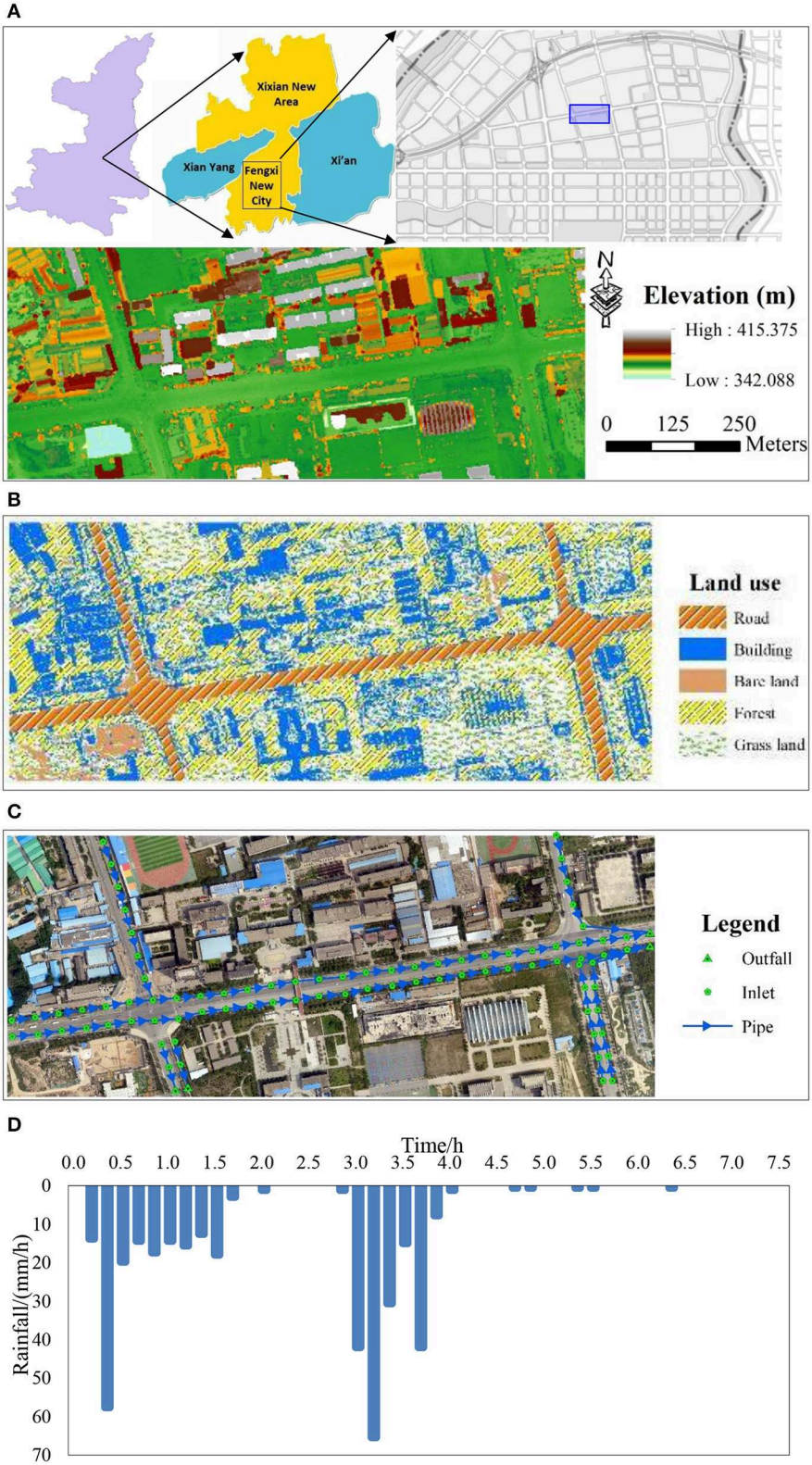

FIGURE 9 | Study catchment in Fengxi New City, Xixian New Area, China. **(A)** Digital Elevation Model (DEM); **(B)** land use map; **(C)** digital orthophoto map and the drainage-pipe layout; **(D)** hyetography in the study area.

TABLE 2 | Infiltration rate (mm/h), Manning coefficient (s/m$^{1/3}$), and proportion (%) under different land use types in the coupled model.

Land use	Road	Building	Bare land	Forest	Grass land
Infiltration rate (mm/h)	0	0	19.99	15.72	8.2
Manning (s/m$^{1/3}$)	0.014	0.015	0.03	0.20	0.06
Area (hm^2)	4.58	12.10	1.36	15.23	14.08
Proportion (%)	9.68	25.55	2.87	32.16	29.73

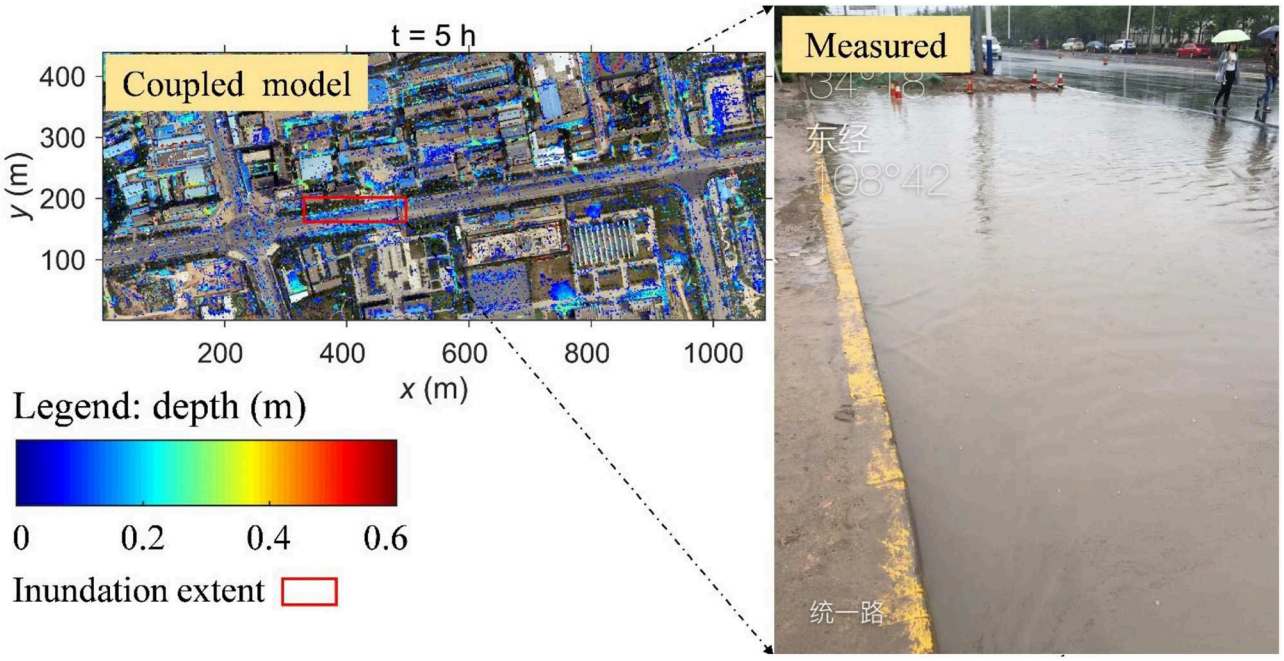

FIGURE 10 | The coupled model extent and observed, measured inundation extent in the study area (5th h).

infiltrometers, which consist of open inner and outer cylinders. Both of the cylinders should be inserted manually into the soil then a constant water head should be maintained. The use of the outer cylinder helps to decrease the error, and the water volume added into the inner cylinder is measured to determine the soil infiltration rate (ASTM, 2009; Fatehnia et al., 2016). The Manning coefficient of different land use types is based on Hou et al. (2018b). **Figure 9B** illustrates the five basic types of land use in the study area—Grassland, Roads, Bare land, Buildings, and Forests. The layout of the drainage pipe network of Fengxi New City urban catchment is shown in **Figure 9C**. It comprises 81 inlets, 4 outlets, and 81 pipes. The diameter of the pipe is 0.8 m. This data information was provided by the Technology Research Center for Sponge City, Fengxi New City. Moreover, **Figure 9D** displays the rainfall hyetograph for the study area, where the maximum rainfall was observed. The data of the flood event that occurred in the Fengxi New City on August 25th, 2016, is adopted for the simulation. The rainfall, which lasted 7.5 h, started at 00:30 and ended at 08:00. The maximum hourly rainfall, at 3.1 h into the storm, was 65.4 mm/h, the total rainfall was 66 mm, and the return period of the storm event is about 50 years. The inundation data were observed on-site, and the measured area inundated at the 5th h was about 1,600 m^2.

The coupled model is used to simulate the rainfall-runoff process in the study catchment under the above rainfall event. The result from the coupled model at the 5th h is 1,596 m^2. The results from the coupled model and an actual observation are shown in **Figure 10**. The red lines represent the inundation extents from the simulation result of the coupled model. The inundation is mainly concentrated at the side of the road, which is consistent with the actual situation. This clearly shows that the inundation areas simulated by the coupled model exhibit good agreement with the measured data. Meanwhile, it also validates the coupled model.

The reduction rate in the existing approach is then calibrated according to the measured data and the results of the coupled model. After many trial calculations, finally, the reduction rate of the existing approach in all areas is 6.9 mm/h. The parameters of the new approach are consistent with the coupled model. The inundation areas on the road under the existing approach and the new approach are 1,612 and 1,524 m^2, respectively. Compared with the measured data, the error of both results is

<5%, which is good agreement with the measured data. This indicates that the reduction rate is reasonable. The measured data and the evolution of areal inundation under different approaches are shown in **Figure 11**. The figure clearly shows that the new approach is more consistent with the coupled model than is the existing approach. Compared with the coupled model, the inundation area in the existing approach is too small in the first 3 h, while it is too high in the latter part of the rainfall process. The inundation extents with both the existing approach and the new approach at the 5th h are very close to the measured data and the coupled model.

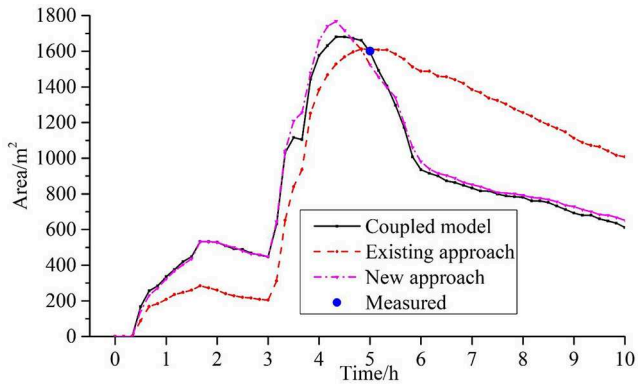

FIGURE 11 | Simulation results of the areal inundation evolution under different approaches.

To systematically compute the effects of the different approaches on runoff process, the design storms from Xi'an County, Shaanxi Province, with different rainfall recurrence intervals (2, 5, 10, and 50 years) and four approaches are imported into the model to simulate the runoff process. The simulation duration is 8 h. **Figure 12** shows the inundated area and the evolution of the inundation extent under rainfall events of different return periods. The results clearly demonstrate that there are significant differences between the existing approach and the new approach, especially in the fading process and the peak inundation. Compared with the coupled model, the inundation areas with the existing approach are low under rainfall with return periods of 2 and 5 years and high under rainfall with return periods of 10 and 50 years. This illustrates that the drainage capacity under rainfall with a small return period may be overestimated in the existing approach and may be underestimated under rainfall with a large return period. However, the inundation evolution of the new approach agrees well with the coupled model; this indicates that the new approach can accurately estimate the drainage capacity under rainfall

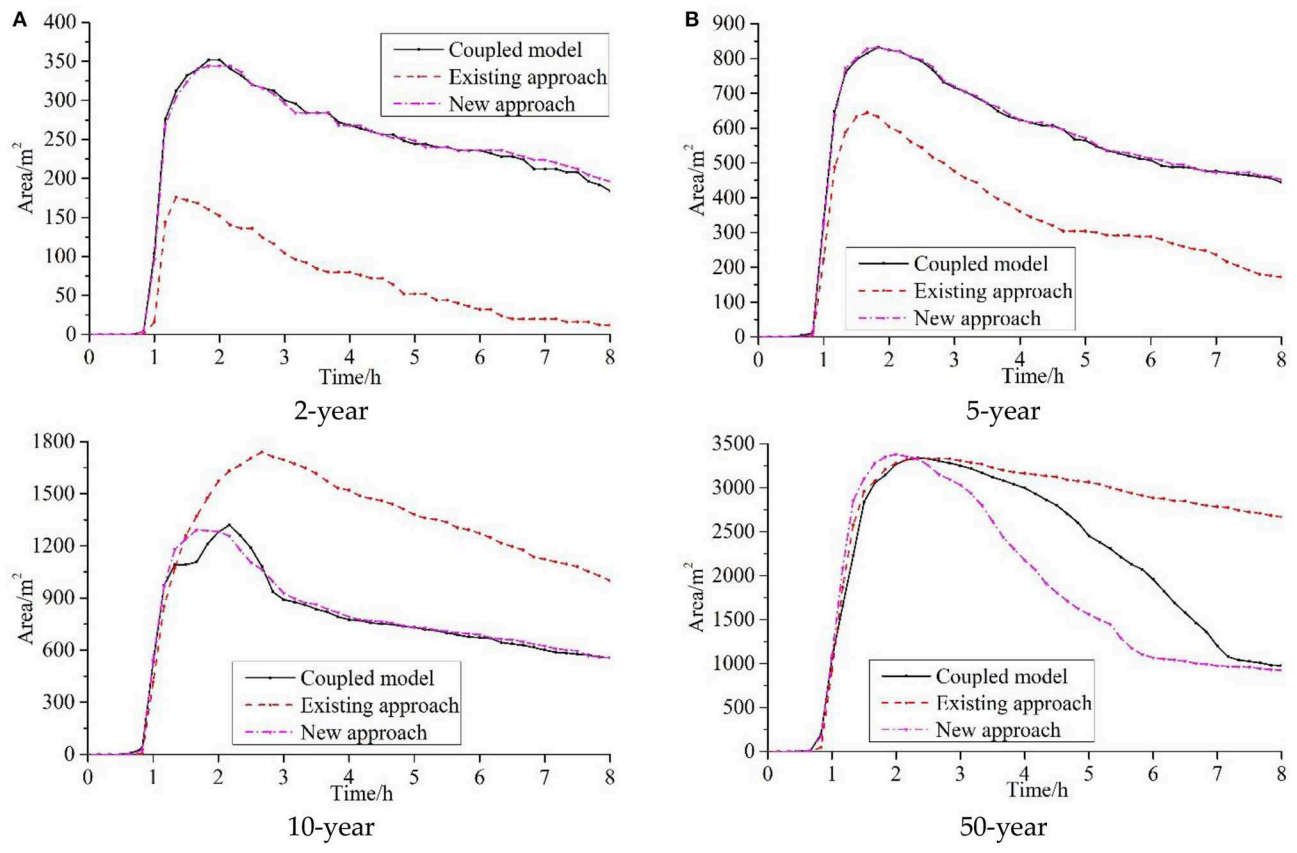

FIGURE 12 | Comparison of inundation extent evolution for different methods (**(A)** 2-year, **(B)** 5-year, **(C)** 10-year, and **(D)** 50-year).

TABLE 3 | Final inundation area (8 h) with the different approaches and the error vs. the coupled model.

Return period of rainfall	Areas (m^2)			Error against the coupled model (%)	
	Coupled model	Existing approach	New approach	Existing approach	New approach
2	184	12	196	93.4	6.52
5	444	172	452	61.26	1.80
10	556	1,000	556	79.86	0.00
50	976	2,668	924	173.36	5.33

with different return periods. The new approach is significantly better than the existing approach under rainfall with different return periods.

The final inundation areas with the different approaches and the error vs. the coupled model are presented in **Table 3**. We can clearly see that the effectiveness of the new approach is better than that of the existing approach in different scenarios. The errors between the coupled model and the existing approach are 93.48, 61.26, 79.86, and 173.36% for rainfall events with return periods of 2, 5, 10, and 50 years, respectively. The error between the coupled model and the new approach is 0.00–6.52%. The new approach can reduce the error with the existing approach by 59.46–168.03% for the rainfall events with the return periods of 2, 5, 10, and 50 years. The results clearly demonstrate that the new approach is very effective for assessing the drainage-pipe capability. In short, the new approach is much more effective, especially when the inundation recedes, which is very similar to the results in the idealized urban catchment, again confirming that this research is valuable for modeling urban areas for which drainage-pipe data are unavailable.

Moreover, the new approach takes only 969.89 s for rainfall with different return periods with 119,460 cells, while the simulation through the coupled model takes 2728.84 s, indicating that this approach can accelerate the computation by 3.29 times while generating results with similar accuracy.

CONCLUSIONS

In this paper, a novel inlet-drainage approach for approximately computing the drainage at inlets is proposed to reflect the effect of drainage pipes in urban areas for which drainage-pipe data are unavailable.

The results of the new approach could more effectively reflect the effect of a drainage pipe than could the existing approach in an ideal urban catchment and an actual urban catchment. The error between the coupled model and the new approach is only 0.00–6.66% in different scenarios. Compared with the existing approach, the error of the new approach can be reduced by 11.10–51.31% in the idealized urban catchment under rainfall with different return periods and can be reduced by 59.46–168.03% in the realistic urban catchment. In addition, the computation time was significantly shorter than with the coupled model while achieving similar accuracy. The new approach accelerates the simulation by 3.29–3.77 times according to the grid properties.

In summary, the simulation results indicate that the new inlet-drainage approach is a more reliable and efficient method for reflecting drainage capacity than is the existing approach. The analysis improves the understanding of urban flood processes and is helpful for decision-making in flood risk management. Meanwhile, the research is valuable for modeling an urban area for which drainage-pipe data are unavailable. However, the new approach is not able to reflect the overflow and backflow process of the drainage pipe. Further research is needed into more advanced methods to fully reflect the effects of drainage pipes of areas for which data are unavailable.

DATA AVAILABILITY STATEMENT

All datasets generated for this study are included in the article/supplementary material.

AUTHOR CONTRIBUTIONS

DL and JH contributed significantly to the analysis and manuscript preparation. JX, YT, and DY performed the data analyses and wrote the manuscript. DZ and XG helped to perform the analysis, with constructive discussions. All authors contributed to the development of ideas and to write the manuscript.

FUNDING

This work was partly supported by the Visiting Researcher Fund Program of State Key Laboratory of Water Resources and Hydropower Engineering Science (2016HLG01), National Key Research Program of China (2016YFC0402704), the Science and Technology Department Project of Shaanxi Province (Grant No. 2017JQ3043), IWHR Research and Development Support Program (JZ0145B772017), and the International Cooperation and Exchange Program for Science and Technology (Grant No. 2017KW-014).

ACKNOWLEDGMENTS

We wish to acknowledge all the data support by Fengxi New City Development and Construction Group Co., Ltd, of Shaanxi Xixian New Area. We thank the State Key Laboratory of Water Resources and Hydropower Engineering Science, National Key Research Program of China, Science and Technology Department Project of Shaanxi Province, IWHR, and International Cooperation and Exchange Program for Science and Technology for their financial support.

REFERENCES

Ali, M., Khan, S. J., Aslam, I., and Khan, Z. (2011). Simulation of the impacts of land-use change on surface runoff of Lai Nullah Basin in Islamabad, Pakistan. *Landsc. Urban Plan.* 102, 271–279. doi: 10.1016/j.landurbplan.2011.05.006

ASTM (2009). *ASTM D3385-2009 D3385-09, Standard Test Method for Infiltration Rate of Soils in Field Using Double-Ring Infiltrometer*. West Conshohocken, PA: ASTM International. Available online at: www.astm.org.

Bi, X., Dang, C., Cheng, L., Luo, H., Shi, M., and Zhao, R. (2015). Study on compiling rainstorm intensity formula in Xi'an urban. *J. Anhui Agric. Sci.* 43, 223–225+228. doi: 10.13989/j.cnki.0517-6611.2015.26.212

Chang, T.-J., Wang, C.-H., and Chen, A. S. (2015). A novel approach to model dynamic flow interactions between storm sewer system and overland surface for different land covers in urban areas. *J. Hydrol.* 524, 662–679. doi: 10.1016/j.jhydrol.2015.03.014

Chao, L., Zhang, K., Li, Z., Wang, J., Yao, C., and Li, Q. (2019). Applicability assessment of the CASCade Two Dimensional SEDiment (CASC2D-SED) distributed hydrological model for flood forecasting across four typical medium and small watersheds in China. *J. Flood Risk Manag.* 12:e12518. doi: 10.1111/jfr3.12518

Chen, X., Ji, P., Wu, Y., Zhao, Y., and Zeng, L. (2017). Coupling simulation of overland flooding and underground network drainage in a coastal nuclear power plant. *Nucl. Eng. Des.* 325, 129–134. doi: 10.1016/j.nucengdes.2017.09.028

Environment Agency (2013). *Updated Flood Map for Surface Water-national Scale Surface Water Flood Mapping Methodology*. Bristol: Environment Agency.

Fan, Y., Ao, T., Yu, H., Huang, G., and Li, X. (2017). A coupled 1D-2D hydrodynamic model for urban flood inundation. *Adv. Meteorol.* 2017, 1–12. doi: 10.1155/2017/2819308

Fatehnia, M., Tawfiq, K., and Ye, M. (2016). Estimation of saturated hydraulic conductivity from double-ring infiltrometer measurements. *Eur. J. Soil Sci.* 67, 135–147. doi: 10.1111/ejss.12322

Hou, J., Guo, K., Liu, F., Hao, H., Liang, Q., Tong, Y., et al. (2018a). Assessing slope forest effect on flood process caused by a short-duration storm in a small catchment. *Water* 10:1256. doi: 10.3390/w10091256

Hou, J., Liang, Q., and Xia, X. (2015). Robust absorbing boundary conditions for shallow water flow models. *Environ. Earth Sci.* 74, 7407–7422. doi: 10.1007/s12665-015-4743-6

Hou, J., Wang, R., Li, G., and Li, G. (2018b). High-performance numerical model for high-resolution urban rainfall-runoff process based on dynamic wave method. *J. Hydroelectr. Eng.* 37, 40–49. doi: 10.11660/slfdxb.20180305

Huang, X., Cao, Y., and Li, J. (2020). An automatic change detection method for monitoring newly constructed building areas using time-series multi-view high-resolution optical satellite images. *Rem. Sens. Environ.* 244:111802. doi: 10.1016/j.rse.2020.111802

Jang, J.-H., Chang, T.-H., and Chen, W.-B. (2018). Effect of inlet modelling on surface drainage in coupled urban flood simulation. *J. Hydrol.* 562, 168–180. doi: 10.1016/j.jhydrol.2018.05.010

Khaing, Z. M., Zhang, K., Sawano, H., Shrestha, B. B., Sayama, T., and Nakamura, K. (2019). Flood hazard mapping and assessment in data-scarce Nyaungdon area, Myanmar. *PLoS ONE* 14:e0224558. doi: 10.1371/journal.pone.0224558

Kratt, C. B., Woo, D. K., Johnson, K. N., Haagsma, M., Kumar, P., Selker, J., et al. (2020). Field trials to detect drainage pipe networks using thermal and RGB data from unmanned aircraft. *Agric. Water Manag.* 229:105895. doi: 10.1016/j.agwat.2019.105895

Lashford, C., Rubinato, M., Cai, Y., Hou, J., Abolfathi, S., Coupe, S., et al. (2019). SuDS & Sponge cities: a comparative analysis of the implementation of pluvial flood management in the UK and China. *Sustainability* 11:213. doi: 10.3390/su11010213

Leandro, J., Chen, A. S., Djordjevic, S., and Savic, D. A. (2009). Comparison of 1D/1D and 1D/2D coupled (Sewer/Surface) hydraulic models for urban flood simulation. *J. Hydraul. Eng. ASCE* 135, 495–504. doi: 10.1061/(asce)hy.1943-7900.0000037

Li, Q., Liang, Q., and Xia, X. (2020). A novel 1D-2D coupled model for hydrodynamic simulation of flows in drainage networks. *Adv. Water Resour.* 137:103519. doi: 10.1016/j.advwatres.2020.103519

Liang, Q., and Marche, F. (2009). Numerical resolution of well-balanced shallow water equations with complex source terms. *Adv. Water Resour.* 32, 873–884. doi: 10.1016/j.advwatres.2009.02.010

Liang, Q., Smith, L., and Xia, X. (2016). New prospects for computational hydraulics by leveraging high-performance heterogeneous computing techniques. *J. Hydrodyn.* 28, 977–985. doi: 10.1016/s1001-6058(16)60699-6

Liang, X., and Cheng, S. (2018). Study on the influence of roadway slope on pavement drainage. *Water Wastewater Eng.* 54, 5–19. doi: 10.13789/j.cnki.wwe1964.2018.0058

Malarvizhi, K., Kumar, S. V., and Porchelvan, P. (2016). Use of high resolution Google Earth satellite imagery in landuse map preparation for urban related applications. *Proc. Technol.* 24, 1835–1842. doi: 10.1016/j.protcy.2016.05.231

Martínez, C., Sanchez, A., Toloh, B., and Vojinovic, Z. (2018). Multi-objective evaluation of urban drainage networks using a 1D/2D flood inundation model. *Water Resour. Manag.* 32, 4329–4343. doi: 10.1007/s11269-018-2054-x

Rossman, L. A. (2010). *Storm Water Management Model: User's Manual Version 5.0*. Washington, DC: Environmental Protection Agency.

Russo, B., Sunyer, D., Velasco, M., and Djordjević, S. (2015). Analysis of extreme flooding events through a calibrated 1D/2D coupled model: the case of Barcelona (Spain). *J. Hydroinform.* 17:473. doi: 10.2166/hydro.2014.063

The Ministry of Housing and Urban-Rural Development of the People's Republic of China (2006). *GB 50014-2006 Code for Design of Outdoor Wastewater Engineering*. Beijing: China Planning Press.

Van Dijk, E., Van der Meulen, J., Kluck, J., and Straatman, J. H. M. (2014). Comparing modelling techniques for analysing urban pluvial flooding. *Water Sci. Technol.* 69, 305–311. doi: 10.2166/wst.2013.699

Wang, Y., Chen, A. S., Fu, G., Djordjević, S., Zhang, C., and Savić, D. A. (2018). An integrated framework for high-resolution urban flood modelling considering multiple information sources and urban features. *Environ. Model. Softw.* 107, 85–95. doi: 10.1016/j.envsoft.2018.06.010

Xia, X., Liang, Q., Ming, X., and Hou, J. (2017). An efficient and stable hydrodynamic model with novel source term discretization schemes for overland flow and flood simulations. *Water Resour. Res.* 53, 3730–3759. doi: 10.1002/2016wr020055

Yu, D., and Coulthard, T. J. (2015). Evaluating the importance of catchment hydrological parameters for urban surface water flood modelling using a simple hydro-inundation model. *J. Hydrol.* 524, 385–400. doi: 10.1016/j.jhydrol.2015.02.040

Zhang, K., Chao, L., Wang, Q., Huang, Y., Liu, R., Hong, Y., et al. (2019). Using multi-satellite microwave remote sensing observations for retrieval of daily surface soil moisture across China. *Water Sci. Eng.* 12, 85–97. doi: 10.1016/j.wse.2019.06.001

Zhang, S., and Pan, B. (2014). An urban storm-inundation simulation method based on GIS. *J. Hydrol.* 517, 260–268. doi: 10.1016/j.jhydrol.2014.05.044

Conflict of Interest: XG was employed by company Northwest Engineering Corporation Limited of the Power Construction Corporation of China, Xi'an, China.

The remaining authors declare that the research was conducted in the absence of any commercial or financial relationships that could be construed as a potential conflict of interest.

frontiers in Earth Science

ORIGINAL RESEARCH
published: 16 July 2020
doi: 10.3389/feart.2020.00305

Rainfall Runoff and Dissolved Pollutant Transport Processes Over Idealized Urban Catchments

Taotao Zhang[1,2,3], Yang Xiao[1,2], Dongfang Liang[4], Hongwu Tang[1,2], Saiyu Yuan[1,2] and Bin Luan[2]*

[1] State Key Laboratory of Hydrology-Water Resources and Hydraulic Engineering, Hohai University, Nanjing, China, [2] College of Water Conservancy and Hydropower Engineering, Hohai University, Nanjing, China, [3] College of Agricultural Engineering, Hohai University, Nanjing, China, [4] Department of Engineering, University of Cambridge, Cambridge, United Kingdom

Urban stormwater runoff is often considered as one of the most significant contributors to water pollution. Particulates are commonly regarded as the primary form of pollutant transport in the urban environment, but the contribution from the dissolved pollutants can also be significant. This study aims to investigate the dissolved pollutant transport process over urban catchments, especially the effects of buildings and spatial distribution of pollutants. The concept of "exchange layer" has been adopted and an equation has been proposed to describe the release process of dissolved pollutant from the exchange layer to the runoff water. A horizontal two-dimensional water flow and pollutant transport model has been developed for predicting dissolved pollutant runoff based on the shallow water assumptions and the advection-diffusion equation. A series of laboratory experiments have been conducted to verify the proposed model. It has been demonstrated that both the rainfall runoff and the pollutant runoff can be predicted accurately. Buildings slow down the runoff and pollutant transport processes, especially when buildings are staggered. The non-uniform distribution of pollutants over the catchment greatly influences the pollutant transport process over the catchment. This work provides insight into the effects of buildings and initial pollutant distribution on the dissolved pollutant transport phenomenon, which can help better design the pollution mitigation strategies.

Keywords: dissolved pollutant, stormwater, rainfall-runoff, pollutant transport, diffused pollution, urban

OPEN ACCESS

Edited by:
Jingming Hou,
Xi'an University of Technology, China

Reviewed by:
Juan Pablo Rodríguez Sánchez,
University of Los Andes, Colombia
Neil McIntyre,
The University of Queensland, Australia

***Correspondence:**
Yang Xiao
sediment_lab@hhu.edu.cn

Specialty section:
This article was submitted to Hydrosphere, a section of the journal Frontiers in Earth Science

Received: *19 September 2019*
Accepted: *29 June 2020*
Published: *16 July 2020*

Citation:
Zhang T, Xiao Y, Liang D, Tang H, Yuan S and Luan B (2020) Rainfall Runoff and Dissolved Pollutant Transport Processes Over Idealized Urban Catchments. Front. Earth Sci. 8:305. doi: 10.3389/feart.2020.00305

INTRODUCTION

Urban stormwater runoff has been widely recognized as an important source for water quality degradation (Brezonik and Stadelmann, 2002; Shaw et al., 2006; Brett and Gavin, 2010; Revitt et al., 2014). Ongoing urbanization and thus the increased urban ground area are likely to exacerbate the problem (Wang et al., 2013; Naves et al., 2017). In this context, an appropriate pollutant transport model for predicting the runoff processes over contaminated grounds will be valuable for understanding the urban pollutant transport process and mitigating water pollution.

Many researchers have focused on the pollutant transport over simple impervious surfaces, such as road and roof surfaces (Metcalf and Eddy Inc, 1971; Sartor et al., 1974; Kim et al., 2005; Egodawatta et al., 2007, 2009; Muthusamy et al., 2018), and have established and improved the first-order decay model. Metcalf and Eddy Inc (1971) proposed the exponential wash-off equation, which assumes that the rate of pollutant transport from an impervious surface is directly

proportional to the runoff rate and the availability of pollutants. Sartor et al. (1974) verified the exponential equation through rainfall simulation experiments. Egodawatta et al. (2007, 2009) applied such a model to pollutant transport on road and the roof surfaces. They suggested that a rainfall event only had the capacity (depending on rainfall intensity) to transport a fraction of pollutants available on the surface. Hence, an additional term referred to as the "capacity factor" is recommended to the exponential equation. Recently, Muthusamy et al. (2018) noted that the capacity factor and the wash-off coefficient were interdependent and further improved the exponential equation. Until now, current urban water quality models are generally based on the above exponential equation (e.g., SWMM, STORM, etc.). This simple exponential relationship neglect spatial heterogeneity of the catchment. The efficacy of this empirical relationship relies heavily on the extensive calibration of the wash-off coefficients, which limits their predictive capacity. Only few studies have been conducted to establish physically-based models of the pollutant transport in urban landscapes. Shaw et al. (2006) developed a saltation-type wash-off model in which particles are repeatedly ejected from the impervious surface by raindrop impacts and are transported laterally by the overland flow, while settling back to the surface. Massoudieh et al. (2008) proposed a wash-off model with the assumption that detachment and reattachment of pollutants are considered as rate-limited processes and the detachment rate varies with the flow velocity according to a power law. Hong et al. (2016) and Hong Y. et al. (2017) presented a two-dimensional pollutant transport model by combining the Hairsine-Rose (H-R) model and the FullSWOF (Full Shallow-Water equations for Overland Flow) model. In the above studies, particulate pollutants (solids) were often chosen as the targeted pollutants or the surrogate of other pollutants, based on the assumption that most of the pollutants are adsorbed on the surface of the solids (Herngren et al., 2005; Miguntanna et al., 2013). In practice, stormwater-borne pollutants should be divided into the dissolved and the particulate phases (Sheng et al., 2008; Hong Y. et al., 2017). Liu et al. (2013) noted that using solids as a surrogate to estimate other pollutant species is inappropriate. Goonetilleke et al. (2005) indicated that some pollutant moved in the dissolved form, which was more bio-available and was therefore more likely to cause water pollution. Pollutants such as nitrogen, bacteria, and heavy metals can be dissolved in water and pose serious water pollution issues, such as eutrophication and pandemics. Hence, the common management strategy that targets the particulate pollutants in urban stormwater management often has only limited efficiency (Goonetilleke et al., 2005). An accurate pollutant transport model can accurately predict the pollutant transport process, which is crucial for the design of pollution mitigation strategies such as rainwater collection and treatment plants.

Previous studies about the dissolved pollutant (solute) transport have mainly focused on the pollutant transport on soil slopes. The mixing layer theory and the exchange theory are the two predominant theories used to describe the mechanism of the solute transport from soil ground into overland flow (Ahuja et al., 1981; Ahuja and Lehman, 1983; Gao et al., 2004, 2005; Walter et al., 2007; Yang et al., 2016). They all have suggested that a "thin layer" (mixing layer or exchange layer) near the soil surface controls the solute transfer between the soil and overland flow. Only few studies (Xiao et al., 2016, 2017) investigated the dissolved pollutant transport over impervious surfaces. To bridge the gap in our understanding of the dissolved pollutant transport, Xiao et al. (2016, 2017) conducted a series of experiments and proposed a mathematical model to describe the transport of dissolved pollutants. However, these studies were conducted on a one-dimensional case and no studies have been reported to take into account the effect of buildings in urban catchments. Buildings' geometry and layout are very complex. Some studies (Cea et al., 2010; Liang et al., 2015) proved that buildings and their layouts can greatly affect the rainfall runoff process, which directly affects the pollutant transport process. Hence, it is essential to consider the layout of buildings when investigating the dissolved pollutant transport over urban catchments.

In addition, many previous studies assumed that the pollutants were uniformly distributed on the ground surface (Sartor et al., 1974; Kim et al., 2005; Egodawatta et al., 2007, 2009; Xiao et al., 2017; Muthusamy et al., 2018). Some researchers (Pan et al., 2017; Hong N. et al., 2017) have suggested that a practical urban catchment was much more complicated with large spatial variations in the degree of ground contamination. Naves et al. (2017) indicated that the total load of pollutant on a road surface was not uniform but was influenced by wind and rainfall characteristics, traffic conditions, catchment characteristics, and human activities. To the knowledge of the authors, there has been insufficient research about the influence of pollutant distribution on the pollutant transport process.

The objective of this study is to investigate the dissolved pollutant transport process over urban catchments, especially the effects of buildings and non-uniform pollutant distribution. To do this, a two-dimensional dissolved pollutant transport model has been developed to simulate the stormwater runoff in built-up areas, combining the shallow water equations, the advection-diffusion equation and an equation to describe the release process of dissolved pollutant from impervious surface to the runoff water. A series of laboratory experiments have been conducted using artificial rainfall simulators and idealized urban catchments. Observed experimental data were used to validate the newly-developed mathematical model. Finally, the model is applied to investigate the sensitivity of the results to the initial non-uniform distribution of pollutants.

MATHEMATICAL MODEL

Shallow Water Equations

The fully-dynamic non-linear shallow water equations (SWEs) are widely used to predict the rainfall-runoff processes (Liang et al., 2015). For a rainfall event on an impermeable urban catchment, the horizontal extent of the surface runoff is much greater than the water depth. Hence, the depth-averaged modeling approach is appropriate for this phenomenon. When neglecting the viscosity and wind effect, the standard SWEs can

be expressed as:

$$\frac{\partial \eta}{\partial t} + \frac{\partial UH}{\partial x} + \frac{\partial VH}{\partial y} = I \tag{1}$$

$$\frac{\partial UH}{\partial t} + \frac{\partial (U^2 H)}{\partial x} + \frac{\partial (UVH)}{\partial y} = -gH\frac{\partial \eta}{\partial x} - \frac{n^2 gU\sqrt{U^2+V^2}}{H^{1/3}} \tag{2}$$

$$\frac{\partial VH}{\partial t} + \frac{\partial (UVH)}{\partial x} + \frac{\partial (V^2 H)}{\partial y} = -gH\frac{\partial \eta}{\partial y} - \frac{n^2 gV\sqrt{U^2+V^2}}{H^{1/3}} \tag{3}$$

where η is the water surface elevation; t is the time; U and V are the two components of the velocity in the x and y directions, respectively; I is the rainfall intensity; H is the water depth; g is the gravitational acceleration; n is the Manning's roughness coefficient.

The above SWEs can be numerically solved by a highly efficient Total Variation Diminishing (TVD) MacCormack scheme. This scheme consists of a predictor step, a corrector step and a TVD modification step. It is of second order accuracy in both time and space. This numerical scheme is not herein repeated, as details can be found in Liang et al. (2006, 2007b). Liang et al. (2015) verified this scheme in idealized catchments containing buildings. In flood inundation modeling, four building representation methods are commonly used to represent the unsteady and three-dimensional flow through urban landscapes: building resistance (BR), building block (BB), building hole (BH), and building porosity (BP). In the BR method, a large resistance coefficient is imposed to cells that fall within building footprints (Liang et al., 2007a). In the BB method, the bed elevation is raised according to the heights of buildings (Cea et al., 2010). In the BH method, the buildings are represented as holes in the numerical mesh, and free-slip wall boundary conditions are enforced at building walls (Cea et al., 2010). In the BP method, spatially distributed parameters, including porosity and drag coefficient, are introduced to model the effects of buildings on flood water movement without resolving their exact geometries (Schubert and Sanders, 2012). By comparing these four methods of representing buildings, the BH method was found to perform best in balancing the numerical accuracy and stability (Cea et al., 2010; Schubert and Sanders, 2012). The BH method is adopted to account for the effect of buildings in this study.

Pollutant Transport Equation

In this study, we focus on the dissolved pollutant transport process, which is governed by the advection-diffusion equation. The governing equation can be written as:

$$\frac{\partial HC}{\partial t} + \frac{\partial UHC}{\partial x} + \frac{\partial VHC}{\partial y}$$

$$= \frac{\partial}{\partial x}\left(HD_{xx}\frac{\partial C}{\partial x} + HD_{xy}\frac{\partial C}{\partial y}\right) + \frac{\partial}{\partial y}\left(HD_{yx}\frac{\partial C}{\partial x} + HD_{yy}\frac{\partial C}{\partial y}\right) + q_C \tag{4}$$

where, C is the depth-averaged pollutant concentration; D_{xx}, D_{xy}, D_{yx} and D_{yy} constitute the dispersion-diffusion tensor for depth-averaged mixing, whose principal direction coincides with the flow direction. q_C represents the source term, which is used to introduce the pollutant distributed on the ground into the simulation.

Liang et al. (2010) proved that the advection-diffusion equation can also be solved by the TVD MacCormack scheme. In this scheme, a second-order accurate central scheme is used in the diffusion stage, and a five-point TVD modification is imposed on the standard MacCormack scheme in the advection stage. Liang et al. (2010) examined this model's performance in both idealized and real-life situations, and suggested that this model has sufficiently high efficiency and accuracy for solving the pollutant transport problems in natural aquatic environments. The detailed theory and treatment with regard to this numerical scheme can be found in Liang et al. (2010). In this study, the values of D_{xx}, D_{xy}, D_{yx}, and D_{yy} are calculated according to Liang et al. (2010).

In modeling the pollutant runoff process, a key issue is the determination of the function of the source term q_C, which describes how pollutants initially located on the ground surface are dissolved into the water column. When studying the dissolved pollutant transport on soil slopes, most researchers (Ahuja et al., 1981; Ahuja and Lehman, 1983; Gao et al., 2004, 2005; Walter et al., 2007; Yang et al., 2016) have suggested that a "thin layer" (mixing layer or exchange layer) near the soil surface controls the pollutant transfer between the soil ground and overland flow. In this study, we also adopt the concept of "exchange layer" and assume that the exchange layer controls the release process of dissolved pollutant into overland flow. According to previous studies (Sartor et al., 1974; Egodawatta et al., 2007, 2009; Xiao et al., 2017; Muthusamy et al., 2018), the amount of pollutant remaining on the surface should taper off during a rainfall event, indicating an exponential function. Therefore, we put forward the following expression for q_C:

$$q_C = \beta e^{-\alpha I t} \tag{5}$$

where α and β are the two empirical parameters; I is the rainfall intensity. According to the law of mass conservation, all the pollutant in a grid cell should be released into the water column given a sufficiently long time, regardless of rainfall intensity.

$$\int_0^\infty q_C dt = P_D \tag{6}$$

where P_D is the pollutant load density equal to the initial amount of pollutant per unit horizontal area. Substituting Eq. (5) into Eq. (6) and integrating Eq. (6), we obtain:

$$\frac{\beta}{\alpha I} = P_D \tag{7}$$

Combining Eqs. (5) and (7), we can obtain the final expression for q_C:

$$q_C = \alpha I P_D e^{-\alpha I t} \tag{8}$$

where α is the comprehensive coefficient with a unit of m^{-1}.

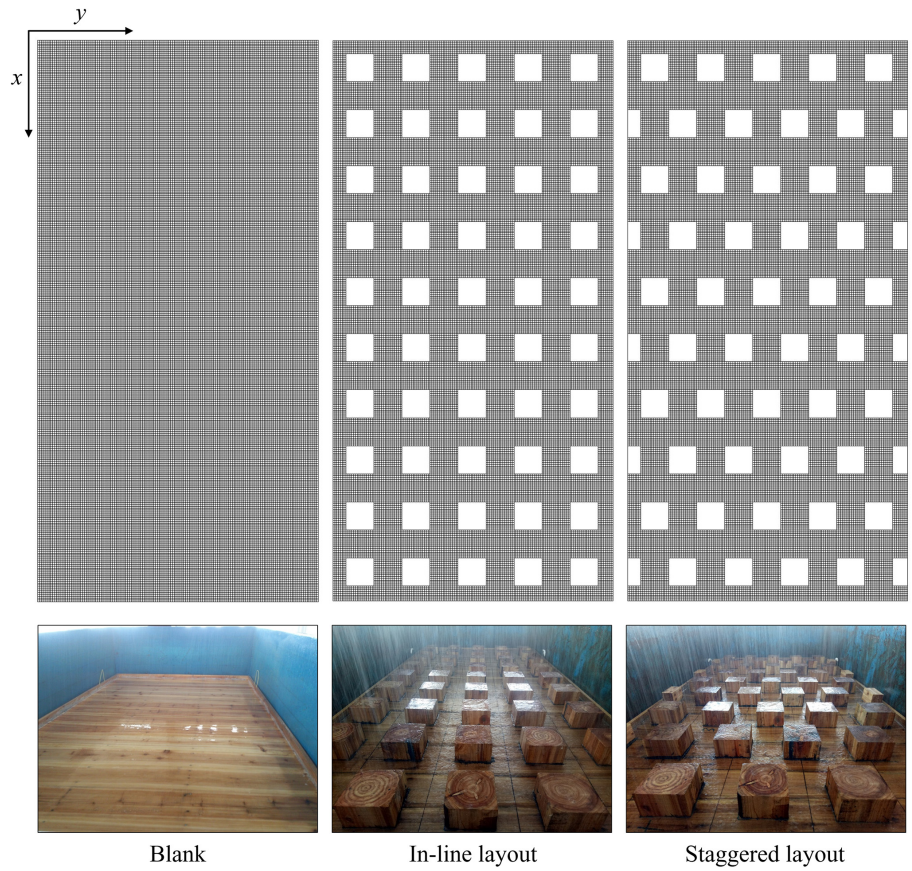

FIGURE 1 | Computational meshes and experimental setups.

EXPERIMENTAL SETUP

A series of laboratory experiments have been conducted in a rainfall-simulation hall to validate the presented model. Only constant rainfall events were considered in this research, with rainfall uniformity of over 90%. The rainfall uniformity is defined as the ratio of the minimum rainfall intensity to the maximum rainfall intensity over the whole catchment. Hence, a rainfall uniformity of 90% means that the minimum rainfall intensity measured at any point is 90% of the maximum rainfall intensity over the catchment. Water nozzles are located 17 m above the model catchment, so that raindrops can reach their final velocity like natural rainfall events. Wooden boards of 2.96 m in length, 1.48 m in width and 0.02 m in thickness are used to simulate the impervious catchments. Three short walls with the height of 4 cm are fixed on three sides of the catchment so that runoff water can only leave the catchment from the downstream outlet. In a real urban area, the configurations of buildings are very complex and vary from place to place. It is unrealistic to test all the configurations of the buildings in this paper, and the main aim of the laboratory experiments is to verify the mathematical model in this study. Hence, following to Liang et al. (2015), only two layouts of buildings (in-line arrangement and staggered arrangement) and one plain catchment without buildings (used as a reference) were constructed in this study, as shown in **Figure 1**. The buildings occupy 25 % of the catchment area, which is within the range of typical urban regions. To ensure the uniformity of the pollutant distribution in the experiments, each wooden board is divided into 50 (5 × 10) small squares and one building is fixed in each square with glue. In China's cities, cubical buildings are very common. Hence, cubical model buildings 0.148 m long, 0.148 m wide, and 0.10 m high are fabricated using the same wooden material. To ensure that the properties of the buildings and impervious catchments are the same, all the surfaces were treated in the same way. Similar to previous studies (Deng et al., 2005; Xiao et al., 2017; Zhang et al., 2018), table salt (NaCl) has been chosen as the dissolved pollutant tracer due to its wide availability and ease of use. In the BH method, buildings are excluded from the computational domain, whereas, the rainwater falling on top of the buildings is compensated by increasing the imposed rainfall intensity over the computational domain. Similarly, salt was spread uniformly on the catchments, except on the top of buildings. The total amount of salt apllied in each experiment is 125 g.

In this study, the catchment is considered to be of a uniform slope with an angle of 1° to the horizontal. For the convenience of collecting runoff samples, the catchment is placed in a steel flume (3 × 1.5 × 0.5 m). The slope of the flume

can be adjusted via a hydraulic system. Four constant rainfall intensities are tested in the experiment. The selection of the rainfall intensity is mainly based on the optimal operation range of the rainfall simulators, rather than the climate of a particular region. When scaling the experiment up, then the used rainfall intensities correspond to heavy downpours in tropic regions. Each rainfall event lasts for 1680 s. Runoff was collected at the downstream outlet of the catchment and monitored by continually measuring the water volumes at short intervals. Salt concentration was determined using a calibrated conductivity meter (Bante 950). The conductivity meter used had a built-in temperature compensation circuit so that all concentration values were referenced to a standard temperature. The detailed information about rainfall-simulation system, pollutant spreading, sample collection and data recording can be found in Xiao et al. (2017) and Zhang et al. (2018).

NUMERICAL MODELING

The Finite difference method (FDM) is applied to solve the set of equations given in section "Mathematical Model." Specifically, as mentioned before, the TVD MacCormack scheme is used to solve both the SWEs and the advection-diffusion equation. The full implementation details of the core numerical scheme can be found in Liang et al. (2006, 2007b), as well as the key numerical treatments regarding wetting/drying, adaptive time stepping, etc. In the actual calculations, the SWEs and the advection-diffusion equation are calculated separately. The SWEs are calculated first and then the computed results (i.e., the variation of H, U, and V with time at every grid point) are used as known data for solving the advection-diffusion equation. Identical numerical mesh is used in the SWEs and the advection-diffusion equation for the same catchment. To suit the rectangular shapes of model catchment and buildings, structured rectangular grid is used in this study. The grid sensitivity analysis is performed for staggered layout of buildings, because the flow pattern is more complex than in other layouts. Three types of mesh with different grid sizes are tested, which are referred to as GS1 (the grid size is 0.0098667 m), GS2 (the grid size is 0.0049333 m), and GS3 (the grid size is 0.0032889 m). Computed results indicate that mesh refinement produces no significant change in the results, while the computational cost increases significantly. Therefore, GS1 is chosen as the numerical mesh to use in the parametric studies. The same grid size is used in all catchments, as shown in **Figure 1**. Each catchment is discretized into 301 evenly distributed grid points in the x direction and 151 evenly distributed grid points in the y direction. The time step is restricted by the well-known Courant-Friedrich-Lewy condition. With a time step of 0.02 s, we estimate that the maximum Courant number $\sqrt{U^2+V^2}\Delta t \Big/ \Delta x$is around 0.5. At the outlet boundary, the flow undergoes a free fall after running out of the domain; at the other three boundaries, the solid wall condition is specified.

RESULTS

Water Runoff Process

A large quantity of experimental data can be obtained in a relatively short period of time with the use of the rainfall simulator over small idealized catchments, which are then used to

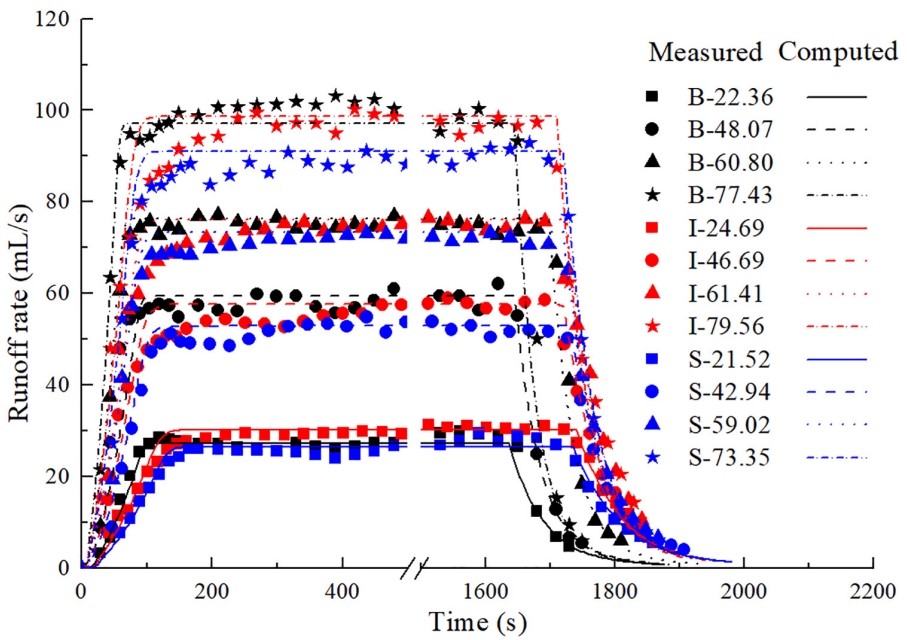

FIGURE 2 | Close-up of the measured and computed runoff rates. In the figure legend, B-22.36 refers to blank board (without building blocks) subject to 22.36 mm/h rainfall. Similar conventions are applicable to other notations, with letter "I" referring to the in-line layout and "S" referring to the staggered layout.

validate the computational model. The Nash-Sutcliffe efficiency (NSE) (Nash and Sutcliffe, 1970) has often been adopted to evaluate the model performance (Yang et al., 2016; Bonhomme and Petrucci, 2017). In this study, the estimation of Manning's parameter (n) is achieved by maximizing the Nash-Sutcliffe efficiency (NSE) of the prediction, with an adjustment interval of 0.005 s/m$^{1/3}$. **Figure 2** shows all the water runoff processes under various conditions, including both measured and computed results. The values of Manning roughness coefficient n has been determined to be 0.045 s/m$^{1/3}$ for the blank board and 0.050 s/m$^{1/3}$ for other two boards. The difference of n between different catchments may be related to the roughness height due to the existence of wooden blocks. In **Figure 2**, the runoff process between 500 s and 1500 s is omitted to improve the visualization of the rising and falling limbs of the curves. It shows that: (1) the SWEs are capable of predicting the rainfall runoff processes over catchments with and without buildings; (2) for each catchment, the runoff rate increases at first and then reaches equilibrium, which is equal to the rate of the rainfall input, followed by a sharp fall when the rainfall stops; (3) buildings can slow down the runoff concentration, and the staggered layout of buildings is more effective in increasing the time of concentration; (4) in the falling limb of the runoff process, buildings can delay the runoff decline and the staggered layout of buildings extends the time of decline more than the in-line layout. These observations can be attributed to: (a) buildings can frequently change the direction of the runoff flow and thus increase the length of the flow path, as shown in **Figure 3**, and (b) the presence of buildings increases the flow resistance. **Figure 4** presents the snapshots of the water depth and velocity distributions over the three considered catchments. At time t = 180 s, all the catchments have attained a steady state. It is evident that buildings in general can reduce the flow velocity and increase the water depth, especially on the upstream side of the buildings. Similar results were found in previous studies (Cea et al., 2010; Liang et al., 2015). The overland flow can only remain laminar in the early stage of the rainfall or when the runoff almost reduces to zero after the rainfall stops. Under the impact of raindrops and surface roughness, turbulence is triggered very quickly soon after the start of the rainfall.

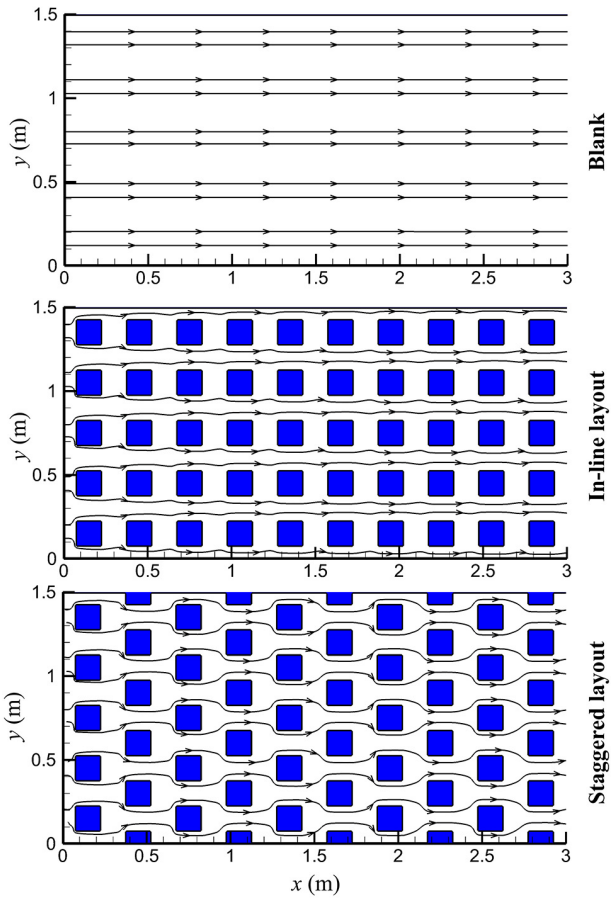

FIGURE 3 | Streamlines of the flow over different catchments.

Runoff of Uniformly-Distributed Pollutant

In the pollutant transport model presented in this study, only one parameter (α) needs to be determined according to the experimental data. As before, the value of α for each experiment is obtained by maximizing the Nash-Sutcliffe efficiency (NSE) of the prediction. The obtained values for different building layouts are listed in **Table 1**. The measured and predicted pollutant concentrations, under different conditions, are shown in **Figure 5**. The pollutant concentration decreases with time and finally approaches zero, which is satisfactorily predicted by the presented transport model. In addition, the pollutant concentration is affected by the rainfall intensity and the layout of buildings. The concentration increases as the rainfall intensity decreases.

Pollutant transport rate directly reflects the pollutant transport process. **Figure 5** shows the measured and predicted pollutant transport rates under different conditions. It is evident that the pollutant transport rate in all conditions show a similar single-peak variation, consisting of a rising limb at the beginning and a falling limb later on. In each case, the pollutant transport rate increases from zero to a maximum and then decreases to zero. The maximum pollutant transport rate in each condition is related to the rainfall intensity and the layout of buildings. The larger the maximum pollutant transport rate, the shorter the time required for the maximum transport rate to occur after the start of rainfall. **Figure 5** indicates that the present model over-predicts the pollutant transport rate, especially with regard to the maximum value. It is mainly because, (a) the release process of dissolved pollutant is described by an empirical relationship rather than by an accurate process-based equation; (b) a small fraction of pollutant on the surface cannot be collected in the experiment because of splashing, small leakage, etc; (c) the measured pollutant transport rate at any time is the average of the pollutant transport rate over the sampling interval of 10 s, which tends to underestimate the maximum value. Overall, the measured pollutant transport rates are in good agreement with those predicted by the presented numerical model.

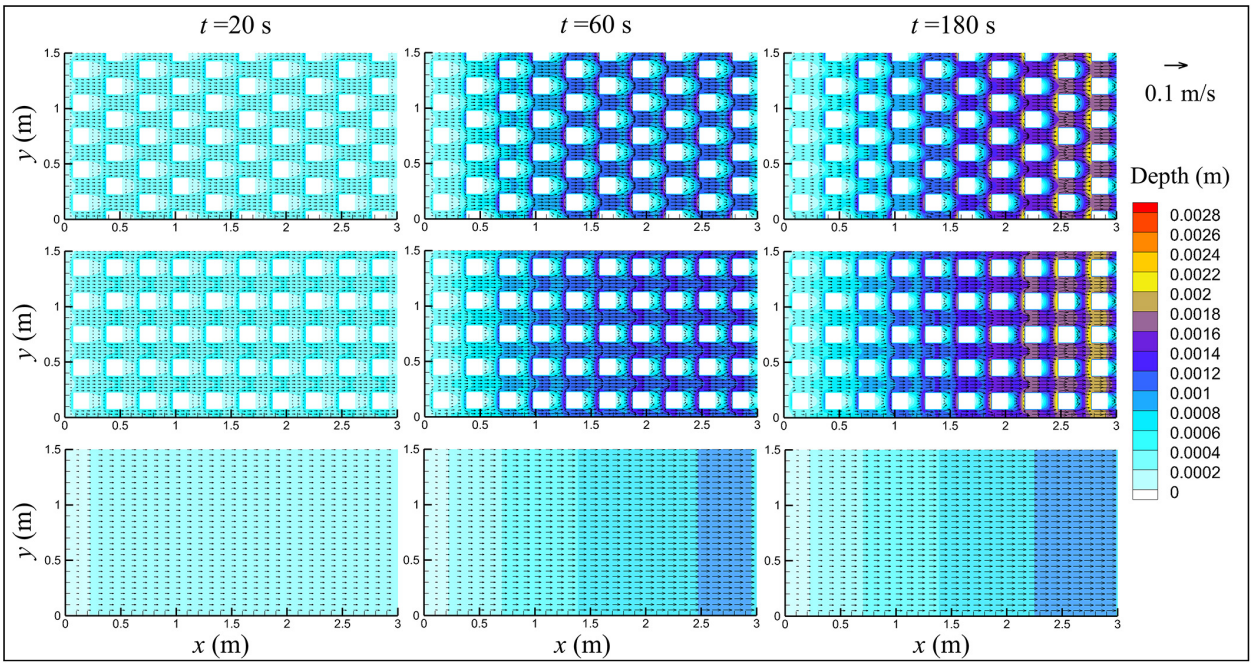

FIGURE 4 | Snapshots of the water depth and velocity distributions in three cases (B-48.07; I-46.69; S-42.94).

TABLE 1 | Estimated values for α and α *I*.

Building layout – rainfall intensity	α (m^{-1})	α*I* (s^{-1})	Building layout – rainfall intensity	α (m^{-1})	α*I* (s^{-1})	Building layout – rainfall intensity	α (m^{-1})	α*I* (s^{-1})
B-22.36	1610	0.010	I-24.69	1460	0.010	S-21.52	1420	0.085
B-48.07	1350	0.018	I-46.69	1310	0.017	S-42.94	1340	0.016
B-60.80	1240	0.021	I-61.41	1170	0.020	S-59.02	1160	0.019
B-77.43	1210	0.026	I-79.56	1040	0.023	S-73.35	1030	0.021

Figure 5 suggests that the differences in the concentration decay among the different building layouts are insignificant. This may be attributed to the small size of the experimental catchments. It is still can be seen that the existence of buildings slows down the pollutant transport rate, especially in the staggered layout case. This is because the buildings slow down the runoff process which drives the pollutant transport. The influence of buildings and their layout on the pollutant transport process can be generally quantified by the values of α and α*I*, as shown in **Table 1**. The value of α*I* is an indicator of the change in the pollutant release rate. The results show that for the same rain event the values of α and α*I* do not change significantly. This is mainly because the buildings do not play a significant role on the pollutant release from the impervious ground into runoff water. They only control the runoff process. **Figure 6** presents the snapshots of the pollutant concentration distributions in the three model catchments. It is evident that buildings do have a significant impact on the pollutant concentration upstream and downstream of buildings, especially in the initial runoff stage. For the same building layout, the value of α increases with the decreasing rainfall intensity, while the opposite is the case for α*I*. It implies that the rainfall intensity is an important factor that controls the pollutant transport process.

Runoff of Non-uniformly Distributed Pollutants

In this section, we mainly study the influence of pollutant distribution on pollutant transport process using the developed transport model. Previous researchers (Sartor et al., 1974; Kim et al., 2005; Egodawatta et al., 2007, 2009; Xiao et al., 2017; Muthusamy et al., 2018) have assumed that the pollutants were distributed uniformly over the catchment. In fact, uniform distribution is a very special case of linear distributions. Hence, we put forward some general linear distributions as sketched in **Figure 7** to study their influence on pollutant transport. In each distribution, the total amount of pollutant applied is 125 g. For convenience, the average amount of pollutant per unit area over the whole catchment is assumed to be 1 (i.e., L1.00). In **Figure 7**, L1.50 refers to the amount of pollutant per unit area at the catchment outlet as 1.50. As the initial pollutant distribution is linear L1.50 leads to the amount of pollutant per unit area of

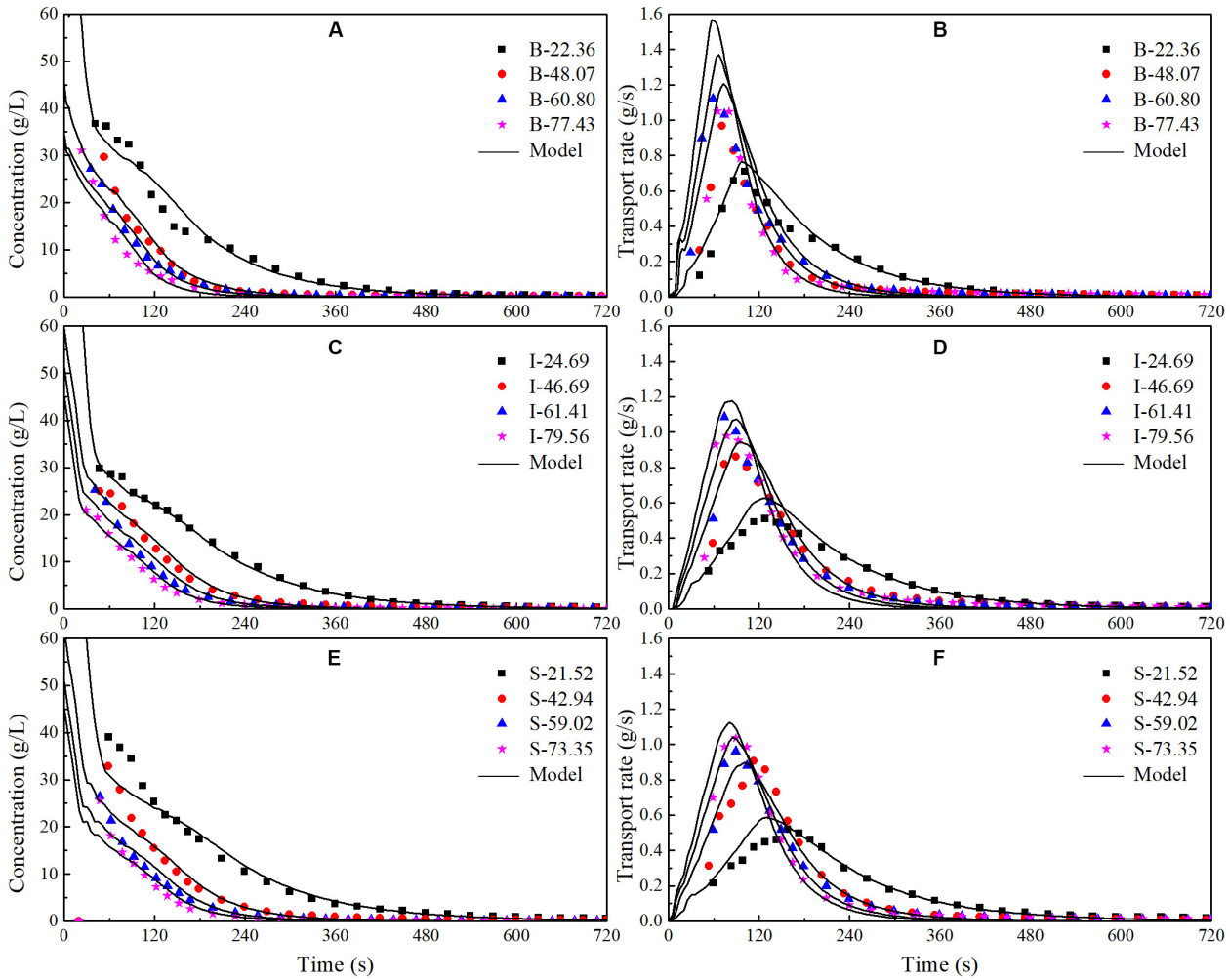

FIGURE 5 | Measured and computed pollutant concentrations and transport rates. **(A)** Concentrations on blank board. **(B)** Transport rates on blank board. **(C)** Concentrations with in-line layout. **(D)** Transport rates with in-line layout. **(E)** Concentrations with staggered layout. **(F)** Transport rates with staggered layout.

0.5 at the upstream end of the catchment. Similar notations apply to other cases. The rainfall intensity, slope, layout of buildings and calibration parameters remain the same for all pollutant distributions. According to the numerical model established in this study, the amount of pollutants has no impacts on the values of parameters (n and α).

Figure 8 presents the computed variations of the pollutant concentration and pollutant transport rate at outlet in different conditions. It shows that, (a) the pollutant distribution has a major impact on the variation of the pollutant concentration at the catchment outlet, especially during the initial runoff process; (b) the amount of pollutants per unit area at outlet directly influences the initial pollutant transport; (c) the pollutant concentration at outlet can increase with time under some initial pollutant distributions; (d) all these concentration variation curves approximately cross at the same point, approximately at the time of concentration. It may be because the waterdrops moves from the farthest point to the catchment outlet at the time of concentration, and thereafter the whole catchment contributes to the pollutant discharge at the outlet. Prior to this instant, the larger amount of pollutants per unit area at outlet leads to a greater concentration at the outlet. After this instant, the opposite trend is observed. As for the pollutant transport rates in different conditions, they all show similar single-peak shapes, although there are differences in the maximum transport rate and the time when it occurs. It should be noted that the maximum transport rates in different conditions are about the same. Similar to the concentration curves, all these transport rate curves cross at the same point, approximately at the time of concentration. At this instant, both the concentration and the runoff rate are the same for the same catchment, regardless of the initial pollutant distribution.

To provide a better understanding of the influence of the initial pollutant distribution on pollutant transport process, the evolutions of the average concentrations at different sections are presented in **Figure 9**. It is evident that different initial distributions give different concentration profiles. The initial concentration distribution shows resemblance to the subsequent

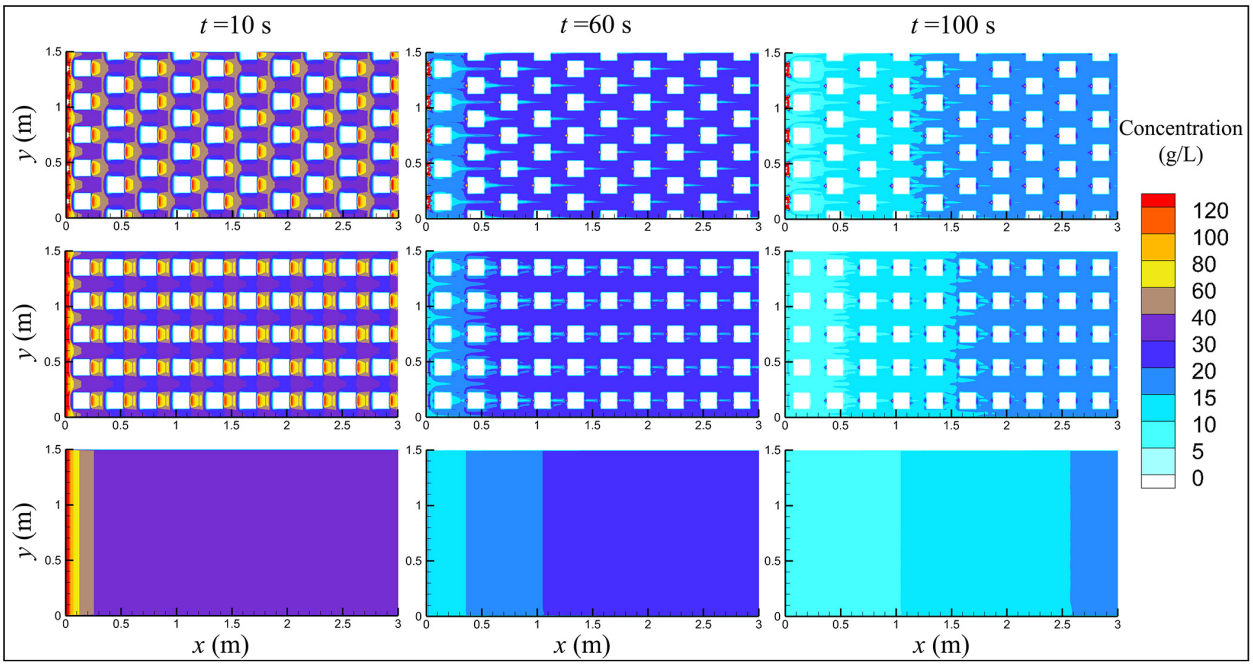

FIGURE 6 | Snapshots of the pollutant concentration distributions in three cases (B-48.07; I-46.69; S-42.94).

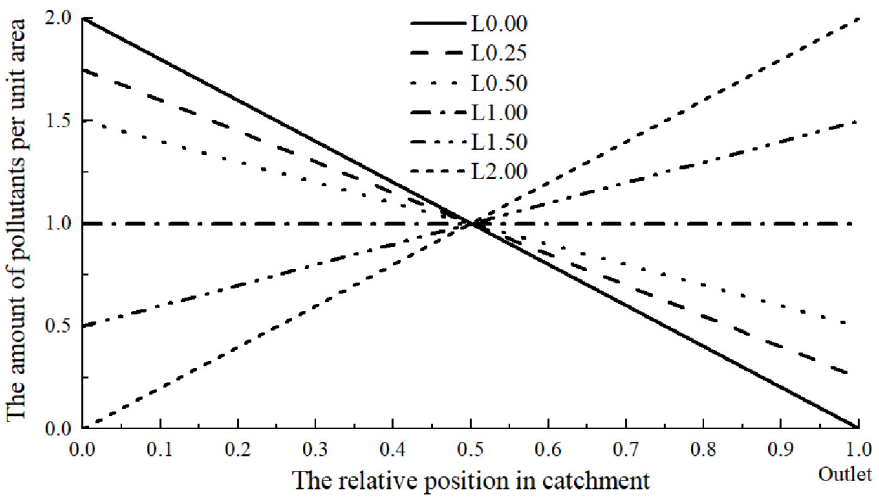

FIGURE 7 | Initial pollutant distributions.

pollutant distribution. When the amount of pollutants per unit area at outlet is lower than the catchment-averaged value (such as L0.00 and L0.50), the downstream concentration may increase at first due to the contribution of pollutant from the upstream area. Later on, the concentrations decrease with time. For other cases, the concentration over the whole catchment decreases simultaneously throughout the rainfall event. In general, as time goes on, the concentration non-uniformity over the catchment becomes smaller and smaller, and the pollutant concentration tends to linearly increase in the direction of the flow.

DISCUSSION

As in previous studies (Deng et al., 2005; Xiao et al., 2017; Zhang et al., 2018), sodium chloride (table salt) has been chosen as the dissolved pollutant tracer in this study. Therefore, in this study, we assume that the table salt dissolves over a short period of time T_r. Taking B-48.07 as an example, **Figure 10** shows the comparisons of the computed results with different values of T_r and the resulted predicted by the present model described in section "Mathematical Model" (labeled as the exponential function in **Figure 10**). **Figure 10** suggests that the vast majority

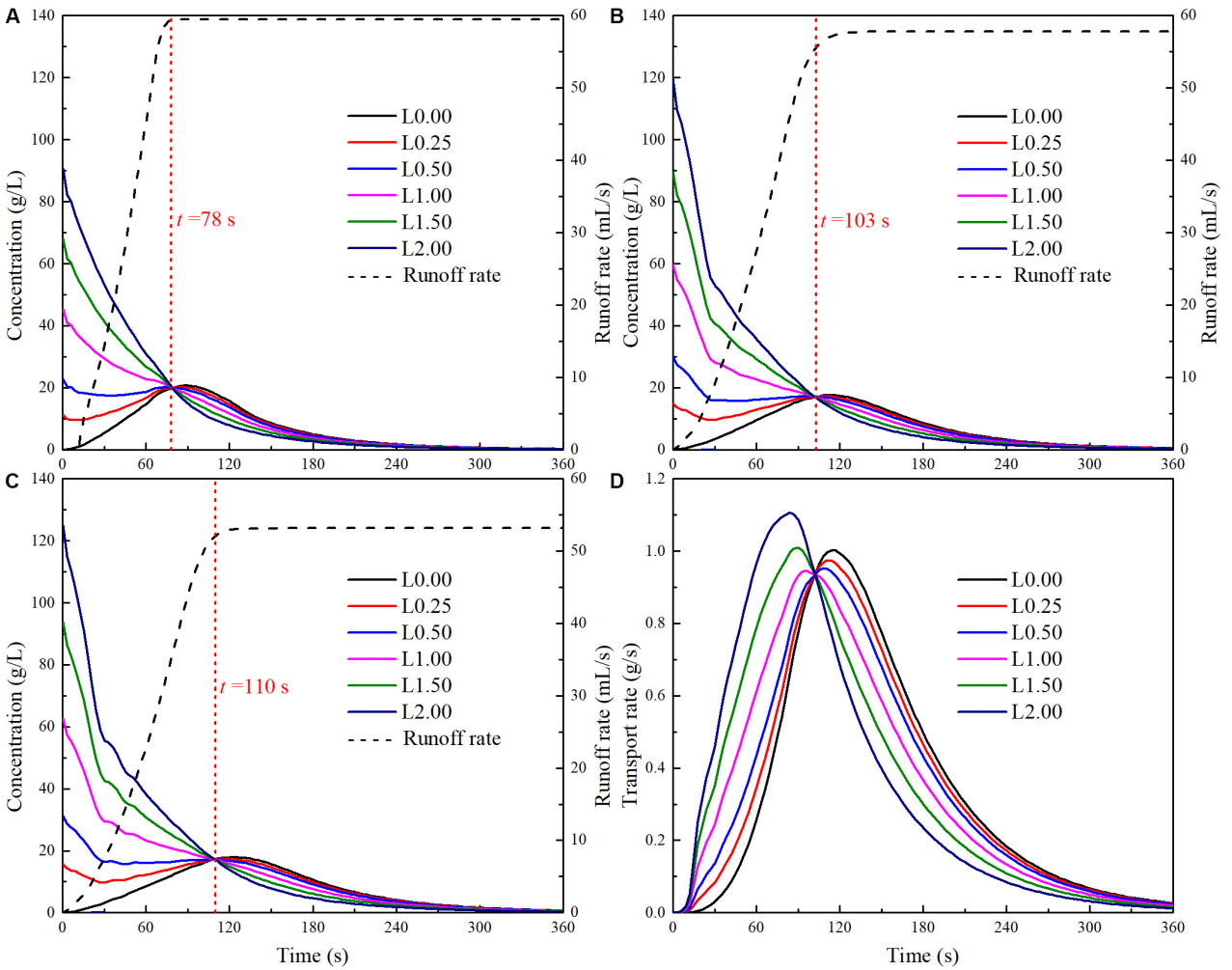

FIGURE 8 | Pollutant concentrations and transport rates corresponding to different initial pollutant distributions. **(A)** Concentration in case B-48.07. **(B)** Concentration in case I-46.69. **(C)** Concentration in case S-42.94. **(D)** Transport rate in case I-46.69.

of table salt can be transported out of the catchment very quickly if the assumption that table salt gets dissolved instantly into water is valid. However, this assumption lead to large disagreement with the experimental results. In contrast, the present model, which assumes that the dissolved pollutant releases gradually into the runoff water, obtains a satisfactory prediction of the pollutant transport process. A question arises as to what controls the dissolved pollutant release from the impervious surface into runoff water.

Deng et al. (2005) have suggested the existence of an active surface layer at the soil surface that controls the pollutant transfer from soil water to runoff water. Coincidentally, Gao et al. (2004, 2005) and Walter et al. (2007) have proposed the idea of "exchange layer" near the soil surface, assuming that chemicals in the soil slowly diffuse into the exchange layer. Similar to the previous studies (Gao et al., 2004, 2005; Deng et al., 2005; Walter et al., 2007), we adopt the concept of the "exchange layer" and assume that a thin water layer exists on the impervious surface and controls the pollutant transfer between the thin water layer immediately above the catchment surface and overland flow. The thin water layer can form before the overland flow occurs. In practice, the surface runoff will not occur as the first drop of rain falls on the catchment. The movement of the small amount of water at the beginning of the rainfall is heavily influenced by the surface tension and the vertical boundary-layer structure of the flow, which are not fully accounted for in the present depth-averaged numerical model. It can be found from the experimental results in **Figure 2** that a short period of time is needed before the overland flow occurs. Even after the overland flow occurs, due to the rough bed surface and viscosity of water, a thin viscous water layer with a low velocity will be formed underneath the overland flow, as shown in **Figure 11B**. In studying the movement of suspended sediments in a turbulent boundary layer, Chang et al. (2015) suggested that sediment particles are released from the viscous sublayer, which is 0.00095 m thick. In the SWEs, the viscous sublayer is neglected. Only the depth-averaged velocity is used in the calculations, which corresponds to uniform transport of pollutant

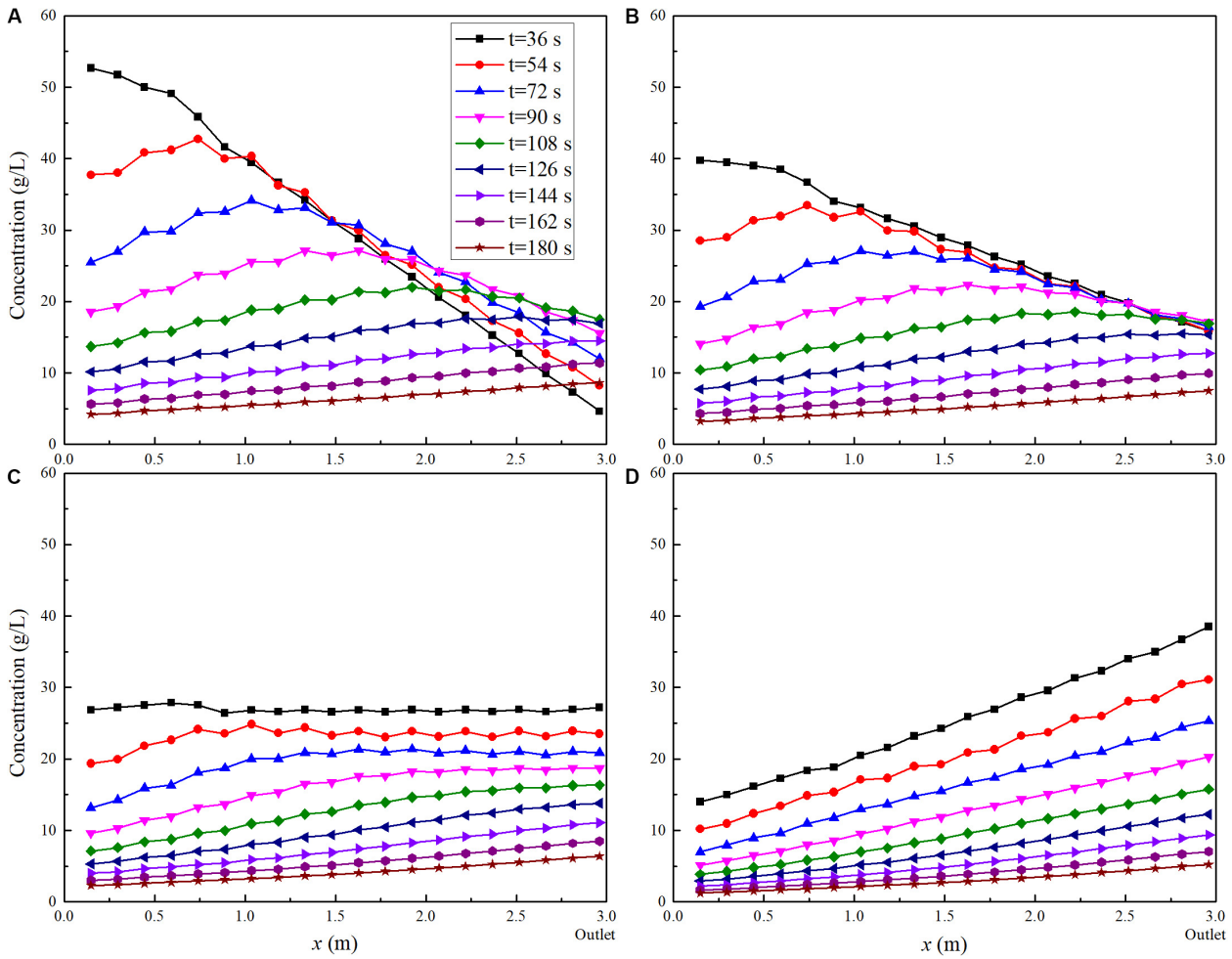

FIGURE 9 | Computed pollutant concentration along the catchment with different initial pollutant distributions (I-46.69). **(A)** L0.00. **(B)** L0.50. **(C)** L1.00. **(D)** L1.50.

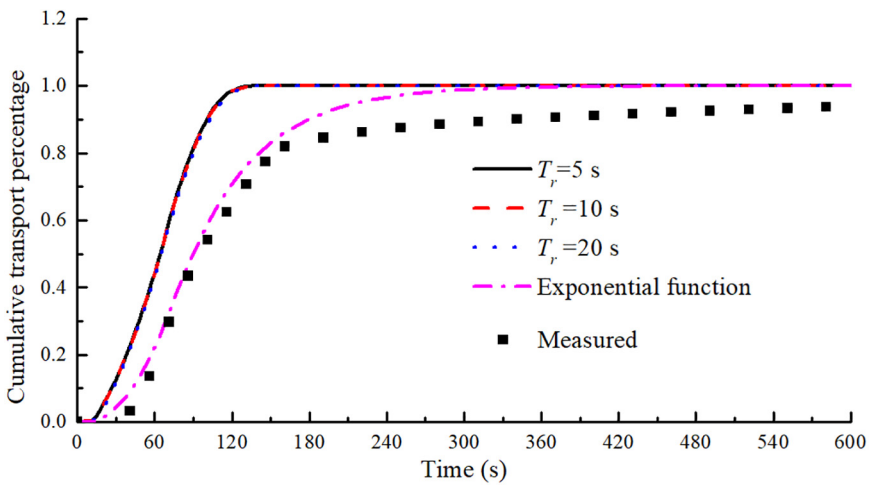

FIGURE 10 | Computed results of different model setups.

over the depth as shown in **Figure 11A**. Once the pollutant enters the runoff water, it is transported out of the catchment quickly. Hence, as shown in **Figure 10**, large amounts of the dissolved pollutant can be transported out of the catchment at the time of concentration. This is based on the assumption that the pollutant can be dissolved instantly into water and the rainwater falling on the most-upstream part of the catchment arrives at the catchment outlet at the time of concentration. Normally, the table salt saturation concentration is about 360 g/L at 20 degrees Celsius. The total amount of table salt used in this study for each rainfall event is 125 g. It only needs 347.2 mL of water to dissolve all these table salts. This volume of water corresponds to a water depth of 0.000079 m, assuming that water evenly spreads over the catchment. This tiny water depth is generally smaller than the thickness of viscous sublayer. Therefore, the amount of rainwater in the thin viscous sublayer is sufficient to dissolve all the pollutants in the catchment. In the viscous sublayer, the flow is much slower than that in the upper runoff flow. Therefore, more time will be needed to transport the dissolved pollutant contained restricted in the viscous sublayer out of the catchment, as shown in **Figure 11B**. In other words, there is a thin water layer with lower velocities, underlying the runoff flow, that control the dissolved pollutant transfer between catchment ground and upper runoff flow. The concept of the "exchange layer" is our assumption for the convenience of modeling the complicated dissolution process and the three-dimensional turbulent mixing phenomenon by a simplified and efficient method. However, our study shows that such simplified approaches are able to obtain a general agreement between modeling and measurements. Hence, we claim that our approaches are satisfactory, at least in the context of engineering applications.

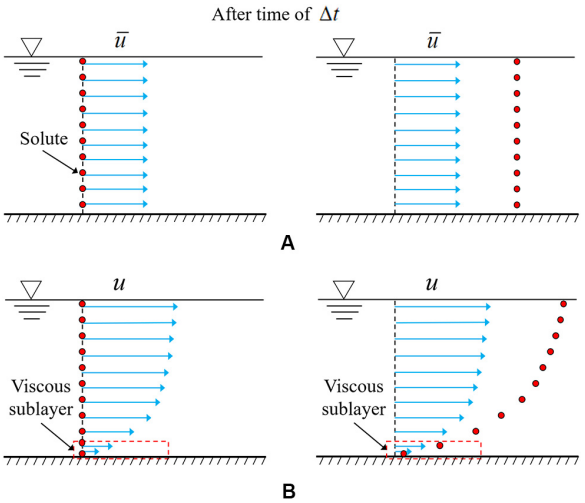

FIGURE 11 | Schematic diagram showing dissolved pollutant transport. **(A)** Ignoring velocity non-uniformity over depth. **(B)** With actual velocity distribution.

As mentioned before, the pollutant distribution has a significantly impact on the pollutant discharge at the outlet, especially at the initial runoff stage. Xiao et al. (2017) noted that the initial transport process is crucial for dissolved pollutants as a significant proportion of them are transported during the initial stage. The initial part of the runoff water is associated with the first flush, which involves disproportionately high concentration of pollutants during the initial runoff hydrograph and can causes rapid degradation of water quality. Therefore, many efficient stormwater treatment measures mainly target the initial runoff water. Zhang et al. (2010) suggested that the initial rooftop runoff and the initial road runoff should be collected and treated separately before being discharged to the environment or being utilized. **Figure 12** illustrates the cumulative pollutant transported over a blank board corresponding to different initial pollutant distributions. It shows that the initial pollutant distribution can significantly influence the cumulative pollutant transport process. For instance, around 50.90% of the total

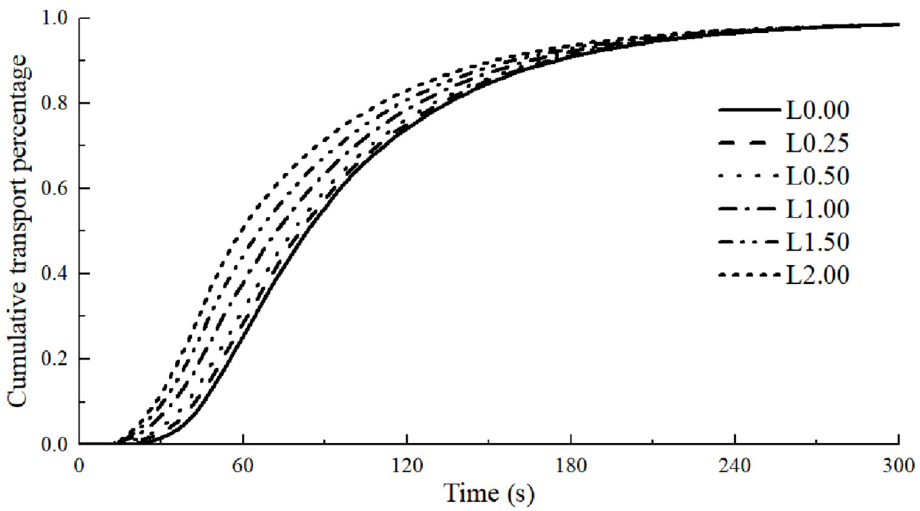

FIGURE 12 | Cumulative transport percentage for different initial pollutant distributions (B-48.07).

pollutants is transported out of the catchment within 60 s with the pollutant distribution of L2.00. However, only half of that is transported with the pollutant distribution of L0.00. Therefore, pollutant distribution should be considered when designing stormwater pollution mitigation strategies.

In this study, sodium chloride (table salt) is chosen as a dissolved pollutant tracer, which is an easily soluble material. In practice, different chemicals may have different physical and chemical properties. Some chemicals may not dissolve quickly in water and thus the dissolved and particulate forms will coexist. This phenomenon has not been considered in this study, but a fraction coefficient may be introduced, according to which the dissolved and particulate materials can be studied separately. In practical applications, catchments involve complex terrains, infiltration and non-uniform rainfalls. To accurately reproduce the behavior of real catchments, distributed hydrological and environmental models should be established, which divide the whole catchments into small areas of uniform properties. Our findings in this paper are based on experiments and analyses with regard to simple idealized urban catchments. However, our results can be used to refine the fundamental assumptions concerning the hydrological and environmental response of each small area. Future research needs to be carried out to take into account the stormwater networks, the distribution of surface imperviousness and rainfall uncertainty. Continued research in this area can help improve the design of urban stormwater management and pollution mitigation strategies.

CONCLUSION

In this study, the dissolved pollutant transport process over idealized urban catchments has been investigated. A two-dimensional transport model has been developed based on the shallow water equations and the depth-averaged advection-diffusion equation, with an assumption of "exchange layer" that controls the pollutant release from the ground surface to runoff water. A series of laboratory experiments have been conducted to validate the presented model, which includes two building layouts. The effects of buildings and initial pollutant distribution are particularly investigated. The following can be concluded:

(1) The existence of buildings slows down the pollutant transport process, especially when the buildings are staggered. Such an effect is consistent with the findings related to the overflow processes.
(2) Overall, the water and dissolved pollutant runoff phenomena can be correctly predicted by the numerical model proposed in this study.
(3) The initial pollutant distribution has a significant influence on the concentration and the pollutant transport rate, especially at the initial runoff stage. The pollutant concentration at the outlet can either increase or decrease with time, depending on the initial distribution.
(4) For a constant rainfall event over the same catchment, the pollutant concentration and transport rate at the time of concentration appear to be insensitive to the initial pollutant distribution.

A real urban area is more complicated, with sewage networks, spatially and temporally varying ground features and rainfall intensity. We will carry out further experiments and computations with variable rainfall intensities.

DATA AVAILABILITY STATEMENT

All datasets generated for this study are included in the article/supplementary material.

AUTHOR CONTRIBUTIONS

TZ, YX, DL, and HT contributed to the conception and design of the study. TZ wrote the first draft of the manuscript and led the data analysis and interpreted the results with YX and SY. TZ and BL designed and conducted the experiments. All authors contributed to manuscript revision, read and approved it for publication.

FUNDING

This work was financially supported by the National Key Research and Development Program of China (Grant No. 2016YFC0402605), the Fundamental Research Funds for the Central Universities (Grant No. 2018B42714), the 111 Project (Grant No. B17015) and the Royal Academy of Engineering UK-China Urban Flooding Research Impact Program (Grant No. UUFRIP\ 100051).

ACKNOWLEDGMENTS

We wish to thank the Prof. Bidya Sagar Pani (Indian Institute of Technology) for providing valuable suggestions and language help.

REFERENCES

Ahuja, L. R., and Lehman, O. R. (1983). The extent and nature of rainfall-soil interaction in the release of soluble chemicals to runoff. *J. Environ. Qual.* 12, 34–40. doi: 10.2134/jeq1983.00472425001200010005x

Ahuja, L. R., Sharpley, A. N., Yamamoto, M., and Menzel, R. G. (1981). The depth of rainfall-runoff-soil interaction as determined by 32P. *Water Re. Res.* 17, 969–974. doi: 10.1029/WR017i004p00969

Bonhomme, C., and Petrucci, G. (2017). Should we trust build-up/wash-off water quality models at the scale of urban catchments? *Water Res.* 108, 422–431. doi: 10.1016/j.watres.2016.11.027

Brett, D., and Gavin, B. (2010). Comparison of heavy metal loads in stormwater runoff from major and minor urban roads using pollutant yield rating curves. *Environ. Pollut.* 158, 2541–2545. doi: 10.1016/j.envpol.2010.05.021

Brezonik, P. L., and Stadelmann, T. H. (2002). Analysis and predictive models of stormwater runoff volumes, loads, and pollutant concentrations from

watersheds in the Twin Cities metropolitan area. Minnesota, USA. *Water Res.* 36, 1743–1757. doi: 10.1016/s0043-1354(01)00375-x

Cea, L., Garrido, M., and Puertas, J. (2010). Experimental validation of two-dimensional depth-averaged models for forecasting rainfall–runoff from precipitation data in urban areas. *J. Hydrol.* 382, 88–102. doi: 10.1016/j.jhydrol.2009.12.020

Chang, Y. S., Hwang, J. H., and Park, Y. G. (2015). Numerical simulation of sediment particles released at the edge of the viscous sublayer in steady and oscillating turbulent boundary layers. *J. Hydro Environ. Res.* 9, 36–48. doi: 10.1016/j.jher.2013.07.002

Deng, Z., de Lima, J. L. M. P., and Singh, V. P. (2005). Transport rate-based model for overland flow and solute transport: parameter estimation and process simulation. *J. Hydrol.* 315, 220–235. doi: 10.1016/j.jhydrol.2005.03.042

Egodawatta, P., Thomas, E., and Goonetilleke, A. (2007). Mathematical interpretation of pollutant wash-off from urban road surfaces using simulated rainfall. *Water Res.* 41, 3025–3031. doi: 10.1016/j.watres.2007.03.037

Egodawatta, P., Thomas, E., and Goonetilleke, A. (2009). Understanding the physical processes of pollutant build-up and wash-off on roof surfaces. *Sci. Total Environ.* 407, 1834–1841. doi: 10.1016/j.scitotenv.2008.12.027

Gao, B., Walter, M. T., Steenhuis, T. S., Hogarth, W. L., and Parlange, J. Y. (2004). Rainfall induced chemical transport from soil to runoff: theory and experiments. *J. Hydrol.* 295, 291–304. doi: 10.1016/j.jhydrol.2004.03.026

Gao, B., Walter, M. T., Steenhuis, T. S., Parlangea, J. Y., Richardsa, B. K., Hogarthb, W. L., et al. (2005). Investigating raindrop effects on transport of sediment and non-sorbed chemicals from soil to surface runoff. *J. Hydrol.* 308, 313–320. doi: 10.1016/j.jhydrol.2004.11.007

Goonetilleke, A., Thomas, E., Ginn, S., and Gilbert, D. (2005). Understanding the role of land use in urban stormwater quality management. *J. Environ. Manag.* 74, 31–42. doi: 10.1016/j.jenvman.2004.08.006

Herngren, L., Goonetilleke, A., and Ayoko, G. A. (2005). Understanding heavy metal and suspended solids relationships in urban stormwater using simulated rainfall. *J. Environ. Manag.* 76, 149–158. doi: 10.1016/j.jenvman.2005.01.013

Hong, N., Zhu, P., and Liu, A. (2017). Modelling heavy metals build-up on urban road surfaces for effective stormwater reuse strategy implementation. *Environ. Pollut.* 231, 821–828. doi: 10.1016/j.envpol.2017.08.056

Hong, Y., Bonhomme, C., Van den Bout, B., Jetten, V., and Chebbo, G. (2017). Integrating atmospheric deposition, soil erosion and sewer transport models to assess the transfer of traffic-related pollutants in urban areas. *Environ. Model. Softw.* 96, 158–171. doi: 10.1016/j.envsoft.2017.06.047

Hong, Y., Bonhomme, C., Le, M. H., and Chebbo, G. (2016). A new approach of monitoring and physically-based modelling to investigate urban wash-off process on a road catchment near Paris. *Water Res.* 102, 96–108. doi: 10.1016/j.watres.2016.06.027

Kim, L.-H., Kayhanian, M., Zoh, K.-D., and Stenstrom, M. K. (2005). Modeling of highway stormwater runoff. *Sci. Total Environ.* 348, 1–18. doi: 10.1016/j.scitotenv.2004.12.063

Liang, D., Falconer, R. A., and Lin, B. (2006). Comparison between TVD-MacCormack and ADI-type solvers of the shallow water equations. *Adva. Water Resour.* 29, 1833–1845. doi: 10.1016/j.advwatres.2006.01.005

Liang, D., Falconer, R. A., and Lin, B. (2007a). Coupling surface and subsurface flows in a depth averaged flood wave model. *J. Hydrol.* 337, 147–158. doi: 10.1016/j.jhydrol.2007.01.045

Liang, D., Lin, B., and Falconer, R. A. (2007b). Simulation of rapidly varying flow using an efficient TVD–MacCormack scheme. *Int. J. Numer. Methods Fluids* 53, 811–826. doi: 10.1002/fld.1305

Liang, D., Özgen, I., Hinkelmann, R., Xiao, Y., and Chen, J. M. (2015). Shallow water simulation of overland flows in idealised catchments. *Environ. Earth Sci.* 74, 7307–7318. doi: 10.1007/s12665-015-4744-5

Liang, D., Wang, X., Falconer, R. A., and Bockelmann-Evans, B. N. (2010). Solving the depth-integrated solute transport equation with a TVD-MacCormack scheme. *Environ. Model. Softw.* 25, 1619–1629. doi: 10.1016/j.envsoft.2010.06.008

Liu, A., Egodawatta, P., Gua, Y., and Goonetilleke, A. (2013). Influence of rainfall and catchment characteristics on urban stormwater quality. *Sci. Total Environ.* 444, 255–262. doi: 10.1016/j.scitotenv.2012.11.053

Massoudieh, A., Abrishamchi, A., and Kayhanian, M. (2008). Mathematical modeling of first flush in highway storm runoff using genetic algorithm. *Sci. Total Environ.* 398, 107–121. doi: 10.1016/j.scitotenv.2008.02.050

Metcalf and Eddy Inc (1971). *Storm Water Management Model, Final Report*, Vol. 1. Washington, D.C: Environmental Protection Agency.

Miguntanna, N. P., Liu, A., Egodawatta, P., and Goonetilleke, A. (2013). Characterising nutrients wash-off for effective urban stormwater treatment design. *J. Environ. Manag.* 120, 61–67. doi: 10.1016/j.jenvman.2013.02.027

Muthusamy, M., Tait, S., Schellart, A., Beg, M. N. A., Carvalho, R. F., and de Lima, J. L. M. P. (2018). Improving understanding of the underlying physical process of sediment wash-off from urban road surfaces. *J. Hydrol.* 557, 426–433. doi: 10.1016/j.jhydrol.2017.11.047

Nash, J. E., and Sutcliffe, J. V. (1970). River flow forecasting through conceptual models part I — A discussion of principles. *J. Hydrol.* 10, 282–290. doi: 10.1016/0022-1694(70)90255-6

Naves, J., Jikia, Z., Anta, J., Puertas, J., Suárez, J., and Regueiro-Picallo, M. (2017). Experimental study of pollutant washoff on a full-scale street section physical model. *Water Sci. Technol.* 45, 2821–2829. doi: 10.2166/wst.2017.345

Pan, H., Lu, X., and Lei, K. (2017). A comprehensive analysis of heavy metals in urban road dust of Xi'an, China: contamination, source apportionment and spatial distribution. *Sci. Total Environ.* 609, 1361–1369. doi: 10.1016/j.scitotenv.2017.08.004

Revitt, D. M., Lian, L., Coulon, F., and Fairley, M. (2014). The sources, impact and management of car park runoff pollution: a review. *J. Environ. Manag.* 146, 552–567. doi: 10.1016/j.jenvman.2014.05.041

Sartor, J. D., Boyd, G. B., and Agardy, F. J. (1974). Water pollution aspects of street surface contaminants. *J Water Pollut. Control Federat.* 46, 458–467. doi: 10.1002/etc.3089

Schubert, J. E., and Sanders, B. F. (2012). Building treatments for urban flood inundation models and implications for predictive skill and modeling efficiency. *Adv. Water Resour.* 41, 49–64. doi: 10.1016/j.advwatres.2012.02.012

Shaw, S. B., Walter, M. T., and Steenhuis, T. S. (2006). A physical model of particulate wash-off from rough impervious surfaces. *J. Hydrol.* 327, 618–626. doi: 10.1016/j.jhydrol.2006.01.024

Sheng, Y., Ying, G., and Sansalone, J. (2008). Differentiation of transport for particulate and dissolved water chemistry load indices in rainfall–runoff from urban source area watersheds. *J. Hydrol.* 361, 144–158. doi: 10.1016/j.jhydrol.2008.07.039

Walter, M. T., Gao, B., and Parlange, J. Y. (2007). Modeling soil solute release into runoff with infiltration. *J. Hydrol.* 347, 430–437. doi: 10.1016/j.jhydrol.2007.09.033

Wang, S. M., He, Q., Ai, H. N., Wang, Z. T., and Zhang, Q. Q. (2013). Pollutant concentrations and pollution loads in stormwater runoff from different land uses in Chongqing. *J. Environ. Sci.* 25, 502–510. doi: 10.1016/S1001-0742(11)61032-2

Xiao, Y., Zhang, T., Liang, D., and Chen, J. M. (2016). Experimental study of water and dissolved pollutant runoffs on impervious surfaces. *J. Hydrodyn.* 28, 162–165. doi: 10.1016/S1001-6058(16)60617-0

Xiao, Y., Zhang, T., Wang, L., Liang, D., and Xu, X. (2017). Analytical and experimental study on dissolved pollutant wash-off over impervious surfaces. *Hydrol. Process.* 31, 4520–4529. doi: 10.1002/hyp.11372

Yang, T., Wang, Q., Wu, L., Zhang, P., Zhao, G., and Liu, Y. (2016). A mathematical model for the transfer of soil solutes to runoff under water scouring. *Sci. Total Environ.* 56, 332–341. doi: 10.1016/j.scitotenv.2016.06.094

Zhang, M., Chen, H., Wang, J., and Pan, G. (2010). Rainwater utilization and storm pollution control based on urban runoff characterization. *J. Environ. Sci.* 22, 40–46. doi: 10.1016/S1001-0742(09)60072-3

Zhang, T., Xiao, Y., Liang, D., and Wang, L. (2018). Experimental and analytical studies of solute transport during runoff over vegetated surfaces. *Hydrol. Process.* 32, 2335–2345. doi: 10.1002/hyp.13132

Conflict of Interest: The authors declare that the research was conducted in the absence of any commercial or financial relationships that could be construed as a potential conflict of interest.

frontiers in Earth Science

ORIGINAL RESEARCH
published: 21 July 2020
doi: 10.3389/feart.2020.00304

Community Mapping Supports Comprehensive Urban Flood Modeling for Flood Risk Management in a Data-Scarce Environment

Louise Petersson[1], Marie-Claire ten Veldhuis[1], Govert Verhoeven[2], Zoran Kapelan[1], Innocent Maholi[3] and Hessel C. Winsemius[1,2]*

[1] Department of Water Management, Delft University of Technology, Delft, Netherlands, [2] Inland Water Systems Unit, Deltares Research Institute, Delft, Netherlands, [3] Humanitarian OpenStreetMap Team, Dar es Salaam, Tanzania

In this paper we demonstrate a framework for urban flood modeling with community mapped data, particularly suited for flood risk management in data-scarce environments. The framework comprises three principal stages: data acquisition with survey design and quality assurance, model development and model implementation for flood prediction. We demonstrate that data acquisition based on community mapping can be affordable, comprehensible, quality assured and open source, making it applicable in resource-strained contexts. The framework was demonstrated and validated on a case study in Dar es Salaam, Tanzania. The results obtained show that the community mapped data supports flood modeling on a level of detail that is currently inaccessible in many data-scarce environments. The results obtained also show that the community mapping approach is appropriate for datasets that do not require extensive training, such as flood extent surveys where it is possible to cross-validate the quality of reports given a suitable number and density of data points. More technically advanced features such as dimensions of urban drainage system elements still require trained mappers to create data of sufficient quality. This type of mapping can, however, now be performed in new contexts thanks to the development of smartphones. Future research is suggested to explore how community mapping can become an institutionalized practice to fill in important gaps in data-scarce environments.

Keywords: community mapping, volunteered geographic information, flood resilience, citizen observations, urban flood risk, drain blockage, asset management

OPEN ACCESS

Edited by:
Jingming Hou,
Xi'an University of Technology, China

Reviewed by:
Guy Jean-Pierre Schumann,
University of Bristol, United Kingdom
Tim van Emmerik,
Wageningen University and Research, Netherlands

****Correspondence:***
Louise Petersson
louise.petersson90@gmail.com

Specialty section:
This article was submitted to Hydrosphere, a section of the journal Frontiers in Earth Science

Received: *06 March 2020*
Accepted: *29 June 2020*
Published: *21 July 2020*

Citation:
Petersson L, ten Veldhuis M-C, Verhoeven G, Kapelan Z, Maholi I and Winsemius HC (2020) Community Mapping Supports Comprehensive Urban Flood Modeling for Flood Risk Management in a Data-Scarce Environment. Front. Earth Sci. 8:304. doi: 10.3389/feart.2020.00304

INTRODUCTION

The global trend of expanding settlements in flood prone areas exposes an increasing share of the world's population to floods (United Nations, 2018; Winsemius et al., 2018). Many regions are, however, still lacking the data needed for flood disaster preparedness, response, and governance (Paul et al., 2018). This paper aims to investigate to what extent data collected through

community mapping contributes to improved assessments of urban flood risks in resource-strained environments, by filling essential data gaps on drainage networks and urban topography using a community mapping approach.

The conventional approach to urban flood modeling strongly relies on availability of detailed geometric data on drainage elements, such as pipe diameters, manhole connections, channel cross-sections and weir levels (Butler et al., 2018) and terrain data (Schumann and Bates, 2018; Winsemius et al., 2019). State-of-the-art urban flood models combine detailed geometric data on sewer pipes and drainage channels with digital terrain data to model flood events, combining both overland flow and channel flow through channels and pipes (Bach et al., 2014). These models simulate the impact of storm events in urban environments, which allow for flood risk assessments at a high level of detail. The density and complexity of urban drainage networks makes urban flood modeling a highly data-intensive endeavor.

In resource-strained environments, where detailed drainage data tend not to be readily available, data acquisition is a critical challenge that inhibits the development of detailed flood risk assessments (Deletic et al., 2012). Furthermore, validation data to evaluate the performance of flood models is often missing. Previous research suggests that citizen observations offers an alternative data source in data-scarce environments to estimate water levels for model calibration (Etter et al., 2019; Strobl et al., 2019). Hence, we propose a framework for acquisition of drainage data and water levels required for flood model development and validation through community mapping. The approach proposed here is based on proactive engagement of the local community that is trained to collect high quantities of flood-related data which allows for extensive flood model development and validation in an affordable way.

The framework has been applied, validated, and demonstrated on a case study in Dar es Salaam, Tanzania. Our hypothesis is that community mapped drainage data can improve urban flood model performance and hence allow for detailed flood risk assessments in contexts where drainage data is normally not available. Specifically, we stipulate that the simulated flood depth in a model that couples community mapped drainage data with digital terrain data (coupled 1D–2D model) corresponds better with citizen's reports on flood depth for a certain storm event, than the simulated flood depth in a model built with terrain data only without community mapped drainage data (2D model). The hypothesis was tested by developing a hydrodynamic model including detailed schematization of a community mapped drainage network and comparing the simulated flood depth with citizen's reports on flood depth for models run with and without the community mapped drainage network.

If the hypothesis is confirmed, the proposed framework opens the way for implementation of citizen observations to support flood modeling on neighborhood scale, a level of detail that has not been possible previously in many regions due to lack of data on drainage system characteristics. Furthermore, it will show that community mapping can be beneficial to fill data gaps for flood resilience in these contexts. The usefulness of a model built this way was demonstrated by using the model to investigate the impact of drains blocked by solid waste on flooding.

The remainder of the paper is organized as follows. We first identify the need for our method and gaps in research in a literature review. Then, we present our methodology, including the components of the framework, presentation of the case study, data acquisition, model development and model implementation. Subsequently, we present the results of data quality analysis, model development and the model implementation. We finally discuss limitations of our proposed method, relating to technical and sustainability issues.

BACKGROUND

Community mapping is the action of producing a map of a certain location together with or by the residents, often featuring local knowledge and resources (Parker, 2006). It can be considered as a form of *Volunteered Geographic Information* (VGI) which arose in the early 2000's through platforms such as OpenStreetMap (OSM),[1] an online world map which can be edited by anyone (Goodchild, 2007; Zook et al., 2010; Ramm et al., 2011). The internet has allowed for open source platforms where geographical information can be produced and stored, which has remarkably lowered the costs to collect the data needed to build urban resilience. This has accommodated the rise of community mapping projects to collect geographical data for pre-disaster, in-disaster, and post-disaster management (Paul et al., 2018).

The earliest examples of large-scale, digital VGI projects, dating around 2010, made use of stand-alone GPS devices and home computers (Zook et al., 2010; Soden and Palen, 2014). Only ten years later, smartphones are now equipped with sensors like GPS receivers, making them suitable for scientific data collection (Haklay, 2013). VGI combined with smartphones has put mapping, a task that for centuries has been reserved for official agencies, in the hands of anyone who wants to contribute to online maps (Flanagin and Metzger, 2008). Davids et al. (2018) suggest that smartphone-based data collection activities should be a part of science and engineering curricula, aiming for standardized data collection methods and open access.

Research shows that the incentive to participate in VGI projects depends on the volunteers' knowledge and interest in the topic being mapped and their available time and resources (Brady et al., 1995; Coleman et al., 2009). A literature review on motivation to participate in VGI projects is presented by Fritz et al. (2017). VGI is produced by heterogeneous contributors with different levels of detail and precision, which introduces errors and variable quality of VGI data sets (Senaratne et al., 2017). Goodchild and Li (2012) note that VGI data quality can be assured through cross-validation, where the contribution of an individual must be controlled by at least one other user before submission. Quality assurance can also be obtained through "gatekeepers," individuals promoted with special privileges to edit content based on their previous contributions, or data mining such as outlier detection and cluster analysis (Flanagin and Metzger, 2008; Senaratne et al., 2017).

[1] www.openstreetmap.org

Many researchers have analyzed the quality of OSM data by comparing it with spatial data from national mapping agencies (Girres and Touya, 2010; Haklay, 2010; Neis et al., 2011; Antoniou and Skopeliti, 2015). Very few studies on OSM data quality have been conducted in Africa. One of few examples is Iliffe (2017) that analyzed the OSM road data in Tandale ward in Dar es Salaam, Tanzania, in terms of positional accuracy and completeness. The results obtained showed that all roads in the OSM dataset lied within a 10 m buffer of the road data provided by the Dar es Salaam City Council (DCC). Furthermore, the OSM data held a much more extensive road network than the DCC dataset. Iliffe (2017) notes that this results from the fact that the official map held by the ward officer was outdated and did not contain all roads present in Tandale ward.

The data abundant World Wide Web seems to add different assets in different contexts, depending on the available geographic information in these contexts. The added value of VGI in planned, mapped, and industrially advanced areas lies in endemic knowledge about the physical environment, and current information about local conditions (Buytaert et al., 2014). But in contexts where authoritative data sets are incomplete or absent, VGI has the potential to, additionally, fill data gaps needed for governance. This makes Iliffe (2017) draw the conclusion that a different framework must be applied for community mapping in industrially developing countries, which emphasizes the elements of open source data and comprehensible data collection methods.

Iliffe developed his framework by studying *Ramani Tandale*, a community mapping project carried out in 2011 in Tandale ward in Dar es Salaam. The project started with a community forum that identified what the community thought should be put on the map; roads, pharmacies, schools, drainage, and features relating to water access, sanitation, and flood impact. The mapping was carried out during 4 weeks in August 2011, resulting in a detailed map of Tandale that later assisted local authorities during a cholera outbreak (Iliffe, 2017). The positive outcome of *Ramani Tandale* made the World Bank in Tanzania upscale the project and put all flood prone wards in Dar es Salaam on the map through the large-scale community mapping project *Ramani Huria*. The flood model developed in this paper utilizes drainage data that was recorded by *Ramani Huria* (see section "Case Study").

To the best of the authors' knowledge, a flood model built with community mapped drainage data has not been developed and examined previously, and previous research has mainly focused on the quality and accuracy of VGI in data abundant contexts. The increasing flood risks caused by expanding settlements in flood prone areas call for flood disaster preparedness and response, but the necessary data to build flood resilience is missing in many resource-strained environments (Paul et al., 2018). Now that data for flood resilience has been collected with a community mapping approach by *Ramani Huria*, it is of interest to investigate if this data can improve flood models on a neighborhood scale. It is also of interest to examine if models built with community mapped drainage data can be used to understand the causes of flooding.

METHODOLOGY

The methodology of this study consists of a framework for flood modeling with community mapped data (section "Framework") that is applied on a case study, the *Ramani Huria* community mapping project in Dar es Salaam. The case study is presented in section "Case Study" and the framework analysis, following the three principal stages of the framework, is presented in section "Data Acquisition–Model Implementation."

Framework

The proposed framework shown in **Figure 1** combines the learnings from the principles of community mapping proposed by Iliffe (2017) for data acquisition with the conventional approach to urban flood modeling that relies on the availability of detailed geometric drainage data (Butler et al., 2018).

Flood model development with community mapped data follows a similar approach compared to traditional model building, i.e., (1) data acquisition, followed by (2) model development and validation, and ending with (3) model implementation. However, the manner through which data is acquired is different from a data abundant context. The framework relies on four conditions. Firstly, the data survey should be *affordable* in the mapping context, using simple and easily accessible local devices and tools for the ones collecting the data. The benefits of VGI and ICT could be utilized by engaging volunteers and students equipped with smartphones and free smartphone applications. Secondly, the campaign should be *comprehensible* for the mapping community but at the same time allow for accurate records to be obtained with relatively little training. Features must be clearly defined and not accidentally overseen. Thirdly, the survey must be *quality assured* for completeness of attributes and topological connectivity. Finally, datasets must be *made available freely and openly* so that other surveyors or users can benefit from the data (Iliffe, 2017).

In the *data acquisition* phase, a comprehensible survey is designed to prepare detailed collection of data required to develop a model. This data may include data on drainage elements, their geographical attributes, as well as system states that may cause flooding such as maintenance states and clogging (ten Veldhuis et al., 2011). After the mapping campaign, a *quality assurance* protocol is applied to ensure that the collected data is of sufficient quality. If errors are encountered, the data must be recorded again or the survey design may be modified, forming an iterative relationship with the previous step of the process. The quality assurance is followed by the *model development* phase during which the acquired data is used to build and calibrate a flood model using suitable hydrodynamic modeling software. The final phase involves *model implementation* to e.g., investigate the causes of flooding, use for operational applications, develop early warning systems, or support long-term decision making and risk assessments.

Case Study

The data applied in this study is collected by *Ramani Huria* ("Open Map" in Swahili), a community mapping project initiated by the World Bank in 2017. It aims to collect the data needed

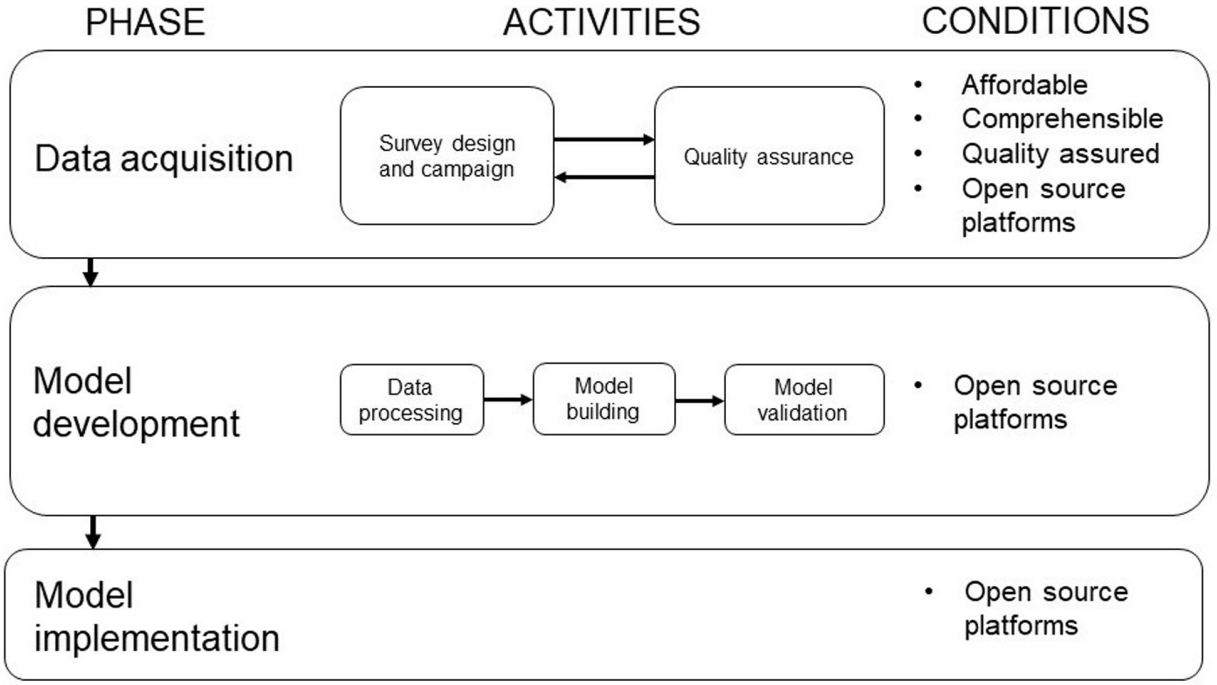

FIGURE 1 | A framework for flood modeling with community mapped data.

to understand flood risk and build flood resilience in Dar es Salaam using a community mapping approach. Humanitarian OpenStreetmap Team (HOT), a non-governmental organization founded in the aftermath of the Haiti earthquake in 2010 (Bilham, 2010; Soden and Palen, 2014) is contracted to organize and supervise the mapping. The largest river flowing through Dar es Salaam is the Msimbazi river, of which both the Msimbazi as well as smaller tributaries and streams are known to cause flash floods. The rapid population growth rate leaves the city highly unplanned and the city center is characterized by a remarkably high building density on lands susceptible to flood risks, mainly in the Msimbazi river basin (UN-HABITAT, 2010).

Ramani Huria upscaled earlier mapping initiatives carried out at smaller and less detailed scale to cover 44 wards in Dar es Salaam between 2017 and 2019. *Ramani Huria*'s approach is to train university students and community members to create maps using open source applications. The training has mainly been conducted in the *Ramani Huria* "summer schools," where university students in urban planning and geomatics participate in a 2-month internship that is part of their program curriculum. The students are divided into specialized teams, focusing on drainage mapping, data processing in GIS, digitizing aerial imagery and community outreach and are awarded with small stipends to cover travel costs, internet bundles and lunches. Collected data sets include, but are not limited to, buildings, roads, sanitary facilities, waste disposals, urban drainage, and soil types. A strong focus has been on accurately mapping small scale drainage channels with locally available tools and open source applications, making this a suitable community mapping project for testing the hypothesis that community mapped drainage data can improve the performance of flood models.

To this end, we focus on a subset of drainage data from *Ramani Huria*, collected for five sub-wards of Kijitonyama ward in Dar es Salaam, covering approximately 2.3 km^2 (see **Figure 2**). The drainage data is freely available.[2] Being located on a hill upstream of main water courses, Kijitonyama is mainly exposed to pluvial flooding. This type of flooding is caused by rainfall that exceeds the conveyance capacity of the drainage system and is therefore independent of overflowing water bodies (Butler et al., 2018), which is desirable to isolate the added value of *Ramani Huria*'s highly localized drainage data on flood predictions. The majority of the drainage network in Kijitonyama consists of open drains that are connected through short culverts.

Data Acquisition

The acquisition of drainage data for developing the flood model followed three stages: survey design, mapping campaign and quality assurance. These stages are further explained below. Subsequently, the acquisition of validation data and solid waste blockages for the model implementation are outlined.

Survey Design for Drainage Data

The drainage data acquisition process started with the design of a survey to collect drainage data using a community mapping approach. This involved identifying which data to be collected,

[2]https://geonode.resilienceacademy.ac.tz/layers/geonode_data:geonode:dar_es_salaam_drain_segments, accessed May 14, 2020.

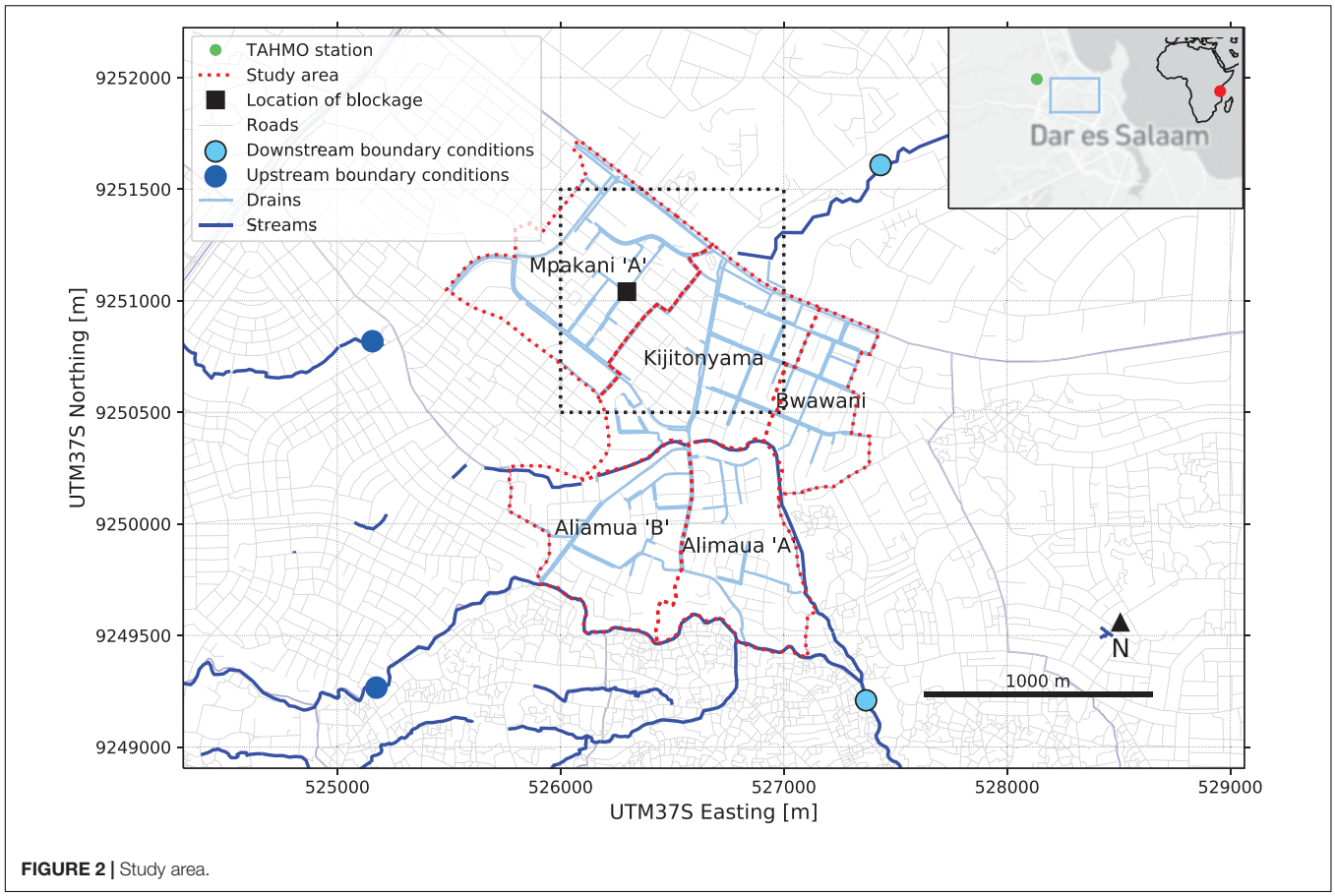

FIGURE 2 | Study area.

how this should be done, but also identifying the affordable tools and open source platforms that could be used in the process.

A summary of schematization data collected, i.e., drainage elements and attributes identified and collected during the mapping process, is provided in **Table 1**. Defining the possible conditional attributes in the survey required several iterations in the field to find the predominant set of possible drainage elements and their characteristics, including dimensions. The drainage elements are divided into four classes: culverts, ditches, drains and decommissioned drains, which in turn can be open or closed and have different cross sections. Decommissioned drains are poorly maintained, e.g., full of vegetation, building materials or other blockages and have no attributes recorded. *Elevation* of the segments was measured to calculate the vertical position of bed levels in relation to a digital terrain model, as altitude cannot be recorded by smartphones with sufficient accuracy.

The Open Data Kit Collect Android application (ODK) was used for data collection, a free survey application for smartphones that can add geopoints and geotraces to each data entry, making it suitable for the record of drainage segments. OpenStreetMap was used as a platform to store data, making it openly and freely available.

Mapping Campaign for Drainage Data

To make the mapping comprehensive and complete, a special drainage data collection team was formed by students that was instructed how to measure the different attributes and in what order to observe the drainage channel so that no drains would be overseen. The overall survey was designed in a way that enabled individual surveys, when combined, to lead to a topologically correct and connected drainage dataset and a complete set of attributes by following a well-defined conditional data model, shared for upscaling elsewhere online.[3]

The team started by identifying the most downstream point of an area, where the drainage system reached a water body, recorded that geopoint and labeled it as *outflow* in the ODK application. If the most downstream segment stopped without reaching a water body, it was labeled as *end*. Then, the team mapped the drainage system starting from the most downstream point and walked upstream. The "geotrace" function of ODK makes it possible to track the reach of a drainage segment by walking along the drain while recording the walked path by using the GPS sensor in the smartphone. This method is well suited for open channel networks, which was observed to be the dominant drain type in Dar es Salaam. Any diverging drains were then mapped consecutively, and the most upstream points of the drainage network were labeled as *begin*. Using labeling of geopoints this way made it possible during quality assurance to distinguish if a drain flows into a next drain or

[3]https://wiki.openstreetmap.org/wiki/Dar_es_Salaam/Ramani_Huria#Drainage, accessed 23 January 2020.

TABLE 1 | Collected drainage data.

Type	Cross section	Attributes				
		Dimensions			Material	Elevation
Culvert	Round	Diameter			Concrete, steel, plastic, sand or other material with free text entry	Vertical distance between the drain bottom and the nearest road, measured at the upstream end of each segment. Used to derive bed level altitude from terrain model.
	Rectangular	Width	Depth			
Ditch	Rectangular	Width	Depth			
Drain (open or closed)	Trapezoidal	Top width	Bottom width	Depth		
	Rectangular	Width	Depth			
	Elliptical	Top width	Depth			
Decommissioned	No attributes recorded					

whether a connection is truly missing, which is not an exception in Dar es Salaam. As local devices, cross sections of drainage segments were measured with locally made measuring sticks and tape rulers and the dimension values and material attributes were recorded in the ODK. The mapping process is illustrated in **Figure 3**.

Data Quality Assurance of Drainage Data

The next step was to undertake data cleaning and quality assurance of the collected drainage data. Within *Ramani Huria*, a team of data cleaners was appointed to quality check the results before uploading the data to OSM. This involved aligning inaccurate geotraces with drainage segments seen on satellite and drone imagery in GIS, checking the completeness and validity of the attributes and checking the topology and connectivity of the network. Automated quality checks were used for both attributes and topology. Codes for quality assurance are openly shared.[4] If errors or missing elements were encountered, the mapping team was instructed to record these again in the field. The data cleaning was taking place typically at the end of each field campaign day.

Remaining quality issues were identified by the authors during the model development phase, despite the data cleaning efforts of *Ramani Huria*. Positional errors were found through visual inspection, and when building the flood model, as positional errors caused a disconnected network in the model and hence introduced simulation errors. Data set completeness was studied with filters in the attribute tables in QGIS. The result of this analysis is presented in section "Drainage Data Quality and Completeness" and proposed solutions to overcome these remaining quality issues are addressed in the discussion section.

Validation Data Collection

The data acquisition further included collection of flood depth validation data, to be compared with simulated flood depth from the flood model. Community observations of flood depth in the study area were recorded in a "flood extent survey" by members of the drainage mapping team a few hours after a heavy rainfall event. Rainfall data from this rain event was used in the model simulation, and the maximum simulated flood depth was compared with community observations, see section "Model Implementation." The respondents were asked to provide information about the depth of water on the street outside of their house the same morning and referred this information relative to a person's height. Water depths were recorded as geopoints in ODK and lumped into 3 classes, as summarized in **Table 2**.

It was considered to be most valid to categorize the responses into a few, wide validation classes because of the likely uncertainty of the community-based flood depth estimates.

FIGURE 3 | Ramani Huria drainage mappers, recording drainage features with a wooden ruler and smartphone. Written informed consent was obtained from the participants for the publication of any potentially identifiable images or data included in this article. Photo Chris Morgan/World Bank.

[4]https://github.com/openearth/hydro-osm

TABLE 2 | Water depth classes used in the model validation.

Reported depth	Water depth in cm
Only puddles and finger depth	0–5
Ankle depth	5–20
Mid-shin and knee depth	>20

Previous research has demonstrated the value of using discrete water level classes in community observations rather than continuous scales in e.g., centimeters (Seibert et al., 2019). It should be noted that the thresholds of the flood depth classes are based on assumptions, and no research to date has investigated appropriate numeric ranges of this reference system. Nevertheless, the classes give an indication of the flood depth at each observation point. In total, 44 observations were collected this way and used for validation of the models used in the model implementation phase, see section "Model Development."

Community Survey of Blockages in Urban Drains

When performing the flood extent survey described above, the mappers were also asked to record blocked drainage segments by recording a geopoint in ODK at the location of each blockage they found along their way. Apart from the position data, the blockage records included extent (50, 75 or 100% blocked) and type of blockage (e.g., solid waste, vegetation, building materials). This information was used to identify an appropriate location to investigate the impact of blocked drainage on urban flooding in the model implementation phase, see section "Model Implementation."

Model Development

This stage of the framework developed the flood model using the SOBEK[5] modeling suite, version 2.16. SOBEK is a modeling suite designed for modeling and analysis of water flows and processes in a wide range of water systems. It computes discharge, velocity, and water level in each computational node for each time step by solving the Saint-Venant equations, stating the conservation of mass and momentum in space and time.

SOBEK allows for 1D–2D modeling, in which a 1D and 2D flood model are coupled to exchange their computed water flows (Butler et al., 2018). A 1D model simulates the storage and conveyance through water networks like channels and drainage systems by introducing the parameters of the network in the model, whereas the 2D model only simulates runoff flows according to overland flow paths generated by topography from a 2D Digital Terrain Model (DTM). A combined 1D–2D model is an effective approach to capture both processes of drainage flow and surface runoff, as the interaction between these processes is simulated (Bach et al., 2014).

Rainfall data for the flood model was measured by Trans African Hydrometeorological Observatory[6] (TAHMO) with 5 minutes temporal resolution at the Ardhi University weather station located about 2 km from the case study ward (see **Figure 2**). The simulation was run with a storm event that occurred in the early morning of 3 March 2019. This event was selected as it was preceded by five dry weeks, which was concluded by studying TAHMO rainfall time series. The dry spell indicated that the drainage system was dry without standing water levels at the beginning of the storm event, which was confirmed during fieldwork around 12 h before the event. The rainfall started at 00:10 in the morning, had two peaks at 01:00 and 06:00 and ended around 09:00. The peak intensity was 114 mm/h and the total rainfall amounted to 150 mm for the whole event, which was expected to cause pluvial flooding in Kijitonyama ward.

First, a 2D model was developed of Kijitonyama ward based on an existing 5×5 m^2 DTM that is freely available.[7] The Manning friction coefficient of the DTM was set to 0.2 s/m$^{1/3}$ and was assumed to be uniform for all grid cells, in the absence of differentiated land use data that could inform spatially distributed surface roughness values. This value was selected as it represents built-up land, which was assessed to be the most common land use type in the study area (Chow et al., 1988). Ozdemir et al. (2013) shows that 2D roughness values in urban flood modeling generally have limited effect on maximum water levels and depths but tend to have larger influence on flow velocities, which was not simulated in this study. Hence, it is expected that the assumption did not decrease validity of the simulated water depths, see results in section "Model Results Without and With Community Mapped Data."

Infiltration was assumed to be negligible as the rainfall intensity was much higher than expected infiltration rates in urban environments (Butler et al., 2018). Relevant inflow and outflow conditions at the boundaries of the ward were included in the model as boundary conditions, i.e., inflowing river discharges upstream and representative water levels of downstream outflow locations. The discharge was measured by TAHMO at 5 min resolution at the southern upstream boundary condition in **Figure 2**, a flow station at the Ubungo bridge located approximately 1 km upstream of the boundary of the study area. The discharge at the northern upstream boundary condition was estimated by the authors around noon 2 March 2019, before the modeled event using a float and stopwatch and multiplying the surface water velocity with the estimated cross section area of the water course (Davids et al., 2018). The estimated discharge was assigned as the initial value of the flow at the northern upstream boundary condition, and then the discharge data from the Ubungo flow station was re-scaled to this initial value. The gap between the northern water course and the drainage system in **Figure 2** appears as the natural stream flows into a part of the drainage system that is outside of the model domain.

A second model was created by extending the 2D overland flow model to a coupled 1D–2D model by incorporating the *Ramani Huria* drainage network data. As 2D boundary conditions, the same setup was used as for the first model, and for the 1D model the simulation was started without any initial water level in the drainage segments, as had been observed during

[5]https://www.deltares.nl/en/software/sobek/

[6]https://tahmo.org/

[7]https://geonode.resilienceacademy.ac.tz/layers/geonode:cowi_dar_/metadata_detail

fieldwork. The 1D model roughness coefficients were assigned from literature based on the drainage segment materials recorded by *Ramani Huria* (see **Table 3**). The sensitivity of the model to 1D roughness values was investigated by first running a simulation where all drains were assumed to be of "normal concrete" as shown in **Table 3**, and subsequently assigning 1D roughness values to the segments according to their reported material (results not shown). The maximum water depth for the two schematizations was studied in 44 observation points inserted at the same coordinates as the geopoints that were recorded in the flood extent survey, which revealed that the maximum water depth difference was less than 0.5 cm in all observation points when implementing distributed 1D roughness values. This aligns with the findings of Ozdemir et al. (2013) that surface roughness mainly influences water velocities and not water depths.

Drainage bed levels were derived from the DTM by subtracting the vertical distance between the bottom of the drain segment and the nearest road (*elevation*, see **Table 1**). The simulation was run with the same storm event, 2D roughness and infiltration capacity as the 2D model, making the community mapped drainage data the only difference between the two schematizations. Hence, differences in modeled output between the 2D and coupled 1D–2D model could be fully attributed to the additional drainage data, that was included in the form of one-dimensional drainage channels added to the 2D-model, see results section "Model Results Without and With Community Mapped Data."

Model performance of the schematizations was validated by inserting 44 observation points in the model at the same coordinates as the geopoints that were recorded in the flood extent survey. Then, the maximum computed water level in each observation point was exported from SOBEK and compared against the community mapped flood observations collected by the drainage mappers a few hours after the storm event. In this way, it was observed if the maximum simulated water depths of the storm event fell below, within or above the reported flood depth classes at 44 locations, see results in section "Model Results Without and With Community Mapped Data."

TABLE 3 | Assigned manning roughness coefficients to drainage segments in the 1D–2D model.

Reported material	Assigned manning friction value [$s/m^{1/3}$]	Number of segments
Normal concrete, in good repair	0.02	430 (77.4%)
Rough concrete, with noticeable holes or cracks	0.025	79 (14%)
Very rough concrete, with loose material, broken areas and/or large cracks	0.03	19 (3%)
Rock	0.04	38 (0.5%)
Decommissioned (see section "Data Acquisition")	0.1	4 (0.7%)
Sand	0.02	23 (4%)
Corrugated steel	0.02	1 (0.2%)
Plastic (assuming it is PVC)	0.01	1 (0.2%)

Values as suggested by Chow et al. (1988) based on drainage material recorded by Ramani Huria drainage mappers.

Model Implementation

After validation, the coupled 1D–2D model was further applied to investigate the impact of solid waste accumulations in the drainage system, to exemplify how the model can be used to simulate network configuration changes and maintenance-states. This was simulated by removing an open drain segment from the 1D model schematization, see location in **Figure 2**. This simulated a similar effect as a fully blocked drain segment, as the whole cross section and conveyance capacity disappears if a drain is fully blocked. The interruption of the drainage channel will result in rising water levels upstream of the blockage and will eventually cause the water to overflow the drainage channel onto the street, where it will generate additional street flooding. From there, the water will flow further downstream based on the 2D topography and possibly flow back into the open drainage network further downstream. A drain location was selected in the Mpakani "A" sub-ward, as this location was reported to be sensitive to blockage during the solid waste blockage survey. Besides, this drain showed considerable drainage flow based on the 1D–2D simulation results, and results from the flood extent survey showed flooding upstream of this drain. Therefore, it was of interest to analyze the potential blocking effect of this drain. The model results were compared to the 1D–2D model without blockage to investigate how the water levels in the drainage system and the flood extent near the reported solid waste blockage were affected.

RESULTS

In this section we first analyze the data quality and completeness of the community mapped drainage data (section "Drainage Data Quality and Completeness"). Then, we compare the results of the flood model without any drainage considered (i.e., 2D-model) against the model with local drainage data obtained via community mapping (i.e., 1D–2D model, section "Model Results Without and With Community Mapped Data"). This is done by validating both models against the surveyed flood levels. Finally, we describe the results of a model run with assumed drain blocked by solid waste (section "Impact of Solid Waste Blockage in Drain Channel").

Drainage Data Quality and Completeness

Analysis of the accuracy of the relevant drainage data was performed by the authors, in addition to the quality assurance performed by *Ramani Huria*'s data cleaners. Positional errors (see **Table 4**) were found through visual inspection, and when building the flood model in SOBEK. These errors caused a disconnected network in the model and hence introduced simulation errors. The positional accuracy of the drainage data was assessed to be high, as only 12 out of 532 segments (i.e., 2.25%) had positional errors. The actions performed to correct positional errors in the 1D model are shown in **Table 4**.

The connectivity of the network was analyzed in SOBEK, which revealed that 36 out of 532 segments, i.e., 6.8%, were disconnected from adjacent drainage segments. Upon further inspection in QGIS, it was found that this problem was caused by

so-called "T-junctions." A T-junction occurs when a side-branch connects to a main branch, while the main branch is recorded as a continuous geotrace. A connection from the side-branch to the main branch is not recognized automatically and the side-branch remains unconnected in the modeling software. This problem was solved manually by splitting the segments at T-junctions in QGIS. When all T-junctions were connected, the number of segments in the study area increased from 532 to 560 segments.

Data set completeness was studied with filters in the attribute table in QGIS, in addition to the automated completeness checks performed by *Ramani Huria* (see **Table 5**). There are 14 decommissioned drains in the study area, which have no dimensions recorded. Fieldwork showed that these drainage segments were ditches with considerable conveyance capacity that could not be neglected in the 1D schematization. Hence, the dimensions of these segments were measured in an extra mapping survey in the field. Apart from the decommissioned drains, only one segment in the study area was missing one feature, which likely was accidentally deleted in *Ramani Huria*'s data cleaning process. The decommissioned drains and most of the ditches were missing material data, constituting 5.3% of the total data set. The decommissioned drains were assigned a high roughness coefficient because of their vegetation observed during fieldwork. Three of the 17 ditches were reported as sand by *Ramani Huria*, and hence it was assumed that the remaining 14 ditches were also made of sand.

When inspecting side views of the drainage segments in SOBEK, it was noted that the bed levels in the network were irregular with elevation gaps between each segment. The upstream and downstream bed level of a segment is calculated by subtracting the measured vertical distance between the bottom and the nearest road from the DTM level. The drainage mappers measure this distance at the upstream end after they have recorded a geotrace, and the vertical distance is assumed to be constant along the whole segment. Given that bed level gaps were present at almost every connection in the dataset, this assumption introduces a systematic error in the bed level data. This was corrected by interpolating between upstream bed levels of neighboring drain segments, ensuring smooth bed level connections, representative of the real situation observed in the field.

Summarizing, the positional accuracy and completeness of the drainage data is very much in line with datasets collected with professional surveys. The sole exception is the altitude of drains, which are so far monitored with simple wooden poles, relative to the nearest road. These would benefit observations with precise absolute positioning referenced to a local geoid datum.

Model Results Without and With Community Mapped Drainage Data

The two models were created following the procedure described in section "Model Development." Both models simulated the same storm event for which flood depth data were collected in a flood extent survey, as described in section "Data Acquisition."

Figure 4 shows maximum water levels computed for the 2D scenario (upper left), at observation points covered by the flood extent survey, expressed in the same referencing system as used in the survey. Water levels are between 0 and 10 cm in most observation points (finger-ankle deep), up to a maximum of 30 cm (mid-shin deep). When the 1D drainage is introduced (upper right), computed maximum water levels decrease for

TABLE 4 | Analysis of positional errors.

Positional error	Description	#faulty segments (out of 532)	Action to correct the error
Tracing error	Drainage segment with an unrealistic shape	3	Parts of or the whole unrealistic reach is deleted, depending on its shape
Disconnected end	End of segment with a visible but very small (<30 cm) gap to the adjacent segment	5	The gap between the segments is closed by extending one of the segments manually
Double segment	Two segments with the same or very similar reach and exactly the same attributes	4	One of the segments is deleted
Total		12 (2.25%)	

TABLE 5 | Analysis of attribute completeness.

Type	#	Cross section	#segments missing dimensions	#segments missing material	Action to correct the error(s)
Culvert	199	Round	None	None	
	4	Rectangular	None	None	
Ditch	17	Rectangular	None	14	Assume material type (sand)
Drain	276	Trapezoidal	1, missing depth	None	Assume same depth as adjacent drain
	11	Rectangular	None	None	
	11	Elliptical	None	None	
Decommissioned	14	No attributes recorded	14	14	Record dimensions and material type (vegetation) in the field
Total	532		15 (2.8%)	28 (5.3%)	

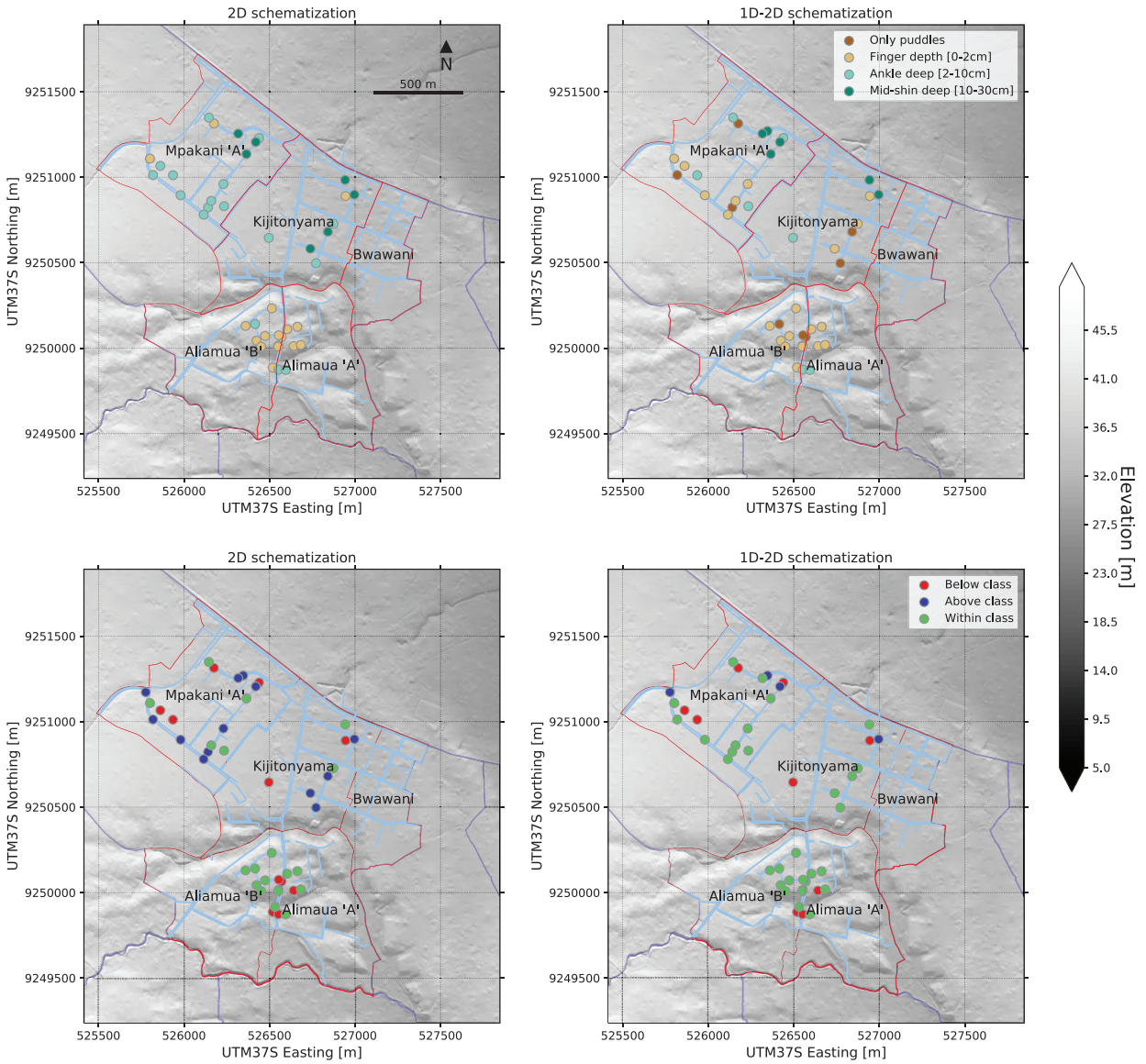

FIGURE 4 | Model results without **(left)** and with **(right)** community mapped data.

most locations, from a few centimeters up to 23 cm decrease (not shown but investigated in the model results), especially in Mpakani "A" and Kijitonyama.

The comparison of maximum computed water levels against flood classes reported in the flood extent survey shows that for the 2D schematization model, simulated water depths fall below reported class at 12 locations, within correct reported class at 19 locations, and above reported class at 13 locations (**Figure 4**, lower left). When introducing the 1D drainage network, i.e., using the 1D–2D model, simulated water depths fall in the correct reported class for 30 out of a total of 44 locations (lower right). Simulated water depths for the 1D–2D model are below reported class at 10 locations and above reported class at 4 locations (**Figure 4** and **Table 6**). This is a considerable improvement.

Differences in computed water levels are most apparent in Mpakani "A" and Kijitonyama, where the 2D-model tends to overestimate water levels corresponding to ankle and mid-shin deep flooding classes, where only puddles and finger-deep flooding was reported in the survey. These smaller water depths are better captured by the 1D–2D model (compare **Figure 4**, lower left and right figures). In Kijitonyama, water flows naturally toward a depression at the north boundary of the ward. However, since terrain gradients are very small, overland flows remain low and relatively high water depths are computed by the 2D model (see **Figure 4**, upper left). Introduction of the drainage channels in the 1D–2D model substantially improves performance in this ward. In Mpakani "A," a natural streambed cuts through the northern part of the area, collecting a lot of flood water in both

TABLE 6 | Summary of model development results.

	2D model	1D–2D model with community mapped 1D data
Below reported class	12 (27%)	10 (23%)
In reported class	19 (43%)	30 (68%)
Above reported class	13 (30%)	4 (9%)

Number of observation points below/in/above reported water depth class (and percentage).

the 2D and 1D–2D models. In the southern part, away from the streambed, drainage channels convey the flow toward adjacent surface waters, as is correctly represented in the 1D–2D model.

Furthermore, in Alimaua, a central drainage channel collects most of the flood water and along this channel minor flooding is reported. This is generally well captured by both models, as the channel follows a natural depression that is represented in the 2D model. The 1D–2D model more correctly represents the dimensions of the channel, which resolves underestimated water levels at a couple of locations in the 2D model in Alimaua (see **Figure 4**, lower left and right).

These results demonstrate that using the 1D network, at this scale, is essential for accurate simulation of flood hazard. More importantly, the results obtained clearly show that the community flood survey is highly valuable when validating model results.

Impact of Solid Waste Blockage in Drain Channel

The simulation with the blocked drain segment due to solid waste accumulation clearly shows a different behavior of water levels in the drainage channel. **Figure 5** shows the resulting differences in maximum flow and maximum water depth between the simulation with and without the blocked drain. As can be expected, when the flow through the drain is blocked, this is leading to a backwater effect in the drainage channel upstream of the blockage, which can be seen clearly on the right-hand side of **Figure 5**. This is further visualized in **Figure 6** with a side view, comparing the maximum water levels of the two simulations in the drain upstream of the blocked drain. Due to the blockage, the drainage water overflows the drain segment, causing additional flooding on the streets. **Figure 7** shows this additional flood extent caused by the blocked drain. The flood extent in this map is only shown where the flood depth is larger than 4 cm.

These results demonstrate that drain blockages can be effectively simulated in the 1D–2D model. They also illustrate that differences introduced by the blockage are relatively small for this blockage scenario, which is explained by the looped nature of the drainage network. As **Figure 2** shows, the main drains in the northern half of the drainage network connect outflow points to rivers and streams both on the northern as well as on the southern ends of the network. This implies that when a drain is blocked, especially in the center of the network, flows can be diverted through other parts of the network, making the system less sensitive to local drain blockage. This type of insight can only be obtained because of detailed information on the 1D drainage network obtained by the community mapping.

DISCUSSION

This paper has proposed and applied a framework for flood modeling with community mapped data. A flood model has been developed and validated utilizing community mapped data as 1D schematization and validation.

The dataset of community mapped drainage achieved a high degree of completeness, with only 2.8 and 5.3% of all segments missing dimensions or information about the material, respectively. Positional errors, amounting to 2.25% of all drainage segments, were easily corrected in the model by connecting loose ends to the nearest node or deleting faulty segments. Connectivity errors amounted to 6.8% of relevant locations and were corrected manually. These errors occurred mainly when side-drains were connecting to a main drain and could be easily avoided in the future by introducing a step in the mapping procedure where ongoing main drains are split into suitable separate segments, to ensure full connectivity to the side branches when implementing the data in a modeling software.

The results of the model development show that community mapped data can indeed improve pluvial flood predictions at neighborhood scale. Using community mapped drainage data to build a detailed schematization of the 1D drainage network increases the model prediction accuracy, from 43 to 68%, measured as percentage of simulated flood depth points that match the reported validation class. Highest benefits are obtained in areas where conveyance capacity and direction of the drainage networks differ substantially from the natural flow paths created by elevation differences of the natural terrain. This applies in particular in areas with small natural terrain gradients, where 1D channel networks induce faster and more concentrated drainage flows, and in areas where street pattern layout differs substantially from natural terrain gradients, as with the rectangular street lay-out in some of the sub-wards in the study area.

Furthermore, the community mapped drainage data makes the model much more versatile in its possible applications. This is because of the 1D schematization which enables simulations where network configuration changes or channel capacities are impacted by maintenance-state. An example of such a model application has been presented here, investigating the impact of solid waste blockages on network flow and flooding. These results demonstrate that community mapping has moved from a disaster response practice (Zook et al., 2010) to serve as reliable and affordable way to support proactivity and planning in data-scarce environments.

The developed model is subject to uncertainties associated with the positional accuracy of the drainage segments, as it has been recorded with GPS units (smartphones) with an accuracy of around 5 meters. These errors have, however, been accounted for to some extent in *Ramani Huria*'s data cleaning process where the drainage geotraces were compared with aerial imagery. The highest uncertainties in the community mapped drainage dataset were found for drain level measurements. Bed levels of drains

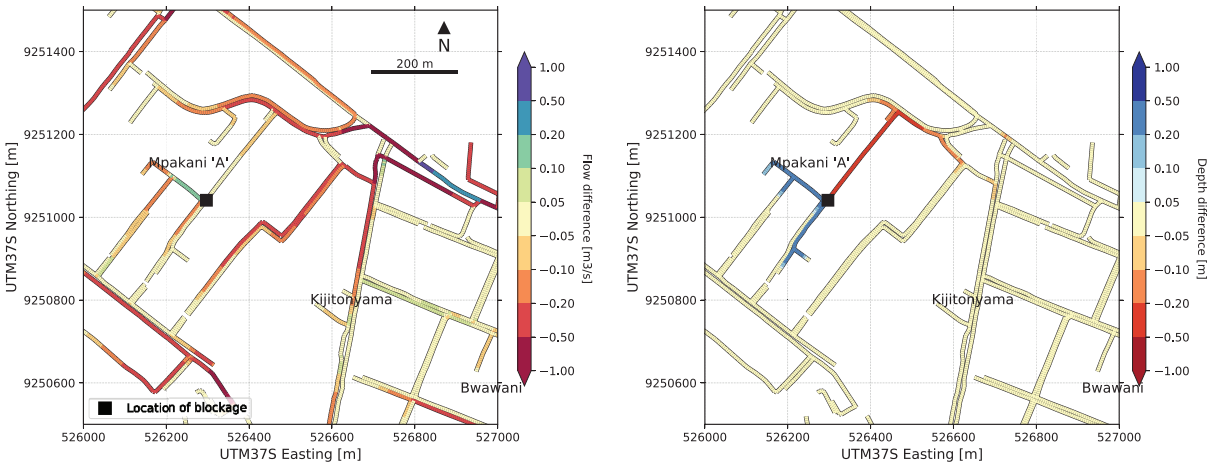

FIGURE 5 | Flow difference and depth difference in drainage channels when blocking a drainage segment.

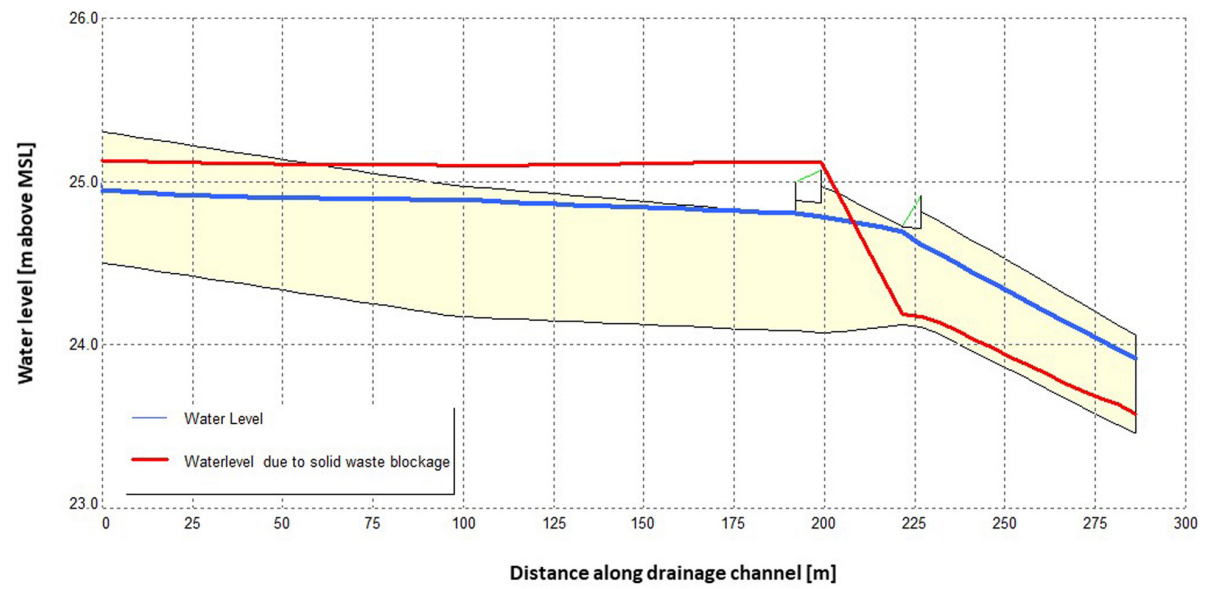

FIGURE 6 | Side view in SOBEK of drainage segment blocked by solid waste (blockage at 225 m). The y-axis shows elevation above DTM datum, and the x-axis shows horizontal distance from the start of the selected side view.

were measured using simple wooden poles, and altitude was estimated relative to the nearest road. This introduced substantial uncertainties in the data. Bed and bank level measurements of drains would benefit from observations with precise (absolute) positioning referenced to a local geoid datum. There is a need to continue investigating low-cost alternatives that allow for accurate elevation measurements. The advent of new low-cost chipsets for multi-frequency Global Navigation Satellite System's positioning, and the first endeavors of smartphone producers to embed these in smartphone models, may also address this soon. These chipsets are currently under investigation for use in community mapping contexts (van Dongen, 2019).

Validation data, obtained in a flood extent survey involving 44 community member's reporting on flood depths a few hours after the simulated rainfall event, proved to be valuable to validate flood modeling results. Earlier studies have shown that community observations provide a valuable source of information for flood risk analysis (Paul et al., 2018; Etter et al., 2019; Strobl et al., 2019). Even if the amount of data collected through flood surveys is small and the uncertainty of the flood depth classes cannot be quantified, the data still provides an effective form of validation. The reporting classes used give an indication of the flood depth at each observation point in the absence of any other validation data set for the study area. Reporting flood depth in terms of flood depth categories associated with a "person's height reference system," i.e., referring to the estimated flood depth as e.g., ankle deep or knee deep, provided a workable trade-off between reliability in terms of what

FIGURE 7 | Additional surface flooding caused by blocked drainage channel.

citizen observations can distinguish and accuracy needed for model validation. Further investigation to optimize the selected thresholds for validation classes is recommended, to identify how accurately observations according to this reference system can represent reality. If implemented systematically, community-based flood extent surveys can allow for model validation at low costs and build trust in the model predictions. As more web- and mobile-based flood reporting systems are being developed, community-based flood observations will become more and more easy to implement (Seibert et al., 2019).

The case study shows a discrepancy between our hypothesized framework and *Ramani Huria*. Our proposed framework relies on the principles of community mapping in industrially developing countries found in literature (Iliffe, 2017). These principles assume that the mapping process is firmly anchored with the leaders and residents of a certain location, and that the same people are participating in all parts of the mapping process (Parker, 2006). However, *Ramani Huria* has trained teams since 2017 to conduct specialized types of mapping independent of where the mappers live. The results of the mapping campaign are not shared with the same people that initiated it, as the mapping is carried out over a long period of time, during which the politically elected ward- and subward officers often have been replaced. This indicates that there are challenges with keeping large-scale mapping projects anchored in the community that is being mapped. However, the authors do not see a contradiction between the proposed framework and the utilization of trained mapping teams.

Literature suggests that the authority of community mapped data springs from the fact that it is collected by the community for the community (Flanagin and Metzger, 2008; Iliffe, 2017), which makes it important to start and end the mapping process with community forums. All data sets identified by the community do not, however, need to be collected by the community itself. The case study shows that the data acquisition of community mapping projects differs depending on the characteristics of the data set that is being mapped. Data sets that are relatively easy to collect and require a high number of records to ensure data quality, like flood extent surveys, can be collected by community members, whereas more technically advanced features like drainage dimensions should be mapped by trained teams. It should be noted, however, that trained mappers increase the costs of the mapping process. Still, they are using inexpensive tools that are far less costly than traditional data acquisition technologies.

The urban landscape is changing rapidly across the world, which implies that urban spatial data needs to be updated with high frequency. VGI and community mapping could serve as an affordable way to overcome this, but an incentive must be developed to keep open source spatial data sets up to date. This requires, on the one hand, clear end users, who see value

in updated, open source data and simulation models derived from this data. On the other hand, it requires an entity such as a company who has a proposition to fulfill that service. As shown, there is a voluntary component in community mapping projects to successfully support flood modeling, as it allows for collection of validation data sets that require a high number and density of data points to be reliable. However, it is shown that volunteers alone do not guarantee the required data quality of technical features like drainage segments. Instead, the main added value of VGI to urban flood risk management in data-scarce environments is the open source tools that are now available to collect technical features with high accuracy in an affordable, comprehensible, and quality-assured way.

CONCLUSION

This paper presented a new framework for developing flood models by using community mapped data. The framework was demonstrated and validated on a case study of the *Ramani Huria* community mapping project in Dar es Salaam.

The results obtained show that:

1. The proposed framework for flood modeling with community mapped data allows for comprehensive modeling in a data-scare context. The framework comprised three principal phases; data acquisition, model development and model implementation, where the data acquisition should be affordable, comprehensible, quality assured and open source to be applicable in resource-strained environments. This framework is generic and flexible in nature, as it allows for different types of community mapped data to be collected and applied. Consequently, it is suggested for future research to apply this framework to other case studies to investigate its validity and robustness.
2. Community mapped data can improve flood modeling on a level of detail that is currently inaccessible in many data-scarce environments. The outputs of the developed model correspond better with validation data when introducing drainage data from a community mapping project as 1D schematization, compared to a scenario run with only terrain data. Moreover, using community mapped data results in a more versatile model being developed.
3. Highest benefits of community-mapped data of the 1D-network are obtained in areas where conveyance capacity and direction of the drainage networks differ substantially from the natural flow paths created by elevation differences of the natural terrain. This applies in particular in areas with small natural terrain gradients, where 1D channel networks induce faster and more concentrated drainage flows and storage, and in areas where street pattern lay-out differs substantially from natural terrain gradients, as with the rectangular street lay-out in some of the sub-wards in the study area. Additionally, 1D-network data is essential in areas where blockage of drainage channels is an issue and need investigation for flood risk management.
4. The community mapping approach is especially appropriate for datasets that do not require extensive training, such as flood extent surveys where it is possible to cross-validate the quality of reports given the high number and density of data points. More technically advanced features, such as collecting dimensions of urban drainage systems (e.g., bed levels), require trained mappers to create data of sufficient quality. Our analysis shows that it is possible to achieve this quality through smartphones with accurate GPS receivers, open source servers, training of students and clever survey designs. These components form a promising framework for reliable flood modeling with community mapped data.

Future research is suggested to explore how community mapping can become an institutionalized practice to fill gaps in data-scarce environments by addressing incentives for participation and sustainability to keep community mapped data up to date. Furthermore, the authors invite a discussion on liability issues of open source data sets, which is expected to arise when open data is increasingly applied in governance.

DATA AVAILABILITY STATEMENT

The datasets generated for this study are available on request to the corresponding author.

AUTHOR CONTRIBUTIONS

LP and IM conducted the literature review for the framework development. HW established the survey design for the drainage data collection. IM supervised the drainage data collection. LP conducted the additional field data collection and performed the drainage data quality analysis. LP and GV performed the model development and validation. LP, HW, and M-CV conducted and reported the data and results analysis. All authors were involved in the writing and editing of this manuscript.

FUNDING

LP was financially supported by Lamminga Fund to perform field work for this research. The Ramani Huria community mapping project is funded by Department for International Development, United Kingdom.

ACKNOWLEDGMENTS

The authors would like to thank the staff and students at Humanitarian OpenStreetMap Team Tanzania for their kind support to this research.

REFERENCES

Antoniou, V., and Skopeliti, A. (2015). Measures and indicators of VGI quality: an overview. *ISPRS Ann. Photogr. Remote Sens. Spatial Inform. Sci.* 2, 345–351. doi: 10.5194/isprsannals-II-3-W5-345-2015

Bach, P. M., Rauch, W., Mikkelsen, P. S., McCarthy, D. T., and Deletic, A. (2014). A critical review of integrated urban water modelling - Urban drainage and beyond. *Environ. Model. Softw.* 54, 88–107. doi: 10.1016/j.envsoft.2013.12.018

Bilham, R. (2010). Lessons from the Haiti earthquake. *Nature* 463, 878–879. doi: 10.1038/463878a

Brady, H. E., Verba, S., and Schlozman, K. L. (1995). Beyond SES: a resource model of political participation. *Am. Political Sci. Rev.* 89, 271–294. doi: 10.2307/2082425

Butler, D., Digman, C. J., Makropoulos, C., and Davies, J. W. (2018). *Urban Drainage*. Boca Raton, FL: CRC Press.

Buytaert, W., Zulkafli, Z., Grainger, S., Acosta, L., Alemie, T. C., Bastiaensen, J., et al. (2014). Citizen science in hydrology and water resources: opportunities for knowledge generation, ecosystem service management, and sustainable development. *Front. Earth Sci.* 2:26. doi: 10.3389/feart.2014.00026

Chow, V. T., Maidment, D. R., and Mays, L. W. (1988). *Applied Hydrology*. New York, NY: Mc Graw-Hill, Inc.

Coleman, D., Georgiadou, Y., and Labonte, J. (2009). Volunteered geographic information: the nature and motivation of producers. *Int. J. Spatial Data Infrastr. Res.* 4, 332–358.

Davids, J. C., Rutten, M. M., Pandey, A., Devkota, N., Oyen, W. D., Prajapati, R., et al. (2018). Citizen science flow - an assessment of citizen science streamflow measurement methods. *Hydrol. Earth Syst. Sci. Discuss.* 23, 1045–1065. doi: 10.5194/hess-23-1045-2019

Deletic, A., Dotto, C. B., McCarthy, D. T., Kleidorfer, M., Freni, G., Mannina, G., et al. (2012). Assessing uncertainties in urban drainage models. *Phys. Chem. Earth Parts ABC* 42, 3–10. doi: 10.1016/j.pce.2011.04.007

Etter, S., Strobl, B., Seibert, J., and Meerveld, I. V. (2019). Value of crowd-based water level class observations for hydrological model calibration. *Water Resour. Res.* 56:e2019WR026108.

Flanagin, A. J., and Metzger, M. J. (2008). The credibility of volunteered geographic information. *GeoJournal* 72, 137–148. doi: 10.1007/s10708-008-9188-y

Fritz, S., See, L., and Brovelli, M. (2017). "Motivating and sustaining participation in VGI," in *Mapping and the Citizen Sensor*, eds G. Foody, L. See, S. Fritz, P. Mooney, A.-M. Olteanu-Raimond, C. C. Fonte, et al. (London: Ubiquity press), 93–117. doi: 10.5334/bbf.e

Girres, J.-F., and Touya, G. (2010). Quality assessment of the french openstreetmap dataset. *Trans. GIS* 14, 435–459. doi: 10.1111/j.1467-9671.2010.01203.x

Goodchild, M. F. (2007). Citizens as sensors: the world of volunteered geography. *GeoJournal* 69, 211–221. doi: 10.1007/s10708-007-9111-y

Goodchild, M. F., and Li, L. (2012). Assuring the quality of volunteered geographic information. *Spatial Stat.* 1, 110–120. doi: 10.1016/J.SPASTA.2012

Haklay, M. (2010). How good is volunteered geographical information? A Comparative study of OpenStreetMap and ordnance survey datasets. *Environ. Plan. B Plann. Design* 37, 682–703. doi: 10.1068/b35097

Haklay, M. (2013). "Citizen science and volunteered geographic information: overview and typology of participation," in *Crowdsourcing Geographic Knowledge*, eds D. Z. Sui, S. Elwood, and M. F. Goodchild (Dordrecht: Springer Netherlands), 105–122. doi: 10.1007/978-94-007-4587-2_7

Iliffe, M. P. (2017). *The Praxis of Community Mapping in Developing Countries*. Doctoral dissertation, University of Nottingham, Nottingham.

Neis, P., Zielstra, D., and Zipf, A. (2011). The street network evolution of crowdsourced maps: OpenStreetMap in Germany 2007–2011. *Future Internet* 4, 1–21. doi: 10.3390/fi4010001

Ozdemir, H., Sampson, C. C., Almeida, G. A., and Bates, P. D. (2013). Evaluating scale and roughness effects in urban flood modelling using terrestrial LIDAR data. *Hydrol. Earth Syst. Sci.* 17, 4015–4030. doi: 10.5194/hess-17-4015-2013

Parker, B. (2006). Constructing community through maps? Power and praxis in community mapping. *Prof. Geogr.* 58, 470–484. doi: 10.1111/j.1467-9272.2006.00583.x

Paul, J. D., Buytaert, W., Allen, S., Ballesteros-Cánovas, J. A., Bhusal, J., Cieslik, K., et al. (2018). Citizen science for hydrological risk reduction and resilience building. *Wiley Interdiscip. Rev. Water* 5:e1262. doi: 10.1002/wat2.1262

Ramm, F., Topf, J., and Chilton, S. (2011). *OpenStreetMap - Using and Enhancing the Free Map of the World*. Cambridge: UIT Cambridge Ltd.

Schumann, G. J.-P., and Bates, P. D. (2018). The need for a high-accuracy. open-access global DEM. *Front. Earth Sci.* 6:225. doi: 10.3389/feart.2018.00225

Seibert, J., Strobl, B., Etter, S., Hummer, P., and Meerveld, H. J. (2019). Virtual staff gauges for crowd-based stream level observations. *Front. Earth Sci.* 7:70. doi: 10.3389/feart.2019.00070

Senaratne, H., Mobasheri, A., Ali, A. L., Capineri, C., and Haklay, M. (2017). A review of volunteered geographic information quality assessment methods. *Int. J./ Geogr. Inform. Sci.* 31, 139–167. doi: 10.1080/13658816.2016.1189556

Soden, R., and Palen, L. (2014). "From crowdsourced mapping to community mapping: the postearthquake work of openstreetmap Haiti. COOP 2014 -," in *Proceedings of the 11th International Conference on the Design of Cooperative Systems*, Nice: Springer International Publishing, 311–326. doi: 10.1007/978-3-319-06498-7_19

Strobl, B., Etter, S., Meerveld, I. V., and Seibert, J. (2019). Accuracy of crowdsourced streamflow and stream level class estimates. *Hydrol. Sci. J.* 65, 823–841. doi: 10.1080/02626667.2019.1578966

ten Veldhuis, M.-C., Clemens, F. H., and Gelder, P. H. (2011).). quantitative fault tree analysis for urban water infrastructure flooding. *Struct. Infrastruct. Eng.* 7, 809–821. doi: 10.1080/15732470902985876

UN-HABITAT (2010). *Informal Settlements and Finance In Dar es Salaam, Tanzania*. Nairobi: UN-HABITAT.

United Nations (2018). *World Urbanization Prospect: The 2018 Revision - Key Facts*. New York, NY: United Nations.

van Dongen, K. (2019). *Community Mapped Elevation Through a Low-cost, Dual-Frequency GNSS Receiver: A Performance Study in Delft (the Netherlands) and Dar es Salaam (Tanzania)*. Master Thesis, Delft University of Technology, Delft.

Winsemius, H. C., Jongman, B., Veldkamp, T. I., Hallegatte, S., Bangalore, M., and Ward, P. J. (2018). Disaster risk, climate change, and poverty: assessing the global exposure of poor people to floods and droughts. *Environ. Dev. Econ.* 2, 1–21. doi: 10.1017/S1355770X17000444

Winsemius, H. C., Ward, P. J., Gayton, I., Veldhuis, M.-C. T., Meijer, D. H., and Iliffe, M. (2019). Commentary: the need for a high-accuracy, open-access global DEM. *Front. Earth Sci.* 7:33. doi: 10.3389/feart.2019.00033

Zook, M., Graham, M., Shelton, T., and Gorman, S. (2010). Volunteered geographic information and crowdsourcing disaster relief: a case study of the haitian earthquake. *World Med. Health Policy* 2, 6–32. doi: 10.2202/1948-4682.1069

Conflict of Interest: The authors declare that the research was conducted in the absence of any commercial or financial relationships that could be construed as a potential conflict of interest.

frontiers in Earth Science

ORIGINAL RESEARCH
published: 05 August 2020
doi: 10.3389/feart.2020.00332

Prediction of Maximum Flood Inundation Extents With Resilient Backpropagation Neural Network: Case Study of Kulmbach

Qing Lin, Jorge Leandro, Wenrong Wu, Punit Bhola and Markus Disse*

Department of Civil, Geo and Environmental Engineering, Technical University of Munich, Munich, Germany

In many countries, floods are the leading natural disaster in terms of damage and losses per year. Early prediction of such events can help prevent some of those losses. Artificial neural networks (ANN) show a strong ability to deal quickly with large amounts of measured data. In this work, we develop an ANN for outputting flood inundation maps based on multiple discharge inputs with a high grid resolution (4 m × 4 m). After testing different neural network training algorithms and network structures, we found resilience backpropagation to perform best. Furthermore, by introducing clustering for preprocessing discharge curves before training, the quality of the prediction could be improved. Synthetic flood events are used for the training and validation of the ANN. Historical events were additionally used for further validation with real data. The results show that the developed ANN is capable of predicting the maximum flood inundation extents. The mean squared error in more than 98 and 86% of the total area is smaller than 0.2 m^2 in the prediction of synthetic events and historical events, respectively.

Keywords: hazard, maximum flood inundation extent, artificial neural network, resilient backpropagation, urban flood forecast

OPEN ACCESS

Edited by:
Mingfu Guan,
The University of Hong Kong,
Hong Kong

Reviewed by:
Huan-Feng Duan,
Hong Kong Polytechnic University,
Hong Kong
Jiahong Liu,
China Institute of Water Resources and Hydropower Research, China
Guangtao Fu,
University of Exeter, United Kingdom

****Correspondence:***
Qing Lin
tsching.lin@tum.de

Specialty section:
This article was submitted to Hydrosphere, a section of the journal Frontiers in Earth Science

Received: *07 March 2020*
Accepted: *17 July 2020*
Published: *05 August 2020*

Citation:
Lin Q, Leandro J, Wu W, Bhola P and Disse M (2020) Prediction of Maximum Flood Inundation Extents With Resilient Backpropagation Neural Network: Case Study of Kulmbach. Front. Earth Sci. 8:332. doi: 10.3389/feart.2020.00332

INTRODUCTION

Flood is one of the most damaging natural hazards hitting settlements which threatens the safety of civilians and the integrity of infrastructures (Berz, 2001). Flooding is the leading cause of damage and losses in many countries in the world (Kron, 2005). Furthermore, as a result of climate and land-use changes, the flood vulnerability of some regions is expected to rise (Vogel et al., 2011). Accurate prediction of floods in urban areas can contribute to the development of essential tools to minimize the risks of flooding.

There are different types of numerical models widely used for urban flood simulation (Henonin et al., 2013). Hydrological rainfall run-off models can be used to simulate distributed river discharges. One-dimensional (1D) drainage model solving the one-dimensional Saint-Venant flow equations, can be applied for simulating the surcharge or drainage of the underground drainage network (Mark et al., 2004). The two-dimensional (2D) Saint-Venant flow equations are ideal tools for simulating the urban surface inundation, and obtain the maximum flood extents, maximum depths and flow velocity on many points on the surface. Furthermore, the 1D–2D coupling model simulates the drainage network and the urban surface simultaneously. Even though they provide

more accurate results than the previous models (Hankin et al., 2008), they are computationally more expensive. All approaches require field measurements for defining the model parameters. The two latter have prohibitive high computation costs and require very detailed data sets which often restrict the application for real-time forecasting (Vogel et al., 2011). With the advances in high-performance computing, graphics processing units (GPU) nowadays are capable of faster 2D simulation in much larger areas (Kalyanapu et al., 2011). Although these scalability techniques reduce the simulation time greatly, it is still unacceptably high in many cases for real-time early warning systems.

Data-driven approaches can be a feasible alternative for established flood simulation models (Mosavi et al., 2018). Unlike conventional numerical models, data-driven models require input/output data only. The fast-growing trend of data-driven models has shown their high performance even for nonlinear problems (Mekanik et al., 2013). Unlike physical-based models, data-driven models do not require field measurements for determining (physically based) model parameters, which alleviates the burden on the users for data gathering and model setup. ANN can be a useful tool for modeling, if properly applied. Indeed some of the pitfalls are the likelihood of over-fitting or under-fitting the data, and insufficient length of the data sets which may lead to erroneous model results (Zhang, 2007). Various data-driven models for short and long term flood forecasts have been developed using neuro-fuzzy (Dineva et al., 2014), support vector machine (SVM) (Bermúdez et al., 2019), support vector regression (Gizaw and Gan, 2016; Taherei et al., 2018) and artificial neural network (ANN) (Kasiviswanathan et al., 2016). Artificial neural network is a popular approach in flood prediction (Elsafi, 2014; Abbot and Marohasy, 2015). Some works have successfully applied ANN for forecasting water levels. Dawson and Wilby (2001) applied ANN to conventional hydrological models in flood-prone catchments in the United Kingdom in 1998. Since then, many studies about flood forecasts in catchment scales arose (Chang L.C. et al., 2018; Yu et al., 2006). Thirumalaiah (1998) compared the water level forecast results along a river using backpropagation, conjugate gradient as well as cascade correlation. Coulibaly et al. (2000) combined Levenberg-Marquardt Backpropagation (Marquardt, 1963) with cross-validation to prevent the under-fitting and overfitting in daily reservoir inflow forecasting. Taghi et al. (2012) applied a backpropagation network and a time lag recurrent network having reached a similar forecast precision in reservoir inflow. Humphrey et al. (2016) joined a conceptual rainfall-runoff model with a Bayesian artificial neural network for improving the precision of the neural network. Sit and Demir (2019) used discretized neural networks for the entire river network in Iowa. By including more location information, they could enhance the forecasting results. Bustami et al. (2007) applied backpropagation ANN model for forecasting water level at gaging stations. Tiwari and Chatterjee (2010) compared different types of ANN predictions of water levels at gaging stations, namely a wavelet-based, a bootstrap based and a hybrid wavelet-bootstrap-ANN (WBANN) and shown that the WBANN model was more accurate and reliable compared to other three ANN. For flood inundation forecast, Simon Berkhahn et al. (2019) trained an ANN with synthetic events of spatial rainfall data for 2D urban pluvial inundation. Chang M.J. et al. (2018) applied a mix of SVM and GIS analysis to expand point forecasts to flooded areas at a sub-catchment scale. Chu et al. (2020) proposed an ANN-based framework for flood inundation prediction based on single inflow data for a 20 m × 20 m grid resolution.

In this article, we develop a method for predicting the maximum flood inundation in an urban area by backpropagation networks based on multiple inflow data for a grid resolution of 4 m × 4 m. Unlike most of the previous studies, this work focuses on applying ANN in an urbanized area for producing high-resolution flood inundation maps from river flooding. For the prediction of maximum flood inundation, only the real-time discharges of the upstream catchments are needed. In Methodology, we introduce the backpropagation artificial neural network, fuzzy c-means clustering methods (FCM) and our criteria for model evaluation. Study Area and Dataset provides basic background information about our study area as well as the synthetic event database for our model training. Results shows the results of our model tuning, the simulation results for synthetic and historical events. To improve the model training behavior by a limited database, we introduce two FCM for the preprocessing of the training dataset. Last sections are the discussion and conclusion of this work.

METHODOLOGY

Resilient Backpropagation Algorithm for Artificial Neural Network

The ANN applied in this work for modeling the study area is a forward-feed neural network (FNN) (Nawi et al., 2007), producing and transmitting the data in a network structure. The basic element of the neural network is the neuron. Each neuron collects values from the previous layer by summing up the results from the previous neuron values multiplying the weight on each input arc and storing the results on itself. Through multiple layered neurons, information is proceeded by the weights and transferred over the network, finally reaching the output layer. The input layer of all ANNs is given by seven inflows upstream contributing to the urban area of Kulmbach from the event database (further details can be found in "HEC-RAS and Synthetic Event Database" section). The output layer is set from the raster flood inundation map from the event database.

Backpropagation is an algorithm widely applied in neural network studies, for optimizing the weights in forward-feed neural networks (Nawi et al., 2007). The procession consists of two phases: the training phase collects a part of data from the existing database, tuning the model by changing the weights on input arcs to minimize the bias on the output layer; the recalling phase produces the new outputs for the testing inputs. The rest individuals in the training dataset are used for evaluating the behavior of the network. The total bias between the output of ANN and the observed values is defined as the error function. In order to reduce the error function in each iteration, the weights

are modified automatically as described below. The chain rule is applied for minimizing the biases, namely written as:

$$\frac{\partial L}{\partial w_{ij}} = \frac{\partial L}{\partial O_i} \cdot \frac{\partial O_i}{\partial net_i} \cdot \frac{\partial net_i}{\partial w_{ij}} \tag{1}$$

where

L is error function of the model.

W_{ij} is weight from i'th neuron to j'th neuron.

O_{i} is output of the model.

net_{i} is weighted sum of the inputs of neuron i.

$$w_{ij}(t+1) = w_{ij}(t) - \epsilon \cdot \frac{\partial \mathbf{L}}{\partial \mathbf{w_{ij}}}(\mathbf{t}) \tag{2}$$

where

ϵ is learning rate taken as 0.01 in our training.

The learning rate is used for scaling the gradient in each iteration of the weight update. It is critical to pick up the correct value. A large learning rate will miss the optimal point, while a small learning rate would slow the training process. Herein, we apply the gradient descent algorithm to calculate the update of the weights. To speed up the convergence of the iteration formula (2), resilient backpropagation as defined in Saini (2008) is applied, which treats the update of weights differently depending on the derivative of the error function. Larger alternative learning rate η^+ could be set for speeding up the iterations if the error gradient remains in the same direction in neighboring time-steps and smaller alternative learning rate η^- when approaching the optimal weights.

$$\Delta_{ij}(t) = \begin{cases} \eta^+ \cdot \Delta_{ij}(t-1), & \frac{\partial L}{\partial w_{ij}}(t) \cdot \frac{\partial L}{\partial w_{ij}}(t-1) > 0 \\ \eta^- \cdot \Delta_{ij}(t-1), & \frac{\partial L}{\partial w_{ij}}(t) \cdot \frac{\partial L}{\partial w_{ij}}(t-1) < 0 \\ \Delta_{ij}(t-1), & else \end{cases} \tag{3}$$

$$w_{ij}(t) = \begin{cases} w_{ij}(t-1) + \Delta_{ij}(t), & \frac{\partial L}{\partial w_{ij}}(t) < 0 \\ w_{ij}(t-1) - \Delta_{ij}(t), & \frac{\partial L}{\partial w_{ij}}(t) > 0 \\ 0, & else \end{cases} \tag{4}$$

In which $0 < \eta^- < 1 < \eta^+$. In our study these were set constant and equal to $\eta^- = 0.5,\ \eta^+ = 1.2$.

Due to the total number data of pixels (resolution of 4 by 4 m) in the city of Kulmbach, a single hidden layer would exceed 365 thousand elements. To reduce the storage requirement and the ANN model training time, the study area is subdivided into 50×50 squared grids, each grid having its own independent ANN (the output layer has 1400 elements) (**Figure 1**). A similar strategy was used by Berkhahn et al. (2019) for an ANN for flood prediction having rainfall as input.

Fuzzy C-Means Clustering and Principal Component Analysis

To further enhance the ANN behavior, we apply clustering to the discharges training dataset. Therefore, we can reduce the size of the training dataset while still keeping the main representative events. As such the training time can be reduced and the overfitting effects minimized. Fuzzy C-means clustering (FCM) (Tilson et al., 1988) is a widely used clustering method, which avoids the deficit of the sub-clusters with unequivocal similarities within its components (Mukerji et al., 2009). In FCM, every single event is given a membership u, which indicates the relation between the event and a certain cluster. If a membership is equal to zero, it means that the event has nothing in common to a specific cluster; if the membership is one, the event is located at the center of the cluster. Once a cluster is set up, the membership u can be calculated by the following equations, and based on the event and the distances between the events. For cluster i and event j, the membership u_{ij} is to quantify distances between events and cluster centers.

$$\begin{cases} u_{ij} \in [0,1] \\ \sum_{i=1}^{c} u_{ij} = 1,\ 1 < j \le n \end{cases} \tag{5}$$

$$u_{ij}^{(k)} = \frac{1}{\sum_{r=1}^{c} \left(\frac{d_{ij}(k)}{d_{rj}(k)} \right)^2} \tag{6}$$

$$d_{ij} = \left|\left| x_j - v_i \right|\right|^2 \tag{7}$$

$$v_i^{(k+1)} = \frac{\sum_{j=1}^{n} u_{ij}^{(k)} x_j}{\sum_{j=1}^{n} u_{ij}^{(k)}} \tag{8}$$

where

c is number of clusters, $2 \le c \le n-1$.

v_{i} is centroid of i-th cluster.

d_{ij} is Euclidean distance between event j and its corresponding centroid.

For optimal clustering, the total sum of distances between events and the cluster centroids have to be the minimum possible. Therefore the following objective function needs to be optimized:

$$J_m(U, V) = \sum_{j=1}^{n} \sum_{i=1}^{c} (u_{ij})^2 d_{ij} \tag{9}$$

Two approaches are applied for deciding the clustering parameters: (a) conventional clustering (by pre-selected hydrograph characteristic parameters); (b) dimension reduction methods. In the former, the clustering variables chosen were P (peak discharge value), T (peak time), V (total volume), $V24$ (volume in the first 24 h). These can be applied individually or combined. The latter clustering method is based on principal component analysis among the hydrographs. The data are projected to the first several principal eigenvectors for dimensionality reduction via PCA, for further clustering by FCM. To determine the optimal number of clustering c, we define the clustering performance index L(c).

$$L(c) = \frac{\sum_{i=1}^{c} \left(\sum_{j=1}^{n} u_{ij}^2 \right) ||v_i - \bar{x}||^2}{\sum_{i=1}^{c} \sum_{j=1}^{n} u_{ij}^2 \left|\left| v_i - x_j \right|\right|^2} \cdot \frac{n-c}{c-1} \tag{10}$$

The optimal cluster number c can be determined by the maximum of L(c).

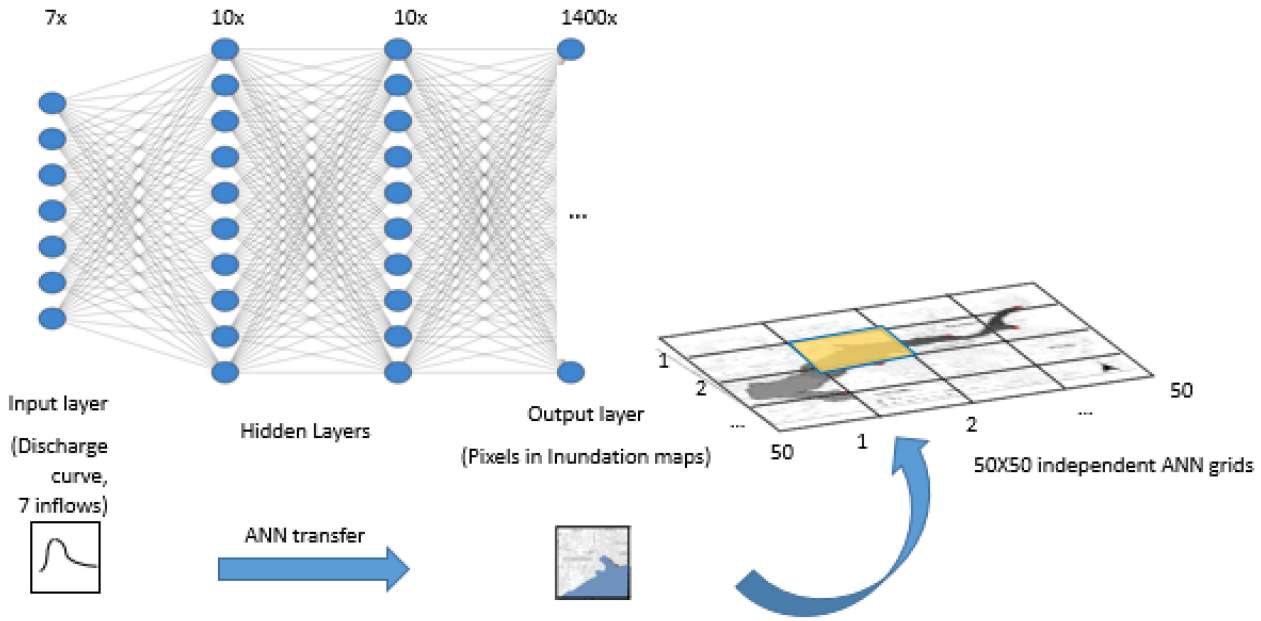

FIGURE 1 | Neural network setups. The study area is divided in 50 × 50 raster each simulated by its own ANN. Input layer: seven input hydrographs. Output layer: flood inundation extent in each grid.

Model Evaluation

To evaluate the performance of the ANN prediction of maximum flood inundation in the study area is based on the mean squared error (MSE) of each grid. It is assumed that the inundation maps from the synthetic events produced using a dynamic model (HEC-RAS) are the observed values. The synthetic events have been produced using the FloodEvac-Tool (Bhola et al., 2018). The model has been validated (Bhola et al., 2019). As each grid has its own independent training network, the MSE is evaluated using all the pixels in each grid.

$$MSE = \frac{1}{n}\sum_{i=1}^{n}(T-S)^2 \tag{11}$$

where

T is predicted value.

S is observed value.

To evaluate the overall behavior of the model across the training and validation data sets, the average of MSE and the standard deviation of MSE are evaluated, indicating the average accuracy and the spread of the ANN predictions.

$$avg.MSE^m = \frac{1}{N}\sum_{n=1}^{N} MSE_n^m \tag{12}$$

where

m is grid index.

n is pixel index in a grid.

N is total number of pixels.

STUDY AREA AND DATASET

Study Area

The study area of Kulmbach is located by the river Main in Bavaria. The city consists of northern and southern parts split by the White Main crossing it. About 27 thousand inhabitants live in this city. The city is classified as a great district city with a population density of 292 inhabitants per km^2 in the area of 92.77 km^2. On May 28, 2006, Kulmbach was heavily flooded from the river and streams nearby. This event was the trigger for decision-makers to review the initiatives of flood prevention for the city. There are seven streams contributing to this area, namely the Red Main, Schorgast, Dobrach, White Main, Kinzelsbach, Kohlenbach, and Mühlbach. The inflows of the seven streams used for training the ANN are the same ones used in the boundary conditions of the hydraulic model. Hence, the two approaches are comparable. The training-validation of the 50 × 50 ANN aims to replace the hydraulic processes within the marked study area (see **Figure 2**). Each ANN aims to generate the inundation map for one sub-divided area. All the inflows are inputted to all the networks to keep the ANN topology identical, and thus avoiding the sudden jump of forecasted water depths at ANN borders (Chu et al., 2020). Since the ANNs are trained on the same data, and using the same inflows as inputs, the inundation maps across the different ANNs are consistent.

HEC-RAS and Synthetic Event Database

The synthetic event database is generated by the 2D hydraulic model HEC-RAS (Hydrologic Engineering Center – River

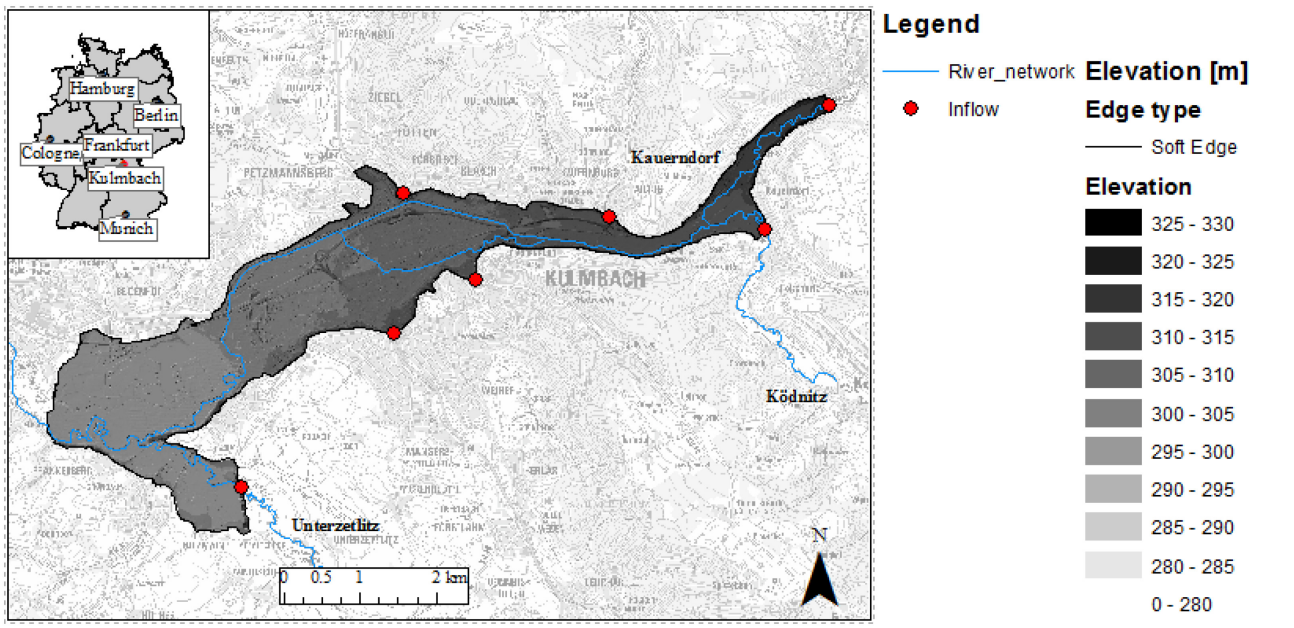

FIGURE 2 | Map of the study area. It shows the location of Kulmbach in Germany. The blue curves represent the river network. The shaded region is the study area with its topography represented. On the marked boundary, the red points represent the seven inflow boundary conditions (three rivers and four smaller streams).

Analysis System, Davis, CA, United States) for various rainfall intensities, distribution, duration (Bhola et al., 2018). The synthetic events are generated following two stages. First, the hydrologic model LARSIM (Large Area Runoff Simulation Model) (Ludwig and Bremicker, 2006) is used for calculating the discharge hydrographs into the city area. LARSIM is a hydrological model applied for flood forecasting at the Bavarian Environment Agency (Disse et al., 2018). Afterward, the 180 convective and advective events are simulated with the 2D hydraulic model HEC-RAS 2D to generate the flood inundation map database. The maps are generated with high temporal resolution (15 min) and projected to a spatial resolution of 4 by 4 m. For further details of the generation of synthetic events please refer to Bhola et al. (2018).

RESULTS

ANN Training Algorithm

Two training algorithms are applied for training the ANN model using the same training dataset (Event #1–#120): resilient backpropagation (RP) and the conjugate gradient (CGF). After that, both generated models are evaluated using the MSE over the remaining runs (60) in the testing dataset (Event #121–#180) (see **Figure 3**). **Figure 4** shows the MSE evaluated over the training dataset just for comparison purposes. In **Figures 3A,B**, most grids have the MSE lower than 0.2 m^2, showing that both RP and CGF networks behave well in general. **Figure 4** shows the MSE from RP is mostly better than that of CGF.

Number of Hidden Layers and Neurons

To improve the performance of the neural networks, the layer number and neuron number for comparison are modified. By optimizing the error function with the training dataset, the optimized number of network layers and neurons per layer are obtained. The layer number is set between two to six, while the neuron number set from 10 to 30. **Table 1** shows the number of grids in each combination (number layers and neurons) which outperform all the others; it shows 70% of all grids fall within the number of layers equal to two or three layers.

Grid Resolution

The grid resolution comparison aims to verify if a finer grid improves the prediction performances. Two grid sizes are tested, namely one with 50 × 50 (each grid has 1400 pixels) and another with 100 × 100 (each grid as 350 pixels) grids (**Figure 5**). The former has 2500 ANN networks that need to be trained, while the latter has 10000. Since the 50 × 50 performed better (see **Table 2**) and is computationally more efficient, the former is selected for this study.

Fuzzy C-Means (FCM) Clustering

Here different results from clustering different sets of parameters obtained from the hydrographs are evaluated using the index $L(c)$ (Tilson et al., 1988). Larger numbers indicate that the selected parameters are more suitable. **Figure 6A** shows the relationship between the index $L(c)$ and the clustering number. The spreads of the 90% confidence intervals of the clusters are listed in **Table 3**. According to **Table 3**, the clustering by four parameters (P, V, $V24$, T) produces the minimum spread, which is the best clustering parameter combination for our studies.

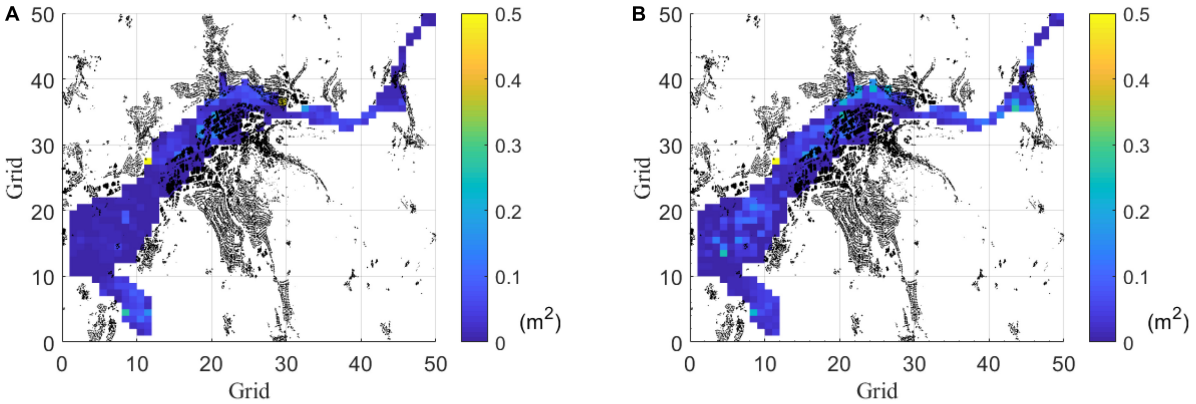

FIGURE 3 | Comparison of average MSE by the two training algorithms in the testing dataset (Event #121 to Event #180). Each grid is an ANN. Black elements are houses. **(A)** Average (among events) MSE by resilient backpropagation (RP). **(B)** Average (among events) MSE by conjugate gradient (CGF).

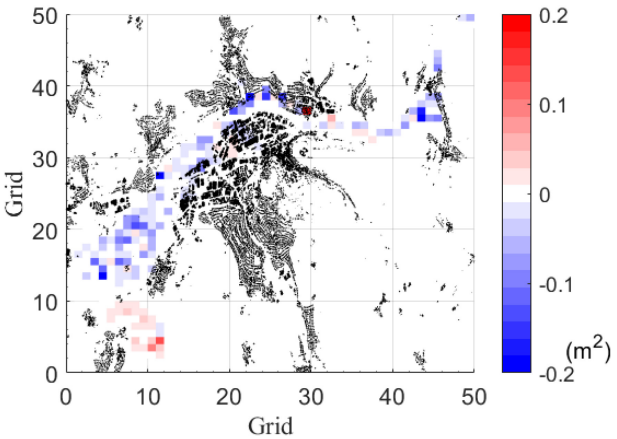

FIGURE 4 | Difference of average MSE by the two training algorithms in the training dataset (Event #1 to Event #120). Each grid is an ANN. Black elements are houses. Negative values indicate that RP performs better than CGF (i.e., smaller MSE). In the plot, 149 grids have positive values and 335 grids have negative values.

TABLE 1 | Number of grids in each combination (number layers and neurons) which outperform all the others.

	Number of Layers				
Number of Neurons	**2**	**3**	**4**	**5**	**6**
10	97	28	7	15	21
15	1	41	10	13	17
20	9	36	8	4	11
25	14	76	19	4	5
30	9	99	29	0	7

Note: highlighted in gray are the combinations tested with a number of optimal grids larger than 70.

Figure 7 also shows that the 90% confidence interval of the four clusters by conventional FCM according to the parameter combination of (P, V, $V24$, T) is the best choice. Besides the conventional FCM, FCM is also quantified based on principal component analysis (PCA-FCM). It is observed that by choosing seven components for clustering we can represent more than 97% of the original data (**Figure 6B**). The clustering results by PCA-FCM are shown in **Figure 8**. The comparison in **Table 3** shows that PCA-FCM generates smaller integrals of the bandwidth area (i.e., the 90% confidence interval shown in **Figure 8**) than those of the conventional FCM. The integral of the bandwidth area is a measure of the spread of the discharge curves in each cluster. An efficient clustering strategy will have a small spread. As such the clusters generated by PCA-FCM are applied in this study. **Table 4** summarizes the sign of the differences among the training results from 100 clustered events to those from original unclustered 120 events and a random unclustered 100 events.

Prediction of Maximum Flood Inundation for Synthetic Events

For the sake of representation of results, **Figure 9** shows one example of the comparison of the flood inundation maps of one single event, Event 180. It is visually possible to infer that the flood inundation maps and water depths from the ANN and the ones from the HEC-RAS database are very similar. To study the overall performance across all 60 events in the testing set, the average and standard deviation of MSE of every testing event in the whole area is evaluated. In **Figure 3A**, most of the area is displayed blue, showing that the MSE is close to 0.1 m^2. Overall, only 1.21% (seven out of 580) of total grids have their MSE over 0.2 m^2.

Prediction of Maximum Flood Inundation for Historical Events

The historical discharges from the historical events are taken from Bavarian Hydrological Services (Bhola et al., 2018). From the historical events, two representative events are selected to validate the ANN. The February 2005 is an example of an advective precipitation with lower peaks and longer duration, with an intensity of 2–3 mm/h. The May 2013 is an example of a convective

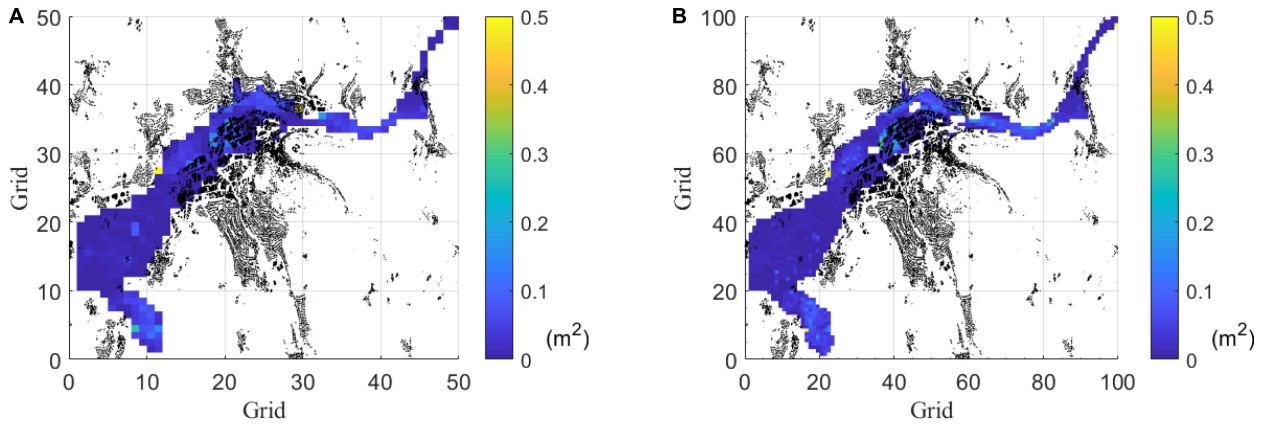

FIGURE 5 | Comparison of average MSE by two grid-size (numbers of ANNs) in the testing dataset (Event 121 to Event #180). Black elements are houses. **(A)** Average (among events) MSE in 50 × 50 grids by RP. **(B)** Average (among events) MSE in 100 × 100 grids by RP.

TABLE 2 | The impact of grid size on the ANN training.

Grid size	Wet grid	Average MSE > 0.1	Percentage of Average MSE > 0.1
50 × 50	485	19	3.92%
100 × 100	1679	82	4.88%

Wet grid = number of grids which have water; Average MSE > 0.1 = number of grids with average MSE larger than 0.1.

precipitation with higher peaks and shorter duration, with an intensity of 5–60 mm/h.

Figures 10, **11** show the MSE obtained for the prediction of the historical event in February2005 and May 2013. In **Figure 10**, the large MSE occurs mainly in the ponding area to the southwest. **Figure 11** shows larger MSE in the southwest than that in February 2005.

DISCUSSION

Training Algorithm

In this section, the two training algorithms, resilient backpropagation and conjugate gradient are discussed. **Figures 3**, **4** support that both algorithms do not show overfitting. Indeed, similar MSE over the training dataset and the testing dataset are observed. However, we still observe a few grids, whose MSE has higher values, suggesting that increasing the size of the training datasets could further improve the performance. **Figure 4** shows that the resilient backpropagation has a lower standard deviation of the MSE for the testing dataset compared to that of the conjugate gradient. As such resilient backpropagation is selected for as training algorithm. This is in line with other researchers which also described resilient backpropagation as efficient with forward-feed neural networks (Bustami et al., 2007; Chibueze and Nonyelum, 2009).

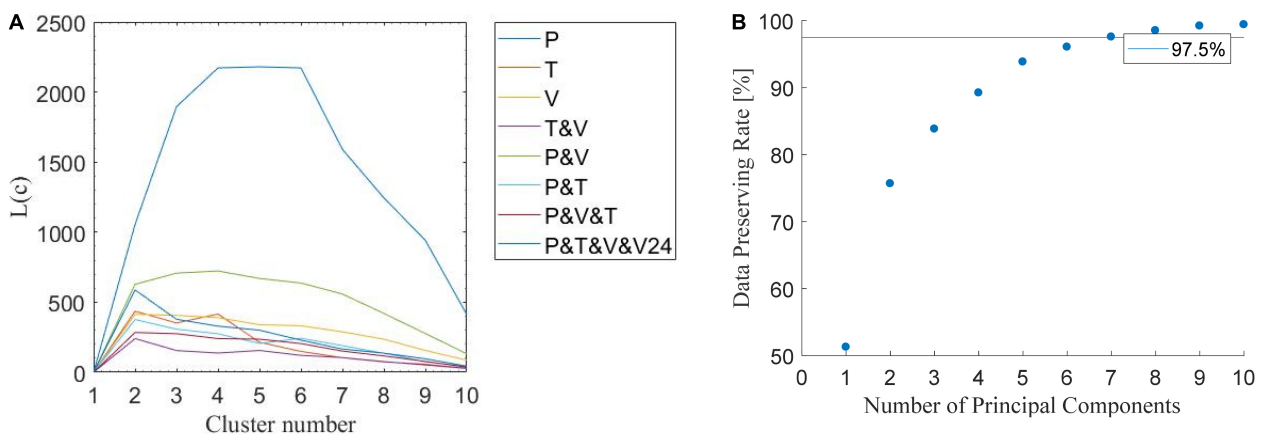

FIGURE 6 | Determine cluster numbers and numbers of principal components. **(A)** Conventional FCM criteria and their corresponding L(c) values: P (peak discharge value), T (peak time), V (total volume), and V24 (volume in the first 24 h). **(B)** Data preserving rate in relation to the numbers of principal components. A minimum data-preserving rate of 97.5% was selected as a good representation of the training database.

TABLE 3 | Integral of the bandwidth (90% confidence interval shown in **Figure 9**) by conventional FCM and PCA-FCM assuming a cluster number equal to 4.

Clustering Parameters	Red Main	Upper Schorgast	Dobrach	White Main	Kinzelsbach	Kohlenbach	Mühlbach
P	20,886	11,916	327	14,275	327	327	656
T	19,808	10,954	277	12,624	277	277	551
V	18,298	10,056	229	11,337	229	229	457
P, V	20,208	10,799	285	12,744	285	285	569
T, V	19,358	10,844	275	12,433	275	275	550
P, T	18,826	10,447	283	12,353	283	283	565
P, V, T	17,964	9494	271	11,452	271	271	539
P, V, V_{24}, T	17,844	9405	244	11,030	244	244	489
PCA	17,311	9799	221	11,378	221	221	443

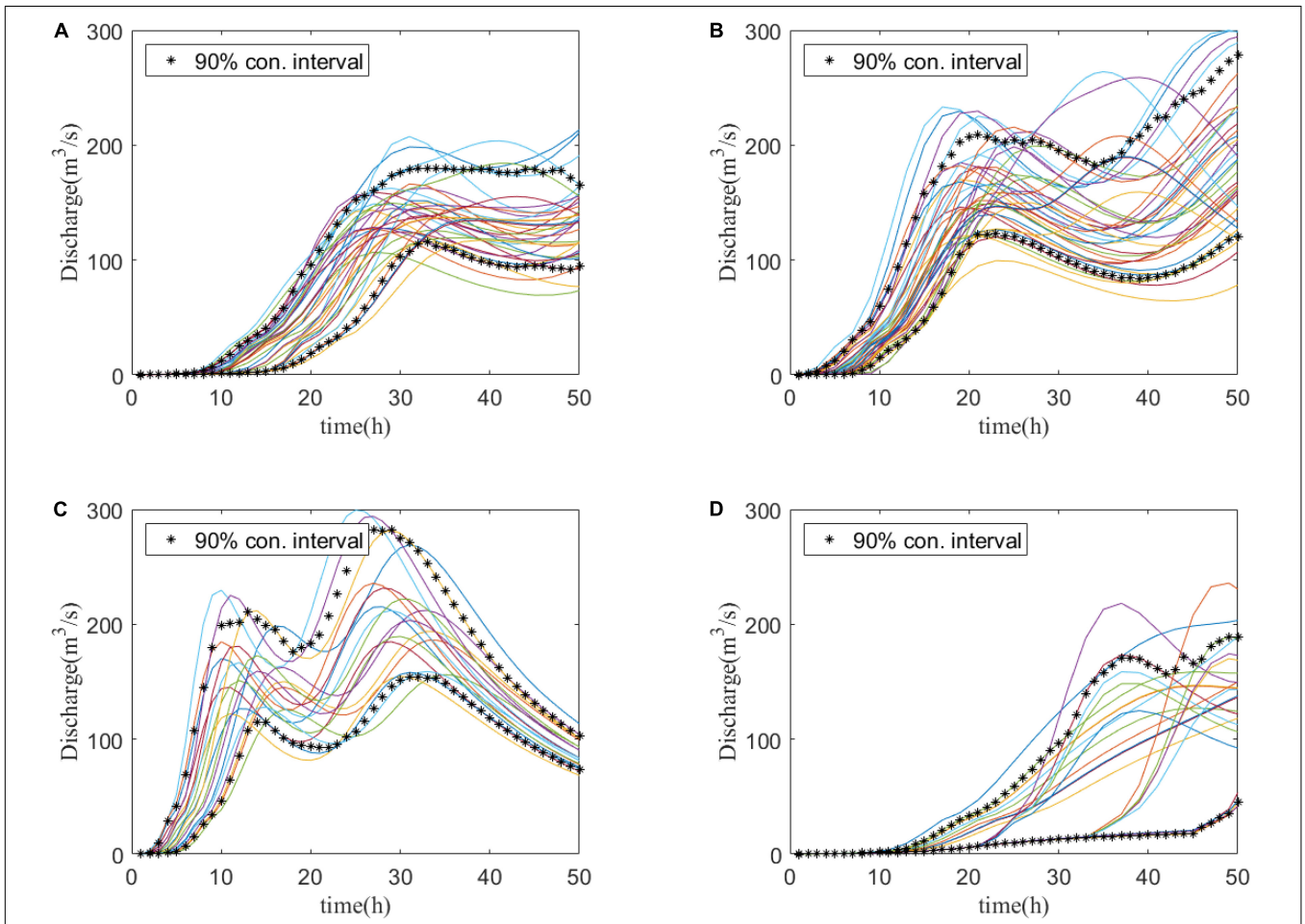

FIGURE 7 | Clustering of all the discharge curves in the training dataset of Stream Red Main (biggest inflow) grouped into four clusters by conventional FCM. Each curve represents a single event. **(A–D)** The curves are clustered into the above four clusters. The clustering is based on the combination of P (peak discharge value), T (peak time), V (total volume), and V24 (volume in the first 24 h). Asterisks represent the 90% confidence intervals of the four clusters **(A–D)**.

Number of Hidden Layers and Neurons

The number of hidden layers and the number of neurons have a decisive impact on the effectiveness of the neural network (Xu and Chen, 2008). Due to their critical importance, different combinations of hidden layer numbers and neuron numbers were tested for finding an optimal combination. The number of layers of two, three, four, five and six, as well as the number of neurons of 10, 15, 20, 25, and 30 were tested, amounting to a total number of combinations tested of 25. In **Table 1**, a grid is "optimal," once the error function reaches the minimum. From the results, it is possible to conclude that the majority of grids (70%) behave better with two or three hidden layers. There is, however, no general trend observed between the number of neurons and the number of hidden layers. The "optimal"

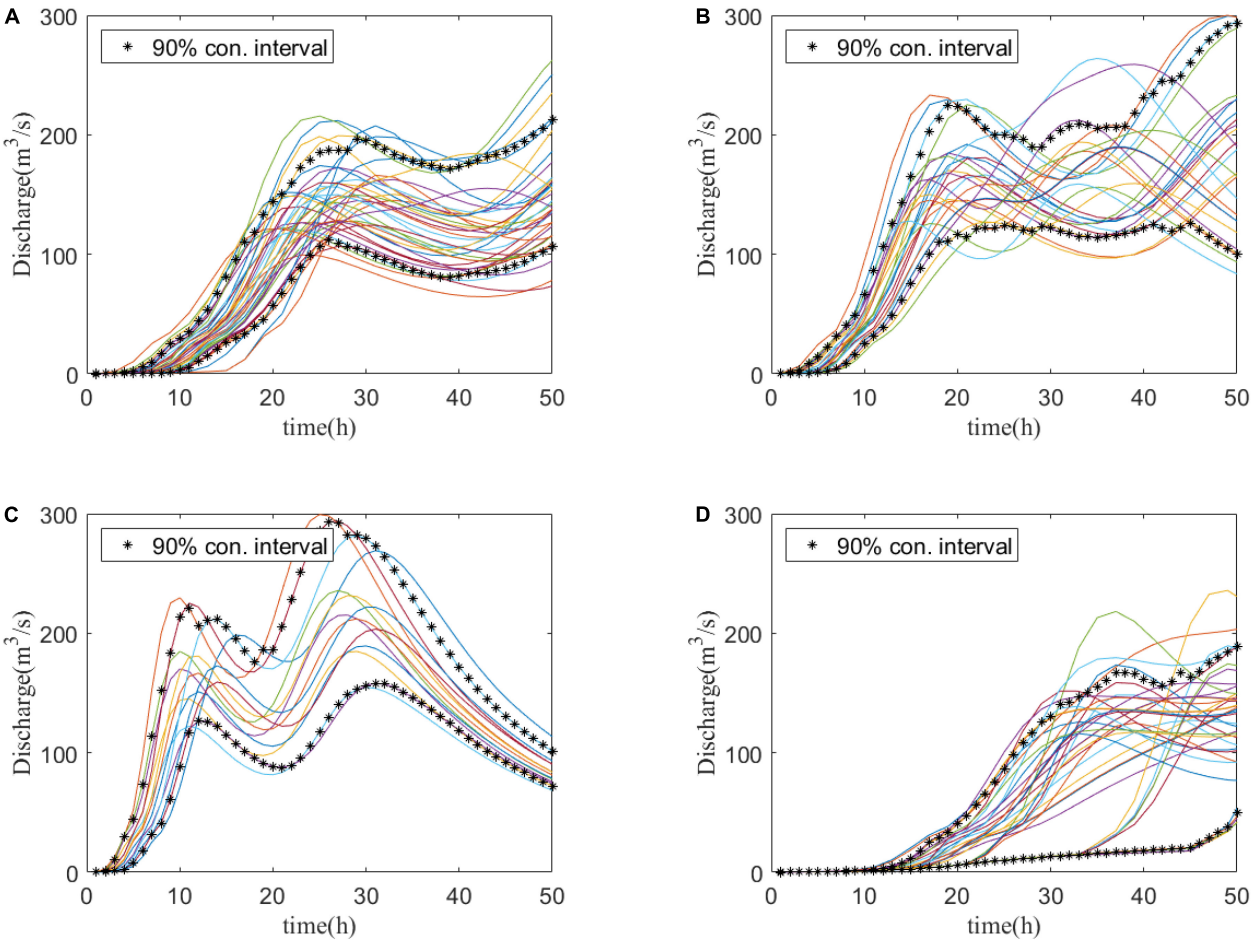

FIGURE 8 | Clustering of all the discharge curves in training dataset of Stream Red Main (biggest inflow) into four clusters by PCA-FCM. Each curve represents a single event. **(A–D)** The curves are clustered into the above four clusters. Asterisks represent the 90% confidence intervals of the four clusters **(A–D)**.

occurs over all the combinations of the number of hidden layers and the number of neurons. When the layer number takes four, five, or six, it is possible to find a widespread "optimal" number of neurons. For the majority cases (70%, where the layer number takes 2 or 3), it is seen that the network with fewer neurons behaves better with only two hidden layers, though the network with more neurons behaves better with three hidden layers. Overall, the complex dependency between hidden layers and neurons reflects the complexity in the input training datasets. In our study, we used two hidden layers with 10 neurons per layer.

Grid Resolution

The results show the capability of the ANN to perform predictions with small MSE (**Figure 5**). Concerning the processing time, the 100 × 100 (finer grids) takes 2 h more only for the initialization of the network. Furthermore, the 100 × 100 grid tends to have a larger MSE during the testing phases, which indicates more overfitting than the solution with 50 × 50. On the other hand, it is obvious that a decrease in the number of grids produces less precise results. Therefore, giving more weight to the training efficiency with less overfitting, it was decided to proceed with the 50 × 50 grid in our study.

TABLE 4 | Sign of MSE difference between PCA-FCM clustered 100 events, original 120 events, and the randomly clustered 100 events.

50 h-Prediction	Number of grids	
Avg.MSE RP100C-Avg.MSE RP120	Positive	Negative
	231	253
Avg.MSE RP100C-Avg.MSE RP100	Positive	Negative
	188	296

All of them use resilient backpropagation for training.

Fuzzy C-Means (FCM) Clustering

In the conventional FCM by hydrograph characteristic parameter the parameters of P (peak value), T (peak time), V (total volume) and $V24$ (volume in the first 24 h), and their combinations were tested. **Figure 6A** and **Table 3** show that the full combination of all four parameters creates the most compact clusters evaluated by the performance index. In the second approach PCA-FCM,

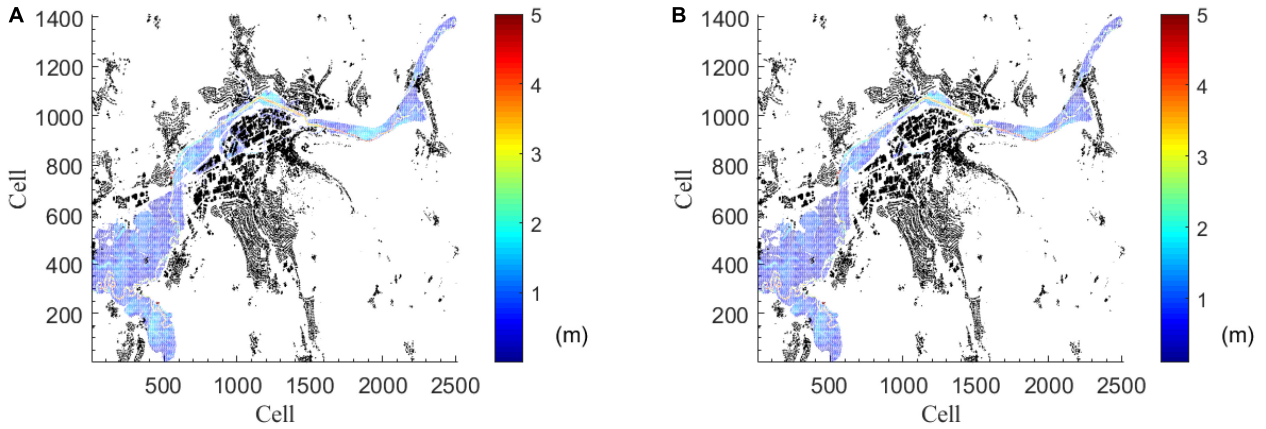

FIGURE 9 | Example of flood inundation prediction in testing dataset (Event #180). Black parts are houses. **(A)** Inundation prediction from ANN model. **(B)** Inundation prediction from the database.

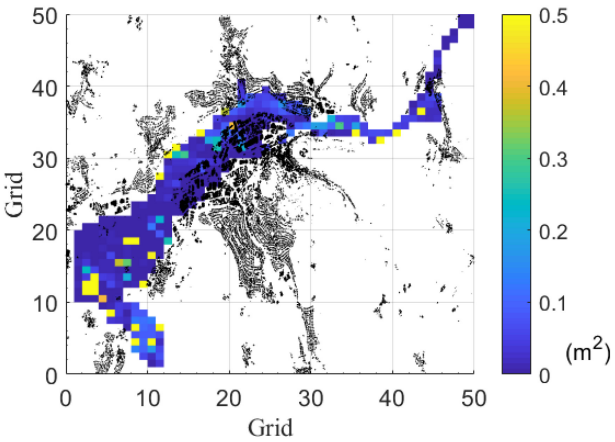

FIGURE 10 | Average MSE difference between the ANN and the hydrodynamic model of the historical event in February 2005. Black elements are houses. Comparison of average MSE to observed inundation depth (historical event in February 2005). Each grid is an ANN.

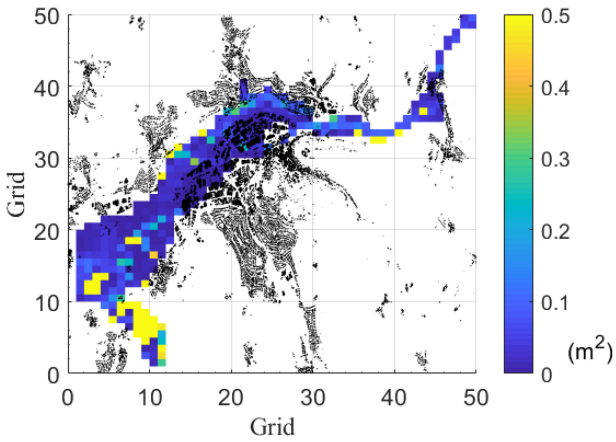

FIGURE 11 | Average MSE difference between the ANN and the hydrodynamic model of the historical event in May 2013. Black parts are houses. Each grid is an ANN.

we conducted PCA over the discharge curves (50 dimensions), to reduce their dimension to the first 10 orthogonal eigenvectors. Projected to the first seven eigenvectors, the data have a preserving-rate of 97% (**Figure 6B**). Therefore, in our research, we choose the first seven principal components for clustering into four groups. Comparing to conventional FCM, we observe five out of seven streams have smaller clustering spread (except Upper Schorgast and White Main), while the rest two are only slightly larger.

It is important to verify that the clustering strategy is efficient. Therefore, we compare it with three other strategies using the MSE: (a) the original training dataset, consisting of the original 120 events in the training dataset from the synthetic database (RP120) (b) randomly select the 100 events from the 120 events (RP100), and (c) randomly select 100 events from the four clusters (RP100C). The results show that the RP100C behaves slightly better than RP120, which means that we can achieve similar good predictions even when with a clustered dataset with a smaller size. The RP100C behaves much better than RP100; this shows that, with the same training database, clustered individuals perform better than random individuals.

Prediction of Maximum Flood Inundation for Synthetic Events

Validation of the results in the synthetic events using the whole testing datasets is shown in **Figure 9**. The majority of the predictions are accurate with MSE around 0.1 m^2. In any case, there are still more than 1.21% of grids with MSE larger than 0.2 m^2. Since the terrain elevation is relatively flat (city center) the impact of a highly variable terrain in the ANN predictions is reduced. This could also add to the good agreement found in our results. In any case, the results show clearly that the ANN prediction is bounded by

the local topography, displaying a very similar inundation extent as the hydraulic model. Despite that, larger error can occur in the water depths particularly in the southwest of our study area. This is the farthest away area from all the seven inflows (model inputs). Hence, it could be anticipated that this area would be more difficult to predict by the ANN model.

Prediction of Maximum Flood Inundation for Historical Events

Finally, the developed ANN is tested in two real events, namely in 2005 and 2013. By evaluating the results, the grids with larger MSE than 0.2 m^2 are 8.97% in 2005 and 13.62% in 2013, which shows that for the real events, our ANN provides an accurate prediction on water depth for more than 85% grids. In both of the synthetic events, we observed that the large MSE part occurs in the southwest of the study area (see **Figures 10**, **11**). This is again a similar behavior also found during the testing phase (**Figure 3**) which can be expected since it is the area further away from the major inflows (see **Figure 2**). As the distance to the inflows (model inputs) increases, the growing uncertainty causes the water depths prediction to deviate from the observed data. It should be noted that the inundation extent is always well predicted. As in the results for the synthetic events, the ANN is able to accommodate the flooded volume within very similar topographic limits as the hydraulic model.

CONCLUSION

This study focuses on using artificial neural networks trained with synthetic events to replace the 2D hydraulic model for flood prediction. A forward-feed network structure was applied and set up with a training dataset with 120 synthetic events and a testing dataset of 60 events.

Two popular algorithms were compared, namely resilient backpropagation and conjugate gradient, with their MSE in the whole domain evaluated. Resilient backpropagation performed better than the conjugate gradient with a smaller MSE on average. An investigation of the number of hidden layers and the number of neurons per layer set this to 2 and 10, respectively. Complex dependencies from the interaction of these two parameters were observed. It was not possible to find a clear trend over all the ANN with a simple set of network layers and neurons. It was nevertheless noticed that 70% of our networks performed better, once two or three hidden layers have been used. This indicates that the prediction of flood inundation extents by inflow hydrographs is more likely to be precise at a low hidden layer number. The impact of the network size 50 × 50 and 100 × 100 over the studied area was also investigated. Both settings produced small errors. However, the 50 × 50 grids have slightly smaller MSE with much less model tuning time, hence chosen in this study.

Conventional FCM and PCA-FCM were investigated in this study. Both clustering methods capture the characteristics in each cluster (by the trend of curves and of confidence intervals). By checking the 90% confidence interval over all the clusters, we could infer that the cluster spread of PCA-FCM was smaller than the spread with the conventional FCM clustering. Hence, the former was preferred. The MSE difference map of the clustering strategy showed that this strategy is efficient in reducing the size of the training set. Thus, clustering is helpful as the preprocessing of the training dataset. With the clustered data, the network could cover a wider range of inputs and avoid overfitting by similar training data. Overall, in our case study, clustering enhanced the performance of the ANN training by reducing the size of the training set and slightly improved the prediction of maximum flood inundation.

The prediction results on the testing dataset are very good. The prediction of maximum flood inundation shows no visible difference from the synthetic events in terms of flood extent and water depth. By comparing the MSE, only 1.21% of the wet grids have values larger than 0.2 m^2, suggesting that the prediction is successful over 98% ANN. Tests on real events showed that the prediction results of the flood inundation are still very good but with some localize disagreements in the maximum water depths. Overall the prediction by grids, 91.03% in 2005 and 86.38% in 2013 events were good, for which the MSE was smaller than 0.2 m^2. It was also seen that the model prediction quality decreased as the area of the forecast was further away from the inputs.

Finally, this work proved that resilient backpropagation networks can be used for replacing the 2D hydraulic model for prediction of flood inundation, requiring only the discharge inflows as inputs.

DATA AVAILABILITY STATEMENT

The datasets generated for this study are available on request to the corresponding author.

AUTHOR CONTRIBUTIONS

QL and WW set up the prediction model in this work. PB provided the database for validation. WW validated the model. QL wrote the first version of the manuscript. JL and MD proofread the manuscript and improved it. All authors contributed to manuscript revision, read and approved the submitted version.

FUNDING

The research presented in this manuscript has been carried out as part of the HiOS project (Hinweiskarte Oberflächenabfluss und Sturzflut) funded by the Bavarian State Ministry of the Environment and Consumer Protection (StMUV) and supervised by the Bavarian Environment Agency (LfU).

REFERENCES

Abbot, J., and Marohasy, J. (2015). Improving monthly rainfall forecasts using artificial neural networks and single-month optimisation:a case study of the Brisbane catchment, Queensland, Australia. *Water Resour. Manag. VIII* 1, 3–13. doi: 10.2495/wrm150011

Berkhahn, S., Fuchs, L., and Neuweiler, I. (2019). An ensemble neural network model for real-time prediction of urban floods. *J. Hydrol.* 575, 743–754. doi: 10.1016/j.jhydrol.2019.05.066

Bermúdez, M., Cea, L., and Puertas, J. (2019). A rapid flood inundation model for hazard mapping based on least squares support vector machine regression. *J. Flood Risk Manag.* 12, 1–14. doi: 10.1111/jfr3.12522

Berz, G. (2001). Flood disasters: lessons from the past-worries for the future. *Water Manag.* 148, 57–58. doi: 10.1680/wama.148.1.57.40366

Bhola, P. K., Leandro, J., and Disse, M. (2018). Framework for offline flood inundation forecasts for two-dimensional hydrodynamic models. *Geosci* 8:346. doi: 10.3390/geosciences8090346

Bhola, P. K., Nair, B. B., Leandro, J., Rao, S. N., and Disse, M. (2019). Flood inundation forecasts using validation data generated with the assistance of computer vision. *J. Hydroinformatics* 21, 240–256. doi: 10.2166/hydro.2018.044

Bustami, R., Bessaih, N., Bong, C., and Suhaili, S. (2007). Artificial neural network for precipitation and water level predictions of bedup river. *IAENG Int. J. Comput. Sci.* 34, 228–233.

Chang, L. C., Amin, M. Z. M., Yang, S. N., and Chang, F. J. (2018). Building ANN-based regional multi-step-ahead flood inundation forecast models. *Water (Switzerland)* 10, 1–18. doi: 10.3390/W10091283

Chang, M. J., Chang, H. K., Chen, Y. C., Lin, G. F., Chen, P. A., Lai, J. S., et al. (2018). A support vector machine forecasting model for typhoon flood inundation mapping and early flood warning systems. *Water (Switzerland)* 10:734. doi: 10.3390/w10121734

Chibueze, T., and Nonyelum, F. (2009). Feed-forward neural networks for precipitation and river level prediction. *Adv. Nat. Appl. Sci* 3, 350–356.

Chu, H., Wu, W., Wang, Q. J., Nathan, R., and Wei, J. (2020). An ANN-based emulation modelling framework for flood inundation modelling: application, challenges and future directions. *Environ. Model. Softw.* 124:104587. doi: 10.1016/j.envsoft.2019.104587

Coulibaly, P., Anctil, F., and Bobée, B. (2000). Daily reservoir inflow forecasting using artificial neural networks with stopped training approach. *J. Hydrol.* 230, 244–257. doi: 10.1016/S0022-1694(00)00214-6

Dawson, C. W., and Wilby, R. L. (2001). Hydrological modelling using artificial neural networks. *Prog. Phys. Geogr.* 25, 80–108. doi: 10.1177/030913330102500104

Dineva, A., Várkonyi-Kóczy, A. R., and Tar, J. K. (2014). "Fuzzy expert system for automatic wavelet shrinkage procedure selection for noise suppression," in *Proceedings of the 2014 18th International Conference on Intelligent Engineering Systems*, Tihany, 163–168. doi: 10.1109/INES.2014.6909361

Disse, M., Konnerth, I., Bhola, P. K., and Leandro, J. (2018). "Unsicherheitsabschätzung für die berechnung von dynamischen überschwemmungskarten – fallstudie kulmbach," in *Vorsorgender und Nachsorgender Hochwasserschutz: Ausgewählte Beiträge aus der Fachzeitschrift WasserWirtschaft Band 2*, ed. S. Heimerl (Wiesbaden: Springer Fachmedien Wiesbaden), 350–357. doi: 10.1007/978-3-658-21839-3_50

Elsafi, S. H. (2014). Artificial neural networks (anns) for flood forecasting at dongola station in the river nile, sudan. *Alexandria Eng. J.* 53, 655–662. doi: 10.1016/j.aej.2014.06.010

Gizaw, M. S., and Gan, T. Y. (2016). Regional flood frequency analysis using support vector regression under historical and future climate. *J. Hydrol.* 538, 387–398. doi: 10.1016/j.jhydrol.2016.04.041

Hankin, B., Waller, S., Astle, G., and Kellagher, R. (2008). Mapping space for water: screening for urban flash flooding. *J. Flood Risk Manag.* 1, 13–22. doi: 10.1111/j.1753-318x.2008.00003.x

Henonin, J., Russo, B., Mark, O., and Gourbesville, P. (2013). Real-time urban flood forecasting and modelling–A state of the art. *J. Hydroinformatics* 15, 717–736. doi: 10.2166/hydro.2013.132

Humphrey, G. B., Gibbs, M. S., Dandy, G. C., and Maier, H. R. (2016). A hybrid approach to monthly streamflow forecasting: Integrating hydrological model outputs into a Bayesian artificial neural network. *J. Hydrol.* 540, 623–640. doi: 10.1016/j.jhydrol.2016.06.026

Kalyanapu, A. J., Shankar, S., Pardyjak, E. R., Judi, D. R., and Burian, S. J. (2011). Assessment of GPU computational enhancement to a 2D flood model. *Environ. Model. Softw.* 26, 1009–1016. doi: 10.1016/j.envsoft.2011.02.014

Kasiviswanathan, K. S., He, J., Sudheer, K. P., and Tay, J. H. (2016). Potential application of wavelet neural network ensemble to forecast streamflow for flood management. *J. Hydrol.* 536, 161–173. doi: 10.1016/j.jhydrol.2016.02.044

Kron, W. (2005). Flood risk = hazard values vulnerability. *Water Int.* 30, 58–68. doi: 10.1080/02508060508691837

Ludwig, K., and Bremicker, M (eds). (2006). *The Water Balance Model LARSIM: Design, Content and Applications*. Germany: Institut für Hydrologie Universität Freiburg.

Mark, O., Weesakul, S., Apirumanekul, C., Aroonnet, S. B., and Djordjeviæ, S. (2004). Potential and limitations of 1D modelling of urban flooding. *J. Hydrol.* 299, 284–299. doi: 10.1016/j.jhydrol.2004.08.014

Marquardt, D. W. (1963). An algorithm for least-squares estimation of nonlinear parameters. *J. Soc. Indust. Appl. Math.* 11, 431–441. doi: 10.1017/CBO9781107415324.004

Mekanik, F., Imteaz, M. A., Gato-Trinidad, S., and Elmahdi, A. (2013). Multiple regression and artificial neural network for long-term rainfall forecasting using large scale climate modes. *J. Hydrol.* 503, 11–21. doi: 10.1016/j.jhydrol.2013.08.035

Mosavi, A., Ozturk, P., and Chau, K. W. (2018). Flood prediction using machine learning models: literature review. *Water (Switzerland)* 10, 1–40. doi: 10.3390/w10111536

Mukerji, A., Chatterjee, C., and Raghuwanshi, N. S. (2009). Flood forecasting using ANN, neuro-fuzzy, and neuro-GA models. *J. Hydrol. Eng.* 14, 647–652. doi: 10.1061/(asce)he.1943-5584.0000040

Nawi, N., Ransing, R., and Ransing, M. (2007). An improved conjugate gradient based learning algorithm for back propagation neural networks. *Int. J. Comput. Intell.* 4, 46–55.

Saini, L. M. (2008). Peak load forecasting using Bayesian regularization, Resilient and adaptive backpropagation learning based artificial neural networks. *Electr. Power Syst. Res.* 78, 1302–1310. doi: 10.1016/j.epsr.2007.11.003

Sit, M., and Demir, I. (2019). Decentralized flood forecasting using deep neural networks. *arXiv*. [Preprint]. arXiv:1902.02308.

Taghi, S. M., Yurekli, K., and Pal, M. (2012). Performance evaluation of artificial neural network approaches in forecasting reservoir inflow. *Appl. Math. Model.* 36, 2649–2657. doi: 10.1016/j.apm.2011.09.048

Taherei, G. P., Darvishi, H. H., Mosavi, A., Bin Wan, Yusof, K., Alizamir, M., et al. (2018). Sugarcane growth prediction based on meteorological parameters using extreme learning machine and artificial neural network. *Eng. Appl. Comput. Fluid Mech.* 12, 738–749. doi: 10.1080/19942060.2018.1526119

Thirumalaiah, D. (1998). River stage forecasting using artificial neural networks. *J. Hydrol. Eng.* 3, 26–32. doi: 10.1061/(asce)1084-0699(1998)3:1(26)

Tilson, L. V., Excell, P. S., and Green, R. J. (1988). A generalisation of the Fuzzy c-Means clustering algorithm. *Remote Sensing* 3, 1783–1784. doi: 10.1109/igarss.1988.569600

Tiwari, M. K., and Chatterjee, C. (2010). Development of an accurate and reliable hourly flood forecasting model using wavelet-bootstrap-ANN (WBANN) hybrid approach. *J. Hydrol.* 394, 458–470. doi: 10.1016/j.jhydrol.2010.10.001

Vogel, R. M., Yaindl, C., and Walter, M. (2011). Nonstationarity: flood magnification and recurrence reduction factors in the united states.

J. Am. Water Resour. Assoc. 47, 464–474. doi: 10.1111/j.1752-1688.2011.00541.x

Xu, S., and Chen, L. (2008). A novel approach for determining the optimal number of hidden layer neurons for FNN's and its application in data mining. *Conf. Inf. Technol. Appl. ICITA* 2008, 683–686.

Yu, P. S., Chen, S. T., and Chang, I. F. (2006). Support vector regression for real-time flood stage forecasting. *J. Hydrol.* 328, 704–716. doi: 10.1016/j.jhydrol.2006.01.021

Zhang, G. P. (2007). Avoiding pitfalls in neural network research. *IEEE Trans. Syst. Man Cybern. Part C Appl. Rev.* 37, 3–16. doi: 10.1109/TSMCC.2006.876059

Conflict of Interest: The authors declare that the research was conducted in the absence of any commercial or financial relationships that could be construed as a potential conflict of interest.

frontiers in Earth Science

CORRECTION
published: 16 July 2021
doi: 10.3389/feart.2021.707556

Corrigendum: Prediction of Maximum Flood Inundation Extents with Resilient Backpropagation Neural Network: Case Study of Kulmbach

Qing Lin, Jorge Leandro, Wenrong Wu, Punit Bhola and Markus Disse*

Department of Civil, Geo and Environmental Engineering, Technical University of Munich, Munich, Germany

Keywords: hazard, maximum inundation extent, artificial neural network, Resilient backpropagation, urban flood forecast

OPEN ACCESS

Edited and reviewed by:
Mingfu Guan,
The University of Hong Kong,
Hong Kong

****Correspondence:***
Qing Lin
tsching.lin@tum.de

Specialty section:
This article was submitted to Hydrosphere, a section of the journal Frontiers in Earth Science

Received: *10 May 2021*
Accepted: *26 May 2021*
Published: *16 July 2021*

Citation:
Lin Q, Leandro J, Wu W, Bhola P and Disse M (2021) Corrigendum: Prediction of Maximum Flood Inundation Extents with Resilient Backpropagation Neural Network: Case Study of Kulmbach. Front. Earth Sci. 9:707556. doi: 10.3389/feart.2021.707556

A Corrigendum on:

Prediction of Maximum Flood Inundation Extents With Resilient Backpropagation Neural Network: Case Study of Kulmbach
by Lin Q, Leandro J, Wu W, Bhola P and Disse M (2020) Prediction of Maximum Flood Inundation Extents With Resilient Backpropagation Neural Network: Case Study of Kulmbach. Front. Earth Sci. 8: 332. doi:10.3389/feart.2020.00332

In the original article, there was a mistake in that **Figures 1–11** and **Tables 1–4** were published as supplementary material. The authors would like to move all figures and tables to the main article and remove the supplementary material to improve readability.

The authors apologize for this error and state that this does not change the scientific conclusions of the article in any way. The original article has been updated.

frontiers in Earth Science

ORIGINAL RESEARCH
published: 13 August 2020
doi: 10.3389/feart.2020.00303

Numerical Simulation of Dam-Break Flood Impacting Buildings by a Volume of Fluid and Immersed Boundary Method

Chinghao Yu[1], *Yulong Li*[2], *Wenkang Meng*[1] *and Ruidong An*[1]*

[1] State Key Laboratory of Hydraulics and Mountain River Engineering, College of Water Resource and Hydropower, Sichuan University, Chengdu, China, [2] School of Marine Engineering and Technology, Sun Yat-sen University, Zhuhai, China

A three-dimensional hydrodynamic model is developed to study the propagation of dam-break-induced flood and the interaction between floods and buildings. In the proposed mathematical model, the volume of fluid (VOF) method and the immersed boundary (IB) method are used to address the air/water interface and fluid/structure interface, respectively. Barely a limited number of publications focus on 3D simulations of the dam-break flood impacting buildings in the long flume heretofore, for researching the dam-break flood impacting buildings involves some hard issues like wave breaking phenomena, flood–building interaction, and computational efficiency. Therefore, the highlights to this paper are as follows: (1) The THINC/SW (THINC with Slope Weighting), which is extremely simple and efficient and meanwhile can also solve the wave breaking process, is adopted in the paper. Furthermore, its numerical accuracy is comparable with the conventional VOF schemes that use geometrical reconstructions. (2) The direct forcing IB method, which can be easily applied to three-dimensional simulation, is adopted to promote the computational efficiency of the three-dimensional numerical model and handle flood–building interaction interface treatment. The proposed VOF/IB model is validated by the physical experiment results and is also compared with the two-dimensional depth-averaged Shallow-Water Equations, and Coupled Level Set/Volume of Fluid and Immersed Boundary models in terms of accuracy and efficiency.

Keywords: three-dimensional hydrodynamic model, volume of fluid method, immersed boundary method, SWEs, CLSVOF

OPEN ACCESS

Edited by:
Mingfu Guan,
The University of Hong Kong,
Hong Kong

Reviewed by:
Guangtao Fu,
University of Exeter, United Kingdom
Xiaoling Wang,
Tianjin University, China

***Correspondence:**
Ruidong An
anruidong@scu.edu.cn

Specialty section:
This article was submitted to Hydrosphere, a section of the journal Frontiers in Earth Science

Received: *31 January 2020*
Accepted: *29 June 2020*
Published: *13 August 2020*

Citation:
Yu C, Li Y, Meng W and An R (2020) Numerical Simulation of Dam-Break Flood Impacting Buildings by a Volume of Fluid and Immersed Boundary Method. Front. Earth Sci. 8:303. doi: 10.3389/feart.2020.00303

INTRODUCTION

Catastrophic consequences such as the losses of human life and properties can occur when severe flood propagate to downstream areas (Schubert and Sanders, 2012). Also, a strong influence can be found on the inundation dynamics and the flood characteristics on account of the buildings in the flooding area. The present research is therefore undertaken to construct an effective and accurate three-dimensional (3D) multi-phase solver to comprehensively understand the fluid/structure interaction and its flow characteristics that arise in dam-break-induced flood events.

These factors, various hydraulic quantities including water depth, velocity field, flood arrival time, and duration of the flood, are of significance to the buildings in flooded areas that need to be figured out. So numerical simulations are considered because of their universality and

practicability, which cannot solely predict force actions on structures located in the flow domain (Aureli et al., 2015) precisely but also tackle irregular topography, and wetting and drying flow with high efficiency. Two-dimensional (2D) Shallow-Water Equations (SWEs) model that considers hydrostatic pressure assumption is supposed to be simple and requires less computational cost to simulate dam-break flow. Thus, the high resolutions of space and time can be sufficiently obtained for real long rivers (Chang et al., 2011). The main concerns regarding numerical challenges of modeling dam-break flow by 2D shallow water equations include the treatment of the propagation of free-surface discontinuities and the resolution of rapidly varying open channel flows interacting with the building. A reliable numerical scheme must have the ability to suppress numerical instability which is particularly severe when transient flows with steep gradients over bumpy dry beds or free-surface discontinuities occur. One way to resolve this difficulty is to apply the Godunov scheme (Savic and Holly, 1993), high-resolution non-oscillatory scheme (Sanders, 2001), Riemann Solvers (Guinot et al., 2009), and total variation diminishing (TVD) scheme (Ying et al., 2004; Liang et al., 2006). While a construction is conducted by the simulation of rapidly varying open channel flows in the buildings or topographical singularities with the 2D SWEs, it is usually categorized as a rigid block with impervious walls or equivalently as a hole in the computational domain (Schubert and Sanders, 2012). Otherwise, the concept of porosity of a built-up area is required (Sanders et al., 2008; Soares-Frazao et al., 2008) to obtain an acceptable level of accuracy for the prediction of the effects of buildings on flood propagation. The weaknesses of the shallow water models are no density or velocity variations in the vertical direction, and, meanwhile, are inadequate to simulate flows involving significant variations of flow depth and wave breaking because 2D shallow water models originate from depth-integrating the 3D continuity and momentum equations. Moreover, they assume that the viscous force is negligible and the vertical acceleration is small, so the pressure field is purely hydrostatic. In other words, the depth-averaged approach cannot be used to simulate flows with significant variations in the vertical direction and the 3D is locally obvious in this phenomenon, which demonstrates strong curvatures of the free surface with non-hydrostatic distribution of pressure along the vertical direction. The alternative to the numerical method is to numerically solve the 3D Navier–Stokes equations for simulating dam-break flow impacting buildings.

The computational method for 3D dam-breaking floods with complex bodies can be generally divided into three categories: the moving grid approach, the fixed grid approach, and meshless approach. In the moving grid methods, body-fitted grids are attached to the solid surfaces or even the interfaces between two different fluids, whereas the overall grids can be unstructured or overlapping grids, which were normally applied to free-surface flows with a single stationary structure. Great progress has been made in moving grid methods. However, it is still time consuming and prone to errors during the process of the grid deformation, re-generation, and overlapping interpolation. A considerable number of studies on this approach for 3D dam-break problem have been done (Hou et al., 2013; Guo et al., 2018; Fourtakas et al., 2019) during the development of a meshless approach (e.g., smoothed particle hydrodynamics, SPH). The basic idea of the SPH method is to describe continuous fluids (or solids) in groups of interacting particles, and each of them can carry various physical quantities (such as mass and velocity), and the mechanical behavior of the whole system can be obtained by solving the kinetic equation and tracing the motion orbit of each particle. The robust numerical simulation of dam-break flow applications depends on the performance of the boundary conditions employed within the SPH model. In the SPH method (Fourtakas et al., 2019) proposed by Fourtakas et al., hence, the new solid boundary formulation adopts a local uniform stencil (LUST) of fictitious particles that surround and move with each fluid particle and are only activated when they are located inside a boundary. The simulation of dam-break flow is achieved by incompressible SPH (Guo et al., 2018) with the advent of high-speed computers. For a comprehensive literature review, see the research work for SPH of Hou et al. (2013) and Cao et al. (2017). SPH, within the entire calculation process, is able to enhance the conservative property without advection errors. Nevertheless, high demand for computational cost is needed and the modeling of boundary conditions is still challenging. Moreover, the SPH method is unstable when tracking interfaces with large deformations.

The VOF/IB method belongs to fixed grid approach. Solid boundaries and phase interfaces can have unrestricted motions across the underlying fixed grid lines, which are usually not aligned with the solid–fluid and/or the fluid–fluid interfaces. Also, in most cases, Cartesian grids, which further simplify the gridding requirements, are used to cover the whole computational domain. In other words, a fixed grid approach has become feasible and is greatly important to simulate 3D dam-break flow problems. For example, 3D Reynolds-averaged Navier–Stokes model, a non-hydrostatic pressure assumption, is developed to complete the simulation of dam-break flow. This model is used to capture the free surface with the volume of fluid (VOF) approach. Kurioka and Dowling present a level set (LS) method which combines with high-order Weighted Essentially Non-Oscillatory scheme to capture free surface evolution for dam-break flows (Kurioka and Dowling, 2009). It is developed as an unstructured-mesh finite element 3D model for simulating dam-break floods through several cases, whose advantage is that the vertical inertia is considered in its 3D model (Zhang et al., 2018). A macroscopic model for describing the interaction between dam-break waves and porous media is presented in Hu et al. (2012). The two-phase model, which uses the LS method with second-order accuracy, is evolved to simulate dam-break flow with the consideration of the total pressure or hydrostatic pressure assumption in Navier–Stokes solutions (Monteiro et al., 2019). From above, the fluid–fluid interface is usually treated in literature utilizing interface capturing methods, such as the VOF (Hirt and Nichols, 1981; Zeng et al., 2010; Wang et al., 2012) and the LS method (Osher and Sethian, 1988; Gu et al., 2018a,b). Both can tackle topology changes or the phases between air and water on account of solving advection equations that use a color function. Furthermore, air entrainment effects and wave breaking phenomena can also be predicted accurately, so the employment of the interface capturing method is advisable.

When the free surface is tracked by the LS method, the mass conservation will rapidly deteriorate as time goes by. This loss of mass problem arises from the use of a lower-order spatial discretization scheme to approximate the highly oscillatory and the dissipation character of the propagating solutions. A mass conservation method, proposed by Olsson et al. (2007), is named as the conservative Level Set (CLS) method. On account of the intrinsic shortage of the Heaviside function, the normals and curvatures of interfaces are sensitive to small spurious oscillations, though the mass conservation property of the advection step can be ensured for the CLS method. To address this issue, an improved CLS method is proposed (Bahbah et al., 2019) for the 3D simulations of the axisymmetric and non-axisymmetric merging of two bubbles. Coupled Level Set and Volume of Fluid (CLSVOF) methods are noteworthy for their ability to overcome mass loss and meanwhile present strong curvatures of the free surface (Sun and Tao, 2010; Wang et al., 2013; Gu et al., 2019; Li and Yu, 2019).

Regarding the simulation of dam-break flow impacting buildings (or fluid–structure interaction), the treatment of fluid–structure interfaces is crucial (Yang and Stern, 2009). The immersed boundary (IB) method, which is advisable to do with problems with irregular solid objects and is not necessarily supposed to conform to Cartesian grids, can be adopted (Yang and Stern, 2009) to simulate fluid–structure interface problems. Namely, the boundary condition is enforced at the immersed boundary as long as an immersed boundary is identified, which is trivial for a body-fitted grid method as the grid lines are made to follow the phase interface. Based on the pioneering work by interface capturing/immersed boundary methods of Zhang et al. (2010), Zhang et al. (2014), and Li (2016), Yu et al. (2019) proposed a Coupled Level Set and Volume of Fluid and an Immersed Boundary (CLSVOF/IB) method for the 3D Navier–Stokes equation to resolve dam-break flow impacting a stationary obstacle problem. In comparison with the 2D shallow equations, the 3D model requires more computational cost and therefore is not the main framework of the dam-break flow computation in the urban area.

Only a limited number of publications focus on 3D simulations of the dam-break flood impacting buildings in the long flume heretofore. The objectives to this paper are (1) to improve the efficiency of the three-dimensional numerical model in Yu et al. (2019) based on VOF and IB methods to, respectively, solve the interface problems of fluid/fluid and fluid/solid, and to address the problem of excessive calculation time in Yu et al. (2019). Moreover, the model can accurately estimate the front location of the dam break and the depth of the downstream water, and reproduce the wave breaking phenomena in the long straight water channel. (2) To compare the result of 2D shallow water and 3D modeling the unsteady multi-phase flow with the outcome of the experiment by Soares-Frazão and Zech (2008) from the University of Leuven. The offered hydraulic quantities forming the experiment are used for model validation in terms of efficiency and accuracy.

This paper is organized as follows: section Mathematical Model presents the 2D shallow water equations, 3D Navier–Stokes equations, and the developed VOF/IB solution algorithm; section Numerical Results and Discussion presents numerical results as the standard practice, and we validate the code against the test case, which is amenable to experiments (Soares-Frazao et al., 2008); concluding remarks are given in section Concluding Remarks.

MATHEMATICAL MODEL

To calculate flood propagation, two mathematical models, depth-averaged water model and depth-resolving simulation model, are useful. Flood whose length is substantially larger than its depth can frequently be approximated by depth-averaged water models. Song et al. (2011) introduced this approach for shallow water flows and later extended to shallow water flows that adopt unstructured grids (Meneveau and Katz, 2000). Various modeling approaches for dam breaking have evolved, spanning the entire range from dimensional analysis to high-resolution DNS, owing to this multitude of, to some extent, relevant flow regimes. Besides VOF-IB method (depth-resolving simulation model), the paper has proposed a way to deal with flooding through buildings with depth-averaged water model (see section Two-Dimensional Depth-Averaged Shallow-Water Equations (SWEs) Model) and compared their accuracy as well. Indeed, the Large-Eddy Simulation (LES), a turbulence model, belongs to depth-resolving simulation model, which can show the turbulent process. In addition, fewer computational resources are required than direct numerical simulations (DNSs) because LES, instead of modeling all of the scales of motion below a cutoff, resolve merely the energy-containing large eddies. This approach often results in the majority of the dissipative scales being modeled (Meneveau and Katz, 2000). The cutoff is determined by a filter width that depends on the grid spacing employed in the LES. DNS represents the most accurate computational approach for studying dam-break flood despite its need for more computational resources. In DNS, all scales of motion are explicitly resolved even which are from the integral scales dictated by the boundary conditions down to the dissipative Kolmogorov scale determined by viscosity are explicitly resolved. Hence, the N-S equation described in this paper is still referred to as DNS.

Depth-Resolving Simulation Model

The paper presents the VOF/IB method in the sequence of solving the VOF equation (Equation 1) at first and then the momentum equation (Equation 4). The step of introducing the CLSVOF/IB method first needs to work out the VOF equation (Equation 1) and then the LS equation $\frac{\partial \phi}{\partial t} + \mathbf{u} \cdot \nabla \phi = 0$ and the momentum equation (Equation 4).

Volume of Fluid (VOF) Method

In the VOF method, the interface is regarded as the cell-wise geometrical reconstruction that can separate the two distinct fluids (e.g., air and water) in the cell. The volume fraction C occupied by the water within each cell with a value between 0 and 1 is advected by the following transport equation under a velocity field u:

$$\frac{\partial C}{\partial t} + \nabla \cdot (\boldsymbol{u}C) - C\nabla \cdot \boldsymbol{u} = 0 \quad (1)$$

It is notable that the geometrical reconstruction procedure that computes the numerical fluxes can be performed through the simple line interface calculation (Noh and Woodward, 1976), piecewise linear interface calculation (Harvie and Fletcher, 2000, 2001), or weighted line interface calculation (Yokoi, 2007) reconstruction. Still, it usually prevents them from being immediately adopted by the users that a geometrical reconstruction makes the computer coding complex and be filled with "if" logic operations. One way of circumventing this geometrical reconstruction procedure is to use the so-called THINC (Tangent of Hyperbola for INterface Capturing) (Xiao et al., 2005) to compute moving interfaces, thus the needed geometrical reconstruction procedures being avoided. With the utilization of the hyperbolic tangent function, the THINC can compute the numerical flux for the fluid fraction function, and also present a solution, which is conservative, oscillation-less, and smearing-less, to the fluid fraction function even for the extremely distorted interfaces of arbitrary complexity. Yet for all that, the interface will be ruffled when flow direction parallels the interface. How to use a scheme to result in a simpler and more accurate algorithm becomes the main subject of the present study. Based on the attractive feature of the 1D THINC building block, the THINC with Slope Weighting (THINC/SW) (Xiao et al., 2011) is adopted by this paper. Our goal of solving the VOF transport equation is to obtain solutions with higher accuracy and less computational cost.

Coupled Level set and Volume of Fluid (CLSVOF) Method

The algorithm for CLSVOF is as follows: The CLSVOF method advects the level set function ϕ and the volume fraction C by solving LS and VOF equations, respectively, from t^n to t^{n+1}. In other words, the evolution of the air/water interface can be tracked by solving the VOF equation (Equation 1) and the level set equation $\frac{\partial \phi}{\partial t} + \mathbf{u} \cdot \nabla \phi = 0$, where $\boldsymbol{u}$ accounts for the fluid velocity field obtained by solving the Navier–Stokes equations. The interface needs to reconstruct, subsequent to the advection of ϕ and C, so that the two interfaces predicted by ϕ and C are close to each other. The reconstruction procedure of LS and VOF functions can be found in Yu et al. (2019).

Navier–Stokes Equations and the Immersed Boundary Method

The following dimensionless Navier–Stokes equations are considered:

$$\frac{\partial \boldsymbol{u}}{\partial t} + (\boldsymbol{u} \cdot \nabla)\,\boldsymbol{u} = -\frac{\nabla p}{\rho\,(C)} + \frac{1}{Re}\frac{\nabla \cdot (2\mu(C)\boldsymbol{D})}{\rho\,(C)} + \frac{1}{Fr^2}\hat{\boldsymbol{e}}_g \quad (2)$$

In this equation, u represents velocity fields, p represents pressure, and Re and Fr denote the Reynolds number and Froude number. Physical properties (density ρ and viscosity μ) are the function of C and defined in the following equations:

$$\begin{aligned} \rho &= C + \left(\frac{\rho_a}{\rho_w}\right)(1 - C) \\ \mu &= C + \left(\frac{\mu_a}{\mu_w}\right)(1 - C) \end{aligned} \quad (3)$$

where ρ_a and ρ_w are air and water density, respectively.

In the IB method, the momentum forcing which is introduced to enforce the boundary condition of the body in the fluid can be prescribed on a fixed mesh (Zhang et al., 2010). Momentum equations can be discretized via the following second-order Adams–Bashforth scheme and the immersed boundary method:

$$\frac{\boldsymbol{u}^{n+1} - \boldsymbol{u}^n}{\Delta t} + \left(\frac{3}{2}\boldsymbol{A}^n - \frac{1}{2}\boldsymbol{A}^{n-1}\right) + \frac{1}{\rho\,(C)}\nabla p^{n+1} = \eta \boldsymbol{f}^{n+1} \quad (4)$$

where

$$\boldsymbol{A} = (\boldsymbol{u} \cdot \nabla)\,\boldsymbol{u} - \frac{1}{\mathrm{Re}}\frac{\nabla \cdot (2\mu(C)\boldsymbol{D})}{\rho\,(C)} - \frac{1}{Fr^2}\hat{\mathbf{e}}_g$$

given that the forcing vector ηf with the solid volume fraction η is introduced as a source term to the momentum equation through the IB method. To calculate the solid volume fraction η accurately, refining the mesh on solid is considered to satisfy this requirement (Yu et al., 2019). In the framework of the projection method discussed in Yu et al. (2019), the velocity u^{n+1} given by the following equations will be obtained:

$$\frac{\boldsymbol{u}^* - \boldsymbol{u}^n}{\Delta t} + \left(\frac{3}{2}\boldsymbol{A}^n - \frac{1}{2}\boldsymbol{A}^{n-1}\right) = 0 \quad (5)$$

$$\nabla \cdot \left(\frac{1}{\rho\,(C)}\nabla p^{n+1}\right) = \frac{\nabla \cdot \boldsymbol{u}^*}{\Delta t} \quad (6)$$

$$\boldsymbol{u}^{n+1} = \boldsymbol{u}^* - \frac{\Delta t}{\rho\,(C)}\nabla p^{n+1} \quad (7)$$

where u^* is intermediate velocity. The point-successive over-relaxation (PSOR) method is applied to solve the discretized linear system of the Poisson pressure equation. The iterative procedures for the PSOR method will not stop until the user's specified tolerance is reached. Moreover, the relaxation factor is set as 1.5 in our calculation. Note that the virtual force f^{n+1} can be calculated as Yu et al. (2019).

$$\boldsymbol{f}^{n+1} = \frac{\boldsymbol{u}_s - \boldsymbol{u}^*}{\Delta t} + \frac{\nabla p^{n+1}}{\rho\,(C)} \quad (8)$$

where u_s symbolizes the velocity of buildings. Note that all the buildings are set in a static state, so $u_s = 0$. While we are calculating the convection terms in the momentum equations, points at the upwind side are considered. Also, in previous experiments, there are no apparent improvements on

a prediction for the position of dam-break fronts under a discretization made by Navier–Stokes equations with the discrete scheme over a second-order precision. Therefore, the second-order accuracy scheme is enough to discretize the convection terms in this study. The viscous terms are discretized by the second-order central difference scheme.

Two-Dimensional Depth-Averaged SWE Model

Governing Equations

When the flood occurs in the urban area, the governing equation is expressed as Wu (2008):

(1) Continuity equation

$$\frac{\partial\left[(1-c)\,\eta\right]}{\partial t}+\frac{\partial\left[(1-c)\,hu_x\right]}{\partial x}+\frac{\partial\left[(1-c)\,hu_y\right]}{\partial y}=0 \quad (9)$$

(2) Momentum equation

To direction X:

$$\begin{aligned}&\frac{\partial}{\partial t}\left[(1-c)\,u_x h\right]+\frac{\partial}{\partial x}\left[(1-c)\,u_x^2 h+(1-c)\,\frac{g}{2}h^2\right]\\&+\frac{\partial}{\partial y}\left[(1-c)\,u_x u_y h\right]\\&=-(1-c)\,gh\frac{\partial z_b}{\partial x}-(1-c)\,\frac{\tau_{b,x}}{\rho}+\frac{gh^2}{2}\frac{\partial\,(1-c)}{\partial x}\\&-\frac{f_{d,x}h}{\rho}+\frac{\partial}{\partial x}\left[(1-c)\,v_e\frac{\partial u_x}{\partial x}\right]+\frac{\partial}{\partial y}\left[(1-c)\,v_e\frac{\partial u_x}{\partial y}\right]\end{aligned} \quad (10)$$

To direction Y:

$$\begin{aligned}&\frac{\partial}{\partial t}\left[(1-c)\,u_y h\right]+\frac{\partial}{\partial x}\left[(1-c)\,u_x u_y h\right]\\&+\frac{\partial}{\partial y}\left[(1-c)\,u_y^2 h+(1-c)\,\frac{g}{2}h^2\right]\\&=-(1-c)\,gh\frac{\partial z_b}{\partial x}-(1-c)\,\frac{\tau_{b,y}}{\rho}+\frac{gh^2}{2}\frac{\partial\,(1-c)}{\partial y}-\frac{f_{d,y}h}{\rho}\\&+\frac{\partial}{\partial x}\left[(1-c)\,v_e\frac{\partial u_y}{\partial x}\right]+\frac{\partial}{\partial y}\left[(1-c)\,v_e\frac{\partial u_y}{\partial y}\right]\end{aligned} \quad (11)$$

in which t is time; η is water level; h is water depth; ρ is water flow density; g is gravity acceleration; u_x and u_y represent the velocity components of water flow in direction x and direction y, respectively; z_b is bed elevation; $\partial z_b/\partial x$ and $\partial z_b/\partial y$ are slopes of the bed; and c represents the distribution density of water blocking obstacles. In Equations (10) and (11), $v_e = v + v_t$, where v is the kinematic viscosity of water flow and v_t is eddy current viscosity produced by turbulent flow; $v_t = 1/6\kappa u_f h$, where κ is von Karman constant and u_f is the friction velocity, generally expressed as $u_f = n(\sqrt{u^2+v^2})h^{1/6}$ (n symbolizes Manning coefficient).

$f_{d,x}$ and $f_{d,y}$ are the resistances of water obstacles along the direction x and direction y on the unit volume, which can be, respectively, expressed as $F_{d,x} = \frac{1}{2}C_{b,x}\rho A_{b,x}|U|\,U_x$ and $F_{d,y} = \frac{1}{2}C_{b,y}\rho A_{b,y}|U|\,U_y$ ($U = \sqrt{u_x^2+u_y^2}$). $A_{b,x} = L_x h$, $A_{b,y} = L_y h$; L_x and L_y are the projected length of the building in the direction x and y. $C_{b,x}$ and $C_{b,y}$ are two drag coefficients of two directions, which can be indicated as $C_{b,x} = \xi_x/L_x$ and $C_{b,y} = \xi_y/L_y \circ \xi_x$ and ξ_y are the local head loss coefficients in their corresponding direction $\circ$; $\tau_{b,x}$ and $\tau_{b,y}$ are bed frictions toward direction x and directions y, which can be expressed as $\tau_{b,x} = \rho g\frac{n^2U}{R^{1/3}}u_x$ and $\tau_{b,y} = \rho gh\frac{n^2U}{R^{1/3}}u_y$ where R is hydraulic radius, but represents the water depth h in this study.

The governing Equations (9), (10), and (11) can also be expressed in the form of a vector:

$$\begin{aligned}&\frac{\partial}{\partial t}\left[(1-c)\boldsymbol{\Phi}\right]+\frac{\partial}{\partial x}\left[(1-c)\boldsymbol{f}(\boldsymbol{\Phi})\right]\\&+\frac{\partial}{\partial y}\left[(1-c)\boldsymbol{g}(\boldsymbol{\Phi})\right]=\boldsymbol{S}+\boldsymbol{D}\end{aligned} \quad (12)$$

in which Φ is conserved variable; $\boldsymbol{f}(\Phi)$ and $\boldsymbol{g}(\Phi)$ are fluxes in direction x and direction y; $\boldsymbol{S}$ and $\boldsymbol{D}$ are, respectively, the source item and the diffusion term, which can be expressed as

$$\begin{aligned}\boldsymbol{\Phi}&=\left[\eta,hu_x,hu_y\right]^T\\\boldsymbol{f}(\boldsymbol{\Phi})&=\left[hu_x,hu_xu_x+\frac{1}{2}gh^2,hu_xu_y\right]^T\\\boldsymbol{g}(\boldsymbol{\Phi})&=\left[hu_y,hu_xu_y,hu_yu_y+\frac{1}{2}gh^2\right]^T\\\boldsymbol{S}&=\left[0,S_{p,x}+S_{f,x},S_{p,y}+S_{f,y}\right]^T\\\boldsymbol{D}&=\left[0,\frac{\partial}{\partial x_j}\left[(1-c)v_e\frac{\partial u_x}{\partial x_j}\right],\frac{\partial}{\partial x_j}\left[(1-c)v_e\frac{\partial u_y}{\partial x_j}\right]\right]^T\end{aligned} \quad (13)$$

$\boldsymbol{S}$ are made up of two factors, $S_{p,x}$ and $S_{p,y}$, which are the source terms generated by the change of bottom gradient and permeable density in direction x and direction y, and its specific calculation formula is

$$\begin{aligned}S_{p,x}&=-(1-c)gh\frac{\partial z_b}{\partial x}+g\frac{h^2}{2}\frac{\partial(1-c)}{\partial x}\\S_{p,y}&=-(1-c)gh\frac{\partial z_b}{\partial y}+g\frac{h^2}{2}\frac{\partial(1-c)}{\partial y}\end{aligned} \quad (14)$$

In Equation (13), $S_{f,x}$ and $S_{f,y}$ are drag source terms of bottom bed friction and water blocking obstacles in direction x and direction y, which can be calculated through the following formula:

$$\begin{aligned}S_{f,x}&=-(1-c)\,gh\frac{n^2u_x\sqrt{u_x^2+u_y^2}}{h^{4/3}}-\frac{f_{d,x}h}{r}\\S_{f,y}&=-(1-c)\,gh\frac{n^2u_y\sqrt{u_x^2+u_y^2}}{h^{4/3}}-\frac{f_{d,y}h}{r}\end{aligned} \quad (15)$$

Equation (12) can be also written as

$$\frac{\partial}{\partial t}\left[(1-c)\boldsymbol{\Phi}\right]+\frac{\partial}{\partial x}\left[\boldsymbol{F}(\boldsymbol{\Phi})\right]+\frac{\partial}{\partial t}\left[\boldsymbol{G}(\boldsymbol{\Phi})\right]=\boldsymbol{S}+\boldsymbol{D} \quad (16)$$

where $\boldsymbol{F}(\boldsymbol{\Phi})=(1-c)\boldsymbol{f}(\boldsymbol{\Phi})$ and $\boldsymbol{G}(\boldsymbol{\Phi})=(1-c)\boldsymbol{g}(\boldsymbol{\Phi})$.

Finite-Volume Discretization

The governing Equation (16) of the fixed bed flood motion can be discretized by finite volume method:

$$\boldsymbol{\Phi}_{i,j}^{n+1}=\boldsymbol{\Phi}_{i,j}^{n}-\frac{\Delta t\left(\boldsymbol{F}_{i+1/2,j}^{n}-\boldsymbol{F}_{i-1/2,j}^{n}\right)}{\Delta x(1-c)}-\frac{\Delta t\left(\boldsymbol{G}_{i,j+1/2}^{n}-\boldsymbol{G}_{i,j-1/2}^{n}\right)}{\Delta y(1-c)}+\frac{\Delta t}{1-c}\left(\boldsymbol{S}_{i,j}^{n}+\boldsymbol{D}_{i,j}^{n}\right) \quad (17)$$

in which the superscript n represents time step; Δt represents the time step, Δx and Δy represent the sizes of grids in direction x and direction y, respectively; $\boldsymbol{F}_{i-1/2,j}^{n}$ and $\boldsymbol{F}_{i+1/2,j}^{n}$ represent the fluxes of grid interfaces $(i-1/2,j)$ and $(i+1/2,j)$; $\boldsymbol{G}_{i,j+1/2}^{n}$ and $\boldsymbol{G}_{i,j-1/2}^{n}$ represent the fluxes of grid interfaces $(i,j+1/2)$ and $(i,j-1/2)$; $\boldsymbol{S}_{i,j}$ and $\boldsymbol{D}_{i,j}$, respectively, represent the source term and the diffusion term at the unit center (i,j). The central-upwind format proposed by Kurganov and Petrova (2007) is applied to calculate the interface fluxes $\boldsymbol{F}_{i+1/2,j}^{n}$ and $\boldsymbol{G}_{i,j+1/2}^{n}$. In order to enable the model to spatially reach a second-order accuracy, the linear reconstruction technique of Liang (2011) is adopted in this paper to reconstruct the conserved variables at both sides of the interface and the bed elevation of the interface. Numerical stability conditions should limit the computational time step since the developed solution procedure is explicit, such as the Courant–Friedrichs–Lewy (CFL) condition for flow computation. The time step should satisfy the following CFL condition:

$$N_{CFL}=\max_{i,j}\left\{\frac{\Delta t}{\Delta x}(|u_x|+\sqrt{gh}),\ \frac{\Delta t}{\Delta y}(|u_y|+\sqrt{gh})\right\}\leq 0.25 \quad (18)$$

NUMERICAL RESULTS AND DISCUSSION

The main contents of this chapter are as follows: (1) validate the accuracy of the 3D model through grid convergence study; (2) analyze the characteristics of the 3D flow fields; (3) compare accuracies and efficiencies amid the proposed VOF/IB, CLSVOF/IB (Yu et al., 2019), and SWE models.

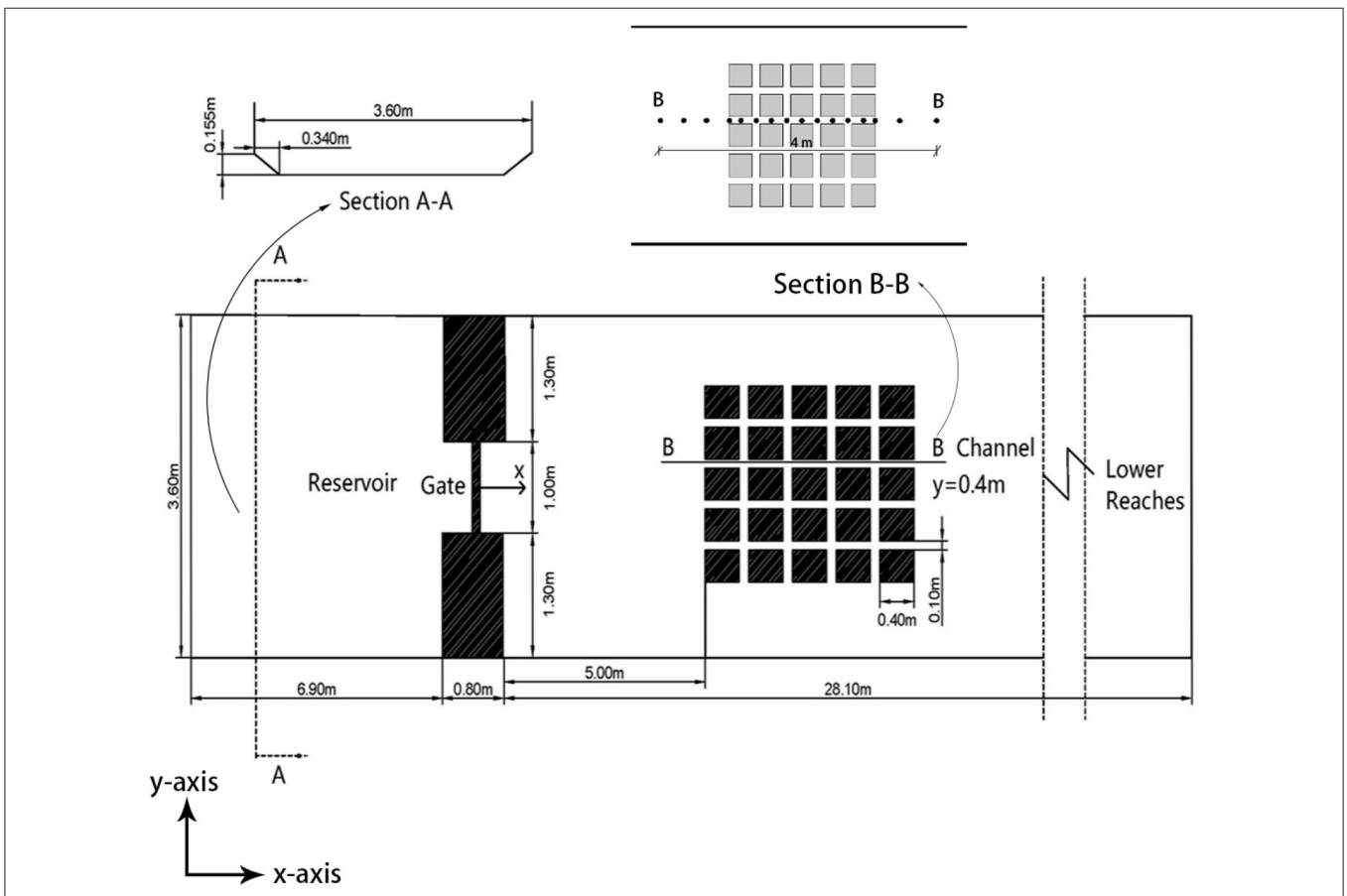

FIGURE 1 | Parameters and setting of numerical simulations after (Yu et al., 2019).

Parameters and Setting of Numerical Simulations

Soares-Frazão and Zech (2008) from the Catholic University of Leuven experimented the evolution process simulation of outburst flood on the urban ground with dense buildings. This experimentation is a classic example of urban flood under fixed-bed condition, where the building here is architectural complex. The experimental area occupies a trapezoidal channel which is 36 m long, 3.6 m wide with a zero slope. The initial water depth in the upstream reservoir is 0.4 m, and that downstream of the reservoir is 0.011 m, as shown in **Figure 1**. In their experiment, water depth was measured by means of several

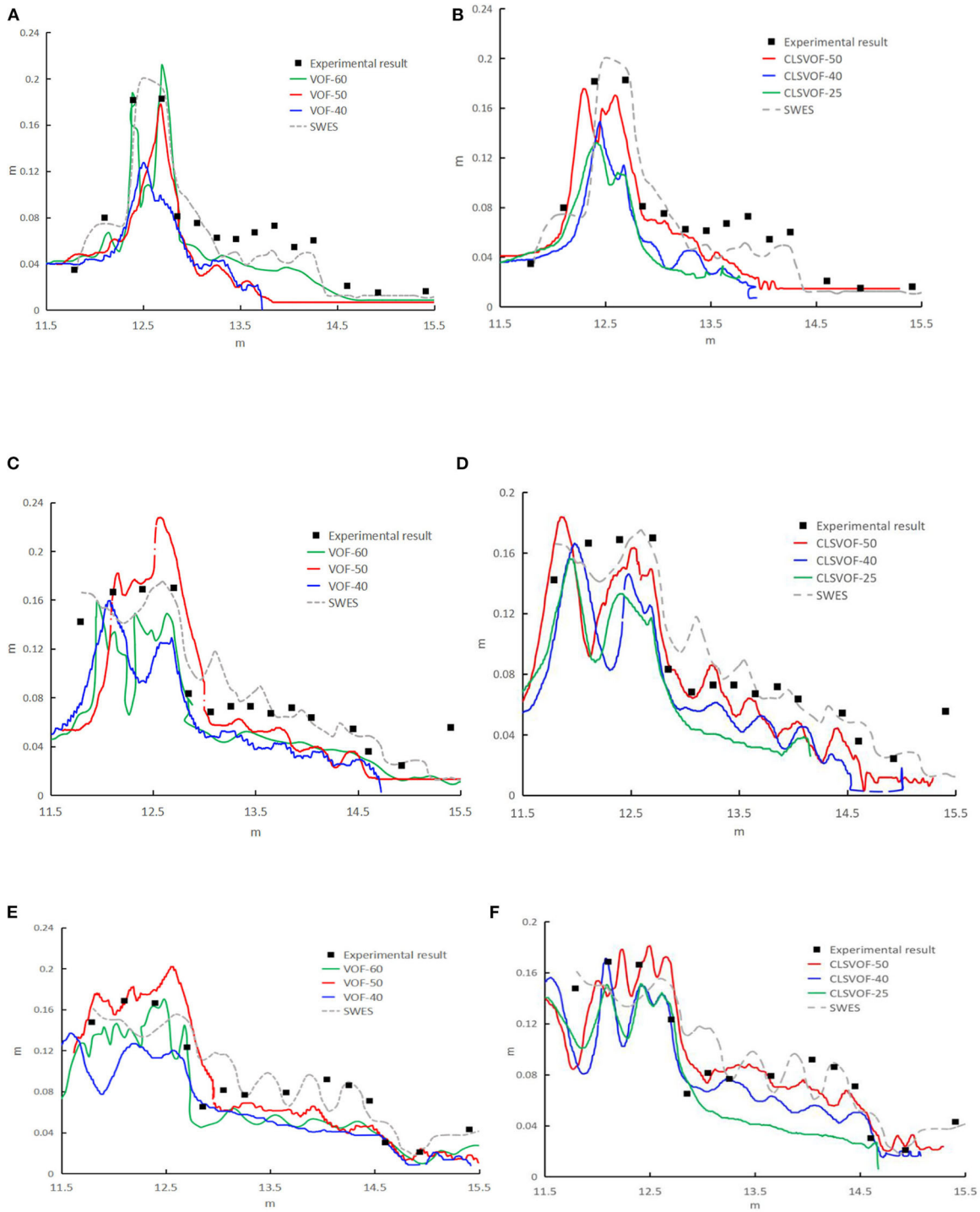

FIGURE 2 | The free surface profile at different time in Section B-B **(A,B)** $t = 4$ s; **(C,D)** $t = 5$ s; **(E,F)** $t = 6$ s.

resistive level gauges. As shown in Section B-B in **Figure 1**, 16 liquid level gauges are placed in Section B-B by Soares-Frazão and Zech. As the gate opens, those begin to record the evolution of the free surface. In this simulation, the continuous water depth of Section B-B is extracted and compared with the water depth data of 16 measuring points of Soares-Frazão and Zech experiments, in which the length range of the section in the x-axis is actually within 4 m from 11.5 to 15.5 m of the x-axis.

Grid Convergence Study

When the grid intervals (h) are 40, 50, and 60, the temporal evolution of water depth over time is proved in **Figure 2**. Both CLSVOF/IB and VOF/IB methods are able to accurately simulate water depth when the grid is finer enough. The relative root means square error (RMSE) between measured values and numerical results obtained from CLSVOF/IB and VOF/IB methods is shown in **Table 1**. The RMES mentioned in **Table 1** is defined as $\text{RMSE} = \sqrt{(1/m_R)\sum_{i=1}^{m_R}[(f_{simu,i} - f_{meas,i})/f_{meas,i}]^2}$, where m_R is the number of measured values; $f_{meas,i}$ is the ith measured value, and $f_{simu,i}$ is the ith simulated value. The smaller the RMES value, the smaller the error between the simulated value and the measured value will be, and the more accurate the simulation result will be. From **Figure 2, Table 1**, it is shown that compared with the coarse grid ($h = 40$), with CLSVOF/IB and VOF/IB methods, the resulting error of water depth at each moment is relatively smaller as the grid is finer ($h = 50$). Therefore, the mesh density has a great influence on the calculation results of the model when the mesh is relatively finer, and the simulation consequences of water depth is more consistent with the measured values.

TABLE 1 | Numerical error estimation.

	VOF-IB			CLSVOF/IB		
	VOF-40	VOF-50	VOF-60	CLSVOF-25	CLSVOF-40	CLSVOF-50
RMSE $t = 4$ s	0.4512	0.4219	0.3653	0.4463	0.3838	0.2329
$t = 5$ s	0.3769	0.3438	0.3135	0.4012	0.3465	0.2529
$t = 6$ s	0.4141	0.3391	0.2837	0.3579	0.2576	0.2098

Free Surface Evolution and Flow Characteristic

After ensuring that the grids are independent of water level, the time-evolving free surface of the flood–building interaction at the

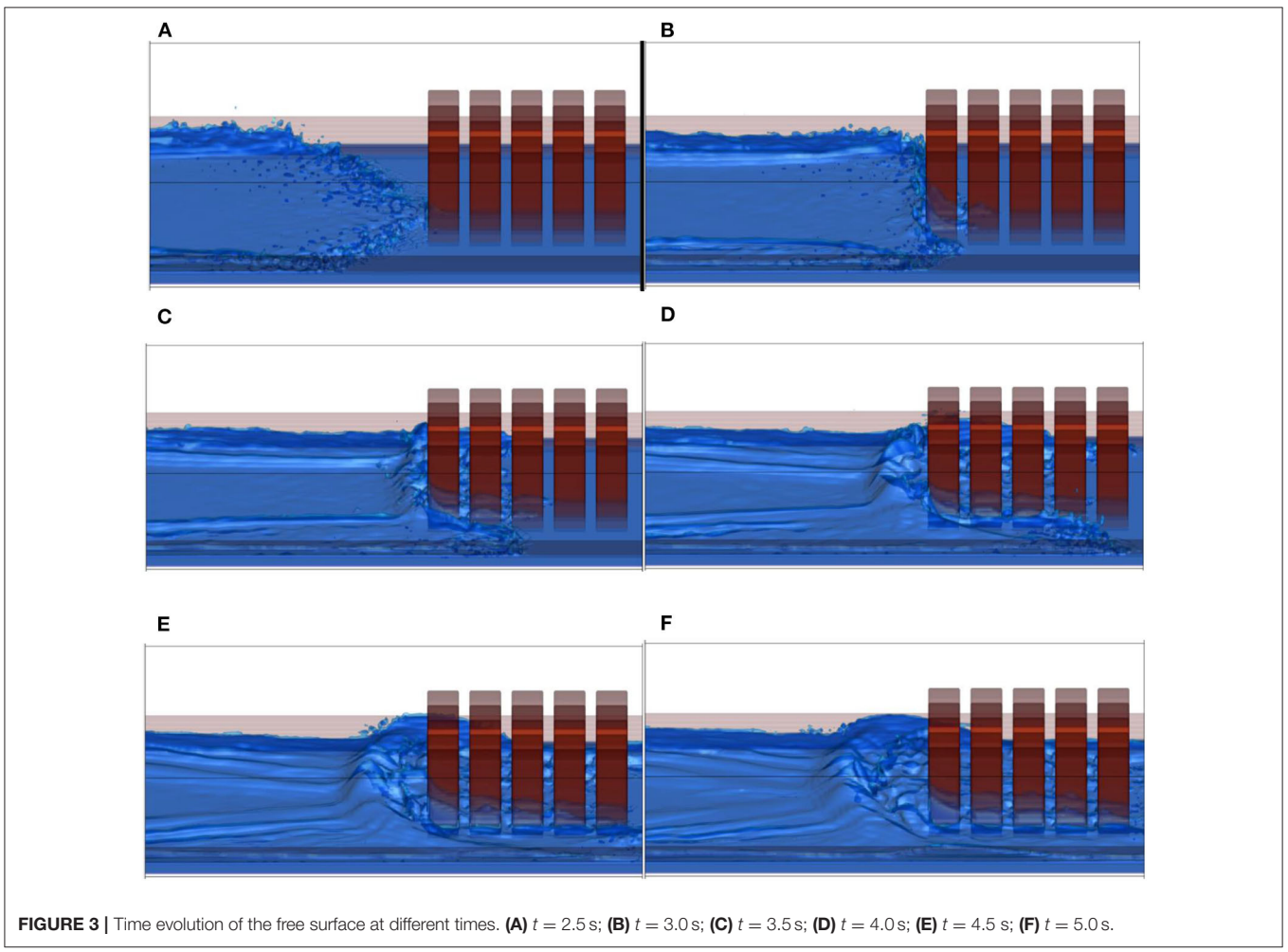

FIGURE 3 | Time evolution of the free surface at different times. **(A)** $t = 2.5$ s; **(B)** $t = 3.0$ s; **(C)** $t = 3.5$ s; **(D)** $t = 4.0$ s; **(E)** $t = 4.5$ s; **(F)** $t = 5.0$ s.

grid interval $h = 50$ is carried out for free surface evolution. **Figure 3** shows the time evolution of the free surface at several instants where results of fine grids are proved. The flooding wave approximately touches the buildings on time $t = 2.5$ s. The run-up jet will break up as **Figure 3B** shows and start to detach from the vertical wall overturning backward as **Figure 3C** shows, when it reaches the maximum elevation under the acceleration of gravity. In **Figure 3D**, the falling jet then collapses onto the water surface of the incoming dam-break wave. New surges, which are created by the spattering of the plunging jet on the back flow, that rebound on the water surface cause a strong free surface mixing with air entrainment as shown in **Figure 3E**. In **Figure 3F**, flood

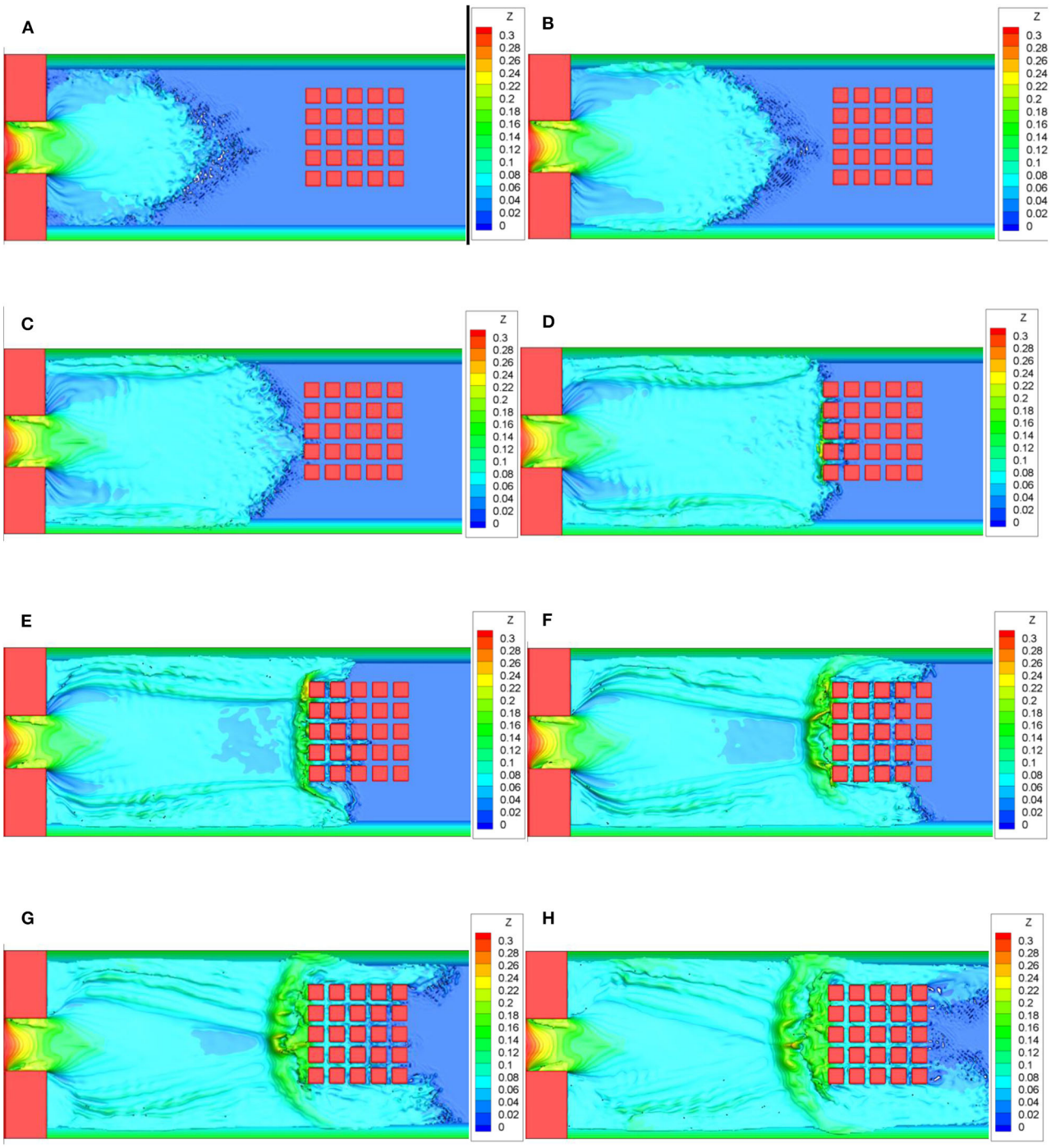

FIGURE 4 | Water depth of the dam-break flow in the $x - y$ plane. **(A)** $t = 1.5$ s; **(B)** $t = 2.0$ s; **(C)** $t = 2.5$ s; **(D)** $t = 3.0$ s; **(E)** $t = 3.5$ s; **(F)** $t = 4.0$ s; **(G)** $t = 4.5$ s; **(H)** $t = 5.0$ s. The unit is set as m.

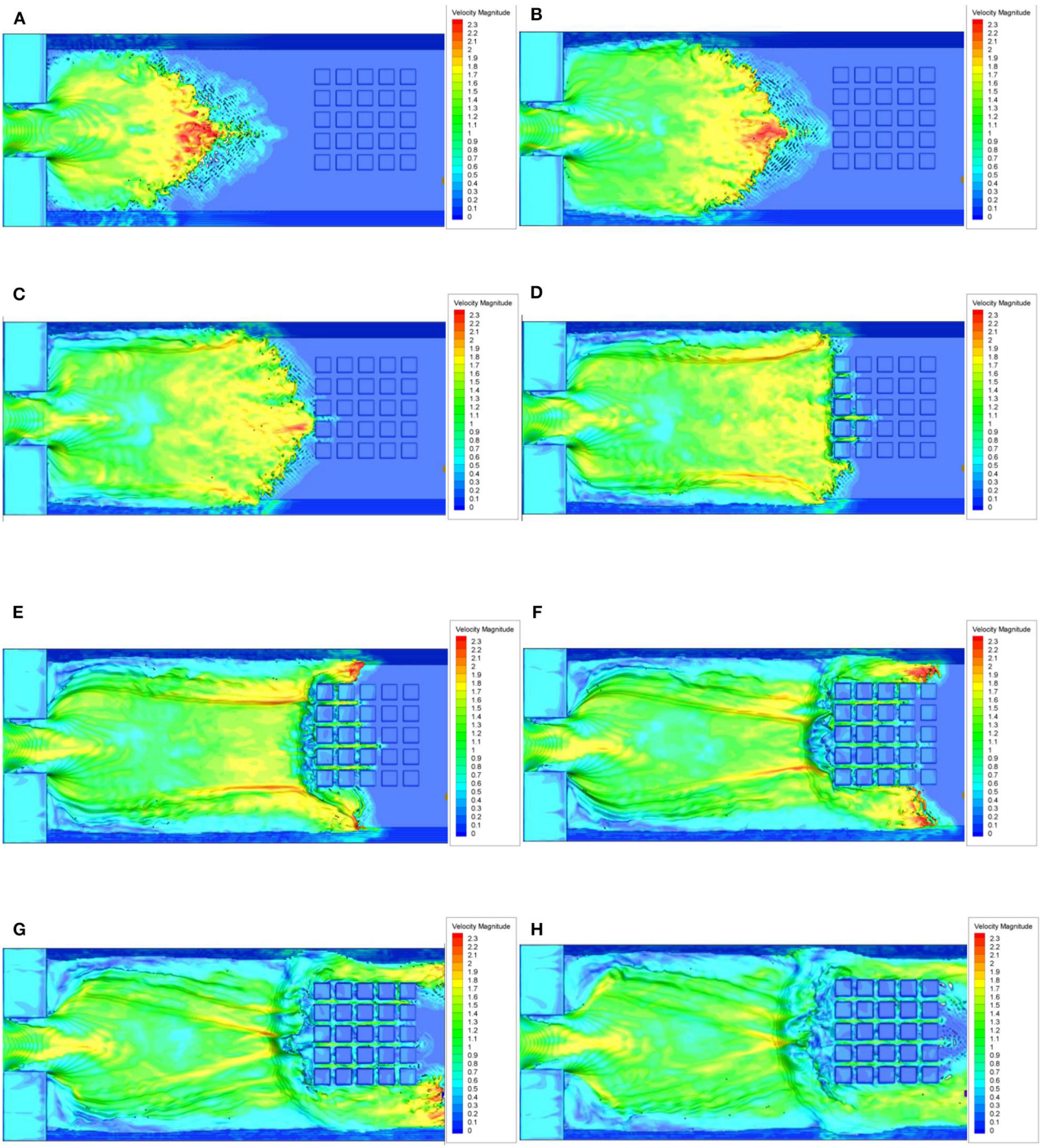

FIGURE 5 | Velocity magnitude of the dam-break flow in the $x - y$ plane. **(A)** $t = 1.5$ s; **(B)** $t = 2.0$ s; **(C)** $t = 2.5$ s; **(D)** $t = 3.0$ s; **(E)** $t = 3.5$ s; **(F)** $t = 4.0$ s; **(G)** $t = 4.5s$; **(H)** $t = 5.0$ s. The unit is set as m/s.

wave (secondary wave) propagate in the upstream at gradually between $t = 5.0$ and 6.0 s.

Figures 4, **5** show the temporal evolution of water depth and velocity magnitude calculated in the plane using VOF/IB methods. It can be indicated that the flood is incapable to flow out rapidly because of the hurdle of multiple buildings, which raises the water level and the flow speed at both sides of the wall. A symmetric and steady wake of velocity magnitude is not demonstrated behind the buildings because of the flow becoming unstable at high Reynolds number and toward being inertial

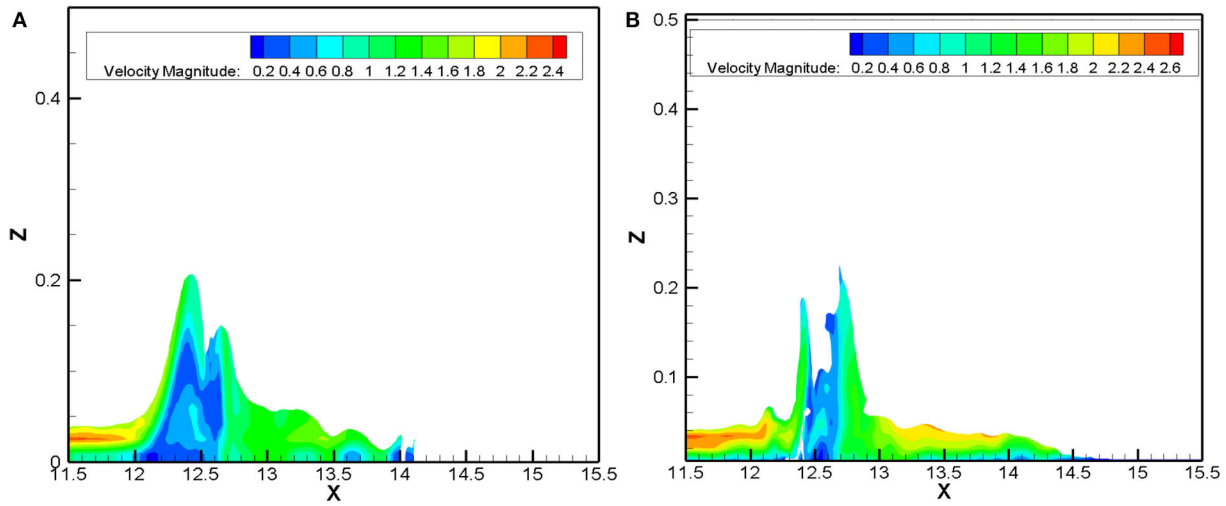

FIGURE 6 | Velocity magnitude of the dam-break flow in the $x - z$ plane. **(A)** $t = 4.0$ s (CLSVOF/IB method); **(B)** $t = 4.0$ s (VOF/IB method). The unit is set as m/s.

force-dominated. The x–z plane at Section B-B (see **Figure 2**) is compared with the velocity fields diagram of CLSVOF/IB and VOF/IB methods. As **Figures 6A,B** show, the velocity fields experience the most drastic change where the flood first impacts the building at around $x = 12$ m. The velocity of the flow intruding into the buildings changes quite significantly. After $x = 12$ m, the velocity attenuates greatly because of the buildings in the front.

Comparison of Efficiency, Mass Conservation, and Free Surface Evolution

From **Table 2**, we can notice that VOF/IB is more efficient than CLSVOF/IB because there is no calculation time spent in solving the level set in the solver of VOF/IB. Compared with other solvers in the aspect of serial computing time, we have come to the conclusion that VOF/IB solver possesses the advantage of saving time. A comparison between the present VOF/IB method and the CLSVOF/IB method in mass conservation shows that both methods perform quite well as **Figure 7** shows.

Figure 8 shows the free surface at (a) $t = 4$ s and (b) $t = 5$ s. The downstream water depth (or tailwater level) is 0.05 m in the blue line and 0.011 m in the red line. Because of the greater resistance imposed by the larger water depth in the blue line, the discharged water moves slower in the blue line than in the red line. For example, at $t = 4$ s as shown in **Figure 8A**, the front moves to 13.7 m in the blue line and 14.6 m in the red line. This implies that the front velocity decrease with increasing downstream water depth.

The evolution of x-force acting on the buildings is plotted in **Figure 9A**. The VOF/IB results with the finest spatial resolution are almost identical to those obtained with CLSVOF/IB method for up to $t = 4.0$ s. However, we found that the VOF/IB method overestimates the peak force slightly at $t = 4.0$ s. At that time, the flow has already hit the right wall of the tank and,

TABLE 2 | CPU time for different methods until $t = 4.0$ s.

	VOF-IB			CLSVOF/IB		
	VOF-40	VOF-50	VOF-60	CLSVOF-25	CLSVOF-40	CLSVOF-50
CPU time (s)	6.20E3	1.48E4	9.168E4	5.40E3	3.60E4	7.78E4

consequently, has generated several complex fluid structures with air entrapment. Two stages for the evolution of $\boldsymbol{x}$-force acting on the buildings with different initial water depth in the downstream reservoir (i.e., different tailwater level) can be identified in **Figure 9B**. The first stage exists during $t = 1 \sim 2$ s before intrusion happens. During this stage, the water is discharged through the left of the dam, but the flow has not reached the downstream buildings, and the impacting force in the buildings is nearly zero. During the second stage $t = 2 \sim 7$ s, the discharge begins to intrude into the building from the left and flows around the buildings. The discharge calculated in the red line moves with a greater front velocity and enters the second stage earlier, but has a smaller impacting force in the buildings. Two reasons account for this phenomenon. First, a greater front velocity induces a larger viscous dissipation and kinematic energy loss. Second, the larger water depth difference makes it easier for flow to intrude into the buildings.

CONCLUDING REMARKS

Adopting a three-dimensional mathematical model, this paper exerts algebraic VOF (THINC/SW) method on free liquid surface tracking, which is simpler and more efficient than the traditional VOF method that needs interface reconstruction. In addition, to tackle liquid (flood) and solid (buildings) interface problems, this method is combined with IB method. The accuracy of the CLSVOF/IB method is higher than VOF/IB methods. However, the main idea of the paper is to develop a mathematical

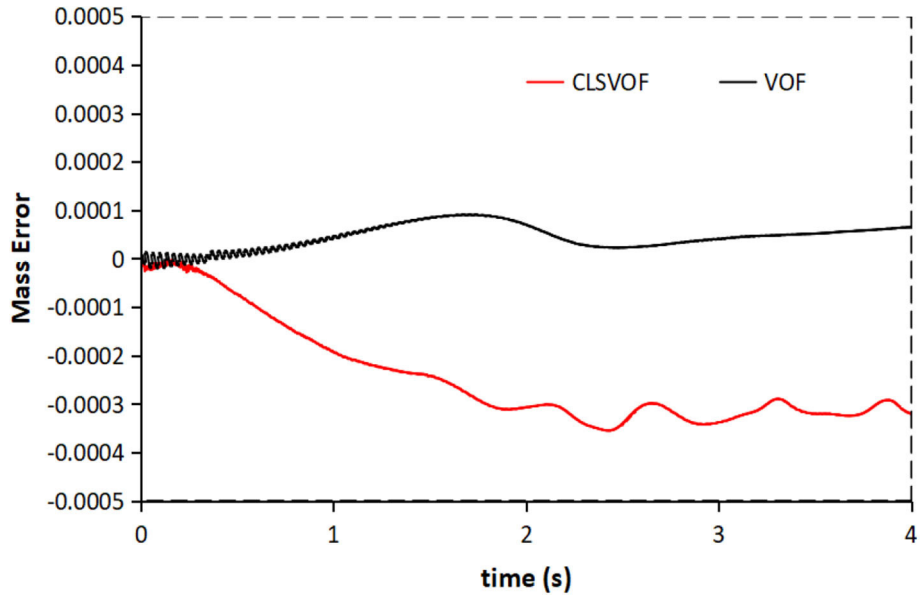

FIGURE 7 | Mass conservation against times for both methods.

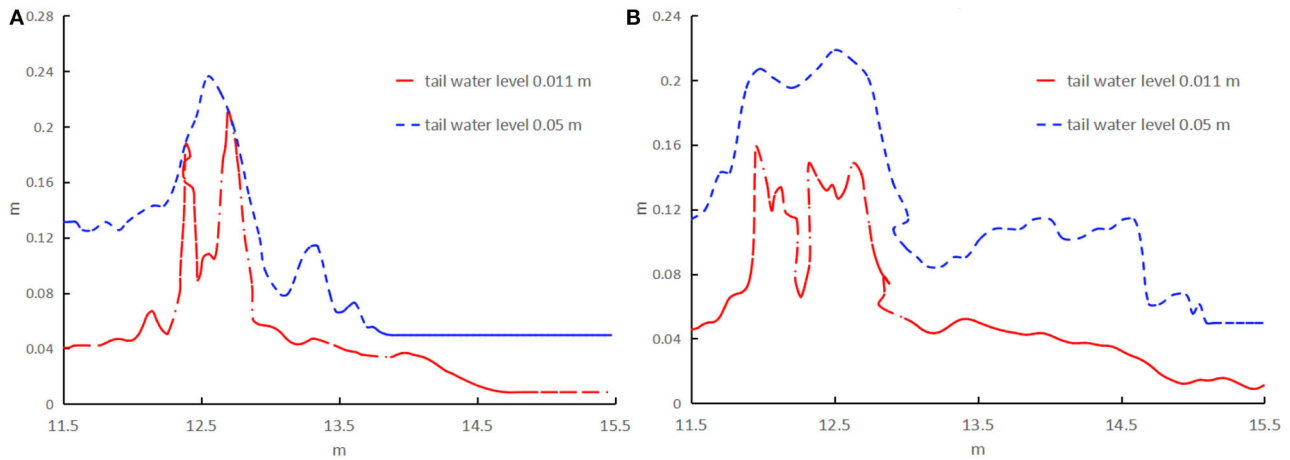

FIGURE 8 | The free surface profile at different times: **(A)** $t = 4.0$ s; **(B)** $t = 5.0$ s.

model with high computational efficiency and the ability to deal with wave breaking so that the matter of the dam-break flood with a larger kilometer scale can also be addressed. In other words, the VOF/IB method developed in this paper mainly aims to overcome the disadvantages of CLSVOF/IB (e.g., poor computational efficiency) and the shallow water models (e.g., inability to handle complex flow conditions). This paper first presents the VOF/IB method in the sequence of solving the VOF equation (Equation 1), and then it presents the momentum equation (Equation 4). While getting the CLSVOF/IB method, it needs to solve the VOF equation (Equation 1), the LS equation, and the momentum equation (Equation 4). The latter possesses a lower calculation efficiency on account of one more step to solve LS equations. Also, the CLSVOF/IB method is mainly applied to tackle the problem of surface tension (e.g., the bubble rising and water droplet collision). Also owing to LS equations included, this method can effectively calculate air bubbles or water droplets free liquid surface curvature. Without constantly considering surface tension concerning the dam-break flood problem, the issue of the dam-break flood is more suitable to be addressed by the VOF/IB method. Cases of irregular buildings can be predicted by the performed VOF/IB method, which induces the formation of wave breaking and wave reflections in flow behavior. However, in numerical simulation, fine mesh is needed to well-represent the irregular topography. Large computational domains are still attracted by SWE-based numerical models because of less computational efforts and time over DNS models.

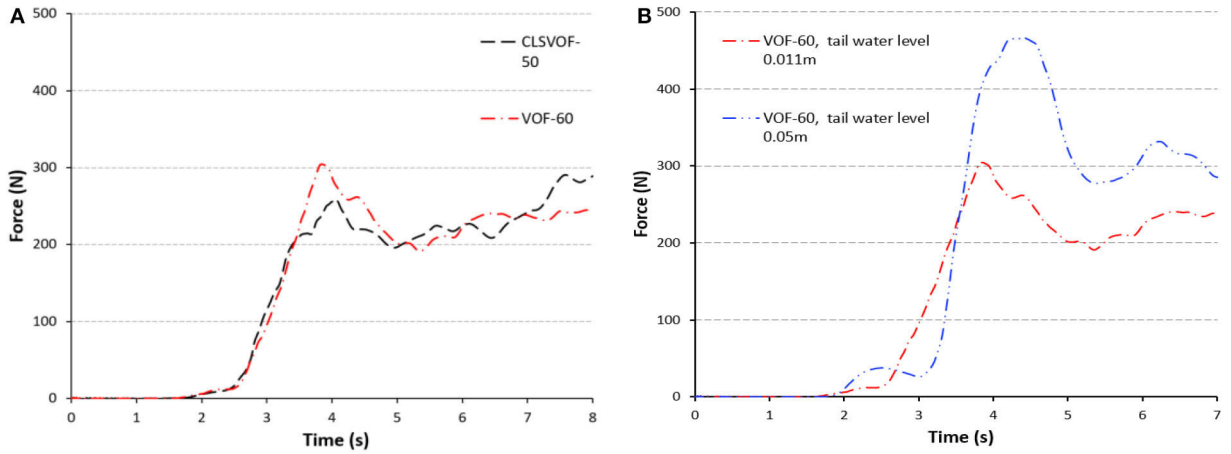

FIGURE 9 | (A) Evolution of *x*-force acting on the buildings using CLSVOF/IB and VOF/IB methods. **(B)** Evolution of *x*-force acting on the buildings using VOF/IB method with different tail water level.

DATA AVAILABILITY STATEMENT

The datasets generated for this study are available on request to the corresponding author.

AUTHOR CONTRIBUTIONS

RA contributed conception and design of the study. CY and WM wrote the manuscript. YL organized the database.

FUNDING

This research was funded by National Key R&D Program of China (2016YFC0502207), National Natural Science Foundation of China (No. 51979178), Department of Science and Technology of Sichuan Province (No. 2019YJ0118), Fundamental Research Funds for the Central Universities (No. YJ201837), and Innovation spark project (No. SCUH0049).

REFERENCES

Aureli, F., Dazzi, S., Maranzoni, A., Mignosa, P., and Vacondio, R. (2015). Experimental and numerical evaluation of the force due to the impact of a dam-break wave on a structure. *Adv. Water Resour.* 76, 29–42. doi: 10.1016/j.advwatres.2014.11.009

Bahbah, C., Khalloufi, M., Larcher, A., Mesri, Y., Coupez, T., Valette, R., et al. (2019). Conservative and adaptive level-set method for the simulation of two-fluid flows. *Comput. Fluids*. 191:104223. doi: 10.1016/j.compfluid.2019.06.022

Cao, X. Y., Ming, F. R., Zhang, A. M., and Tao, L. (2017). Multi-phase SPH modelling of air effect on the dynamic flooding of a damaged cabin. *Comput. Fluids*. 163, 7–19. doi: 10.1016/j.compfluid.2017.12.012

Chang, T. J., Kao, H. M., Chang, K. H., and Hsu, M. H. (2011). Numerical simulation of shallow-water dam break flows in open channels using smoothed particle hydrodynamics. *J. Hydrol.* 408, 78–90. doi: 10.1016/j.jhydrol.2011.07.023

Fourtakas, G., Dominguez, J. M., Vacondio, R., and Rogers, B. D. (2019). Local uniform stencil (LUST) boundary condition for arbitrary 3-D boundaries in parallel smoothed particle hydrodynamics (SPH) models. *Comput. Fluids*. 190, 346–361. doi: 10.1016/j.compfluid.2019.06.009

Gu, Z. H., Wen, H. L., Yao, Y., and Yu, C. H. (2019). A volume of fluid method algorithm for simulation of surface tension dominant two-phase flows. *Numer. Heat Transfer Part B* 76, 1–17. doi: 10.1080/10407790.2019.1642048

Gu, Z. H., Wen, H. L., Ye, S., An, R. D., and Yu, C. H. (2018b). Development of a mass-preserving level set redistancing algorithm for simulation of rising bubble. *Numer Heat Transfer Part B.* 74:699–727. doi: 10.1080/10407790.2018.1525157

Gu, Z. H., Wen, H. L., Yu, C. H., and Sheu, T. W. H. (2018a). Interface-preserving level set method for simulating dam-break flows. *J. Comput. Phys.* 374, 249–280. doi: 10.1016/j.jcp.2018.07.057

Guinot, V., Delenne, C., and Cappelaere, B. (2009). An approximate Riemann solver for sensitivity equations with discontinuous solutions. *Adv. Water Resour.* 32, 61–77. doi: 10.1016/j.advwatres.2008.10.002

Guo, X. H., Rogers, B. D., Lind, S., and Stansby, P. K. (2018). New massively parallel scheme for Incompressible Smoothed Particle Hydrodynamics (ISPH) for highly nonlinear and distorted flow. *Comput. Phys. Commun.* 233, 16–28. doi: 10.1016/j.cpc.2018.06.006

Harvie, D. J. E., and Fletcher, D. F. (2000). A new volume of fluid advection algorithm: the stream scheme. *J. Comput. Phys.* 162, 1–32. doi: 10.1006/jcph.2000.6510

Harvie, D. J. E., and Fletcher, D. F. (2001). A new volume of fluid advection algorithm: the defined donating region scheme. *Int. J. Numer. Methods* 35, 151–172. doi: 10.1002/1097-0363(20010130)35:2<151::AID-FLD87>3.0.CO;2-4

Hirt, C. W., and Nichols, B. D. (1981). Volume of fluid (VOF) method for the dynamics of free boundaries. *J. Comput. Phys.* 39, 201–225. doi: 10.1016/0021-9991(81)90145-5

Hou, J. M., Simons, F., Mahgoub, M., and Hinkelmann, R. (2013). A robust well-balanced model on unstructured grids for shallow water flows with wetting and drying over complex topography. *Comput. Comput. Methods Appl. Mech. Eng.* 257, 126–149. doi: 10.1016/j.cma.2013.01.015

Hu, K. C., Hsiao, S. C., Hwung, H. H., and Wu, T. R. (2012). Three-dimensional numerical modeling of the interaction of dam-break waves and porous media. *Adv. Water Resour.* 47, 14–30. doi: 10.1016/j.advwatres.2012.06.007

Kurganov, A., and Petrova, G. (2007). A second-order well-balanced positivity preserving central-upwind scheme for the Saint-Venant system. *Commun. Math. Sci.* 5:133–160. doi: 10.4310/CMS.2007.v5.n1.a6

Kurioka, S., and Dowling, D. R. (2009). Numerical simulation of free surface flows with the level set method using an extremely high-order accuracy WENO advection scheme. *Int. J. Comut. Fluid Dyn.* 23, 233–243. doi: 10.1080/10618560902776786

Li, Q. (2016). Numerical simulation of melt filling process in complex mold cavity with insets using IB-CLSVOF method. *Comput. Fluids*. 132, 94–105. doi: 10.1016/j.compfluid.2016.04.005

Li, Y. L., and Yu, C. H. (2019). Research on dam-break flow induced front wave impacting a vertical wall based on the CLSVOF and level set methods. *Ocean Eng.* 178, 442–462. doi: 10.1016/j.oceaneng.2019.02.064

Liang, D., Falconer, R. A., and Lin, B. (2006). Comparison between TVD-MacCormack and ADI-type solvers of the shallow water equations. *Adv. Water Resour.* 29, 1833–1845. doi: 10.1016/j.advwatres.2006.01.005

Liang, Q. H. (2011). Flood simulation using a well-balanced shallow flow model. *J Hydraulic Eng.- ASCE* 136, 669–675. doi: 10.1061/(ASCE)HY.1943-7900.0000219

Meneveau, C., and Katz, J. (2000). Scale-invariance and turbulence models for large-eddy simulations. *Annu. Rev. Fluid Mech.* 32, 1–32. doi: 10.1146/annurev.fluid.32.1.1

Monteiro, L. R., Lucchese, L. V., and Schettini, E. B. C. (2019). Comparison between hydrostatic and total pressure simulations of dam-break flows. *J. Hydraulic Res.* doi: 10.1080/00221686.2019.1671509. [Epub ahead of print].

Noh, W. F., and Woodward, P. (1976). "SLIC (simple line interface calculation)," in P*roceedings of the Fifth International Conference on Numerical Methods in Fluid Dynamics*, 5th, Enschede, Netherlands. (Berlin; New York, NY: Springer-Verlag), 330–340. doi: 10.1007/3-540-08004-X_336

Olsson, E., Kreiss, G., and Zahedi, S. (2007). A conservative level set method for two phase flow II. *J. Comput. Phys.* 225, 785–807. doi: 10.1016/j.jcp.2006.12.027

Osher, S., and Sethian, J. A. (1988). Fronts propagating with curvature dependent speed: algorithms based on Hamilton-Jacobi formulations. *J. Comput. Phys.* 79, 12–49. doi: 10.1016/0021-9991(88)90002-2

Sanders, B. F. (2001). High-resolution and non-oscillatory solution of the St. Venant equations in non-rectangular and non-prismatic channels. *J Hydraulic Res.* 39, 321–330. doi: 10.1080/00221680109499835

Sanders, B. F., Schubert, J. E., and Gallegos, H. A. (2008). Integral formulation of shallow-water equations with anisotropic porosity for urban flood modeling. *J. Hydrol.* 362, 19–38. doi: 10.1016/j.jhydrol.2008.08.009

Savic, L. J., and Holly, F. M. (1993). Dambreak flood waves computed by modified Godunov method. *J. Hydraulic Res.* 31, 187–204. doi: 10.1080/00221689309498844

Schubert, J. E., and Sanders, B. F. (2012). Building treatments for urban flood inundation models and implications for predictive skill and modeling efficiency. *Adv. Water Resour.* 41, 49–64. doi: 10.1016/j.advwatres.2012.02.012

Soares-Frazao, S., Lhomme, J., Guinot, V., and Zech, Y. (2008). Two-dimensional shallow-water model with porosity for urban flood modelling. *J. Hydraulic Res.* 46, 45–64. doi: 10.1080/00221686.2008.9521842

Soares-Frazão, S., and Zech, Y. (2008). Dam-break flow through an idealised city. *J Hydraulic Res.* 46, 648–658. doi: 10.3826/jhr.2008.3164

Song, L. X., Zhou, J. Z., Guo, J., Zou, Q., and Liu, Y. (2011). A robust well-balanced finite volume model for shallow water flows with wetting and drying over irregular terrain. *Adv. Water Resour.* 34, 915–932. doi: 10.1016/j.advwatres.2011.04.017

Sun, D., and Tao, W. (2010). A coupled volume-of-fluid and level set (VOSET) method for computing incompressible two-phase flows. *Int. J. Heat Mass Transf.* 53, 645–655. doi: 10.1016/j.ijheatmasstransfer.2009.10.030

Wang, T., Li, H., Feng, Y., and Shi, D. (2013). A coupled volume-of-fluid and level set (VOSET) method on dynamically adaptive quadtree grids. *Int. J. Heat Mass Transf.* 67, 70–73. doi: 10.1016/j.ijheatmasstransfer.2013.08.006

Wang, Z., Yang, J., and Stern, F. (2012). A new volume-of-fluid method with a constructed distance function on general structured grids. *J. Comput. Phys.* 231, 3703–3722. doi: 10.1016/j.jcp.2012.01.022

Wu, W. M. (2008). *Computational River Dynamics*. London: Taylor & Francis Ltd. doi: 10.4324/9780203938485

Xiao, F., Honma, Y., and kono, T. (2005). A simple algebraic interface capturing scheme using hyperbolic tangent function. *Int. J. Numer. Methods Fluids*. 48, 1023–1040. doi: 10.1002/fld.975

Xiao, F., Ii, S., and Chen, C. (2011). Revisit to the THINC scheme: a simple algebraic VOF algorithm. *J. Comput. Phys.* 230, 7086–7092. doi: 10.1016/j.jcp.2011.06.012

Yang, J., and Stern, F. (2009). Sharp interface immersed-boundary/level-set method for wave-body interactions. *J. Comput. Phys.* 228, 6590–6616. doi: 10.1016/j.jcp.2009.05.047

Ying, X., Khan, A. A., and Wang, S. Y. (2004). Upwind conservative scheme for the Saint Venant equations. *J Hydraulic Eng-ASCE* 130, 977–987. doi: 10.1061/(ASCE)0733-9429(2004)130:10(977)

Yokoi, K. (2007). Efficient implementation of THINC scheme: a simple and practical smoothed VOF algorithm. *J. Comput. Phys.* 226, 1985–2002. doi: 10.1016/j.jcp.2007.06.020

Yu, C. H., Wen, H. L., Gu, Z. H., and An, R. D. (2019). Numerical simulation of dam-break flow impacting a stationary obstacle by a CLSVOF/IB method. *Commun. Nonlinear Sci. Numer. Simul.* 79:104934. doi: 10.1016/j.cnsns.2019.104934

Zeng, L., Luo, Z. L., Chen, B., Yang, Z. F., Li, Z., Lin, W. X., et al. (2010). Numerical analysis of a lock-release oil slick. *Commun. Nonlinear Sci. Numerical. Simulat.* 15, 2222–2230. doi: 10.1016/j.cnsns.2009.08.023

Zhang, C., Lin, N., Tang, Y., and Zhao, C. (2014). A sharp interface immersed boundary/VOF model coupled with wave generating and absorbing options for wave-structure interaction. *Comput. Fluids*. 89, 214–231. doi: 10.1016/j.compfluid.2013.11.004

Zhang, T., Peng, L., and Feng, P. (2018). Evaluation of a 3D unstructured-mesh finite element model for dam-break floods. *Comput. Fluids*. 160, 64–77. doi: 10.1016/j.compfluid.2017.10.013

Zhang, Y., Zou, Q., Greaves, D., Reeve, D., Hunt-Raby, A., Graham, D., et al. (2010). A level set immersed boundary method for water entry and exit. *Commun. Comput. Phys.* 8, 265–288. doi: 10.4208/cicp.060709.060110a

Conflict of Interest: The authors declare that the research was conducted in the absence of any commercial or financial relationships that could be construed as a potential conflict of interest.

frontiers in Earth Science

ORIGINAL RESEARCH
published: 05 October 2020
doi: 10.3389/feart.2020.527363

Research on Flood Propagation for Different Dam Failure Modes: A Case Study in Shenzhen, China

Weiqi Wang[1], *Wenjie Chen*[1] *and Guoru Huang*[1,2,3]*

[1] School of Civil Engineering and Transportation, South China University of Technology, Guangzhou, China, [2] State Key Laboratory of Subtropical Building Science, School of Civil Engineering and Transportation, South China University of Technology, Guangzhou, China, [3] Guangdong Engineering Technology Research Center of Safety and Greenization for Water Conservancy Project, Guangzhou, China

Dam-break flood simulation can evaluate the impact of a dam break, and is significant in conducting risk analyses, creating emergency plans, and mitigating calamities. In this study, the dam-break flood evolution process in the downstream areas of Minzhi Reservoir in Shenzhen, China, was investigated using a two-dimensional shallow-water model. The two-dimensional shallow-water model was utilized for solving two-dimensional shallow water equations for free-surface flow using the finite volume method. A refined grid with an unstructured mesh of triangular cells constrained by building walls was constructed in this model to represent urban structures. The dam-break flood hydrograph and the process of the expansion of the flood under different failure conditions were determined by adopting two breach mechanisms, namely, the instantaneous and gradual dam break mechanisms. The results indicated that the peak flow of the instantaneous dam break was relatively large at the beginning of the dam break. The peak flow in the case of the gradual dam break was comparatively small when seepage failure deformation occurred near the upper part of the dam. The inundation information obtained during the evolution of the dam-break flood, including information regarding the regularity of the flood evolution, distribution of the maximum water depth, and variation of the depth and velocity with time, were also analyzed.

Keywords: dam-break, flood propagation, shallow-water equations, numerical models, urban area

OPEN ACCESS

Edited by:
Mingfu Guan,
The University of Hong Kong,
Hong Kong

Reviewed by:
Zhiguo He,
Zhejiang University, China
Ilhan Özgen-Xian,
Lawrence Berkeley National Laboratory, United States

****Correspondence:***
Guoru Huang
huanggr@scut.edu.cn

Specialty section:
This article was submitted to Hydrosphere, a section of the journal Frontiers in Earth Science

Received: *16 January 2020*
Accepted: *18 September 2020*
Published: *05 October 2020*

Citation:
Wang W, Chen W and Huang G (2020) Research on Flood Propagation for Different Dam Failure Modes: A Case Study in Shenzhen, China. Front. Earth Sci. 8:527363. doi: 10.3389/feart.2020.527363

INTRODUCTION

Dams and reservoirs are vital hydraulic structures used for flood storage and energy supply, and they also play an increasingly important role in regional and national economic development. However, the use of reservoirs creates potential risks because of the massive quantity of water that is stored in reservoirs. A broken reservoir dam results in dam-break flood, leading to the rapid release of large volumes of water. It may have devastating consequences on human lives, property, and infrastructure (Penna et al., 2013; Azeez et al., 2019), especially in urban areas and in areas with a high population density and high property concentration.

Compared to other types of dams, such as concrete and rubber dams, earth dams have simple structures, and their loose soil particles have a relatively high probability of breaching. There are two major types of dam-break mechanisms: gradual dam break and instantaneous dam break. Currently, significant progress, with high stability and accuracy, has been made in research on the instantaneous

dam-break mechanism (Renzhi, 1982). However, stability and accuracy cannot be guaranteed in the case of a gradual dam break although several cases of gradual dam breaks have been investigated; this is because vital information regarding the gradual failure process is obtained through visual inspection. Studies on gradual failure can be classified into two categories. In the studies belonging to the first category, the regression equation is established using key parameters, such as dam height and reservoir storage capacity, to simulate the dam-break process (Macdonald and Langridgemonopolis, 1984; Wahl, 2004). In the studies belonging to the second category, the failure process of the internal structure of the dam is investigated based on fluid mechanics, dam hydraulics, and other disciplines to construct a considerably objective failure process model, such as dam-break model (Bechteler and Broich, 1991), BEED model (Singh, 1996), and Breach model (Fread, 1988). These models were developed based on previous failure instances, and essential details regarding the gradual failure process are not sufficiently accurate. Furthermore, these models are generalized at various levels, and researchers cannot determine the levels of generalization that provide satisfactory results. In general, although significant achievements have been made on dam-break simulations, theoretical developments are still required to improve the accuracy and stability of the results.

Studies on urban floods in urban areas are significant both theoretically and in actual flood control planning. In the last few decades, shallow water equations (SWEs) have been developed to provide relatively accurate numerical solutions that describe the flow characteristics of dam breaks. These SWEs were derived via the vertical integration of the Navier–Stokes equations using the boundary conditions of bottom and surface water. Academically, the three principal numerical approaches for simulating the urban floods are the finite difference method (Seyoum et al., 2012), the finite element method (Quecedo and Pastor, 2002; Hervouet, 2007; Karna et al., 2011), and the finite volume method (FVM) (Gallegos et al., 2009; Xia et al., 2019; Xing et al., 2019). With the development of numerical simulation technology, researchers gradually pay attention to the computational efficiency of the model. Neal et al. (2012) stated that the simplified form of the SWEs can achieve the same accuracy as the SWEs with a relatively less calculation time. In recent decades, several main simplified forms, such as the diffusive wave equations, the inertial formulation equations, and the kinematic wave equations, have been widely used in simulating urban floods (Chen et al., 2005; Yin et al., 2015; Li et al., 2020). Meanwhile, the graphic processing units (GPUs) accelerated computing technology has been noticed in reducing computational cost. Liang et al. (2015) presented a GPU-accelerated urban flood model and they accelerated the model's computational process up to nine times faster with the GPU parallel computing technology. The model proposed in this paper, the two-dimensional shallow-water model (SWM-2D) (Yu, 2015; Yu et al., 2015), is a FVM-based model for urban flood modeling. An implicit dual time-stepping method is implemented in SWM-2D to improve computational efficiency and it can reduce computational cost by 55–78% compared to the explicit time scheme with the same algorithm. The SWM-2D utilizes the Godunov-type FVM and the Harten-Lax-van Leer-Contact approximate Riemann solver to overcome the primary difficulties encountered in solving the SWEs including the wetting-drying boundary and hydraulic jumps problems. Chen et al. (2018) coupled the SWM-2D and the storm water management model and applied the validated model to simulating the inundation response to rainstorm patterns in an urban area. These studies showed that the SWM-2D has been exhibited an outstanding performance in modeling urban floods.

With the more frequent occurrence of urban flooding, urban flood modeling has increasingly gained the attention of researchers. As a significant feature in urban areas, the obstruction of impervious structures and preferential flow paths between buildings is an important factor that should be considered. In recent years, several studies have focused on the influence of impervious structures (Yu and Lane, 2006; Schubert et al., 2008; Neal et al., 2009). These studies have demonstrated that impervious structures and street slopes are significant factors with regard to flow paths in urban flood modeling. Furthermore, different methods have been proposed for describing the impact of impervious structures, such as building hole methods (Aronica and Lanza, 2005; Schubert et al., 2008), building resistance methods (Liang et al., 2007; Gallien et al., 2011), and building block methods (Hunter et al., 2008). These different methods are based on various data requirements with different complexities. However, the relationships between the complexity of the data and the accuracy of the method are unclear.

This paper researches the dam-break flood propagation process caused by various hypothetical dam failure modes of the Minzhi Reservoir Dam in Shenzhen, China. We firstly obtained the flood discharge hydrographs under four dam-break modes. Then the SWM-2D model was applied to simulate possible dam-break scenarios in urban areas. The flood propagation processes under different dam-break scenarios were illustrated and compared. The main innovations of this paper are 1) the different characteristics of flood flows under four dam failure modes were presented; 2) the significant impact of impervious buildings on dam-break flood propagation was studied with a self-developed model, SWM-2D model. The remainder of this study is organized as follows: *Materials and Methods* presents the flood discharge hydrographs and the SWM-2D model; *Results* shows the results obtained by the numerical simulation. Finally, discussion and conclusion are drawn in *Discussion and Conclusion*.

MATERIALS AND METHODS

Research Area

Minzhi Reservoir is situated in the Longhua New District in Shenzhen, China. The total reservoir capacity is 4.02 million m^3 at a check water level of 82.36 m, and the constant reservoir capacity is 2.71 million m^3 at a water level of 79.58 m. Minzhi Street, which covers a total area of 26 km^2 with a population of 427,000, is located in the downstream area of the Minzhi

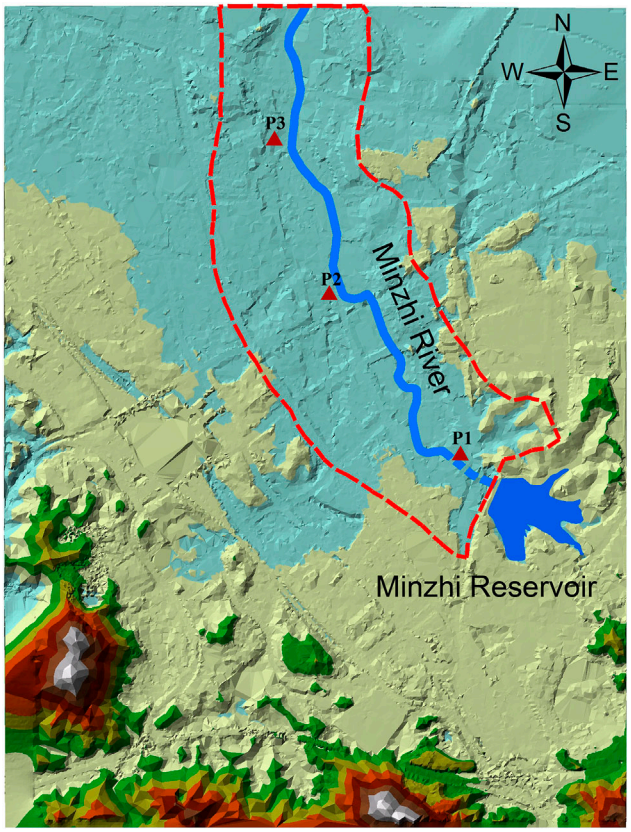

FIGURE 1 | Location of the study area and the three typical positions: P1, P2, and P3.

Reservoir. If the dam in the Minzhi Reservoir is broken, the dam-break flood from the rapidly released water will cause severe damages to lives, property, and infrastructure downstream. Considering the topography and area that would probably be submerged, a study area of 4 km^2 was examined in this study. Furthermore, three typical positions, Hengling Village in the upstream area near the reservoir (P1), residential and business districts around the midstream (P2), and the Shuiwei New Village in the downstream area (P3) were selected for detailed analysis. **Figure 1** shows the research area highlighted with red-bordered lines and three typical positions.

Failure Modes and Dam-Break Discharge

The main dam of the Minzhi Reservoir is an earth dam, and a gradual dam break is the most probable case. Because the risk of an instantaneous dam break owing to potential earthquakes or other natural factors (e.g., landslides) is higher than that of the occurrence of a gradual dam break, two breach mechanisms were adopted in this study to simulate the dam failure process and plot the flood hydrograph. These are the instantaneous (including partial and complete dam break) and gradual dam break mechanisms.

Regarding the calculation of the instantaneous dam-break discharge, there is a slight difference between the two methods. Following the approach used by Renzhi (1993), a series of formulas was used to calculate the peak discharge of the dam-break in this study. The discharge equation is expressed as follows:

$$Q_{\max} = \frac{8}{27}\sqrt{g}\left(\frac{B}{b_m}\right)^{0.25} b_m H_0^{1.5} \tag{1}$$

where $Q_{\max}$ is the peak discharge (m^3/s); g is the acceleration due to gravity (9.81 m^2/s); b_m is the width of the dam (m); B is the width of the breach (m); and H_0 is the water depth (m).

Assuming that Q is the discharge at time t (m^3/s), W is the capacity of the reservoir (m^3), and t is the duration of flood (s), the discharge-time equation is expressed as follows.

$$Q = Q_{\max}\left(\frac{Q_{\max}}{5W}t - 1\right)^4 \tag{2}$$

For the calculation of the gradual dam-break discharge, we assume that the dam initially undergoes seepage deformation to a certain extent, after which the dam body undergoes instantaneous failure. The seepage deformation of the dam begins with the formation of a small hole and expands gradually. In this case, the dam-break flood discharge is calculated using the following equation proposed by Yuanfang (2010):

$$Q_{\max} = A\left[2g\left(H - H_P\right)/\left(1 + fL/D\right)\right]^{0.5} \tag{3}$$

where H is the water level of the reservoir (m); A is the sectional area of the small hole (m^2); H_P is the elevation of the small hole (m); f is the Darcy's friction coefficient calculated using the Moody curve; L is the length of the hole (m); and D is the width of the hole (m). The initial shape of the hole is rectangular, and subsequently, the dam body undergoes instantaneous failure after the hole width gradually increases to 30 m. Furthermore, the calculation for the dam-break discharge after an instantaneous failure occurs is based on **Eq. (2)**.

Two breach mechanisms were adopted in this study: instantaneous dam-break (including partial and complete dam-break) and gradual dam-break. Four failure conditions were considered to simulate the dam-break. **Table 1** lists the details of the failure conditions.

The Two-Dimensional Shallow Water Model

The SWM-2D is a FVM based model used for modeling free-surface flow by solving the two-dimensional SWEs, which is the simplified form of the three-dimensional Navier–Stokes equations considering the vertical average, where the non-linear terms necessitate the adoption of certain assumptions and approximations when the horizontal length scale is significantly larger than the vertical scale. The matrix form of governing equations is expressed as follows:

$$\frac{\partial \boldsymbol{U}}{\partial t} + \frac{\partial \boldsymbol{E}}{\partial x} + \frac{\partial \boldsymbol{G}}{\partial y} = \boldsymbol{S} \tag{4}$$

where x, y are the two direction of Cartesian coordinates, $\boldsymbol{U}, \boldsymbol{E}$, and $\boldsymbol{G}$ are the vectors of conserved variables, $\boldsymbol{S}$ is source terms

TABLE 1 | Four different failure conditions.

Failure condition	Detailed information
C1	Instantaneous partial dam-break caused by natural factors with a normal water level of 79.58 m and a breach width of 100 m
C2	Instantaneous partial dam-break caused by natural factors with normal water level of 79.58 m, breach width of 320 m
C3	Instantaneous total dam-break caused by natural factors with a check water level of 82.36 m, breach width of 320 m
C4	Gradual dam-break with an initial rectangular hole, a normal water level of 79.58 m and a final breach width of 100 m

consisted of the bed slope source $\boldsymbol{S}_b$ and friction source $\boldsymbol{S}_f$, t is the time. The vectors are as following:

$$\boldsymbol{U} = \begin{bmatrix} h \\ hu \\ hv \end{bmatrix} \boldsymbol{E} = \begin{bmatrix} hu \\ hu^2 + g\left(h^2 - b^2\right)/2 \\ huv \end{bmatrix} \boldsymbol{G} = \begin{bmatrix} hv \\ huv \\ hv^2 + g\left(h^2 - b^2\right)/2 \end{bmatrix}$$

$$\boldsymbol{S} = \boldsymbol{S}_b + \boldsymbol{S}_f = \begin{bmatrix} 0 \\ g\,(h+b)\boldsymbol{S}_{ox} - gh\boldsymbol{S}_{fx} \\ g\,(h+b)\boldsymbol{S}_{oy} - gh\boldsymbol{S}_{fy} \end{bmatrix}$$

where h, b are water depth and bottom elevation, u, v are flow velocity in the x- and y-directions. G is the acceleration of gravity at 9.81 m/s^2; $\boldsymbol{S}_{ox}$, $\boldsymbol{S}_{oy}$ and $\boldsymbol{S}_{fx}$, $\boldsymbol{S}_{fy}$ are bed slopes and friction slopes in the x- and y-directions respectively.

A Godunov-type FVM based on an unstructured mesh is implemented in the SWM-2D. The integral form of governing equations is:

$$\int_{\Omega} \frac{\partial \boldsymbol{U}}{\partial t} d\Omega + \int_{\Omega} \left(\frac{\partial \boldsymbol{E}}{\partial x} + \frac{\partial \boldsymbol{G}}{\partial y} \right) d\Omega = \int_{\Omega} \boldsymbol{S} d\Omega \tag{5}$$

where Ω is the control volume. In the SWM-2D, a dual time-stepping approach with an effective implicit nonlinear lower–upper symmetric Gauss–Seidel algorithm is adopted to improve the model efficiency. The Harten-Lax-van Leer-Contact approximate Riemann solver (Toro, 2001) is applied to estimate the Riemann states to solve the Riemann problems. More detailed solution schemes to the SWM-2D are introduced in Yu et al. (2015). And five extensive test cases including two analytical benchmark cases and experimental and actual dam-break cases have been applied to validate the proposed model. The model showed good performance, which indicates the capabilities of the present model to achieve effective convergence to the steady state, to capture the discontinuous flows, and to accurately and efficiently handle complex shallow-water flows involving alternating wetting and drying episodes over highly irregular terrain.

Several sets of data were obtained to establish the flood inundation model. 1) A digital elevation model constructed using discrete elevation data was developed for constructing the terrain model. 2) According to the previous relevant investigations by Shenzhen Water Planning & Design Institute Co., Ltd., China, the value of the Manning coefficient n was set to 0.03 in this study. 3) Information on building footprints was outlined based on a computer-aided design file for the mesh generation using the building-hole method.

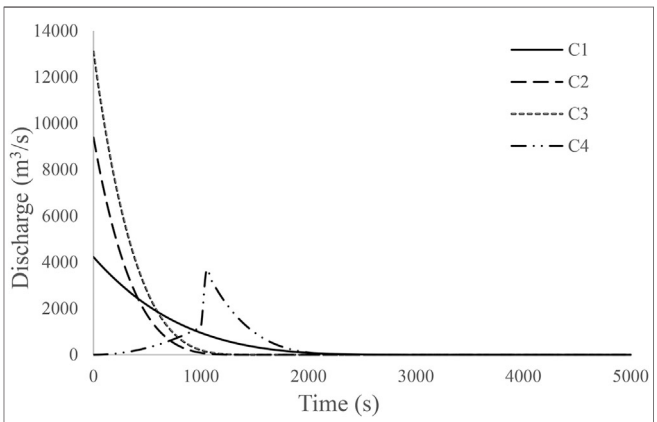

FIGURE 2 | Flood hydrographs under different conditions.

In this study, the mesh consisted of 65,089 triangle cells, and the meshes around the buildings were refined for the detailed analysis of the effect of impervious structures. The minimum mesh size around the buildings was approximately 1 m^2. Three types of boundary conditions were used in the model. The first boundary condition was the free-slip wall boundary condition, which was formulated for the building walls; the interior of this boundary type does not participate in the water exchange. The second boundary condition was the dam-break flood discharge, which was determined in the previous section and is applied at the breach position. The third condition was the free outflow boundary condition, which exists along the research area boundaries.

RESULTS

Analysis of Dam-Break Flood Hydrographs

The flood hydrographs of the dam-break under four hypothetical conditions, as shown in **Figure 2**, were plotted based on the different reservoir water levels (normal water level and check water level) using the equations in *Failure Modes and Dam-Break Discharge* section.

Figure 2 shows that for the instantaneous dam break, the discharge reaches its maximum value at the initial moment of the breaking of the dam, and then drops rapidly with a continuous decrease in water level in the reservoir because of the flood

TABLE 2 | Flood parameters under different conditions.

Condition	Water level (m)	Breach width (m)	Max. discharge (m^3/s)	Duration (min)
C1	79.58	100	4,220	52
C2	79.58	320	9,386	23
C3	82.36	320	13,101	25
C4 (gradual)	79.58	100	3,632	48

TABLE 3 | Analysis of water balance.

Duration (min)	Discharge flow (m^3)	Inundation flow (m^3)	Relative error (%)
1	7.272×10^5	7.194×10^5	0.99
5	2.671×10^6	2.679×10^6	0.29
10	3.696×10^6	3.716×10^6	0.54
25	4.04×10^6	4.059×10^6	0.47
40	4.04×10^6	4.065×10^6	0.61

outflow. In addition, there was a significant positive correlation between the maximum peak discharge and the breach width, and a negative correlation with the duration of the flood. Regarding the gradual dam break, the dam-break discharge slowly increased with the gradual widening of the hole width of the hole at the initial seepage deformation. Owing to the failure of the dam body after seepage deformation developed, the flood discharge rapidly reached the maximum value, similar to the case of the instantaneous dam break. During this discharge process, the maximum discharge in the seepage deformation stage was 1,206 m^3/s, and it rapidly reached 3,632 m^3/s when the dam body experienced failure. The detailed parameters of the flood discharge under different operating conditions are listed in **Table 2**.

Analysis of Water Volume Balance

To ensure the rationality of this model based on the SWM-2D, the analysis of water balance is essential. The discharge flow was calculated using the dam-break flood hydrograph, and the water volume in the inundation area was obtained from the simulation results. The approach for verifying the water volume balance involved comparing their differences. **Table 3** shows the comparison between the discharged flow and water volume in flood model inundation areas under the failure condition 3 at 1, 5, 10, 25, and 40 min. From **Table 3**, the water volumes obtained using the two statistical methods were almost equal, and the model was rational with respect to the water balance because the maximum relative error was only 0.99%.

Flood Inundation Information

The most severe submerged condition (condition 3) was selected for detailed analysis. The flood inundation maps at different times are shown in **Figure 3**.

From the flood inundation maps in **Figure 3**, we can observe the complete process of flood routing in the research area. Within 1 min of the dam break, the upstream residential areas were rapidly submerged owing to the outflow of a significant quantity of flood water at a high flow velocity. Within 20 min, the flood submerging range extended to the middle reaches, where residential and commercial buildings were concentrated, and the dam-break flood continued to expand as it traveled downstream. Within 40 min, downstream areas are affected by the dam-break flood. The flood began to recede slowly because of the influence of dense impervious structures after 80 min.

The maximum submerged depth of water refers to the maximum submerged water level during the evolution of a dam-break flood. It is an indicator of the severity of flood submergence: the higher the maximum submerged water depth, the more severe the damages. The maximum submerged depth of the flood can aid in evaluating the distribution of the areas severely affected owing to the dam-break flood in the urban area. From the simulation results, the maximum submerged depth information of each grid under the four conditions was extracted, as displayed in **Figure 4**.

Form the maximum submerged depth maps, we can observe that during the occurrence of an urban dam-break flood, the maximum submerged water depth was significantly influenced by the local buildings. The maximum water depth can reach 18 m in the worst case (condition 3) in the front of the building which is most closed to the dam breach. And the water depth between the buildings is relatively lower owing to the restrictions provided by the streets on the flood discharge. The main reason for this trend was that the flood water was obstructed by local impervious structures when the dam-break flood entered the city. Thus, it could not flow out within a short period through the roads or streets, where the terrain was flat or the surface elevation was significantly lower, but the channel is considerably narrow. Hence, the water level rose rapidly in the region in front of the buildings.

Analysis of Water Depth and Velocity

We selected three typical positions in the analysis of the flood routing results to demonstrate the regularity of the flood evolution process of a dam-break flood and to provide a better representation of the developmental process. The positions were in the concentrated residential areas and were severely affected by the flood; the positions included Hengling Village at the upstream near the reservoir (P1), the residential and business districts around the midstream (P2), and Shuiwei New Village at the downstream (P3). **Figures 5**, **6** show the water depth and velocity variations, respectively, with time, at the typical positions under the four failure conditions.

For the instantaneous dam break, the depth-time graphs indicate that the water depth at each typical position increases rapidly with the occurrence of the upstream flood, and there was variation in the increase in the water depth with respect to different reservoir water levels. The dam-break flood arrived at

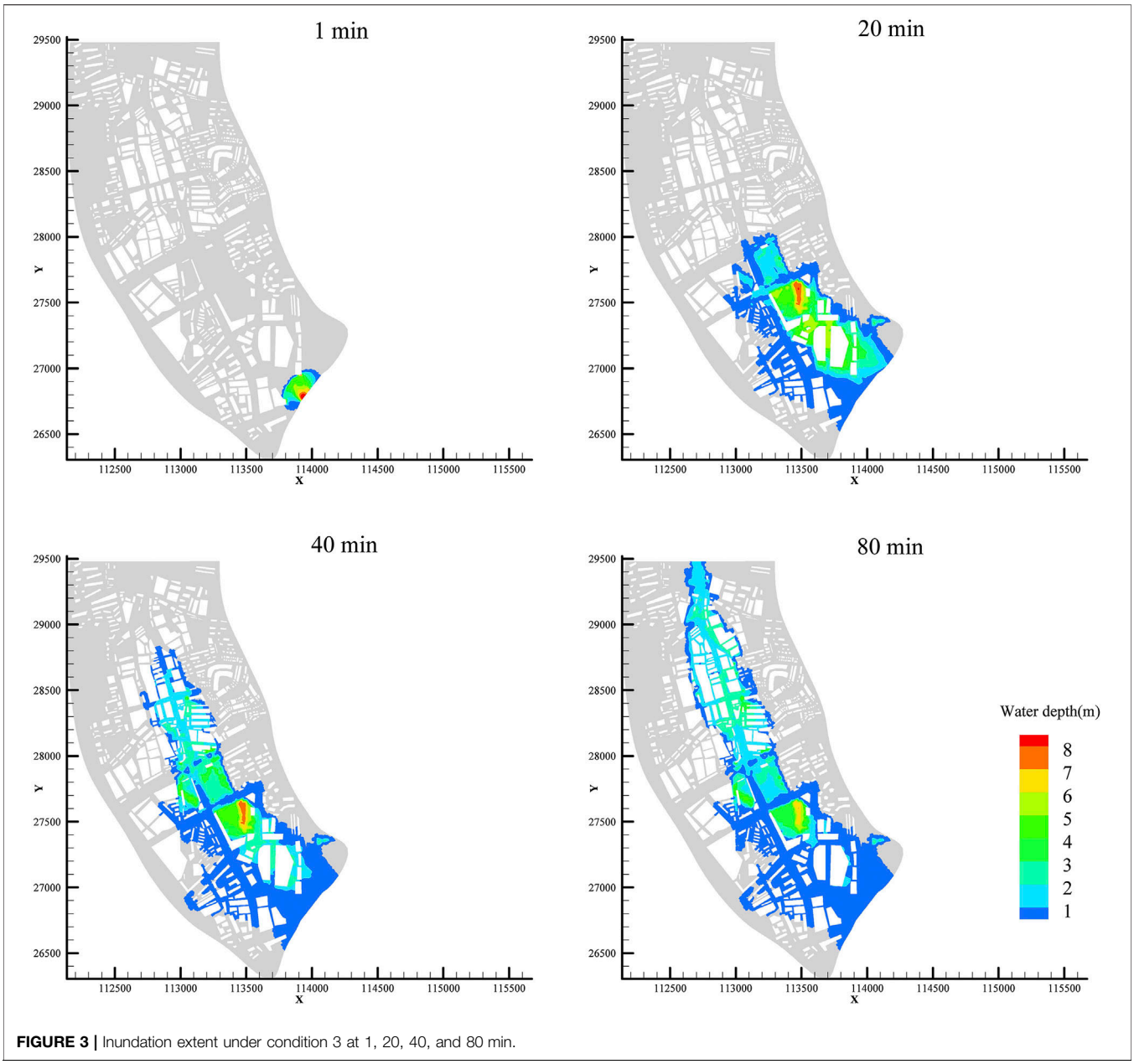

FIGURE 3 | Inundation extent under condition 3 at 1, 20, 40, and 80 min.

Hengling Village within 50 s with rapidly rising water levels, and the water depth could reach a maximum of 11.91 m under failure condition 3. Subsequently, the water depth decreased significantly until the reservoir was empty. Moreover, the maximum water depths were comparatively low under the other failure conditions. And there is still a pounding after the flood receded because of the relatively low topography. The regularity of the flood evolution processed at P2 and P3 was similar. But there still exists some differences that compared to condition 1, the maximum water depth at P2 and P3 are lower under condition 2, although the peak discharge of condition 2 is larger. The reason for this situation can be indicated by the flood hydrographs and the flood wave propagation. In condition 2, the flood extent in upstream areas is much larger because of the wider breach of the dam and the higher flood peak discharge. With the same total volume of dam-break flood water, the water depth at P2 and P3 is lower under condition 2 because of the more powerful restrictions provided by more impervious structures upstream on the flood discharge. Unlike in the case of the instantaneous dam-break, the rate of increase in the water depth for the gradual dam break was slower when the dam-break flood had just arrived at P1 because of the effect of the initial seepage deformation stage. However, this phenomenon was observed only at P1 because P2 and P3 were far from the dam breach position, and the deformation effect becomes slighter and can be neglected. The maximum water depth slightly decreased, and the flood arrival time is delayed evidently because the dam-break discharge is small and increases slowly at the initial time of failure.

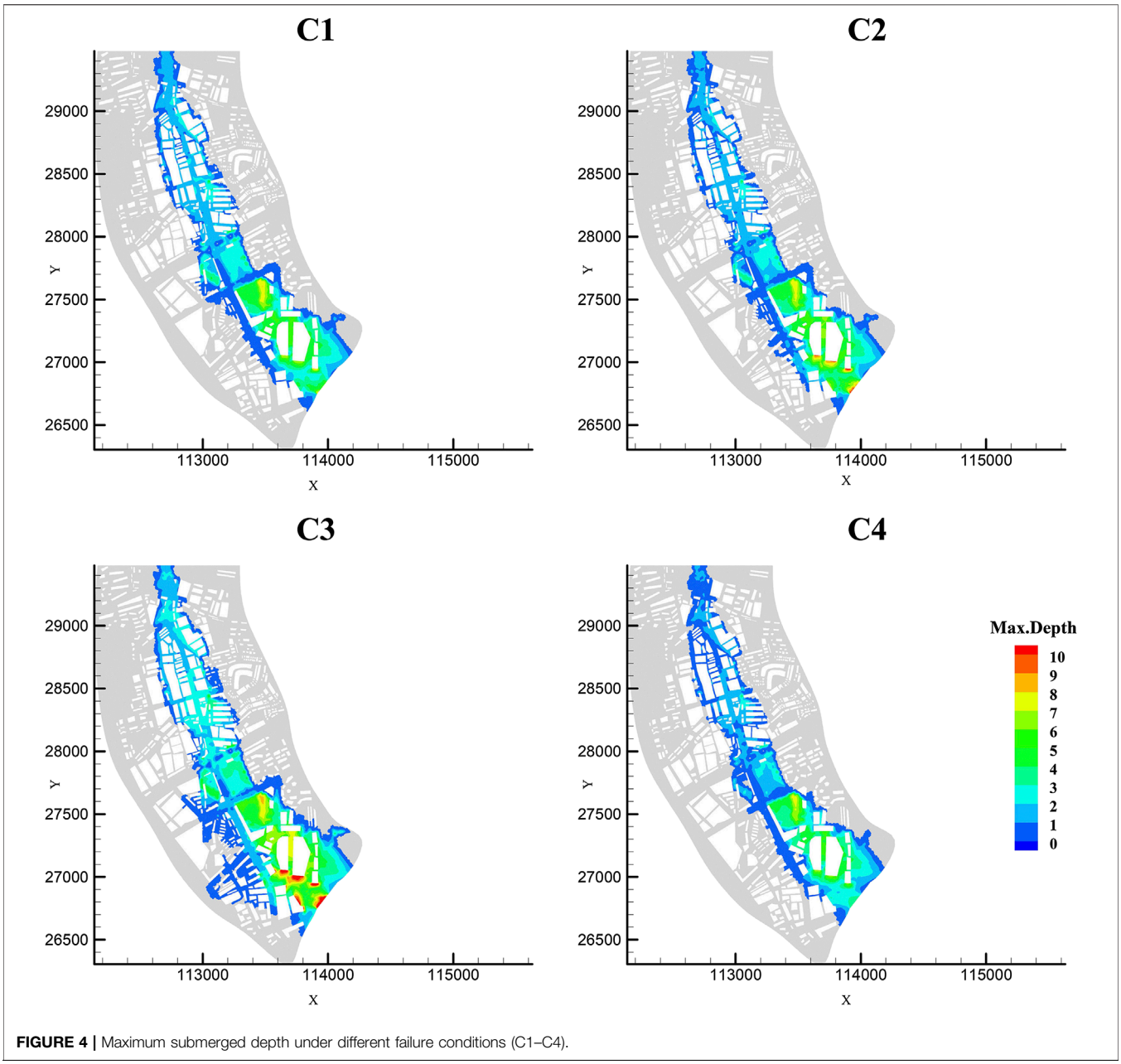

FIGURE 4 | Maximum submerged depth under different failure conditions (C1–C4).

The velocity–time graphs presented above show the regularity of the velocity variation with time at each typical position. The maximum flow velocity along the typical positions decreased gradually as the flood flowed downstream. At Hengling Village (P1), a maximum flow velocity exceeding 10.7 m/s can be attained under failure conditions 3, which may damage the buildings. the water depth decreased significantly until the reservoir was empty. However, at positions 2 and 3, which were far from the breach position, the flow velocity dropped to below 2.5 m/s and had a slight influence on the structural safety of the buildings. The flow velocity in the case of the gradual dam break was significantly slower than that in the case of the instantaneous dam break, and this phenomenon was particularly evident in the area near the breach position. Furthermore, a similar phenomenon was observed in the case of the regularity of the water depth. This could be owing to the dam-break flood effect caused by the different failure modes (instantaneous dam break and gradual dam break), which gradually becomes evident with a decrease in the distance between the affected area and the breach position. **Table 4** shows the key parameters in the flood routing progress.

DISCUSSION AND CONCLUSION

In this study, the dam-break flood hydrographs under various hypothetical failure modes, including instantaneous dam-break

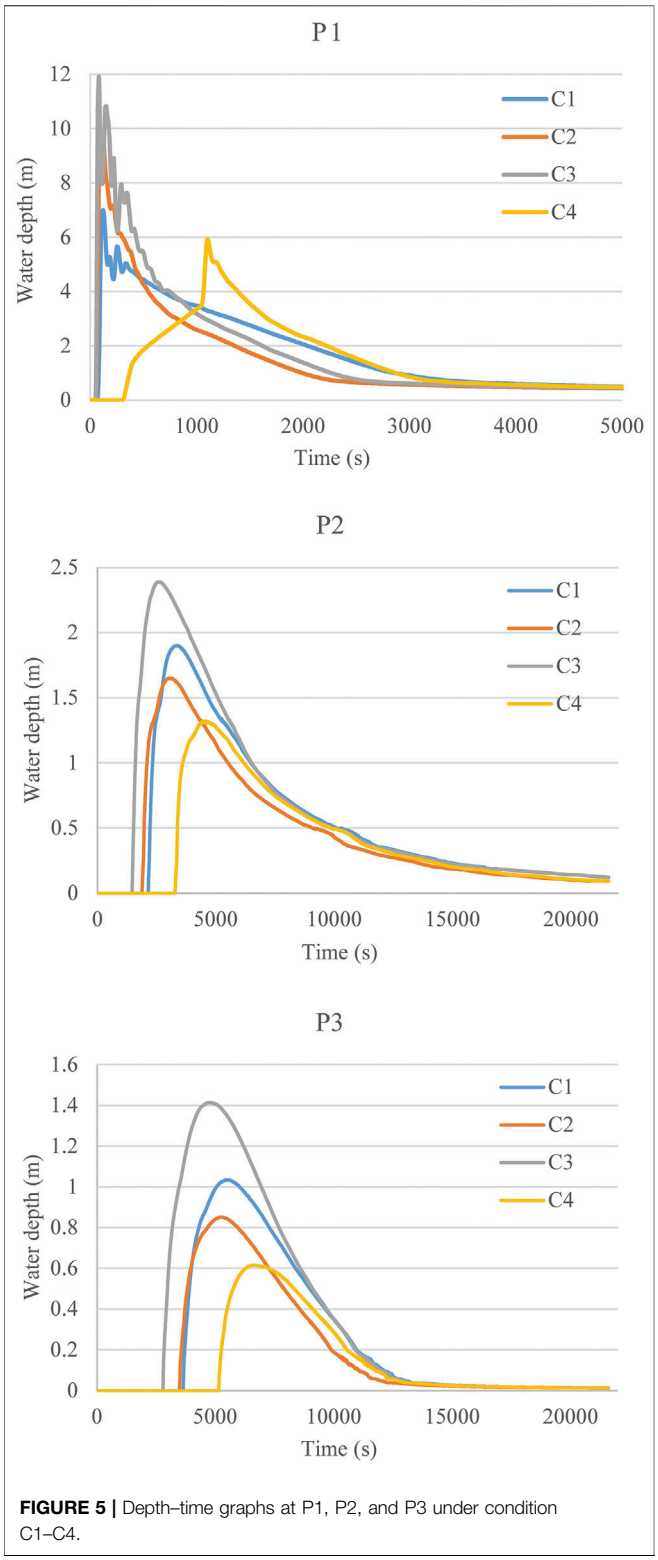

FIGURE 5 | Depth–time graphs at P1, P2, and P3 under condition C1–C4.

and gradual dam-break, were calculated. The 2D hydrodynamic model based on the SWM-2D was built to study the flood wave propagation caused by four different hypothetical failure modes for the downstream urban areas of the Minzhi Reservoir Dam in Shenzhen, China.

Dam-break floods in urban areas can lead to different flow problems and it is difficult to resolve these problems using numerical methods, such as flows with highly unsteady, hydraulic jumps, and wetting and drying problems. In this study, the feasibility of the dam-break model based on the SWM-2D is verified preliminarily, according to the analysis results of the water volume balance and hazard data (such as data regarding the regularity of the flood evolution, the variation of water depth and velocity with time, and the distribution of the

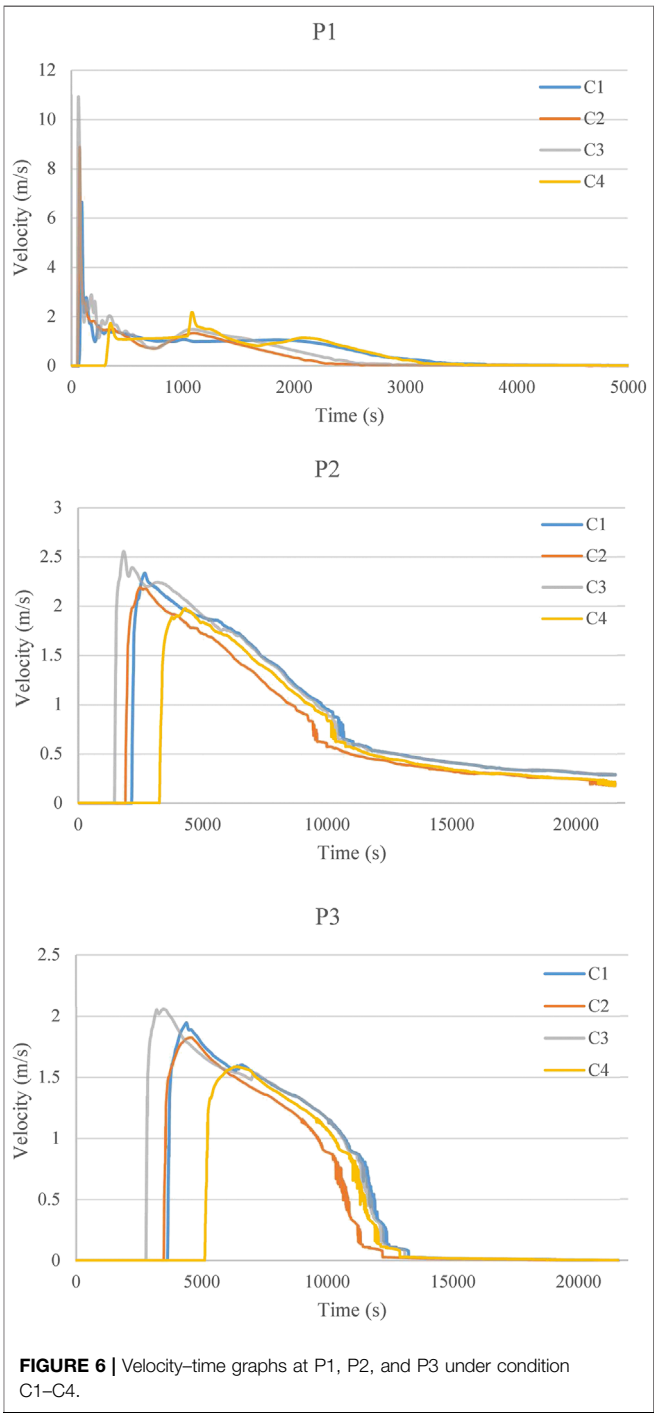

FIGURE 6 | Velocity–time graphs at P1, P2, and P3 under condition C1–C4.

TABLE 4 | Key parameters in the flood routing progress.

Condition	C1			C2			C3			C4		
Position	**P1**	**P2**	**P3**	**P1**	**P2**	**P3**	**P1**	**P2**	**P3**	**P1**	**P2**	**P3**
Max. depth (m)	6.99	1.9	1.03	9.69	1.65	0.85	11.91	2.38	1.41	5.9	1.32	0.62
Duration (s)	70.5	2,130	3,638	60	1,870	3,482	50	1,451	2,781	321	3,265	5,137
Pounding (m)	0.33	0.09	0	0.33	0.09	0	0.33	0.09	0	0.33	0.09	0
Max. velocity (m/s)	6.6	2.34	1.95	8.87	2.2	1.83	10.7	2.56	2.06	2.16	1.98	1.59

maximum water depth) obtained during the evolution of the dam-break flood.

The flood hydrographs indicate that the water level in a reservoir when the dam break occurs plays a significant role in discharge forecasting, especially for the upstream areas. In addition, particularly for the gradual dam break, the prediction of the breach geometry is a critical factor in the dam-break simulation, but the accuracy of the prediction is difficult to guarantee. Hence, the real-time monitoring of the reservoir water level is a significant prerequisite in dam safety programs and the flood risk management of dam failure.

The various flood inundation maps show that impervious structures have a crucial impact on the regular pattern of dam-break flood propagation in urban areas. And the distance in-between adjacent impervious buildings is a important parameter to the influence of impervious structures on inundation flow because this aspect is related to the possibility for water to penetrate inside a block of buildings. As Bruwier et al. (2018) indicated, in flood-resilient urban planning, increasing the spacing between buildings will significantly reduce the backwater effect of impervious buildings on inundation flow. The variation of flood hydrographs has a significant influence on the submerged condition of the upstream areas. But with the obstruction of impervious structures and the consumption of flood energy, the impact of variation of flood hydrographs decreases gradually, especially in the residential areas with dense impervious structures. And the results also indicate that a higher peak flood discharge does not always lead to a higher water depth. The reason for this situation can be that the flood extent in upstream areas may be much larger with a higher flood peak discharge, while the total volume of dam-break flood is the same. This situation can result in a lower water depth in the downstream areas with a higher peak flood discharge.

Compared to other flood models, the effect of impervious structures is particularly significant in the urban flood model. The building hole method can be used to describe the shape of buildings accurately, and the method demonstrates exceptional performance in simulating the obstruction of impervious structures. However, considering the significant complexities of building shapes, the use of this method can result in unexpected mesh refinements. This phenomenon also occurs around the narrow gaps between the impervious structures and facilities with complex outlines, which can increase the calculation time.

AUTHOR CONTRIBUTIONS

WW, WC developed the model and analyzed the simulation results; WW, WC discussed the results; WW drafted the manuscript and WC critically revised the paper; GH designed and supervised the study.

FUNDING

This work was funded by the National Key R&D Program of China (2017YFC1502704); the National Natural Science Foundation of China (51739011).

REFERENCES

Aronica, G. T., and Lanza, L. G (2005). Drainage efficiency in urban areas: A case study. *Hydrol. Process.* 19 (5), 105–1119. doi:10.1002/hyp.5648

Azeez, O., Elfeki, A. M. M., Kamis, A. S., and Chaabani, A. (2019). Dam break analysis and flood disaster simulation in arid urban environment: The Um Al-Khair dam case study, Jeddah, Saudi Arabia. *Nat. Hazards.* 100, 1011–1995. doi:10.1007/s11069-019-03836-5

Bechteler, W., and Broich, K. (1991). *Effects in Dam-Break Modeling*. Madrid, Spain: Congress of the International Association Hydraulic Research, IAHR.

Bruwier, M., Mustafa, A., Aliaga, D. G., Archambeau, P., Erpicum, S., Nishida, G., et al. (2018). Influence of urban pattern on inundation flow in floodplains of lowland rivers. *Sci. Total Environ.* 622–623, 446–458. doi:10.1016/j.scitotenv.2017.11.325

Chen, A. S., Hsu, M. H., Chen, T. S., and Chang, T. J. (2005). An integrated inundation model for highly developed urban areas. *Water Sci. Technol.* 51 (2), 221–229. doi:10.2166/wst.2005.0051

Chen, W., Huang, G., Zhang, H., and Wang, W. (2018). Urban inundation response to rainstorm patterns with a coupled hydrodynamic model: A case study in Haidian Island, China. *J. Hydrol.* 564, 1022–1035. doi:10.1016/j.jhydrol.2018.07.069

Fread, D. (1988). *BREACH, An Erosion Model for Earthen Dam Failures*. MD, United States: Hydrologic Research Laboratory, National Weather Service, NOAA.

Gallegos, H. A., Schubert, J. E., and Sanders, B. F. (2009). Two-dimensional, high-resolution modeling of urban dam-break flooding: A case study of Baldwin Hills, California. *Adv. Water Resour.* 32 (8), 1323–1335. doi:10.1016/j.advwatres.2009.05.008

Gallien, T. W., Schubert, J. E., and Sanders, B. F. (2011). Predicting tidal flooding of urbanized embayments: A modeling framework and data requirements. *Coast Eng.* 58 (6), 567–577. doi:10.1016/j.coastaleng.2011.01.011

Hervouet, J.-M. (2007). *Hydrodynamics of Free Surface Flows: Modelling with the Finite Element Method*. New York: Wiley Online Library.

Hunter, N. M., Bates, P. D., Neelz, S., Pender, G., Villanueva, I., Wright, N. G., et al. (2008). Benchmarking 2D hydraulic models for urban flood simulations. *Water Manag.* 161 (1), 13–30. doi:10.1680/wama.2008.161.1.13

Karna, T., De Brye, B., Gourgue, O., Lambrechts, J., Comblen, R., Legat, V., et al. (2011). A fully implicit wetting-drying method for DG-FEM shallow water models, with an application to the Scheldt Estuary. *Comput. Methods Appl. Mech. Eng.* 200 (5), 509–524. doi:10.1016/j.cma.2010.07.001

Li, H., Gao, H., Zhou, Y., Xu, C.-Y., Ortega, M. R. Z., and Sælthun, N. R. (2020). Usage of SIMWE model to model urban overland flood: A case study in Oslo. *Hydrol. Res.* 51 (2), 366–380. doi:10.2166/nh.2020.068

Liang, D., Falconer, R. A., and Lin, B. (2007). Coupling surface and subsurface flows in a depth averaged flood wave model. *J. Hydrol.* 337 (1), 147–158. doi:10.1016/j.jhydrol.2007.01.045

Liang, Q., Xia, X., and Hou, J. (2015). Efficient urban flood simulation using a GPU-accelerated SPH model. *Environ. Earth Sci.* 74 (11), 7285–7294. doi:10.1007/s12665-015-4753-4

Macdonald, T. C., and Langridgemonopolis, J. (1984). Breaching characteristics of dam failures. *J. Hydraul. Eng.* 110 (5), 567–586. doi:10.1061/(ASCE)0733-9429(1984)110:5(567)

Neal, J. C., Bates, P. D., Fewtrell, T. J., Hunter, N. M., Wilson, M. D., and Horritt, M. S. (2009). Distributed whole city water level measurements from the Carlisle 2005 urban flood event and comparison with hydraulic model simulations. *J. Hydrol.* 368 (1), 42–55. doi:10.1016/j.jhydrol.2009.01.026

Neal, J., Villanueva, I., Wright, N., Willis, T., Fewtrell, T., and Bates, P. (2012). How much physical complexity is needed to model flood inundation? *Hydrol. Process.* 26 (15), 2264–2282. doi:10.1002/hyp.8339

Penna, I. M., Derron, M. H., Volpi, M., and Jaboyedoff, M. (2013). Analysis of past and future dam formation and failure in the Santa Cruz River (San Juan province, Argentina). *Geomorphology* 186 (2), 28–38. doi:10.1016/j.geomorph.2012.12.011

Quecedo, M., and Pastor, M. (2002). A reappraisal of Taylor–Galerkin algorithm for drying–wetting areas in shallow water computations. *Int. J. Numer. Methods Fluid.* 38 (6), 515–531. doi:10.1002/fld.225

Renzhi, X. (1982). Computation for the discharge from the site of dam-break. *J. Nanjiang Hydraul. Res. Inst.* (1), 43–58. doi:10.16198/j.cnki.1009-640x.1982.01.004

Renzhi, X. (1993). *Hydraulics of Dam Break*. Jinan: Shandong Science and Technology Press.

Schubert, J. E., Sanders, B. F., Smith, M. J., and Wright, N. G. (2008). Unstructured mesh generation and landcover-based resistance for hydrodynamic modeling of urban flooding. *Adv. Water Resour.* 31 (12), 1603–1621. doi:10.1016/j.advwatres.2008.07.012

Seyoum, S. D., Vojinovic, Z., Price, R. K., and Weesakul, S. (2012). Coupled 1D and noninertia 2D flood inundation model for simulation of urban flooding. *J. Hydraul. Eng.* 138 (1), 23–34. doi:10.1061/(asce)hy.1943-7900.0000485

Singh, V. P. (1996). *Dam Breach Modeling Technology*. Netherlands: Springer.

Toro, E. F. (2001). *Shock-Capturing Methods for Free-Surface Shallow Flows*. New York: John Wiley.

Wahl, T. L. (2004). Uncertainty of predictions of embankment dam breach parameters. *J. Hydraul. Eng.* 130 (5), 389–397. doi:10.1061/(asce)0733-9429(2004)130:5(389)

Xia, X., Liang, Q., and Ming, X. (2019). A full-scale fluvial flood modelling framework based on a high-performance integrated hydrodynamic modelling system (HiPIMS). *Adv. Water Resour.* 132, 103392. doi:10.1016/j.advwatres.2019.103392

Xing, Y., Liang, Q., Wang, G., Ming, X., and Xia, X. (2019). City-scale hydrodynamic modelling of urban flash floods: The issues of scale and resolution. *Nat. Hazards.* 96 (1), 473–496. doi:10.1007/s11069-018-3553-z

Yin, J., Yu, D., Yin, Z., Wang, J., and Xu, S. (2015). Modelling the anthropogenic impacts on fluvial flood risks in a coastal mega-city: A scenario-based case study in Shanghai, China. *Landsc. Urban Plann.* 136, 144–155. doi:10.1016/j.landurbplan.2014.12.009

Yu, D., and Lane, S. N. (2006). Urban fluvial flood modelling using a two-dimensional diffusion-wave treatment, part 1: Mesh resolution effects. *Hydrol. Process.* 20 (7), 1541–1565. doi:10.1002/hyp.5935

Yu, H., Huang, G., and Wu, C. (2015). Efficient finite-volume model for shallow-water flows using an implicit dual time-stepping method. *J. Hydraul. Eng.* 141 (6), 04015004. doi:10.1061/(asce)hy.1943-7900.0000998

Yu, H. (2015). Research on numerical simulation technology of urban floods. dissertation/doctoral thesis. Guangzhou: South China University of Technology.

Yuanfang, Z. (2010). Study on numerical simulation of dam-break flood on the Da Nanshan Reservoir. dissertation/master's thesis. Changsha: Changsha University of Science & Technology.

Conflict of Interest: The authors declare that the research was conducted in the absence of any commercial or financial relationships that could be construed as a potential conflict of interest.

frontiers in Earth Science

ORIGINAL RESEARCH
published: 27 October 2020
doi: 10.3389/feart.2020.00346

Discrete Boltzmann Numerical Simulation of Simplified Urban Flooding Configurations Caused by Dam Break

Michele La Rocca, Stefano Miliani and Pietro Prestininzi*

Department of Engineering, Roma Tre University, Rome, Italy

The Discrete Boltzmann Equation (DBE) is a versatile simulation method, consisting of linear advection equations, which can be applied to the Shallow Water Equations (SWE). The aim of this study is to assess the accuracy of the DBE to simulate dam-break of shallow water flows in presence of obstacles. Dam-break flows in the presence of obstacles can be regarded as simplified models for floods in urban areas. In this study, three cases of dam-break flows in the presence of obstacles are considered: two with an isolated obstacle and the third in presence of an idealized city. A comparison between DBE and benchmark results shows a fair agreement, confirming the validity of the DBE as simulation method for the SWE.

Keywords: Shallow Water Equations (SWE), discrete Boltzmann method, dam-break flow, urban flooding, experimental dam break

OPEN ACCESS

Edited by:
Jingming Hou,
Xi'an University of Technology, China

Reviewed by:
Alexander Maria Rogier Bakker,
Directorate-General for Public Works and Water Management, Netherlands
Jianmin Zhang,
Sichuan University, China

****Correspondence:***
Michele La Rocca
michele.larocca@uniroma3.it

Specialty section:
This article was submitted to Hydrosphere, a section of the journal Frontiers in Earth Science

Received: *25 December 2019*
Accepted: *27 July 2020*
Published: *27 October 2020*

Citation:
La Rocca M, Miliani S and Prestininzi P (2020) Discrete Boltzmann Numerical Simulation of Simplified Urban Flooding Configurations Caused by Dam Break. Front. Earth Sci. 8:346. doi: 10.3389/feart.2020.00346

1. INTRODUCTION

Flooding is considered one of the most significant hazards society is facing. Huge losses in terms of human lives, damages to buildings, houses, and civil infrastructures are caused every year by hurricanes and flooding. Moreover, the impact of flooding in the future is expected to become increasingly important due to deforestation and depopulation of rural zones (Sanders and Schubert, 2019).

Urban flooding are particularly fearsome events, considering that more than half of the world's population lives in urban areas and that the urban population is continuously increasing (Song et al., 2019). The prediction of expected consequences of urban flooding as well as the design and the adoption of mitigation measures is a crucial issue that nowadays takes advantages of numerical simulations.

The main mathematical model for flood simulation is based on the two-dimensional Shallow Water Equations (SWE), which is obtained by averaging mass and momentum balance equations along the vertical direction under the classical assumption of hydrostatic pressure distribution (Valiani and Begnudelli, 2006). In the last decades, great attention has been paid to the development of numerical solvers for the SWE (Toro and Garcia-Navarro, 2007; Toro, 2009). The latter tackle directly the SWE by means of the finite volumes discretization and have reached a sufficient level of complexity so that they are able to account for crucial issues such as to cite just a few, the treatment of topography source terms (Duran and Marche, 2014; Hou et al., 2018), the use of unstructured grids (Zhao et al., 2019), and the evolution of wet-dry fronts (Ferrari et al., 2019).

An alternative option is represented by the Smoothed Particle Hydrodynamics (SPH) formulation of the SWE (Chang et al., 2018). The latter give rise to strongly non-linear equations

whose numerical treatment needs particular care. Moreover, the numerical algorithms of SPH-based methods are intrinsically non-local, thus implying typically a high computational burden.

Solution methods for the SWE have also been developed in the Lattice Boltzmann Equation (LBE) framework (Zhou, 2004); these methods take advantage of the simplicity and versatility of the stream and collide LBE algorithm (Succi, 2001). The LBE proposes a mesoscopic representation of the flows based on the concept of the probability density function associated to a fluid particle traveling along a given direction with a given particle velocity (Succi, 2001). The finite set of particle velocities is defined in such a way that a symmetric regular spatial lattice is generated (Succi, 2001). Macroscopic quantities, such as vertically averaged velocity and water depth in shallow water flows, are calculated as statistical moments of the probability density functions (Zhou, 2004). However, no matter how appealing the application of the LBE to shallow water flows may be, the LBE is limited to the simulation of subcritical flows unless an *ad hoc*-defined lattice is adopted instead of the usual one, as in Hedjripour et al. (2016), where only one-dimensional transcritical shallow water flows have been considered. This is an unacceptable limitation, as the simulation of flooding problems cannot rule out the occurrence of transcritical flows. This fact addressed the research toward the use of multispeed particle velocity sets together with a finite difference discretization of the Boltzmann equation. The resulting model, the multispeed Discrete Boltzmann Equation (DBE), is able to deal with transcritical flows, both 1D and 2D, preserving the linearity of the LBE numerical algorithm (La Rocca et al., 2015). The DBE has been also successfully applied to the investigation of the dynamics of two-phase (La Rocca et al., 2018) and polydisperse (La Rocca et al., 2019) shallow granular flows.

The aim of this paper is to assess the ability of the DBE in simulating dam-break flows impacting on obstacles as a preliminary step for the simulation of urban flooding events on real topography. Indeed dam-break flows impacting on obstacles can be considered as simplified models of urban flooding, and the scientific literature abounds with experiments and numerical simulations of dam-break flows impacting on obstacles. In this paper, the experimental and numerical dam-break flows of Kleefsman et al. (2005), Soares-Frazão and Zech (2007), and Soares-Frazão and Zech (2008) are considered as benchmarks. In Kleefsman et al. (2005) and Soares-Frazão and Zech (2007), the dam-break flow interacts with an isolated obstacle, while in Soares-Frazão and Zech (2008) the dam-break flow interacts with an idealized city, which realized by means of a regular array of parallelepipeds.

In these works, water depth and velocity are measured at given measurement points and/or are numerically calculated by means of previously validated finite volume-based numerical solvers

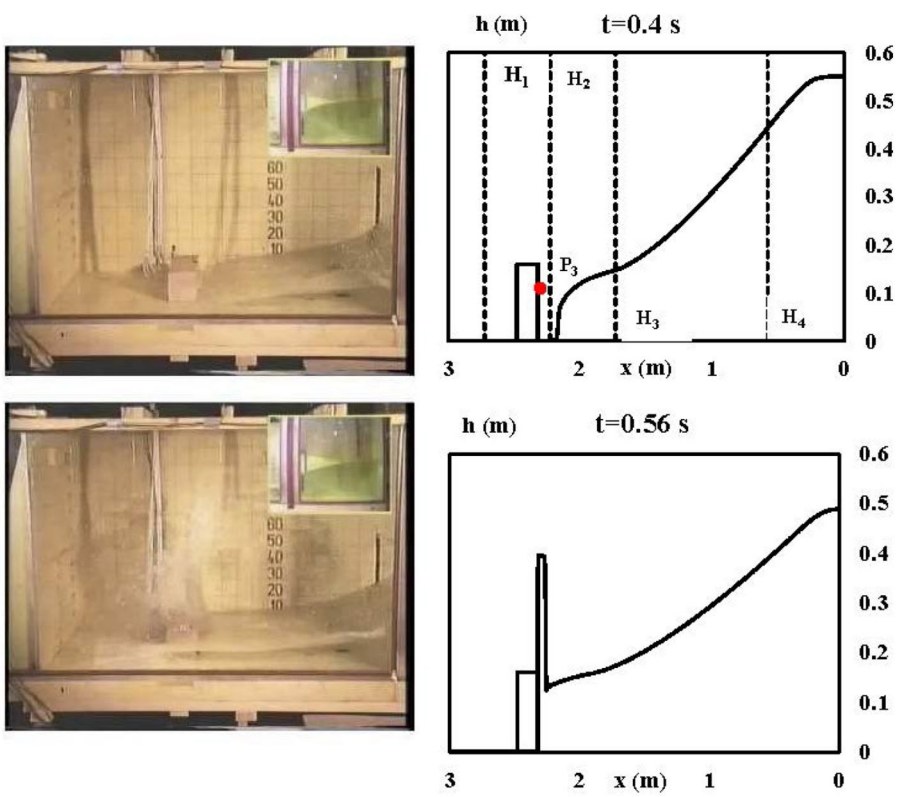

FIGURE 1 | Test case I. Experimental and numerical free surface profiles at $t = 0.4s$ and $t = 0.56$. **Right**: numerical free surface profiles. Top right panel shows gauges positioning along the centreline. Vertical dashed lines: positions of the height probes $H_1, H_2, H_3, and\ H_4$; dot on the obstacle: position of the $P3$ pressure probe. **Left**: experimental profiles of Kleefsman et al. (2005).

either applied to the SWE (Soares-Frazão and Zech, 2007, 2008), or to the Navier-Stokes equations (Kleefsman et al., 2005). A comparison between numerical results obtained solving the SWE by means of the DBE and reference results is encouraging and proves the ability of the DBE as a simulation tool of dam break flows interacting with obstacles.

The structure of the paper is as follows: first, the mathematical model is briefly presented; second, the considered benchmarks are described; third, results are reported and commented on; and fourth, conclusions are drawn.

2. THE MATHEMATICAL MODEL

The SWE, obtained by averaging mass and momentum balance equations along the vertical direction under the classical assumption of hydrostatic pressure distribution (Valiani and Begnudelli, 2006), assume the following form:

$$\begin{aligned}
&\frac{\partial h}{\partial t}+\frac{\partial Uh}{\partial x}+\frac{\partial Vh}{\partial y}=0\\
&\frac{\partial Uh}{\partial t}+\frac{\partial}{\partial x}\left(U^2h+g\frac{h^2}{2}\right)+\frac{\partial}{\partial y}(UVh)=\frac{\partial}{\partial x}\left(g\frac{h^2}{2}\right)\Bigg|_{\eta}\\
&-g\frac{n_m^2}{h^{1/3}}U\sqrt{U^2+V^2}\\
&\frac{\partial Vh}{\partial t}+\frac{\partial}{\partial x}(UVh)+\frac{\partial}{\partial y}\left(V^2h+g\frac{h^2}{2}\right)=\frac{\partial}{\partial y}\left(g\frac{h^2}{2}\right)\Bigg|_{\eta}\\
&-g\frac{n_m^2}{h^{1/3}}V\sqrt{U^2+V^2}
\end{aligned}\tag{1}$$

where h is the water depth and U, V the vertically averaged velocity components along the horizontal directions x, y respectively. n_m is the Manning friction coefficient.

The first term at right hand side of the second and third Equation (1) accounts for the bottom slope and is calculated as in Valiani and Begnudelli (2006), i.e., taking as a constant the free surface elevation η, defined as the following: $\eta = z_f + h$, being z_f the bottom elevation. This formulation of the bottom slope term ensures the correct balance between flux gradients and source terms (Valiani and Begnudelli, 2006). The free surface η is considered instantaneously and locally constant: i.e., it is constant within the computational cell during the time step.

The DBE is given by (La Rocca et al., 2015):

$$\frac{\partial f_k}{\partial t}+c_{xk}\frac{\partial f_k}{\partial x}+c_{yk}\frac{\partial f_k}{\partial y}=\frac{f_k^{eq}-f_k}{\tau^*}+2\frac{F_x^e c_{xk}+F_y^e c_{yk}}{\sum_k(c_{xk}^2+c_{yk}^2)}\tag{2}$$

where f_k is the probability density function relative to the kth particle velocity, whose cartesian components along x, y are respectively c_{xk}, c_{yk}. The particle velocity set as the kth equilibrium probability density function f_k^{eq} is defined in La Rocca et al. (2015) and reported concisely in the **Appendix** for the reader's convenience. τ^* is the dimensional relaxation time,

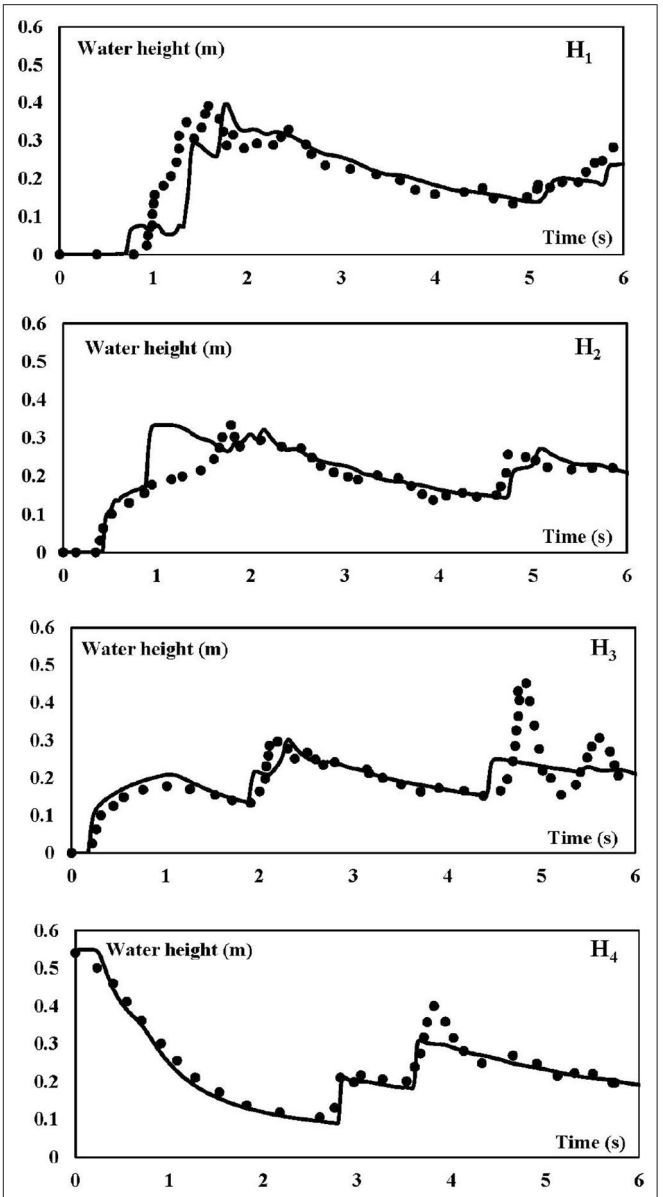

FIGURE 2 | Test case I. Time history of the water height at probes $H_1, H_2, H_3, and\ H_4$. Solid lines: DBE numerical results. Dots: Experimental results.

F_x^e, F_y^e are the cartesian components of the external forces acting on the flow. In this case, they are defined by the following:

$$\begin{aligned}
F_x^e&=\frac{\partial}{\partial x}\left(g\frac{h^2}{2}\right)\Bigg|_{\eta}-g\frac{n_m^2}{h^{1/3}}U\sqrt{U^2+V^2}\\
F_y^e&=\frac{\partial}{\partial y}\left(g\frac{h^2}{2}\right)\Bigg|_{\eta}-g\frac{n_m^2}{h^{1/3}}V\sqrt{U^2+V^2}
\end{aligned}\tag{3}$$

The DBE (2) is equivalent to the SWE (1) in the sense that the water depth h and the unit discharges Uh, Vh, obtained as the zero

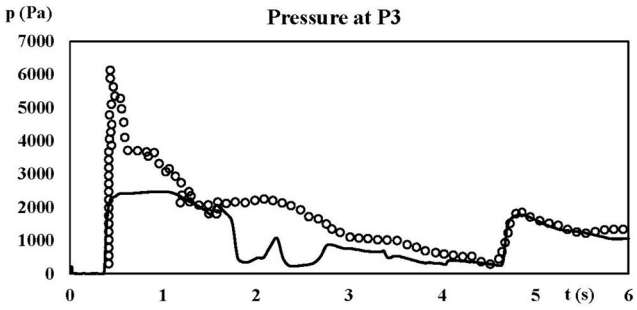

FIGURE 3 | Test case I. Time history of the pressure at probe P_3. Solid line: DBE numerical results. Dots: Experimental results.

and first order moments of f_k

$$h = \sum_k f_k$$
$$Uh = \sum_k c_{xk} f_k \quad (4)$$
$$Vh = \sum_k c_{yk} f_k$$

coincide with the water depth h and the unit discharges Uh, Vh that are obtained by solving the SWE (1) provided that the ratio Fr/Re of the Froude and the Reynolds number of the flow is small (La Rocca et al., 2015).

It is worth observing that the DBE (2) that consists of a set of uncoupled, linear advection equations with constant advection velocity; this is the most appealing aspect of the DBE, when compared with the highly non-linear SWE, and it is an advantage *per se*. Indeed, the numerical solution of the DBE can be tackled by means of computational methods that are rather simple in comparison with those needed to treat the complex non-linearities of the SWE. Such an advantage may involve a gain of efficiency, whose quantification is, however, very difficult, as it depends on a variety of factors, such as e.g., the level of coding optimization and parallelization, the performance of the processors, etc., and this is beyond the scope of this work.

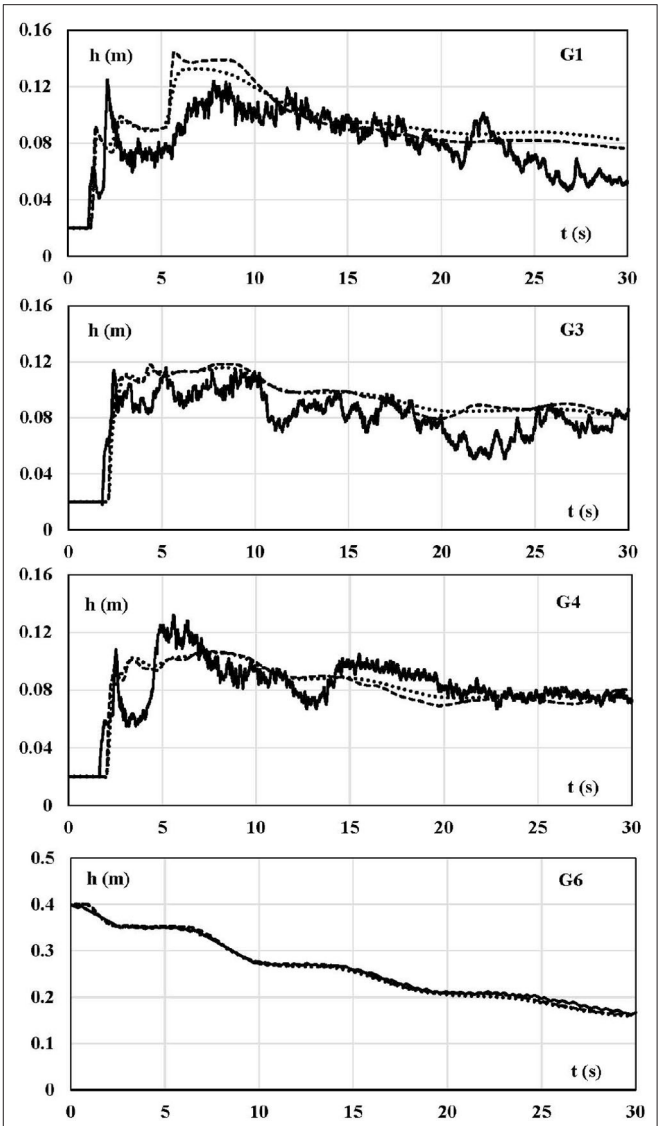

FIGURE 4 | Test case II. Experimental and numerical free surface time histories. Solid line: experimental measurements from Soares-Frazão and Zech (2007). Dotted line: DBE numerical results obtained with the coarse grid. Dashed line: DBE numerical results obtained with the fine grid.

3. EXPERIMENTAL DAM BREAK FLOWS

3.1. Computational Details

The DBE (2) is discretized by means of an explicit first order approximation of the time derivative and a first order upwind approximation of the space derivative (La Rocca et al., 2015). Details of the numerical discretization, which is rather standard, can be found in Fletcher (2012) and are not reported here for the sake of concision. Boundary conditions are imposed on the macroscopic variables (water depth and vertically averaged velocity); then, the probability density functions at equilibrium are calculated and the values assigned as boundary values to the probability density functions (Ubertini et al., 2003). Stability is ensured by setting the order of magnitude of the Courant number C ($C = U_{max} \times \Delta t/\Delta s$) to $O(10^{-1})$, $U_{max}, \Delta t, and\ \Delta s$ being the highest celerity of flow perturbations, the time step, and the space step, respectively. The adopted numerical method introduces numerical viscosity proportional to Δs, whose effect decreases by increasing the number of computational grid points. Finally, the value of the dimensionless relaxation time τ, defined as $\tau = \tau^*/\Delta t$ has been chosen in the range $0.5 < \tau < 0.6$.

3.2. Dam-Break Flow Impacting on an Isolated Obstacle-I

This case has been considered in Kleefsman et al. (2005) and many subsequent works, as it is widely used as benchmark to validate free-surface software (Kees et al., 2011). The reader can refer to Kees et al. (2011) for a detailed description of the

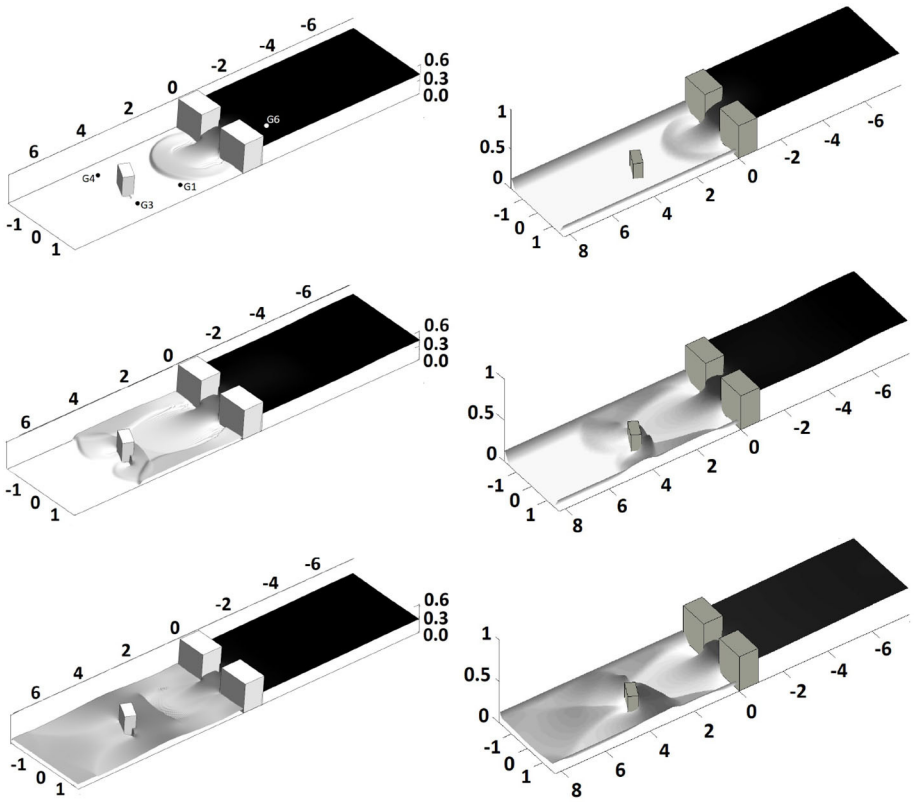

FIGURE 5 | Test case II. Free surface at $t = 1s$, $t = 3s$, $t = 10s$. **Left**: DBE results; **right**: numerical results from Soares-Frazão and Zech (2007) ; top-left panel shows gauges positioning.

experimental setup. The experimental configuration, realized at the Maritime Research Institute Netherlands (MARIN) in a tank ($3.22 \times 1.00 \times 1.00\ m$), consists of a column of water at rest (height $0.55\ m$, length $0.58\ m$, and width $1\ m$) separated by a sliding gate from the rest of the tank where the water level is zero. By lifting the gate, the water column collapses under the action of gravity and impinges on a fixed parallelepiped ($0.40 \times 0.16 \times 0.16\ m$) placed at $2.40\ m$ from the right end of the tank, giving rise to a complex dam-break flow traveling back and forth within the tank. The Manning coefficient is estimated to the following: $n_m \approx 0.01\ s/m^{1/3}$. The experimental setup is equipped with four heights ($H_1, H_2, H_3, and\ H_4$) and four pressure probes ($P_1 - P_4$) (Kees et al., 2011).

In **Figure 1**, the plots of the DBE numerical profiles of the free surface at $t = 0.4s$ and $t = 0.56$ are compared to the corresponding experimental profiles of Kleefsman et al. (2005). At $t = 0.4s$ the flow has almost reached the obstacle, while at $t = 0.56$ the impact has occurred, and the formation of a water splash with a height of around $0.4\ m$ is evident both in the experiment and in the numerical simulation. The position of the height ($H_1, H_2, H_3, and\ H_4$) and pressure (P_3) probes is also reported in **Figure 1**.

In **Figure 2**, the time history of the water height at probes $H_1, H_2, H_3, and\ H_4$ is plotted. Dots represent the experimental results obtained at MARIN, while the solid line represents the DBE numerical results. The latter are those obtained with the finest grid (800×280). The space step Δs is equal to $4 \times 10^{-3} m$, while the order of magnitude of the time step Δt is $O(10^{-4})s$. The general agreement is fairly good. The main discrepancy between experimental and numerical results is evident for the probe H2, where the DBE results overestimate the peak of water height due to the impact of the flow on the obstacle, and this is attributed to the fact that the shallow water model does not describe correctly the strong vertical dynamics involved during impact; the duration is, however, very short in comparison to the duration of the considered experiment. However, it is interesting to observe that the instant of impact of the flow on the obstacle ($t \approx 0.5s$) is correctly predicted by the DBE numerical results. The experimental and numerical time history of the pressure measured by the probe P_3 is shown in **Figure 3**. In the framework of the shallow water equations, the numerical pressure is calculated assuming a hydrostatic pressure distribution: $p = \rho g(h - z)$, z being the elevation of the pressure gauge from the bottom of the tank. The experimental pressure shows an isolated peak, due to the sudden impact of the water against the obstacle, which is a typical dynamic feature and of course cannot be reproduced by the numerical hydrostatic pressure distribution. However, as time goes by, dynamic effect loose importance and the hydrostatic pressure distribution becomes a fair representation of the pressure field.

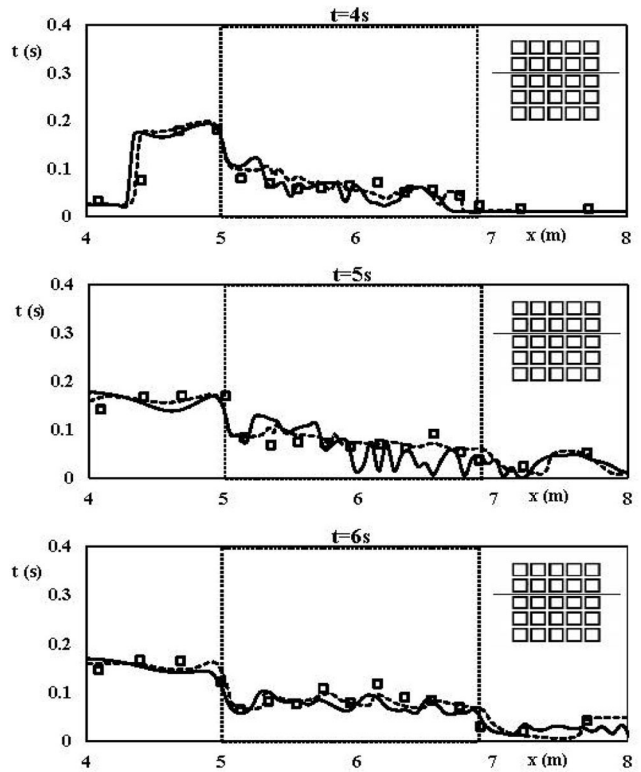

FIGURE 6 | Test case III. Experimental dam break flow through an idealized city of Soares-Frazão and Zech (2008). Free surface profile at 4, 5, *and* 6*s* along the third longitudinal street, as indicated by the sketch. Solid line: DBE numerical results. Dashed line: Soares-Frazão and Zech (2008) numerical results. Dots: Soares-Frazão and Zech (2008) experimental values. Dotted box: area occupied by the buildings.

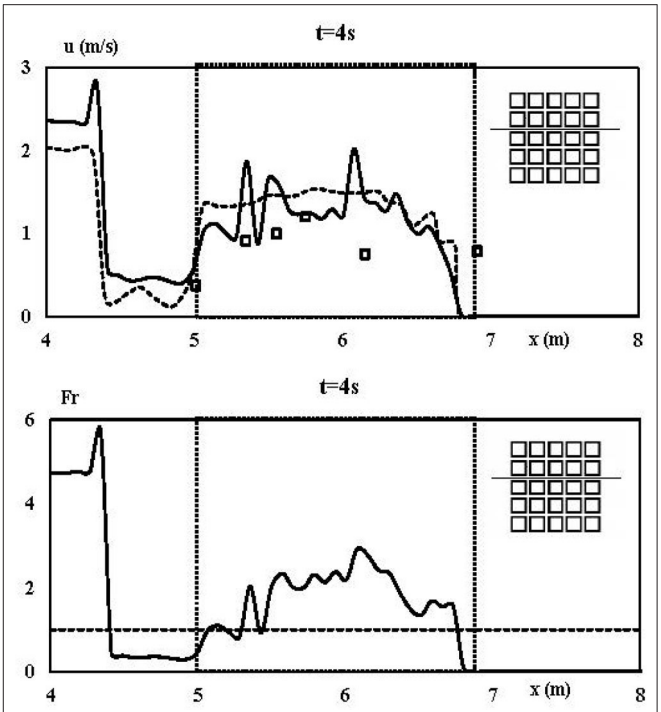

FIGURE 7 | Test case III. Experimental dam break flow through an idealized city of Soares-Frazão and Zech (2008). **Bottom**: Froude number profile at 4*s* along the third longitudinal street, as indicated by the sketch. Solid line: DBE numerical results. Dotted box: area occupied by the buildings. **Top**: u velocity profile at 4*s* along the third longitudinal street, as indicated by the sketch. Solid line: DBE numerical results. Dashed line: shallow water numerical results of Soares-Frazão and Zech (2008). Dots: experimental results of Soares-Frazão and Zech (2008).

3.3. Dam-Break Flow Impacting on an Isolated Obstacle-II

This case has been considered in Soares-Frazão and Zech (2007), where the reader can find a detailed description of the experimental setup. The experiments have been realized in a tank 36 m long, 3.6 m wide, with a trapezoidal cross section. A gate (width 1 m), placed 7.70 m from the left end of the tank, separates the reservoir from the part of the tank representing a valley with an isolated building. The latter is a parallelepipedal obstacle, with a 0.8×0.4 m base area. The 0.8 m long side is inclined at an angle of 64° with respect to the y axis (Soares-Frazão and Zech, 2007). The water level is set to 0.4 m and 0.02 m within the reservoir and the rest of the tank, respectively.

Finally, the Manning coefficient is set to $n_m \approx 0.01\ s/m^{1/3}$ as in Soares-Frazão and Zech (2007). Water height and velocity measurements have been performed at several points (Soares-Frazão and Zech, 2007). Velocity values are measured at 0.036 m from the bottom and cannot be compared with the DBE numerical vertically averaged velocity, as the flow presents intense re-circulation zones with high values of the vertical velocity component.

In **Figure 4** are plotted the time histories of the free surface at measurement points $G_1, G_3, G_4, and\ G_6$. Solid lines represent experimental values, while dotted and dashed lines represent the DBE numerical values obtained with a coarse (600×67) and a fine (1500×165) grid, respectively. The difference between the DBE numerical results obtained with the two grids is not meaningful, mainly at measurement point G_6. The differences with the experimental results observed at measurement points $G_1, G_3, G_4, and\ G_6$ are ascribed to the fact that there the vertical motions are not negligible and that the shallow water model loses consistency. Nevertheless, the DBE numerical results grab the main features of the flow, and the general agreement with experiments can be considered fairly good. The DBE numerical results are in satisfying agreement with the numerical results of Noël et al. (2003), reported in Soares-Frazão and Zech (2007) and obtained by directly integrating the SWE. This fact is depicted in **Figure 5** where the snapshots of the free surface at $t = 1s, t = 3s, and\ t = 10s$ reproduce the same flow features observed in the numerical calculation of Noël et al. (2003).

3.4. Dam-Break Flow Impacting on an Idealized City

This case is reported in Soares-Frazão and Zech (2008), where the experimental setup is described with great detail, and has been

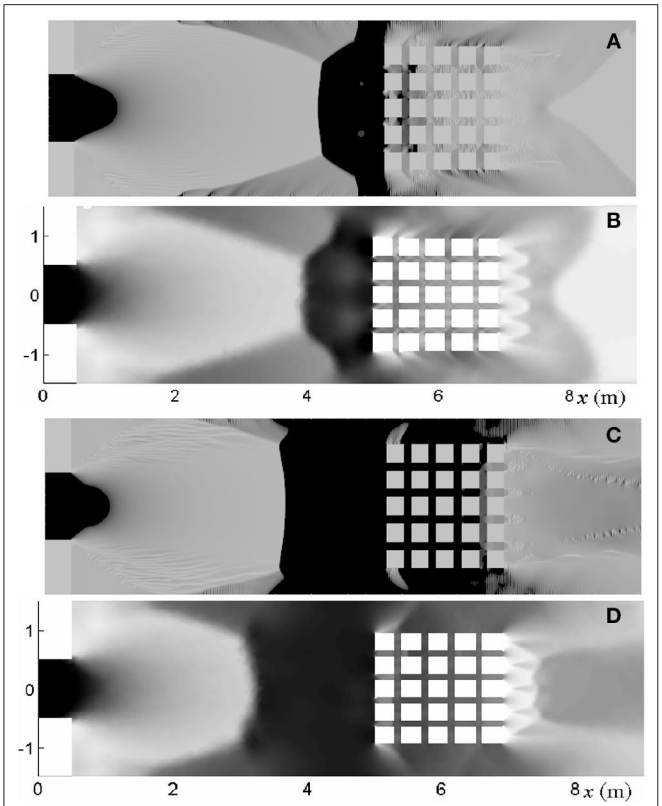

FIGURE 8 | Test case III. Computed water depth map. Darker color for larger depth values. Top panels **(A,B)**: $t = 5s$; bottom panels **(C,D)**: $t = 10s$. Panels **(A,C)**: DBE numerical results. Panels **(B,D)** are numerical values from Soares-Frazão and Zech (2008).

performed with the same experimental setup tank used in Soares-Frazão and Zech (2007). The idealized city has been realized by means of 25 impervious wooden blocks of 0.30 $m \times 0.30$ m, representing buildings, separated by streets 0.10 m wide and arranged in a regular array of 5×5. According to Soares-Frazão and Zech (2008), the ratio of the street to building width is realistic despite the strong simplification of the representation of the city.

A gate (width 1 m), placed 7.70 m from the left end of the tank, separates the reservoir from the part of the tank containing the idealized city. The water level is set to 0.4 m and 0.011 m within the reservoir and the rest of the tank, respectively. Finally, the Manning coefficient is set to $n_m \approx 0.01\ s/m^{1/3}$ as in Soares-Frazão and Zech (2008). Water height has been measured by means of several resistive level gauges, placed along straight lines along the streets of the city, while velocity has been measured both on the free surface, by means of a digital-imaging technique, and close to the bottom by means of an acoustic doppler velocimeter (ADV) (Soares-Frazão and Zech, 2008).

In **Figure 6**, the DBE numerical results and the experimental and numerical results of Soares-Frazão and Zech (2008) relative to the free surface profile at $4s, 5s, and\ 6s$ are shown. The free surface profile is plotted along the third longitudinal street. The agreement is satisfying. Minor discrepancies at $t = 5s$ can be attributed to numerical oscillations in the central part of the obstacles' array. In **Figure 7**, the DBE numerical Froude number profile at $t = 4s$ along the third longitudinal street, as indicated by the sketch, is shown. The high values attained by the Froude number allow to state that the DBE is a robust tool to investigate super- and transcritical flows. It is worth observing the fairly good agreement among the DBE numerical and experimental velocity values and that the position of the main hydraulic jump ($x \sim 4.3 \div 4.4\ m$), shown in **Figure 6**, matches with the sudden change from $Fr > 1$ to $Fr < 1$ of the Froude number shown in **Figure 7**. Finally, in **Figure 8** the computed water depth in the neighborhood of the city area is shown at $t = 5s, t = 10s$, respectively. The complex features of the flow comply with those shown in Soares-Frazão and Zech (2008).

In particular, at $t = 5s$ (**Figures 8A,B**), the flow between the gate and the city is mainly supercritical; it forms a sort of hat-like shaped subcritical zone downstream of a hydraulic jump which front is placed at $x_H = 3.95\ m$ along the centerline of the tank. From the edges of the subcritical zone, at $x_E = 4\ m, y_{EN} = 0.7\ m$, and $x_E = 4\ m, y_{ES} = -0.7\ m$, two symmetrical oblique waves detach and end at the wall of the tank (**Figures 8A,B**). Points $x_H, x_E, y_{EN}, and\ y_{ES}$ coincide in **Figures 8A,B**. Within the longitudinal street of the city the flow is mainly supercritical, as in Soares-Frazão and Zech (2008). Finally, the wake zone immediately downstream of the city, where a triangular wave is observable, is qualitatively similar to that observed in Soares-Frazão and Zech (2008).

At $t = 10s$ (**Figures 8C,D**), the structure of the flow is similar to that observed at $t = 5s$. The subrictical zone is almost rectangular, the front being located at $x_H = 3.4\ m$ along the centerline of the tank. The two symmetrical oblique waves detach from the points $x_E = 3.3\ m, y_{EN} = 1.0\ m$ and $x_E = 3.3\ m, y_{ES} = -1.0\ m$. Points $x_H, x_E, y_{EN}, and\ y_{ES}$ coincide in **Figures 8C,D**. Within the longitudinal street of the city the flow is mainly subcritical, as in Soares-Frazão and Zech (2008), while it becomes supercritical in the wake zone immediately downstream of the city.

4. CONCLUDING REMARKS

The multispeed Discrete Boltzmann Equation (DBE) is a method recently developed to simulate transcritical shallow water flows, and the main advantage is the simplicity of the mathematical model: a set of linear, uncoupled, purely advective equations. In this paper, the DBE has been assessed as solution method for the Shallow Water Equation (SWE) when dam-break flows impacting on obstacles are considered. These flows are strongly unsteady and present frequent sub-supercritical and super-subcritical (hydraulic jumps) transitions.

The consideration of dam-break flows impacting on obstacles is important as they represent simplified models of urban flooding, thus constituting a benchmark for numerical methods,

thanks to the wide variety of reference numerical and experimental data published in literature.

In this paper, three dam-break flows impacting obstacles have been considered: two on an isolated obstacle and one on an idealized city that has realized by means of a regular array of parallelepipeds.

The experimental configurations were realized within tanks with a smooth, though sloping, bottom. The latter has been treated in order to account for the correct balance between flux gradients and source terms.

The comparison between DBE and reference results (both numerical and experimental) shows that the DBE can be considered as a reliable solution method for dam break flows impacting on obstacles, even in the presence of complex flow configurations, such as e.g., the case of the idealized city. Discrepancies between DBE and reference results can be attributed both to the use of coarse grids and to the accuracy of the numerical method and to the occurrence of violent vertical motions, which undermine the consistency of the shallow water model. It is worth observing that, for what regards the specific performance of the proposed models in urban areas, there are no restrictions for the DBE on the attainable grid resolutions. Any grid convergence rate can be achieved by just adopting a higher order numerical scheme. Future works will be addressed to the consideration of realistic topography as well as to the implementation of more efficient numerical methods, such as e.g., the finite volume method with unstructured, adaptive grids.

DATA AVAILABILITY STATEMENT

The datasets generated for this study are available on request to the corresponding author.

AUTHOR CONTRIBUTIONS

ML has formulated the Discrete Boltzmann Equation. PP performed the numerical simulations. SM analyzed the results and prepared graphics. All the authors have discussed together about the outcomes and their interpretation. All authors contributed to the article and approved the submitted version.

FUNDING

The authors acknowledged funding from the Italian Ministry of Education, University and Research (MIUR), in the frame of the Departments of Excellence Initiative 2018–2022, attributed to the Department of Engineering of Roma Tre University.

ACKNOWLEDGMENTS

Valuable discussions with Dr. A. Montessori are kindly acknowledged.

REFERENCES

Chang, K. H., Sheu, T. W. H., and Chang, T. J. (2018). A 1D–2D coupled SPH-SWE model applied to open channel flow simulations in complicated geometries. *Adv. Water Resour.* 115, 185–197. doi: 10.1016/j.advwatres.2018.03.009

Duran, A., and Marche, F. (2014). Recent advances on the discontinuous Galerkin method for shallow water equations with topography source terms. *Comput. Fluids* 101, 88–104. doi: 10.1016/j.compfluid.2014.05.031

Ferrari, A., Viero, D. P., Vacondio, R., Defina, A., and Mignosa, P. (2019). Flood inundation modeling in urbanized areas: a mesh-independent porosity approach with anisotropic friction. *Adv. Water Resour.* 125, 98–113. doi: 10.1016/j.advwatres.2019.01.010

Fletcher, C. A. J. (2012). *Computational Techniques for Fluid Dynamics 1: Fundamentals and General Techniques*. Berlin; Heidelberg; New York, NY: Springer Science & Business Media.

Hedjripour, A. H., Callaghan, D. P., and Baldock, T. E. (2016). Generalized transformation of the lattice Boltzmann method for shallow water flows. *J. Hydraul. Res.* 54, 371–388. doi: 10.1080/00221686.2016.1168881

Hou, J., Wang, R., Liang, Q., Li, Z., Huang, M. S., and Hinkelmann, R. (2018). Efficient surface water flow simulation on static Cartesian grid with local refinement according to key topographic features. *Comput. Fluids* 176, 117–134. doi: 10.1016/j.compfluid.2018.03.024

Kees, C. E., Akkerman, I., Farthing, M. W., and Bazilevs, Y. (2011). A conservative level set method suitable for variable-order approximations and unstructured meshes. *J. Comput. Phys.* 230, 4536–4558. doi: 10.1016/j.jcp.2011.02.030

Kleefsman, K. M. T., Fekken, G., Veldman, A. E. P., Iwanowski, B., and Buchner, B. (2005). A volume-of-fluid based simulation method for wave impact problems. *J. Comput. Phys.* 206, 363–393. doi: 10.1016/j.jcp.2004.12.007

La Rocca, M., Montessori, A., Prestininzi, P., and Elango, L. (2018). A discrete Boltzmann equation model for two-phase shallow granular flows. *Comput. Math. Appl.* 75, 2814–2824. doi: 10.1016/j.camwa.2018.01.010

La Rocca, M., Montessori, A., Prestininzi, P., and Elango, L. (2019). Discrete Boltzmann Equation model of polydisperse shallow granular flows. *Int. J. Multiphase Flow* 113, 107–116. doi: 10.1016/j.ijmultiphaseflow.2019.01.008

La Rocca, M., Montessori, A., Prestininzi, P., and Succi, S. (2015). A multispeed discrete Boltzmann model for transcritical 2d shallow water flows. *J. Comput. Phys.* 284, 117–132. doi: 10.1016/j.jcp.2014.12.029

Noël, B., Soares-Frazão, S., and Zech, Y. (2003). *Computation of the Isolated Building Test Case and the Model City Experiment Benchmarks*. IMPACT Investigation of Extreme Flood Processes and Uncertainty.

Sanders, F. B., and Schubert, J. E. (2019). PRIMo: Parallel raster inundation model. *Adv. Water Resour.* 126, 79–95. doi: 10.1016/j.advwatres.2019.02.007

Soares-Frazão, S., and Zech, Y. (2007). Experimental study of dam-break flow against an isolated obstacle. *J. Hydraul. Res.* 45, 27–36. doi: 10.1080/00221686.2007.9521830

Soares-Frazão, S., and Zech, Y. (2008). Dam-break flow through an idealized city. *J. Hydraul. Res.* 46, 648–658. doi: 10.3826/jhr.2008.3164

Song, J., Chang, Z., Li, W., Feng, Z., Wu, J., Cao, Q., et al. (2019). Resilience-vulnerability balance to urban flooding: a case study in a densely populated coastal city in China. *Cities* 95:102381. doi: 10.1016/j.cities.2019.06.012

Succi, S. (2001). *The Lattice Boltzmann Equation: For Fluid Dynamics and Beyond*. Oxford; New York, NY: Oxford University Press.

Toro, E. F. (2009). *Riemann Solvers and Numerical Methods for Fluid Dynamics: A Practical Introduction*. Berlin; Heidelberg; New York, NY: Springer Science & Business Media.

Toro, E. F., and Garcia-Navarro, P. (2007). Godunov-type methods for free-surface shallow flows: a review. *J. Hydraul. Res.* 45, 736–751.

Ubertini, S., Bella, G., and Succi, S. (2003). Lattice Boltzmann method on unstructured grids: further developments. *Phys. Rev. E* 68:016701. doi: 10.1103/PhysRevE.68.016701

Valiani, A., and Begnudelli, L. (2006). Divergence form for bed slope source term in shallow water equations. *J. Hydraul. Eng.* 132, 652–665. doi: 10.1061/(ASCE)0733-9429(2006)132:7(652)

Zhao, J., Özgen-Xian, I., Liang, D., Wang, T., and Hinkelmann, R. (2019). An improved multislope MUSCL scheme for solving shallow water equations on unstructured grids. *Comput. Math. Appl.* 77, 576–596. doi: 10.1016/j.camwa.2018.09.059

Zhou, J. G. (2004). *Lattice Boltzmann Methods for ShallowWater Flows*. Berlin; Heidelberg: Springer.

Conflict of Interest: The authors declare that the research was conducted in the absence of any commercial or financial relationships that could be construed as a potential conflict of interest.

APPENDIX

Definition of the Velocity Set

The *kth* particle velocity vector is defined as:

$$\mathbf{c}_k = c_{xk}\mathbf{i} + c_{yk}\mathbf{j} \tag{A1}$$

being c_{xk}, c_{yk} the cartesian components of the vector $\mathbf{c}_k$ along x, y, respectively, and $\mathbf{i}, \mathbf{j}$ the basis unit vectors of the frame of reference.

The cartesian components of the vector $\mathbf{c}_k$ are in turn defined:

$$\begin{aligned}
c_{xk} &= 0,\ k = 0 \\
c_{yk} &= 0,\ k = 0 \\
c_{xk} &= ac_0 \cos\frac{4\pi k}{N_T},\ 1 \le k \le \frac{N_T}{2} \\
c_{yk} &= ac_0 \sin\frac{4\pi k}{N_T},\ 1 \le k \le \frac{N_T}{2} \\
c_{xk} &= bc_0 \cos\frac{4\pi k}{N_T},\ \frac{N_T}{2} < k \le N_T \\
c_{yk} &= bc_0 \sin\frac{4\pi k}{N_T},\ \frac{N_T}{2} < k \le N_T
\end{aligned} \tag{A2}$$

The particle velocity vectors can be grouped into two subsets, hereinafter referred to as shells, based on their magnitude ac_0, bc_0, a, b being the dimensionless velocity magnitudes of the two shells and c_0 a velocity scale representative of the surface waves celerity. a, b, c_0 have been set to $1, 2, \sqrt{gH_0}$, respectively, H_0 being the initial water height. The total number of velocity vectors $N_T + 1$ must be higher than the minimum value 13, corresponding to $N_T = 12$, below which the simulation becomes unstable.

Definition of the Equilibrium Probability Density Function

A polynomial form is assumed for the equilibrium probability density function f_k^{eq}:

$$\begin{aligned}
f_k^{eq} = h\Bigg(A_k + B_k\frac{\mathbf{u}\cdot\mathbf{c}_k}{gh} + C_k\frac{\mathbf{u}\cdot\mathbf{u}}{gh} + D_k\left(\frac{\mathbf{u}\cdot\mathbf{c}_k}{gh}\right)^3 + \\
F_k\frac{(\mathbf{u}\cdot\mathbf{u})(\mathbf{u}\cdot\mathbf{c}_k)}{(gh)^2} + G_k\left(\frac{\mathbf{u}\cdot\mathbf{c}_k}{gh}\right)^2 + H_k\frac{(\mathbf{u}\cdot\mathbf{u})(\mathbf{u}\cdot\mathbf{c}_k)^2}{(gh)^3} \\
+ I_k\left(\frac{\mathbf{u}\cdot\mathbf{c}_k}{gh}\right)^4\Bigg)
\end{aligned} \tag{A3}$$

where the $\mathbf{u} = U\mathbf{i} + V\mathbf{j}$ is the vertically averaged flow velocity vector. The coefficients $A_k, ..., I_k$ have to be determined by matching the discrete hydrodynamic moments with those obtained from the shallow water Maxwellian equilibrium distribution function $f(h, \mathbf{u}, \mathbf{c}) = \frac{1}{\pi g}e^{-\frac{(\mathbf{c}-\mathbf{u})\cdot(\mathbf{c}-\mathbf{u})}{gh}}$:

$$\sum_{k=0}^{N_T} c_{xk}^m c_{yk}^n f_k^{eq} = \frac{1}{\pi g}\int_{-\infty}^{\infty}\int_{-\infty}^{\infty} c_{xk}^m c_{yk}^n f(h, \mathbf{u}, \mathbf{c})dc_x dc_y \tag{A4}$$

The following expressions are obtained: for $k = 0$:

$$\begin{aligned}
A_0 &= 1 - \frac{a^2 + b^2 - \frac{2}{\phi^2}}{(\phi ab)^2} \\
B_0 &= \frac{\frac{4}{\phi^2} - a^2 - b^2}{(ab)^2} \\
C_0 &= \frac{1}{(ab)^2}
\end{aligned} \tag{A5}$$

for $1 \le k \le \frac{N_T}{2}$:

$$\begin{aligned}
A_k &= 2\beta\frac{2 - \phi^2 b^2}{a^2\phi^4} \\
B_k &= 4\beta\frac{2 - \phi^2 b^2}{a^2\phi^2} \\
C_k &= -2\beta\frac{2 - \phi^2 b^2}{a^2\phi^2} \\
D_k &= 8\beta\frac{3 - b^2\phi^2}{a^4\phi^2} \\
E_k &= 16\frac{\beta}{3a^4} \\
F_k &= 0 \\
G_k &= -\frac{\beta}{a^2} \\
H_k &= 0 \\
I_k &= \beta\frac{8}{a^6}
\end{aligned} \tag{A6}$$

for $\frac{N_T}{2} < k \le N_T$:

$$\begin{aligned}
A_k &= 2\beta\frac{\phi^2 a^2 - 2}{b^2\phi^4} \\
B_k &= 4\beta\frac{\phi^2 a^2 - 2}{b^2\phi^2} \\
C_k &= -2\beta\frac{\phi^2 a^2 - 2}{b^2\phi^2} \\
D_k &= 8\beta\frac{a^2\phi^2 - 3}{b^4\phi^2} \\
E_k &= 16\beta\frac{2a^2 - 3b^2}{3b^6} \\
F_k &= -8\beta\frac{a^2 - b^2}{b^4} \\
G_k &= \beta\frac{3a^2 - 2b^2}{b^4} \\
H_k &= -24\beta\frac{a^2 - b^2}{b^6} \\
I_k &= 8\beta\frac{3a^2 - 4b^2}{b^8}
\end{aligned} \tag{A7}$$

ϕ, β being defined by:

$$\begin{aligned}
\phi_0 &= \frac{c_0}{\sqrt{(gH_0)}} \\
\beta &= \frac{1}{N_T(a^2 - b^2)}
\end{aligned} \tag{A8}$$

frontiers in Earth Science

METHODS
published: 30 March 2021
doi: 10.3389/feart.2021.540473

Multi-Mode Surface Generalization Supports a Detailed Urban Flooding Simulation Model

Mei Xu[1], Yonghui Yao[2], Shu Liu[1], Yang Sun[3] and Yuexin Yan[3]*

[1] Research Center on Flood & Drought Disaster Reduction of the Ministry of Water Resources, China Institute of Water Resources and Hydropower Research, Beijing, China, [2] State Key Laboratory of Resources and Environment Information System, Institute of Geographic Sciences and Natural Resources Research, Chinese Academy of Sciences, Beijing, China, [3] Beijing Water Authority, Beijing, China

With the aim of achieving high precision and high efficiency, recent research on hydraulic flood models has tended to focus on the algorithms for solving the shallow water equations of Saint-Venant. While development of the algorithms will help to improve the simulation precision and the solving of specific problems, the other influential factor in flood risk modeling is the precision and reasonable generalization of the data. This is even more important for increasing the model's computational accuracy and efficiency but is frequently undervalued. Frequent rainstorm waterlogging is having a serious impact on China's large cities. Early warning of waterlogging risk following a rainstorm forecast is an effective method for preventing or reducing potential losses. Concrete waterlogging information including locations, depth, and process is essential for early warnings. This paper focuses on the influence of data precision and reasonable generalization on an urban flooding model. A detailed hydraulic urban flooding model characterized by detailed data processing and component coupling can help to provide advance information. In Beijing city, road networks, overpasses, and buildings are so highly concentrated that rainstorms easily result in waterlogging in low-lying locations. Therefore, partial microrelief is the determinate factor in waterlogging simulation. This paper shows that multi-mode surface data generalization and detailed model coupling support a perfect simulation of a Beijing urban flooding model. The influence of buildings, roads, and overpasses on surface water flow was carefully considered based on the innovative aspect of a fine generalization of partial microrelief. One novelty is the simulation of the whole overland flow from the beginning of rainfall to mesh, not only from manhole overflow, because the waterlogging is caused mainly by initial surface water runoff rather than by manhole overflow. A second novelty is the use of a new kind of coupling mode based on physical mechanisms between surface and pipe models. Here, rain perforated strainers instead of manholes play a role as flow exchange points between pipe and surface. This coupling mode is much closer to the real world. Based on a detailed Beijing urban flooding model, a scenarios library of typical rainfall events

OPEN ACCESS

Edited by:
Mingfu Guan,
The University of Hong Kong, Hong Kong

Reviewed by:
Xilin Xia,
Loughborough University, United Kingdom
Haixing Liu,
Dalian University of Technology, China

****Correspondence:***
Yonghui Yao
yaoyh@lreis.ac.cn

Specialty section:
This article was submitted to Hydrosphere, a section of the journal Frontiers in Earth Science

Received: *05 March 2020*
Accepted: *09 March 2021*
Published: *30 March 2021*

Citation:
Xu M, Yao Y, Liu S, Sun Y and Yan Y (2021) Multi-Mode Surface Generalization Supports a Detailed Urban Flooding Simulation Model. Front. Earth Sci. 9:540473. doi: 10.3389/feart.2021.540473

and corresponding waterlogging results was constructed. Several years of practice have demonstrated that a rich library of scenarios can be used effectively for the quick identification and early warning of waterlogging risk for a forecast rainfall. Test results show that multi-mode surface generalization is effective in improving outcomes and useful for scientific decision making in controlling urban waterlogging.

Keywords: detailed urban flooding model, urban waterlogging, surface generalization, elevation amendment, Beijing city

INTRODUCTION

Increasing urbanization and frequent occurrences of rainstorms with aging storm networks increase flood risk. Hydroinformatic tools such as flood models are valuable assets for integrated water management in cities, as within the digital city concept proposed by Price and Vojinovic (2008).

Recent research has tended to focus on two aspects of hydraulic flood models. One is the algorithm for solving the shallow water equations of Saint-Venant and its application to solving specific problems, and the other aspect is the acceleration of the algorithm (Huxley, 2017). Funke et al. (2011) and Tsakiris and Bellos (2014) conducted research on the treatment of wetting and drying. Research has also been carried out on the trade-offs between accuracy and computational efficiency (Fewtrell et al., 2008; Gallegos et al., 2009; Wang et al., 2010). Gallegos et al. (2009) used an unstructured grid, Godunov-type, finite volume model to simulate a dam-break flooding event in an urban residential area and validated their model with high-resolution data. Yu (2015) attempted to apply an implicit dual time-stepping method to improve run-time efficiency and stability in dealing with urban floods. Liang et al. (2008) applied an adaptive quadtree grid-based shallow water equations solver which dynamically adapted the grid to represent the critical flow features such as steep water surface gradients and wetting–drying fronts. This method has a proven ability to improve the computational efficiency of two-dimensional numerical models for large-scale flood simulation Chen et al. (2012) and Zang (2019) proposed a surface multilayer modeling technology and Zang (2019) applied it to the calculation of waterlogging at overpass locations. Other researchers have suggested that hydraulic modeling needs to reduce complexity to achieve rapid solutions (Song et al., 2014). The general objective is high precision and high efficiency in flood simulation.

A further question is the influence of data input to the model. This has also been the subject of close attention from many engineers and researchers in recent years. It has been widely recognized that the resolution and quality of the topographical data may have a significant influence on the simulation results (Zoppou and Roberts, 1999; Gourbesville and Savioli, 2002). Hénonin et al. (2015) concluded that low-resolution simulations could not properly represent the complex urban geometrics and topographical features to provide reliable flood predictions. Two-dimensional models are well adapted to represent urban pluvial flooding. However, urban infrastructures such as buildings and streets have a significant influence on surface flows (Beretta et al., 2018). Higher resolution is needed to represent features at city scale (Hénonin et al., 2013) and to ensure a proper representation of such floods (Hénonin et al., 2015). Generally, researchers have concluded that high-resolution simulation is necessary to interpret accurately urban geometrics and topography and subsequently provide reliable urban flood predictions (Xing et al., 2018).With the availability of high-quality topographical data and an increase in computational power, there is now an increased emphasis on developing highly accurate modeling techniques for flood inundation (Bradbrook et al., 2004; Werner et al., 2005; Hunter et al., 2008; Krebs et al., 2014).

Flood modeling methods for surface flow can give the dynamics of the floodwater (Bulti and Abebe, 2020). For urban models, the accuracy of a simulation depends mainly on both topographical data resolution and model grid size. Urban applications usually require a fine 2-D grid so that the main urban features such as buildings and streets can be represented (Hénonin et al., 2013). The 2D model grid scale influences the resolution of the flood computation, but a high resolution is also needed for the topographical data input to a 2D model (Gourbesville, 2009). High-resolution topographical data, such as data from Light Detection and Ranging (LIDAR) systems, are now in common use and can have a very fine scale of the order of 20 cm or even less (Fewtrell et al., 2008). Traditional terrain analysis procedures need to be modified to account for human-made low-relief features such as streets which can intercept and redirect surface flows apart from the dominant topographic gradient as described by Djokic and Maidment (1991). Fewtrell et al. (2008) evaluated the effectiveness of coarse grids to represent flooding in urban environments by applying a 2D storage cell model, LISFLOOD-FP, and pointed out that critical length scales related to building dimensions and building separation distances determine the coarsest useful grid resolutions. Hunter et al. (2008) pointed out that terrain data available from modern LIDAR systems are sufficiently accurate and resolved for simulating urban flows, but such data need to be fused with digital map data of building topology and land use to gain maximum benefit from the information contained therein. Hunter et al. (2008) study also compared the relative impact of uncertainty over terrain data and model parameters on hydraulic model output. While the conclusions partly depend on the parameter and terrain error ranges fed into the analysis, it is clear that once fine spatial resolution, high-accuracy terrain data are available, uncertainty over model parameters becomes the more dominant of these factors (Dottori et al., 2013).

The precision of digital elevation models (DEMs) in traditional topographic products is insufficient for a detailed

flooding model, especially in urban areas. It is frequently necessary to supplement topographic products with either photogrammetric mapping or LIDAR-generated data and detailed ground surveys in areas of interest. Vehicle-mounted LIDAR is suitable for generating DEM for a lower concave type of overpass because the lowest layer is easily waterlogged, but the high-precision elevation cannot be gained through other means. When airborne LIDAR systems or photogrammetric mapping is applied to collect digital elevation data, post-processing for the removal of vegetation that covers the land, rooftops, and roads is crucial for obtaining the actual land surface instead of the reflective surface (Cobby et al., 2001). Generally, defined data are required for a detailed surface description and subsequently for a detailed flood simulation (Yuan and Li, 2019). How to prepare ideal data for improving the model's simulation results is an important research topic and the main theme of this paper.

In urban flood modeling, flow through the drainage networks has a strong influence on the simulation results (Hu et al., 2010). For large cities, however, complete and detailed information on drainage networks is normally unavailable or inaccurate. Drainage collection points (assumed to be manholes) are distributed along roads and streets at certain intervals according to design regulations (Xing et al., 2018). Flood modeling needs an adequate understanding of important processes that occur in the drainage system from the input (rainfall) to the output (outflow) (Josef, 2012; Jaafar et al., 2015). The sewer–surface coupling approach enables representation of the urban dual-drainage system, as it considers the flow exchange between major and minor systems and provides accurate descriptions of flood conditions (Leandro et al., 2009). The flow exchange between the two systems takes place at gully inlets, manholes, and river outfalls (Leandro et al., 2009; Hénonin et al., 2015). The belowground and aboveground flows must be strongly coupled because the interaction between sewer and surface models cannot be split into distinct processes (Sui and Maggio, 1999; WeiFeng et al., 2009). Leandro and Martins (2016) pointed out that tight coupling enables the implementation of real-time interactions between the two models. Tightly-coupled models can be operated as a single unit (single simulation package). There are several commercial and open-source simulation packages that provide such access (e.g., XPSWMM and MIKE FLOOD). Leandro and Martins (2016) proposed a methodology for linking 2D overland flow models with the sewer network model SWMM 5.1 based on dynamic link libraries. The China Institute of Water Resources and Hydropower Research (IWHR) Urban Flooding Model applied to Beijing also provides such access, enabling two novelties in the simulation of the Beijing urban flooding model described in this paper. One is the simulation of the whole overland flow from rainfall to mesh, instead of from manhole overflow only. The second is a new coupling mode based on rain perforated strainers (instead of manholes) between surface and pipe model.

Building a comprehensive and detailed urban flood model in a city as large as Beijing is a huge challenge. In this paper, many information of methods and techniques about building the model will be documented.

CASE STUDY

The city of Beijing covers more than a thousand square kilometers. It includes the seven districts of Dongchen, Xicheng, Chaoyang, Haidian, Fengtai, and Shijingshan. The two main rivers that flow around the city are the Yongdinghe River on the west and the Beiyunhe River on the east. Inside the urban area of the city, there are four main rivers. From north to south, they are the Qinghe River, Bahe River, Tonghuihe River, and the Liangshuihe River. Almost all of them flow roughly from the west to the east and finally into the Beiyunhe River.

Beijing faces flood risk from three sources: the Yongdinghe River flood, the west mountain flood, and waterlogging in the urban interior caused by rainstorms. The threats from the Yongdinghe River flood and the west mountain flood have been controlled through several years of engineering renovation. The flood control standard for the protection dike on the Yongdinghe River located in Beijing city is so high that almost no flood risk exists. The flood from the west mountain can be stored in the west suburb gravel pit before flowing into the main city. However, the problem of waterlogging in the city interior still exists and is becoming increasingly serious. The waterlogging risk is decided by the drainage system (Xiang et al., 2018).

Beijing's rivers present a natural drainage system. It is composed of four basins in the main city (**Figure 1**). The Qinghe River is the main river in the north of Beijing and carries the drainage of the northern region of the city. The Bahe River and the Tonghuihe River run through the center of Beijing and carry the drainage of the central region. The Liangshuihe River is the main river in the south of Beijing and carries the drainage of the southern region. Finally, the Beiyunhe River carries almost all of the floodwaters from the four drainage rivers.

Under normal rainfall conditions, the four main rivers take on the drainage burden for the whole of Beijing city. Under heavy rainfall conditions, the northern Qinghe River will divide floodwaters from the Anhe gate on the upstream to the northern region outside of the main city, and the middle Tonghuihe River will divide floodwaters from the Fenghongdao gate to the Liangshuihe River in order to lessen the drainage burden of the main city.

Flood risk management in downtown Beijing has become increasingly urgent in recent years under the current conditions of frequent flooding and waterlogging caused by extreme weather and rapid urbanization (Cheng and Li, 2015). Advance waterlogging alarms based on rainstorm forecasts is an effective method for the prevention or reduction of potential losses caused by flooding. In the past, an urban flood risk alarm was issued immediately only after a rainstorm alarm and as a direct response to the rainfall forecast. It means that the range of flood risk is consistent with the spatial range of the rainfall. This relationship is one-sided which can easily lead to unreasonable and unreliable flood risk information. In urban areas, flood risk depends not only on the total rainfall and intensity, but also on drainage capacity. The relationship between rainfall and waterlogging is very complex in urban areas. A comprehensive urban flooding model is currently a more effective method for simulating frequent waterlogging events (Ren, 2004; Xue, 2016).

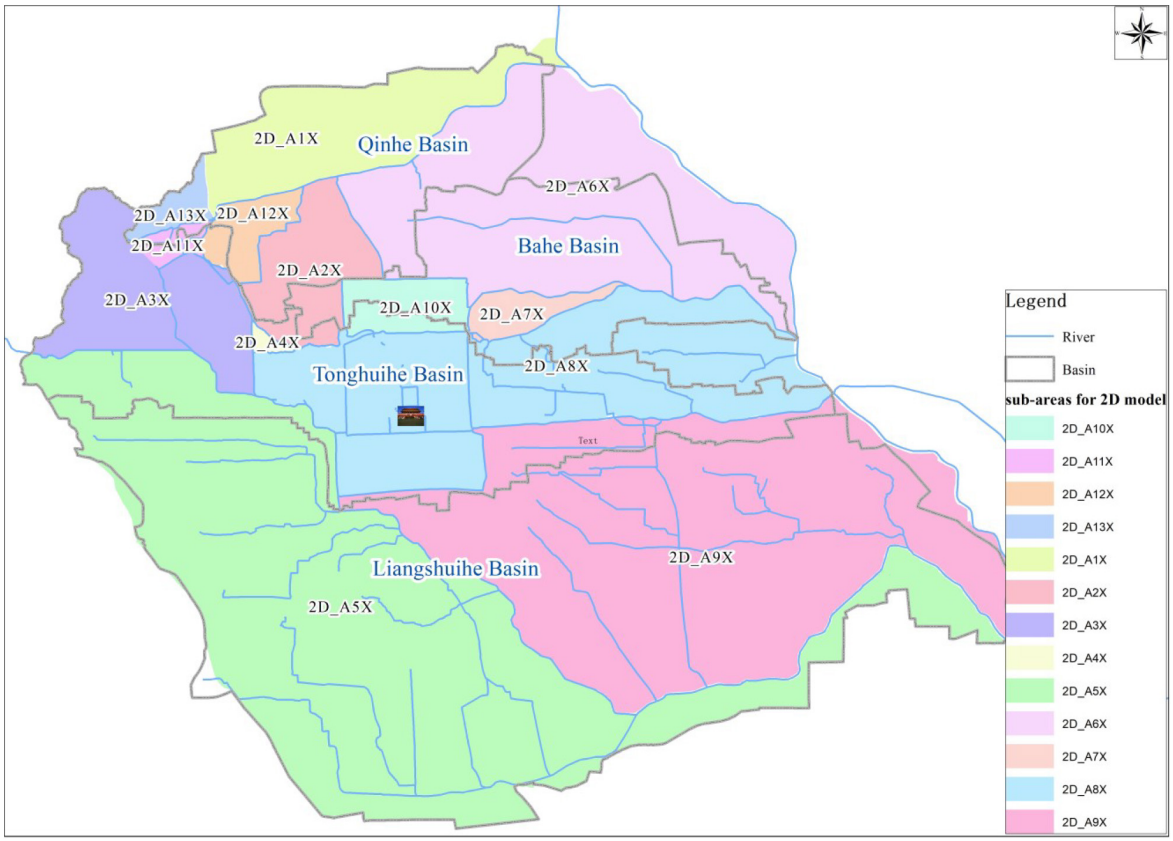

FIGURE 1 | The four river basins of Beijing city.

The Beijing urban flooding model was built gradually over several years and has been put into use during the flooding season from the year 2018 (Xu et al., 2020b). The simulation results have served not only for waterlogging alerts but also for scheduling a water conservancy project dealing with Beijing's urban rivers and for analyzing the floodwater capacity of river and pipe. In making improvements to the flood simulation results for urban areas, the methods of obtaining accurate data and of generalizing from special objects are highly significant. In developing the Beijing urban flooding model, multi-mode surface terrain data acquisition and generalization methods supported the model's construction and fine simulation effectively. Buildings, roadways, and overpasses were described carefully and in detail for simulating the depth of waterlogging more accurately. The partial microrelief of lower concave overpasses and many barricades, including even notable curbs, were obtained using several techniques such as local traditional measurement, vehicle-borne LIDAR scanning, remote sensing interpretation (Neelz et al., 2006), and extrapolations from street views of a publicly accessible online map.

In this study, GIS play an important role in preparing and processing multifarious data for the detailed urban flooding model. GIS tools serve not only for preprocessing the input data also for demonstrating the input–output data of the model intuitively.

DATA AND METHODS

Range

The Beijing urban flooding model covers a much wider area than the main city. To maintain the integrity of the river basins, the range of the model is extended from Beijing city outward to the Qinghe basin boundary in the north and to the Liangshuihe basin boundary in the south. It covers an area of 1486 square kilometers. It is therefore a significant challenge to construct, maintain, update, and run such a large and detailed hydraulic urban flooding model.

Overall Structure

The Beijing urban flooding model is based on the China IWHR Urban Flooding Model. The IWHR holds the independent intellectual property rights of the IWHR Urban Flooding Model. The IWHR model includes its own program and modeling platform which is integrated with GIS tools. It includes four components as follows: a 1D river model based on an explicit-scheme finite-difference formulation of the kinematic wave approach; a 2D surface model based on the Godunov-type finite-volume method for 2D shallow water flows on an unstructured grid; an underground rainstorm pipe model based on an explicit-scheme finite-difference formulation combined with the

Preissmann virtual narrow seam method; and a coupling module. The rainfall runoff procedure based on the Xin'anjing model is embedded in the 2D surface model.

The IWHR Urban Flooding Model operates as follows. First, the net rainfall is calculated after inputting rainfall data and is loaded directly on the 2D meshes according to the spatial position. The procedure of net rainfall calculation is reduced to two steps. The first accounts for water loss at an earlier stage which includes evaporation, vegetation interception, and land depression storage; the second accounts for land infiltration. After subtracting earlier water loss and land infiltration from the total rainfall, the remainder is net rainfall. The computation of surface convergence is performed on each mesh of the surface model. It differs from many commercial flooding models in which the rainfall–runoff procedure is always performed on each sub-catchment. This method leads to a computational burden but is essential for simulating the process of waterlogging caused by initial surface flow. The experience of flooding in Beijing city shows that most waterlogging is caused by initial surface water runoff because of insufficient capacity in the pipe system rather than by pipe node overflow. The surface runoff of each mesh is equal to the net rainfall, the computation of which is performed on each mesh.

Second, the runoff convergence procedure is composed of three steps as follows: surface convergence; underground rainstorm pipe convergence; and river convergence. After the rainfall–runoff based on each mesh, the surface runoff begins to participate in surface convergence based on the surface model. In the process of surface convergence, the surface runoff may flow into the underground rainstorm pipe when meeting entrance points (manhole or rain perforated strainer) and begins to participate in the pipe network convergence based on the underground pipe model. The pipe runoff will flow into the river at the outlet and begins to participate in river convergence based on the river model. It is also obvious that surface runoff may flow into the river directly when meeting the river and will then begin to participate in river convergence likewise. The exchange and transmission of hydraulic parameters between different models are performed via the coupling module.

Based on the above structure of the IWHR urban flooding model, the Beijing urban flooding model is composed of one river model, several surface models, several underground pipe models, and one coupling module.

The Beijing urban flooding model can simulate the whole procedure of rainfall–runoff–convergence while taking into account water dispatching via all reservoirs, water gates, dams, pumping stations, and other flood prevention and drainage projects. Thanks to the support of the exterior hydrological model, it can simulate the procedure of flooding caused by exterior river flood and waterlogging caused by rainstorm and interior river flood at the same time. Flooding and waterlogging cannot be separated clearly because they interact with each other. Some urban flooding models may be more suited for the simulation of river flooding; some more suited for the simulation of waterlogging. In actuality, however, many cities face the risk of river flooding and waterlogging simultaneously. The city of Beijing is an example of this.

Surface Model

Surface Division

The area covered by the main city of Beijing is so large (in excess of 1000 square kilometers) that a surface model of the whole area would be expensive in terms of computational resources and computing time. GIS tools face a considerable challenge in constructing and maintaining the spatial topology relations for a surface mesh layer and it is almost impossible to update topology and coupling relations manually because of the huge amounts of mesh. To avoid this problem, the whole study area is divided into several subareas with the main river as a cut-off line. The surface model is built individually for each subarea (**Figure 1**). But the river system is built as a whole model for the main city. Each surface model exchanges water through the river system and pipe drainage system. There is no water exchange directly between the different surface models. They are dynamically and indirectly lined with each other through the river model. The river model supplies the boundary condition dynamically for each surface model in the simulation.

The advantages of this approach are obvious. First, it is less difficult to maintain and update each middle-sized surface model individually. Second, the resolution and scale of the surface model of each subarea can be varied according to the attention level, the data condition, and the terrain complexity. A further advantage is an obvious improvement in computing speed by making use of multicore processing.

The surface of the whole Beijing city is divided into 15 subareas based on the four main interior rivers and their branches. The average area of each surface model is about 100 square kilometers, but their areas are uneven, with the largest about 200 square kilometers.

Mesh Generation

As the basic simulated unit of the surface model, the mesh should be generated on the basis of thorough planning, especially for a detailed flooding model. In constructing the Beijing urban flooding model, the main problems in planning mesh generation include mesh size, combining subareas with different mesh sizes, control lines, and mesh shape.

When constructing a hydraulic flooding model for a large city such as Beijing, one challenge is to find a suitable balance between efficiency and precision. The mesh size determines the balance. If the mesh is coarse for an overview of the whole city, then the topographical detail of the urban area cannot be expressed adequately. It may lead to a wrong surface convergence and reduced precision if a thin water-blocking object is ignored because of the coarse mesh. If the mesh is refined for high precision of the surface information, then a large number of meshes will lead to a reduction in computational efficiency. The mesh should be as fine as possible within the limits of computing power.

Taking into account both precision and efficiency in flood simulation, two kinds of surface models were established for the main city of Beijing. The difference between them is the description precision of the land surface and other modeling objects. The most obvious difference is mesh size. The coarse-mesh model is called a generalized model in which the mesh

size is about 100 m. The refined-mesh model is called a detailed model in which the mesh size is about 5–10 m. The generalized model is quick to run but the result is less accurate, whereas the detailed model needs more computing time but the result is more accurate. There are 15 subareas in the main city, and each subarea includes these two types of surface models with different precision levels. They can be combined together according to practical requirements. The advantage is that a high precision model of a region can be realized with due consideration given to the basin integrity of the whole city.

Control lines and methods of extracting them are another important factor when generating a mesh. DEMs are usually displayed as uniformly spaced grids. Because of the uniform point spacing, DEMs can "jump over" break lines without identifying ditches, stream centerlines, steep banks, roads, and other similar features. Here, it means that the width of these features is insufficient to be treated as a 2D mesh. However, these linear features generally influence the overland flow because of special elevation such as narrow walls or roads. They may constitute a passageway for water or a water-blocking object. Not taking them into account will lead to incorrect analysis and poorer results. These linear features affect the water flow and need special consideration. Identifying the linear features from high-resolution remote sensing imagery and matching them with mesh edges automatically using a spatial analyzing function based on GIS is effective in solving the problem of setting special edge types of a 2D model artificially. These edges are set to a special elevation in the 2D model for simulating their influence on overland flow (Duke et al., 2003). Another factor is the outlines of wide roads and buildings which are also considered as control lines for the mesh. The purpose is to ensure that the mesh of road and building is "pure." The outstanding curb and the isolation belt of a road may also hold back surface water and therefore should also be set as control lines and assigned an especial elevation in the 2D model. Main roads and auxiliary roads are divided into different meshes to describe differences in elevation. The pure building mesh benefits not only from the expression of more reasonable waterlogging but also from the calculation of the surface water flux between the roof of a building and the ground using the Weir formula. The outlines of buildings and wide roads can also be extracted from remote sensing imagery based on GIS tools.

Given that too many irregular control lines present limitations to mesh generation, the ideal mesh should be properly boundary-fitted. To describe irregular control lines in the Beijing urban flooding model, an unstructured quadrilateral mesh mixed with a small triangular mesh is a good choice when taking into account both a boundary-fitted mesh and small quantities. In **Figure 2**, the red line is a special mesh line which is generated using a control line. Using a control line in mesh generation can reflect the true surface in more detail.

Elevation Assignment and Amendment

Surface flow paths are easily modified by human-made features; hence, the flow diversion effects of buildings should be fully recognized. In urban areas, a detailed description of the ground surface is most crucial for a detailed model. However, the terrain data currently available from conventional cartographic surveys do not provide sufficient detail or timeliness to satisfy the need for a detailed hydraulic model, especially in urban areas where change is constant.

The elevation for each mesh in the Beijing urban flooding model is initially assigned using DEM data at a scale of 1:2000; the data are sourced from surveying and mapping departments and describe the dominant terrain gradients. This may be adequate for rural areas, mountainous areas, and heavy flood simulation. In Beijing city, however, the natural terrain is quite flat as a whole except for small local areas. Dense buildings and road networks lead to complex artificial terrain areas where many partially low-lying places appear and are easily waterlogged. In an artificial low-lying area, the partial microrelief plays a decisive role in the process of runoff flow concentration during a rainstorm. For those special meshes, the elevation was amended, respectively. They include roads, bridges, and buildings. For many roads, the more detailed and believable elevation data were gathered from the transportation departments and overlaid on the initial elevation data.

There are hundreds of overpasses in the main urban area of Beijing, and the majority are the lower concave type. In the bottom floor of a lower concave overpass, waterlogging occurs frequently in the flooding season and has a serious impact on traffic, even posing a danger to life. For better simulation, the partial microrelief of the lower concave overpasses and many barricades, even notable curbs, was obtained and amended separately using numerous techniques and generalization, such as local measurement, vehicle-borne LIDAR scanning, aerial imagery, and extrapolation according to the street view of online maps such as Baidu maps. Generating the surface model by detailed processing and reasonable data is an innovative aspect of the Beijing model and has been effective in improving the simulation results.

Figure 3 shows the obvious change in mesh terrain after elevation amendment.

In the Beijing urban flooding model, the elevation amendment of those special meshes is a labor-intensive manual procedure.

Rainfall Runoff

Another novel aspect of the Beijing urban flooding model is that the simulation of rainfall runoff and surface convergence is processed on each mesh of the surface model. It leads to a computational burden but is essential for simulating both the waterlogging caused by initial surface runoff and by pipe node overflow.

In simulating urban flooding, the hydrological process is separated conceptually from the hydraulic process. The computation of the surface runoff from rainfall can be carried out by a surface runoff model. In the Beijing urban flooding model, the rainfall–runoff process of the main city and that of the exterior were treated separately.

For the rainfall–runoff process of the exterior range, a surface runoff hydrograph is computed for each sub-catchment. Runoff hydrographs from each sub-catchment are then used as input to the hydraulic model. The processes of several river inflows to the main city which result from the exterior hydrological

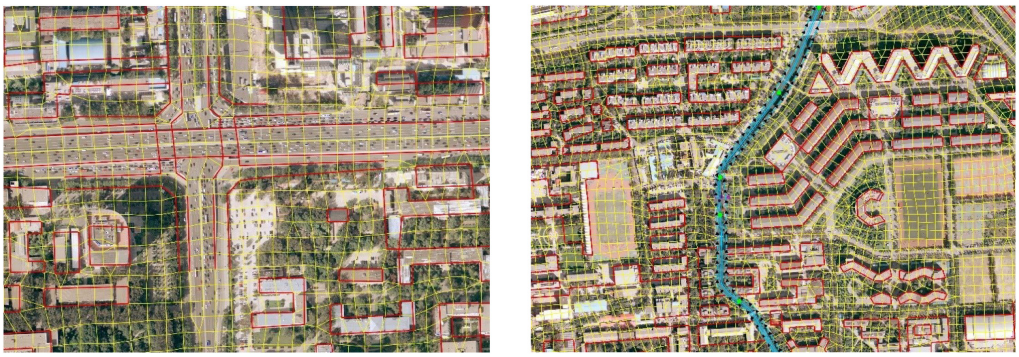

FIGURE 2 | Control line for mesh generation (the red line).

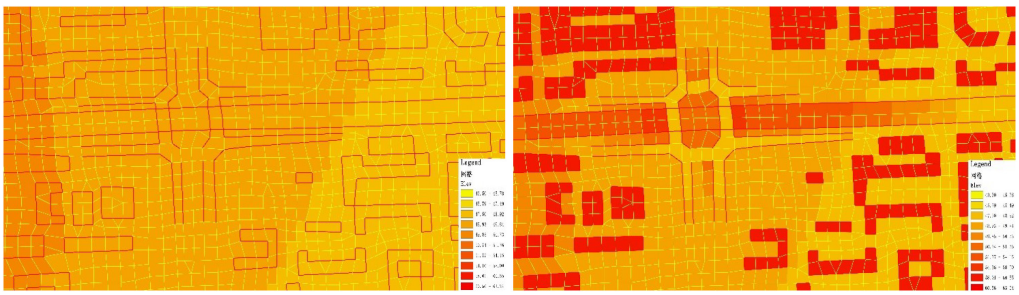

FIGURE 3 | Elevation map before and after amendment.

model were considered as 1D boundary conditions of the Beijing urban flooding model.

However, it is a different challenge when dealing with the rainfall–runoff process in the range of the 2D surface model. Rainfall was applied as a direct boundary condition over the 2D surface. Net rainfall is obtained after subtracting earlier water loss and land infiltration from the total rainfall. The earlier water loss includes evaporation, vegetation interception, and land depression storage at an earlier stage. The surface runoff of each mesh is equal to the net rainfall, and the computation of net rainfall is performed on each mesh. When simulating rainfall that has already occurred, a Thiessen polygons approach is applied to create 2D rain input files for distributing rainfall using records from several dozen rainfall stations. When simulating rainfall that is about to occur, a rainfall data product at kilometer level can be used directly to create 2D rain input files. After the rainfall–runoff process on each mesh, surface runoff begins to participate in surface convergence based on the surface model.

In some generalized flooding models, both infiltration and evaporation are neglected given the high density of impervious areas in a large city. However, in the urban area of Beijing, many areas of vegetation have been planted and many waterbodies have been impounded in recent years. According to recent data, the proportion of the vegetation area is about 33% in the range of the flooding model. Additionally, much of the rainfall in Beijing is not heavy. This means that infiltration and evaporation consume a rather higher proportion of the rainfall. In a detailed flooding model, infiltration and evaporation should not be neglected.

Earlier water loss in this model is set to a constant which is related to the land-cover type. The infiltration is calculated using Houghton's infiltration formula. The infiltration parameters, such as initial infiltration and stable infiltration after saturation, are also set for each mesh according to the mesh's land-cover type. However, many meshes are not pure. Three steps were taken to solve this problem. First, the basic infiltration parameters which are related to the land-cover type were measured for each type. In Beijing city, the land-cover types include buildings, vegetation (including green areas around buildings), bare land, waterbodies, blacktop, gravel or cement roads, and semi-hard pavements (such as pathways within the green belt). The measurements of earlier water loss and basic infiltration parameters for Beijing city are listed in **Table 1**. Second, high-resolution remote sensing data for the year 2018 were interpreted to produce a detailed land-cover type map of Beijing city. Third, the infiltration parameters for each mesh were calculated based on the basic infiltration parameters and the weighted averages of each land-type area in the mesh. Surface roughness for each mesh was calculated using the same method.

The impact of land cover and the underlying surface on flooding is reflected in two aspects. One is the quantity of runoff, which depends on the strength of rain and the type of land cover. A surface with high vegetation coverage will produce less runoff than a surface with low vegetation coverage. Normally, the parameters for runoff production, such as initial hypotonic and stable hypotonic after saturation, will have been set or changed according to the mesh's land-cover type. The second

TABLE 1 | The basic infiltration parameters for runoff in Beijing city.

Land type	Im (mm)	F0 (mm/h)	Fc (mm/h)	β (1/h)	r
Building	3	3	3	0.2	0.070
Vegetation	5	15	20	0.2	0.065
Blacktop	3	0	0	0.2	0.035
Bare land	5	15	20	0.2	0.040
Waterbody	0	0	0	0	0.035
Semi-hard pavement	4	8	10	0.2	0.070
Gravel or cement road	3	5	5	0.2	0.035

Note: Im, water loss quantity; F0, initial infiltration speed; Fc, stable infiltration speed; β, Horton attenuation coefficient; r, roughness of each land type.

aspect is the roughness of the land surface, which affects the water flow velocity. The smoother the surface, the smaller the roughness, and the faster the water flow. In a similar way, the parameters for surface roughness of a mesh in the 2D model and of a cross-section in the 1D model can be set according to the land-cover type.

Underground Pipe Model

In the underground pipe model, the pipeline, rain perforated strainer, manhole, and pumping station are four kinds of important objects. There are two modes of drainage from surface to pipe system. One is through a rain perforated strainer, and the other is through a manhole. Rain perforated strainers and manholes need different treatments when modeling. A manhole receives water from many meshes that are located in the manhole's catchment range. There is a virtual reservoir on top of each manhole for the temporary storage of a quantity of water equal to the catchment area's drainage capacity. Extra water will be overland flow. The discharge from the virtual reservoir into the pipe system is calculated using the Weir formula based on the water level difference of two nodes. The overflow from the pipe system will spray out from the manhole if the pipe is full and the water head of the manhole is much higher than that of the surface. On the whole, this is a generalized mode of drainage. The most significant problem is making a reasonable catchment division and assigning each one a reasonable maximum drainage capacity. However, it is very difficult in those areas with a great complex of pipes which intersect each other.

The other mode of drainage through rain perforated strainers instead of manholes is purely physical. This mode of drainage is a novelty of the Beijing flood model. A rain perforated strainer receives water only from the surface mesh where it is located. For those other meshes with no rain perforated strainers in the locality, the surface runoff will not enter the pipe system until it meets a rain perforated strainer. This mode of drainage is much closer to reality, but the need for a perfect pipe system is a vital necessity to obtain an ideal simulation result. Additionally, the coverage of the rain perforated strainers is so dense in urban areas that it is not easy to obtain perfect data. The problem of deciding on the kind of drainage mode should be determined by the quality of the rain perforated strainer data. In many cases, these two drainage modes can be used simultaneously.

The other object that the model supports is the pumping station, which is considered as a kind of operating condition in the pipe system. In Beijing city, many lower concave overpasses mainly depend on a pumping station for drainage during a heavy rainstorm because the inherent routine facility based on gravity cannot fulfill the need for fast drainage. After the heavy rainstorm of 2012-07-21, many rainwater traps were built under the main bridges. When simulating a heavy rainstorm, neglecting the function of the pumping stations and rainwater traps will lead to "false" serious surface waterlogging in the lower concave overpasses.

River Model

In constructing the river model, there are two points worth mentioning. One is that there are many flood control engineering facilities located at the river in Beijing city. Their control of waterflow should be simulated in the 1D river model. Another point concerns river cross-sections.

Flood control based on engineering facilities through the urban river system is an important measure to reduce flood risk in Beijing city. In recent years, a number of small lakes were landscaped in city parks, except for the big gravel-pit parks in wet suburbs. The rivers joining these new lakes and several of the existing large lakes, such as the Kunminghu lake, Yuyuantan lake, and Longtanhu lake, form a dense water system with a considerable flood capacity. It is necessary to set down a series of reasonable control rules and pre-arranged planning for the water system to play a constructive role in flood control. There are more than a hundred water gates in the river system of Beijing city. Several are always used for flood control, while others are used only during heavy rainstorms. However, rainfall is often light in Beijing, and more water gates are partially opened according to the upstream water level and the forecast rainfall in order to maintain a landscaped water level in the lower reaches, because water resources are so valuable in Beijing. Each water gate has its own operating water level which is preset based on experience. The gate will be completely closed if the current water level at the gate is lower than its operating water level. The gate will be partially open if the current water level is a little higher than its operating water level, and completely open if the current water level is about half a meter higher than the operating level and heavy rainfall is forecast. Such careful consideration of the gates in the river model improves the simulation result and is especially significant for simulating a medium level of rainfall. An initial water level for each reach is set according to the routine river level before rainfall in the

flooding season, instead of simulating from a dry riverbed. This is a better method for simulating short-term rainfall. Setting actual initial water levels and refining the flood control rules in the 1D river model ensures that the simulation result is more reasonable both for heavy rainfall and regular rainfall. Another problem concerns river cross-sections. It is very costly in terms of human and material resources to survey river cross-sections (including underwater elevations) and the cross-sections are always changeable. Generally, a relatively small number of cross-sections, especially where a significant change in conveyance occurs, are selected as representative of average conditions in those reaches without permitting excessive conveyance change between cross-sections. However, this does not satisfy the requirements for a refined hydraulic river model, especially for natural rivers. Automated procedures normally use high-density elevation points that are sourced from stereo-photogrammetric models or LIDAR datasets. Computer generation of a potentially large number of cross-sections can supplement those from surveys as long as there is no significant change in the stream channel geometry below the water level.

Model Coupling

In the process of surface convergence, surface runoff will flow into the underground pipe network when meeting rain perforated strainers and will begin to participate in pipe convergence. Pipe runoff will flow into the river at the outlet and begin to participate in river convergence. Obviously, surface runoff may also flow into a river directly. Exchanging and transmitting hydraulic parameters between different models are performed via a coupling module. The Beijing urban flooding model includes a 1D river model, several 2D surface models, an underground pipe model, and a coupling module. The purpose of coupling different models is to transmit real-time parameters such as water levels or the discharge of junction objects which connect the models. The duty of the coupling module is to search and find the correspondence relations between junction objects.

The Coupling of the 2D Surface Model With the Underground Pipe Model

Runoff generally starts as overland flow on the ground surface before entering the underground pipe system. Surface water can enter the pipe system by flowing through rain perforated strainers. In many commercial hydraulic models, manholes are normally generalized as the water entrance of many surrounding meshes from surface to underground pipe. In the Beijing urban flooding model, the junction object of the 2D surface model with the pipe model is meshes and rain perforated strainers or manholes. Manholes are generalized as the drainage entrances of many surrounding meshes in areas except for main roads. In main road areas, the mesh runoff will continue as surface convergence until it meets a rain perforated strainer and flows into the pipe system. Of course, overflows from manholes will turn into overland flow with existing runoff. The processing is much closer to reality. The coupling mode between surface and pipe was the first to be established.

The Coupling of the 2D Surface Model With the 1D River Model

Water exchange will happen between river and surface when the water level of river or mesh is higher than dike elevation. The junction objects of the 2D surface model with the 1D river model are river cross-sections and nearby edges of the surface mesh.

The Coupling of the Underground Pipe Model With the 1D River Model

In normal conditions, pipe drainage will flow into a river at an outlet if the pipe water level is higher than that of the nearest river cross-section. Otherwise, if the water level of the river is much higher, pipe drainage will be restrained because of river flood prevention. At this point, the drainage function of the pipe network is no longer in force and may result in waterlogging. The junction objects of the 1D river model with the underground pipe model are river cross-sections and pipe outlets.

The main content of the coupling module includes the junction object's corresponding relations between different models and the methods of calculating the discharge transmitted. Building the junction object's corresponding relations for different models is a heavy duty for the coupling module. However, it would cost much more time and energy and be difficult to update using artificial matching methods. It can be realized effectively, accurately, and automatically based on GIS spatial analyzing functions and the modeling tools of the IWHR urban flooding model.

RESULTS

Here, we describe some of the simulation results based on the Beijing urban flooding model, built as above, and their application to Beijing city's flood control system.

Analysis of Model Rationality

After constructing the Beijing urban flooding model, three historic rainstorm events were selected to simulate the flood process within the study area and to analyze the model's rationality. These were the rainstorm events of 2012-07-21, 2016-07-20, and 2017-06-21. Three of Beijing city's key hydrological observation stations on the main rivers were selected as the validation points of the 1D river model. Their locations are the Shenjiafeng gate on the Qinghe River, the Lejiahuayuan gate on the Tonghuihe River, and the Fenhongdao gate on the Lianghsuihe River. For the surface model, about 30 lower concave bridge areas and sections were selected, and some monitoring data of water accumulation and statistically reported data were collected for verification. For the pipe network, two monitoring points were selected for rationality analysis.

The rainstorm of 2012-07-21 lasted a short period. The rainfall was mainly concentrated in 10 h with an average rainfall of 215 mm in urban areas. However, the heavy rainfall lasted for rather longer and the maximum hourly rain was up to 101 mm. The rainstorm of 2016-07-20 lasted a long period and was concentrated in 43 h with an average rainfall of

291 mm in urban areas, but the rainfall intensity was smaller than that of the famous 2012-07-21. The maximum hourly rain intensity was 56.8 mm. The rainstorm of 2017-06-21 was wide-ranging and uniform. The cumulative rainfall was large with the heavy rainfall appearing in the later period and lasting about 50 h.

Figure 4 demonstrates the simulated and the measured discharge of the rivers for the rainstorm of 2012-07-21 at the three selected cross-sections. The measured peak discharge at Shenjiafen was 629 m^3/s, and the simulated discharge was 641 m^3/s. The difference in peak discharge was +12 m^3/s (+1.9%). At Lejiahuayuan, the measured peak discharge was 440 m^3/s and the simulation was 386 m^3/s. The difference in peak discharge was −54 m^3/s (−12%). At Dahongmen, the measured peak discharge was 515.9 m^3/s and the simulation was 513.2 m^3/s. The difference in peak discharge was −2.62 m^3/s (−0.51%). For the rainstorm of 2016-07-20, the measured peak discharge at Shenjiafen was 389 m^3/s and the simulation was 355 m^3/s. The difference in peak discharge was −34 m^3/s (−8.8%). At Lejiahuayuan, the measured peak discharge was 224 m^3/s and the simulation was 260.67 m^3/s. The difference in peak discharge was +36.67 m^3/s (+16.4%). At Dahongmen, the measured peak discharge was 513 m^3/s and the simulation was 429 m^3/s. The difference in peak discharge was −84 m^3/s (−16.4%). The results show that the simulated flood process was not in high accordance with the actual measures, but the difference in the total flood volume of the three cross-sections was less than 8.8%. For the rainstorm of 2017-06-21, the measured peak discharge at Dahongmen was 124 m^3/s and the simulation was 115 m^3/s. The difference in peak discharge was −9 m^3/s (−7.24%). The difference in the total flood volume was −8.47%. The main river discharge calculated by the model was similar to the measured volume, and the simulation result of the 1D model was therefore considered to be reasonable.

A number of waterlogging sites with risk levels were selected as the factor for the verification of surface simulation results. The risk level was graded according to the maximum waterlogging depth. In the Outdoor Drainage Design Code, it is generally considered that rainwater amounts that are less than 15 cm will not affect traffic or other hazards (Zhang et al., 2012). Ordinarily, water depth greater than 27 cm will affect traffic, while a depth greater than 40 cm will affect pedestrian safety. According to this standard, levels between 15 and 27 cm water depth were considered low level, levels between 27 and 40cm water depth medium level, and levels greater than 40 cm water depth high level.

Since 2019, about 100 waterlogging monitoring stations have been built in Beijing. The rainstorm of 2020-08-12 was the strongest and the most wide-ranging in the last 2 years. It lasted about 24 h, and the total rainfall was about 158 mm. The time and space distribution of this rainfall was very uneven. The strongest point of the rainfall was about 40 mm in 10 min, causing much waterlogging. The model results showed that 142 sites were waterlogged, and about 40 of them were seriously waterlogged. After the rainstorm, the waterlogging data collected from 16 monitoring stations were considered valid. **Table 2** compares the waterlogging depth and risk level results of the simulated data (via the model) with those of the measured data (via the monitoring stations).

Simulation of Typical Rainstorm Scenarios

The original intention in constructing the Beijing urban flooding model was to produce a quick simulation of a forecast rainstorm. The aim is to provide concrete data about the coming waterlogging for flood control. The simulation results of a forecast rainstorm can help people to identify flood risk at an early stage and provide early warnings about waterlogging locations and processes. However, the problem at present is that the model is so large that it is difficult to obtain a real-time simulation result quickly. A simulation using a detailed model of the whole city will need so much time that it cannot satisfy the requirement for real-time reporting. The combination of a generalized model of most subareas with a detailed model of some areas of the most concern is a good method for obtaining a result as quickly as possible.

Another method is to identify possible waterlogged locations quickly according to the results of a similar rainfall which has been simulated in advance and saved in a scenarios library. Based on the rainfall characteristics of Beijing city, many kinds of typical rainfall scenarios were designed and simulated in advance. A scenarios library of rainfall–waterlogging in Beijing city was then constructed, based on the design of different rainfall scenarios and their simulation results.

The rainfall scenarios include the recurring intervals of 1, 2, 5, 10, 20, 50, 100, and 200 years with short durations (1 and 3 h) and long durations (12 and 24 h). The scenarios of different frequencies were calculated according to the Beijing Hydrological Manual and Rainstorm Atlas. The amount of rainfall for a 1 h rainstorm of the above recurrences is 16, 27, 50, 68, 78, 96, 108, and 120 mm, respectively. The amount for a 24 h rainstorm of the above recurrences is 45, 72, 140, 200, 255, 340, 400, and 460 mm, respectively. Many scholars have proposed a variety of methods to establish a rainfall type of short duration. Among them, the Chicago rainfall pattern is generally applied to the design of a short duration rain distribution. It is based on the rain intensity formula and the rain coefficient of the non-constant rainfall synthesis method (Zhang et al., 2002). However, research on the rainfall features of Beijing city, based on 50 historic rainfall events spanning a 20-year period, showed that the rainfall pattern of Beijing was different from the Chicago rainfall pattern. The process of designing typical rainfall scenarios of long and short durations was based on the Beijing urban rainfall pattern instead of the generally used Chicago rainfall pattern, combined with actual measures. **Figure 5** shows the simulation results for road and Lianhuaqiao bridge waterlogging using typical scenarios for a 24 h rainstorm with recurrence intervals of 10, 20, 50, and 100 years. It is obvious that Beijing city will suffer serious waterlogging if the rainfall is much heavier than the 20 year recurrence interval.

There are already more than 500 scenarios and corresponding simulation results in the scenarios library. They can and

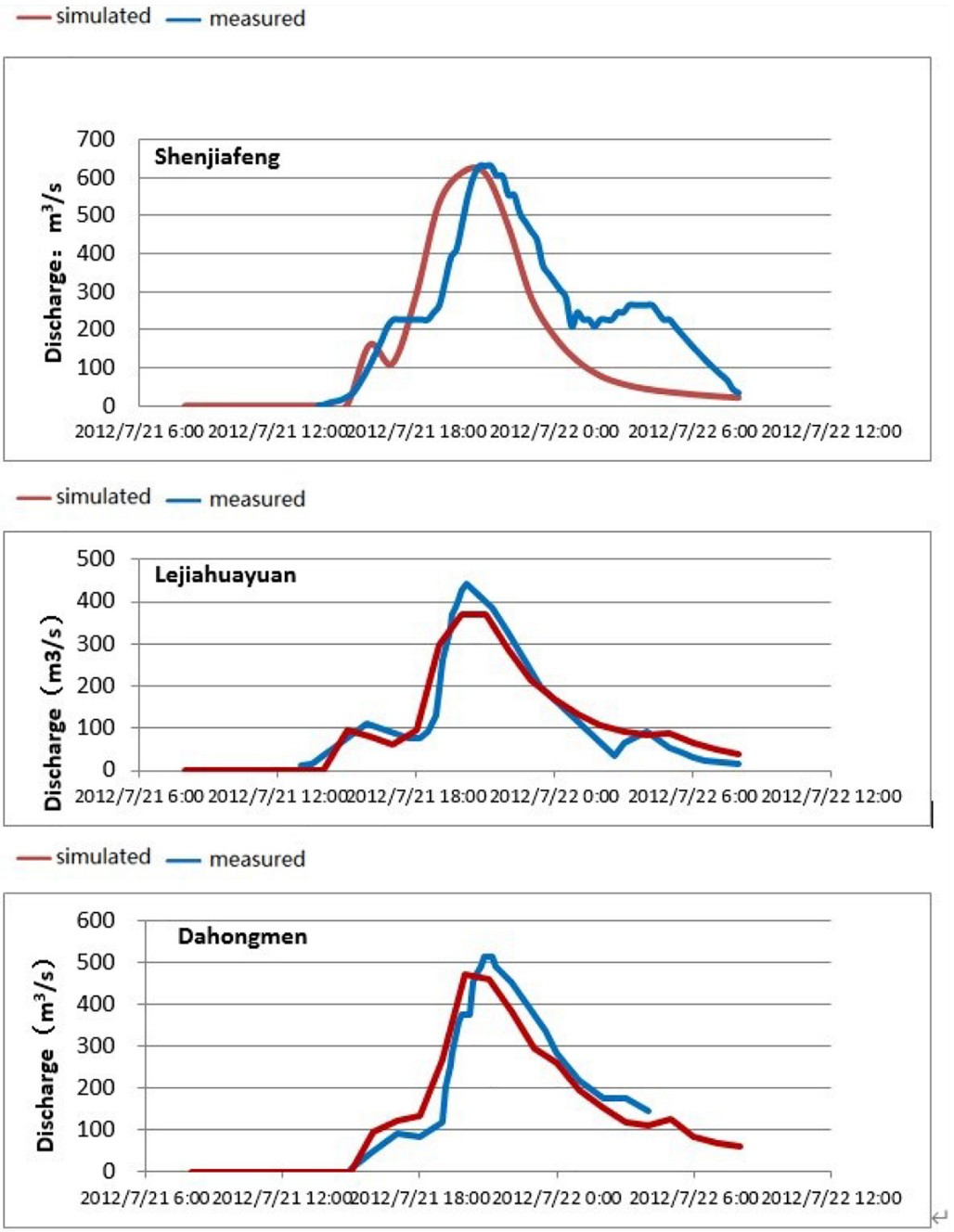

FIGURE 4 | The simulated and the measured river discharge of the 2012-07-21 rainstorm.

have been applied to many fields such as early warnings of waterlogging, analysis of the urban river flood discharge capacity, urban river and lake control, evaluation of the pipe network drainage capacity, perfecting drainage facilities deployment, drainage planning, and so on. Waterlogging in the urban area of Beijing occurs mostly in the lower concave bridge areas and the lower roads or residential areas. Through a detailed flood simulation, the reasons for water accumulation can be analyzed one by one according to the load state of the drainage facilities. This provides the basis for later engineering measures such as pipeline, rain grate, pumping station, and underground reservoir construction in the affected areas.

Early-Warning of Waterlogging Risk

At present, quickly simulating a forecast rainstorm and identifying the locations where waterlogging risk is high are the most important duties of the Beijing urban flooding model. Currently, however, with an approaching short duration rainfall

TABLE 2 | The simulated and the measured depth of waterlogging of the 2020-08-12 rainstorm.

Location	Measured depth (m)	Measured risk level	Simulated depth (m)	Simulated risk level
Yuzhidong Road Railway Bridge	2.45	High	1.48	High
Auxiliary road on east side of the Shangqin Bridge	0.21	Low	0.80	High
Fengyu Railway Bridge	1.22	High	1.64	High
Tiancun East Road Railway Bridge	0.31	Medium	0.55	High
Huilongguan Railway Bridge	0.28	Medium	0.61	High
Lower concave bridge of the Fengtai West Station	1.60	High	1.02	High
Jingbao Railway Bridge	0.39	Medium	0.24	Low
Wanquanhe Bridge	0.28	Medium	0.22	Low
Chengzhuangzi Railway Bridge	0.67	High	0.39	medium
South Shawo Bridge	0.92	High	0.31	Medium
Xiaojin Bridge	0.29	Medium	0.17	Low
Lantai Railway Bridge	1.66	High	1.10	High
East channel of the West Station	0.46	High	0.36	Medium
Liuzhuangzi Railway Bridge	0.35	Medium	0.78	High
Jinjiacun Railway Culvert	0.26	Low	0.67	High
Xiangquan Island	0.17	Low	0.31	Medium

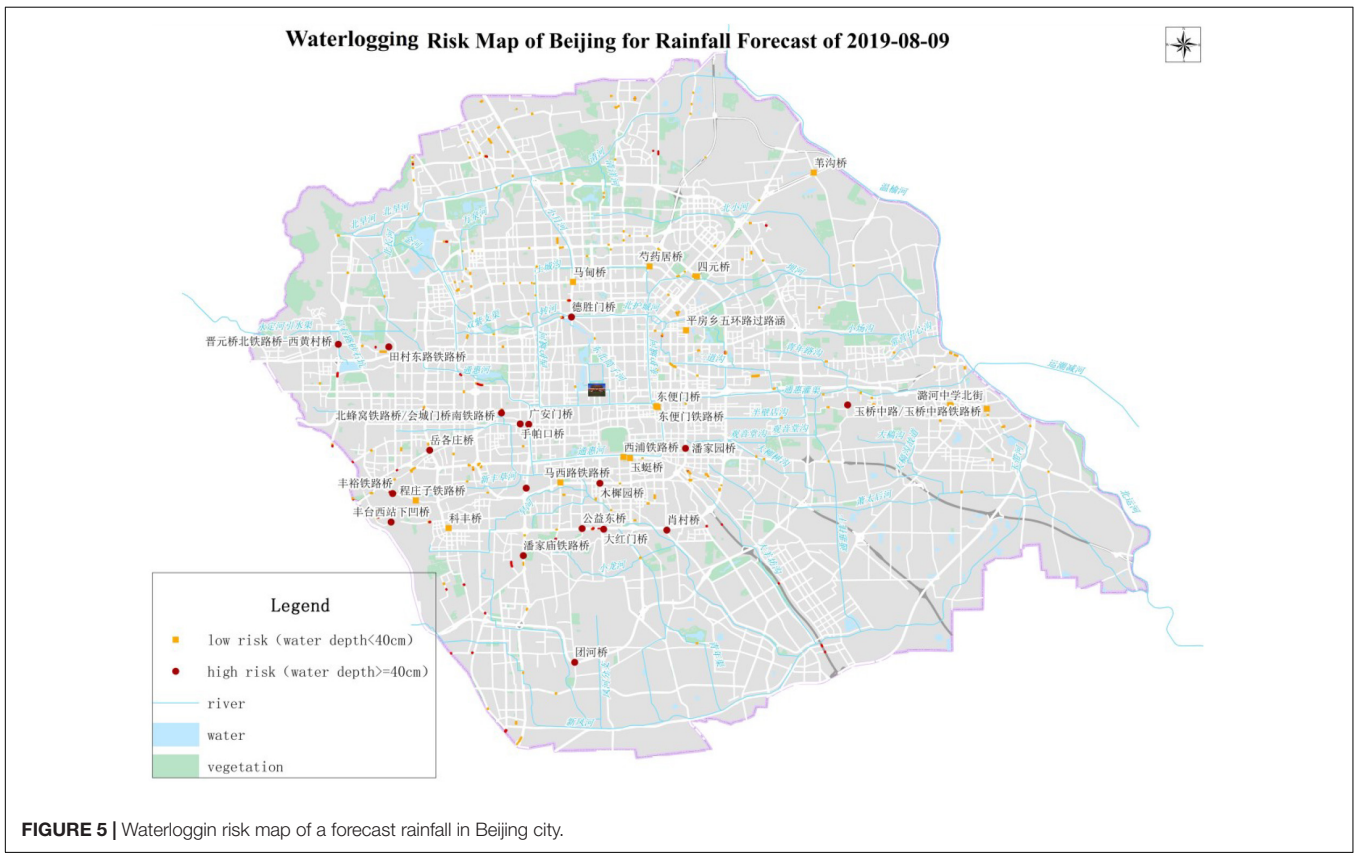

FIGURE 5 | Waterloggin risk map of a forecast rainfall in Beijing city.

of 1 h, the model can barely finish a simulation in 3 h to obtain peak flow at the downstream in 1 h. Most simulations of a forecast rainfall event need more than 1 h to finish the process and cannot satisfy those urgent demands because time is so expensive in a large city. In such a situation, the scenarios library of rainfall–waterlogging in Beijing city can play an important role (Xu et al., 2020a). According to the weather forecast, one or several rainfall scenarios can be designed quickly and the main parameters such as amount, intensity, spatial distribution, and approximate time duration of the forecast rainfall can be quantified. The next step is to find the most similar rainfall scenario through matching of rainfall parameters and to extract the corresponding simulation results from the scenarios library directly. Based on the possible water depth data, the waterlogging

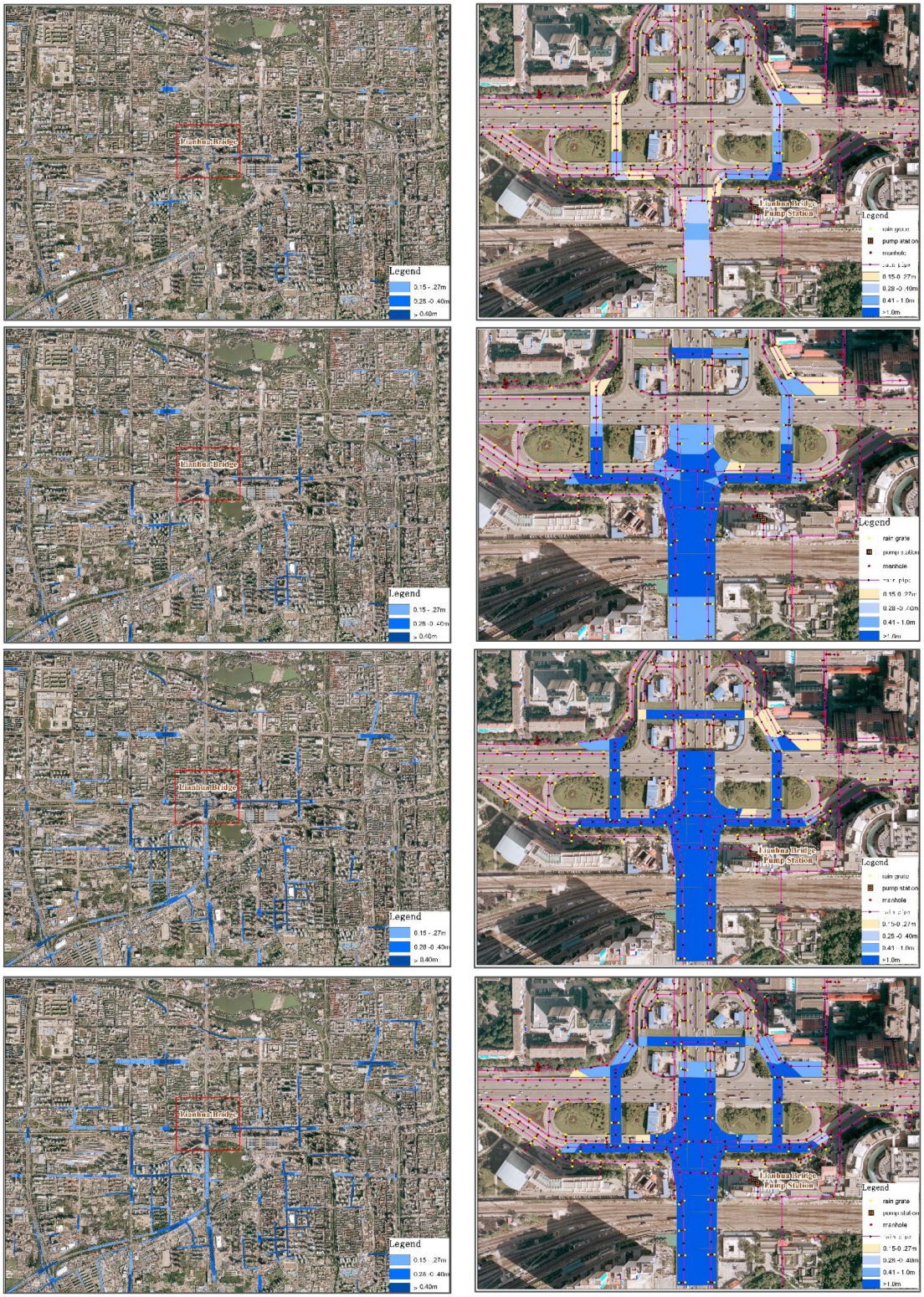

FIGURE 6 | Waterlogging simulationg result of 10, 20, 50, and 100 year recurrence intervals.

risk will be identified quickly. Early warning of waterlogging risk will provide a better basis for scientific decisions on flood control. **Figure 6** shows the waterlogging risk level map of a forecast rainfall.

CONCLUSION AND DISCUSSION

Conclusion

(1) The simulation result of a flooding model depends not only on the flow algorithm, but also on the accuracy of the surface characterization of urban areas. The accuracy of the data input determines the reasonability of the simulation results. Local microtopography is the decisive factor in water flow, especially for urban areas because of the influence of buildings and roads. When constructing the detailed urban flooding model of Beijing, much work was spent on a fine-grained description of the complex surface of the urban area so that the simulated waterlogging information is defined accordingly. The results indicate that the multi-mode generalization method described in this paper is effective and worth the time and effort invested in the process.

(2) The Beijing flooding model described in this paper can simulate the whole process of rainfall–runoff convergence. The rainfall is loaded directly on each mesh of the 2D model. Although a large amount of computation when calculating surface flow convergence reduces the efficiency of the model, a fine-grained simulation must satisfy the demand for precision first and for efficiency second. In addition, the procedure of this model provides a closer approximation to the real world and can simulate the whole waterlogging process. Of course, improving the model's efficiency is the next most urgent goal.

(3) This model adopts a variety of coupling methods for the surface model and drainage pipe network according to the different data status of the pipe network. It is helpful in solving practical problems. In particular, the unique pure physical coupling mode in which rainwater enters the pipe system through rain perforated strainers is much closer to reality.

(4) Besides the goal of flood control, floodwater redistribution between water systems should also focus on maintaining the river landscape in terms of water levels. It means that the open extent of the water gates depends on the water level of the upstream and the coming rainfall strength. The model can optimize and improve the fine-grained regulation of river water resources, which is especially important in a city such as Beijing where water resources are scarce.

(5) This detailed urban flooding model is suitable for the integrated simulation of internal and external flooding and waterlogging. Internal flooding means the flood comes from the river through the city. External flooding means the flood comes from the surrounding rivers. In addition to supporting early warnings of waterlogging, it can also support the analysis of urban river flood discharge capacity, redistribution of floodwater between urban rivers and lakes, evaluation of the pipe network drainage capacity, perfecting drainage facilities deployment, drainage planning, and so on.

(6) GIS tools have become the most popular method for constructing, updating, and maintaining a complex hydraulic model. It makes the flooding model easy to understand and easy to construct. Visual expression by GIS tools makes the simulation results, which are always output in text format, intuitive, dynamic, and in real-time.

Discussion

(1) The high density of buildings and roads in urban areas creates a complex microtopography in flood risk modeling. Most of these areas may suffer waterlogging easily during rainstorms if the drainage capacity and efficiency are not strong enough. The detailed flooding model depends mainly on a refined surface microtopography. To realize a detailed flooding model of Beijing city, the microtopography of the road network and bridge areas was amended one by one through a variety of methods and was expensive in terms of time and effort. Hopefully, improvements in the technology and methods of spatial data acquisition and processing will make it easier in the future to construct a detailed urban flooding model.

(2) To achieve a more realistic modeling result, mesh generation needs considerable thought. In particular, the fineness of the mesh and the efficiency of the model produce contradictory demands. Additionally, using too many control lines aimed at achieving a pure mesh creates difficulties for mesh dividing tools, such as low efficiency and instability.

(3) Calibration is the only way to reduce uncertainty over model parameters, but there are little data available for urban areas. Despite the frequent occurrence of urban floods, effective field observations of surface water and pipe water during urban flooding are insufficient.

(4) The quality of the weather forecast has a major influence on the quality of a flood simulation result. Because of the great uncertainty of a weather forecast, the result of flood modeling using forecast rainfall may differ from the actual situation. Fast updating and timely rainfall forecast products will be available with improvements in meteorological forecasting technology. The products could be input into the model directly and perform waterlogging analysis quickly to facilitate the early deployment of flood prevention measures. A detailed flooding model and a high-precision rainfall forecast can greatly improve the accuracy of the waterlogging analysis, thus realizing the integration of rainfall with early warnings of waterlogging. Ultimately, disaster prevention is more important than disaster relief.

DATA AVAILABILITY STATEMENT

The raw data supporting the conclusions of this manuscript will be made available by the authors, without undue reservation, to any qualified researcher.

AUTHOR CONTRIBUTIONS

SL supplied model program. YS and YXY supplied much data for the research. YHY helped draw figures for this manuscript and edited several chapters. All authors contributed to the article and approved the submitted version.

FUNDING

This research was funded by the Strategic Priority Research Program of the Chinese Academy of Sciences (Grant No. XDA 20030302) and the National Key Research and Development Plan of China (No. 2016YFC0803107).

REFERENCES

Beretta, R., Ravazzani, G., Maiorano, C., and Mancini, M. (2018). Simulating the influence of buildings on flood inundation in urban areas. *Geoscience* 8:77.

Bradbrook, K., Lane, S., Waller, S., and Bates, P. (2004). Two dimensional diffusion wave modelling of flood inundation using a simplified channel representation. *Int. J. River Basin Manag.* 2, 211–223. doi: 10.1080/15715124.2004.9635233

Bulti, D. T., and Abebe, B. G. (2020). A review of flood modeling methods for urban pluvial flood application. *Modeling Earth Syst. Environ.* 6, 1293–1302. doi: 10.1007/s40808-020-00803-z

Chen, A. S., Evans, B., Djordjevic, S., and Savic, D. A. (2012). Multi-layered coarse grid modelling in 2D urban flood simulations. *J. Hydrol.* 47, 1–11. doi: 10.1016/j.jhydrol.2012.06.022

Cheng, X., and Li, C. (2015). The evolution trend, key features and countermeasures of urban flood risk. *China Flood Drought Manag.* 25, 6–9.

Cobby, D. M., Mason, D. C., and Davenport, I. J. (2001). Image processing of airborne scanning laser altimetry for improved river flood modelling. *ISPRS J. Photogramm. Remote Sensing* 56, 121–138. doi: 10.1016/s0924-2716(01)00039-9

Djokic, D., and Maidment, D. R. (1991). Terrain analysis for urban stormwater modelling. *Hydrol. Process.* 5, 115–124. doi: 10.1002/hyp.3360050109

Dottori, F., Baldassarre, G. D., and Todini, E. (2013). Detailed data is welcome, but with a pinch of salt: accuracy, precision, and uncertainty in flood inundation modeling. *Water Resour. Res.* 49, 6079–6085. doi: 10.1002/wrcr.20406

Duke, G. D., Kienzle, S. W., Johnson, D. L., and Byrne, J. M. (2003). Improving overland flow routing by incorporating ancillary road data into Digital Elevation Models. *J. Spatial Hydrol.* 3, 23–49.

Fewtrell, T., Bates, P., Horritt, M., and Hunter, N. (2008). Evaluating the effect of scale in flood inundation modelling in urban environments. *Hydrol Process.* 22, 5107–5118. doi: 10.1002/hyp.7148

Funke, S., Pain, C., Kramer, S., and Piggott, M. (2011). A wetting and drying algorithm with a combined pressure/free surface formulation for non-hydrostatic models. *Adv. Water Resour.* 34, 1483–1495. doi: 10.1016/j.advwatres.2011.08.007

Gallegos, H. A., Schubert, J. E., and Sanders, B. F. (2009). Two-dimensional, high-resolution modeling of urban dambreak flooding: a case study of Baldwin Hills. *California. Adv. Water Resour.* 32, 1323–1335. doi: 10.1016/j.advwatres.2009.05.008

Gourbesville, P. (2009). Data and hydroinformatics: new possibilities and challenges. *J. Hydroinform.* 11, 3–4.

Gourbesville, P., and Savioli, J. (2002). "Urban runoff and flooding: interests and difficulties of the 2D approach," in *Proceedings of the 5th International Hydroinformatics*, (Cardiff).

Hénonin, J., Ma, H., Yang, Z.-Y., and Hartnack, J. (2015). Citywide multi-grid urban flood modelling: the July 2012 flood in Beijing. *Urban Water J.* 12, 52–66. doi: 10.1080/1573062x.2013.851710

Hénonin, J., Russo, B., Ole, M., and Gourbesville, P. (2013). Real-time urban flood forecasting and modelling: state of the art. *J. Hydroinform.* 15, 717–736. doi: 10.2166/hydro.2013.132

Hu, W., He, W., Huang, G., and Feng, J. (2010). Review of urban storm water simulation techniques. *Adv. Water Sci.* 1, 137–144.

Hunter, N. M., Bate, P. D., Neelz, S., Pender, G., Villanueva, I., Wright, N. G., et al. (2008). Benchmarking 2D hydraulic models for urban flooding. *Proc. Inst. Civil Eng. Water Manag.* 161, 13–30. doi: 10.1680/wama.2008.161.1.13

Huxley, C. (2017). "Rapid and accurate stormwater drainage system assessments using GPU technology," in *Proceedings of the IECA-SQ Conference*, (Brisbane).

Jaafar, K., Ismail, N., Tajjudin, M., Adnan, R., and Rahiman, M. H. F. (2015). "A review on flood modelling and rainfall-runoff relationships," in *2015 IEEE 6th Control and System Graduate Research Colloquium* (UiTM, Shah Alam: Malaysia), 158–162. doi: 10.1109/ICSGRC.2015.7412484

Josef, S. (2012). *Dynamic Modelling Of Urban Rainfall Runoff And Drainage Coupling DHI MIKE URBAN and MIKE FLOOD*. University of SalzBurg: SalzBurg.

Krebs, G., Kokkonen, T., Valtanen, M., Setäläb, H., and Koivusaloa, H. (2014). Spatial resolution considerations for urban hydrological modelling. *J. Hydrol.* 512, 482–497. doi: 10.1016/j.jhydrol.2014.03.013

Leandro, J., Chen, A. S., Djordjević, S., and Savić, D. A. (2009). Comparison of 1D/1D and 1D/2D coupled (sewer/surface) hydraulic models for urban flood simulation. *J. Hydraul. Eng.* 135, 495–504. doi: 10.1061/(asce)hy.1943-7900.0000037

Leandro, J., and Martins, R. (2016). A methodology for linking 2D overland flow models with the sewer network model SWMM 5.1 based on dynamic link libraries. *Water Sci. Techno.* 73, 3017–3026. doi: 10.2166/wst.2016.171

Liang, Q., Du, G., Hall, J. W., and Borthwick, A. G. (2008). Flood inundation modeling with an adaptive quadtree grid shallow water equation solver. *J. Hydraul. Eng.* 134, 1603–1610. doi: 10.1061/(asce)0733-9429(2008)134:11(1603)

Neelz, S., Pender, G., Villanueva, I., Wilson, M., Wright, N. G., Bates, P., et al. (2006). Using remotely sensed data to support flood modelling. *Proc. Inst. Civil Eng. Water Manag.* 159, 35–43.

Price, R. K., and Vojinovic, Z. (2008). Urban flood disaster management. *Urban Water J.* 5, 259–276. doi: 10.1080/15730620802099721

Ren, B. (2004). *Study on the Urban Design Rainstorm and Rainfall Runoff Calculation Model*. Chongqing University, Chongqing.

Song, X., Zhang, J., Wang, G., and He, R. (2014). Development and challenges of urban hydrology in a changing environment II: Urban stormwater modeling and management. *Adv. Water Sci.* 5, 752–764.

Sui, D., and Maggio, R. (1999). Integrating GIS with hydrological modeling:practices, problems, and prospects. *Comput. Environ. Urban Syst.* 23, 33–51. doi: 10.1016/s0198-9715(98)00052-0

Tsakiris, G., and Bellos, V. (2014). A numerical model for two-dimensional flood routing in complex terrains. *Water Resour. Manag.* 28, 1277–1291. doi: 10.1007/s11269-014-0540-3

Wang, X., Cao, Z., Pender, G., and Tan, G. (2010). Modelling of urban flooding due to Yangtze river dike break. *Proc. ICE Water Manag.* 164, 3–14. doi: 10.1680/wama.900074

WeiFeng, L., Qiuwen, C., and Jingqiao, M. (2009). Development of 1D and 2D coupled model to simulate urban inundation: an application to Beijing Olympic Village. *Chin. Sci. Bull.* 54, 1613–1621. doi: 10.1007/s11434-009-0208-1

Werner, M., Blazkova, S., and Petr, J. (2005). Spatially distributed observations in constraining inundation modelling uncertainties. *Hydrol. Process.* 19, 3081–3096. doi: 10.1002/hyp.5833

Xiang, L., Zhang, D., He, X., Li, N., Liu, S., Sun, D., et al. (2018). Research progress in flood control and disaster reduction. *J. China Inst. Water Resour. Hydropower Res.* 5, 362–372.

Xing, Y., Liang, Q., Wang, G., Ming, X., and Xia, X. (2018). City-scale hydrodynamic modelling of urban flash floods: the issues of scale and resolution. *Nat. Hazards* 69, 473–496. doi: 10.1007/s11069-018-3553-z

Xu, M., Liu, S., Sun, Y., and Yao, Y. (2020a). Rapid identification and early warning of urban waterlogging risk using flooding model. *Geomat. Inf. Sci. Wuhan Univ.* 45, 1185–1194.

Xu, M., Sun, Y., and Liu, S. (2020b). Preliminary building and application of Beijing urban flood models. *China Flood Drought Manag.* 30, 16–21.

Xue, W. (2016). *Numerical Simulation of Stormwater and Street Flood in City*. Tianjin University, Tianjin.

Yu, H. (2015). Research on numerical simulation technology of urban floods. *South China University of Technology, Guangzhou*.

Yuan, F., and Li, W. (2019). Research on modeling method of city high-accuracy DEM. *Geomatics Spatial Inform. Techno*. 1, 80–82.

Zang, W. (2019). Research on urban flood refined simulation system. *J. China Inst. Water Resour. Hydropower Res., Beijing*.

Zhang, C., Zhi, X., Zhou, G., and Chen, Y. (2012). Interpretation for the partial modification in the new edition of 'code for design of outdoor wastewater engineering'. *Water Wastewater Eng.* 38, 34–38.

Zhang, Q., Okada, N., Tatano, H., and Hayakawa, S. (2002). Risk assessment and zoning of flood damage caused by heavy rainfall in Yamaghchi Prefecture. *Jpn. Flood Def.* 2002, 162–169.

Zoppou, C., and Roberts, S. (1999). Catastrophic collapse of water supply reservoirs in urban areas. *J. Hydraul. Eng.* 125, 686–695. doi: 10.1061/(asce)0733-9429(1999)125:7(686)

Conflict of Interest: The authors declare that the research was conducted in the absence of any commercial or financial relationships that could be construed as a potential conflict of interest.

frontiers in Earth Science

ORIGINAL RESEARCH
published: 14 April 2021
doi: 10.3389/feart.2021.554588

Analysis of the Migration Characteristics of Stormwater Runoff Pollutants on Different Underlying Surfaces in Guangzhou, China

*Yongjun Pan[1], Zhiqi Li[1], Yaoyao Gao[1], Yongmei Xiong[1], Yu Qiao[1], Yuzhu Tao[2], Qiaohua Wu[1], Wen Lin[1], Yueqiang Qi[1], Jiayi Long[1], Lin Ruan[1], Seping Dai[1] and Chuanfu Zang[3]**

[1]Guangzhou Institute of Forestry and Landscape Architecture, Guangzhou National Field Station for Scientific Observation and Research of Urban Ecosystem, Guangzhou, China, [2]Guangdong Academy of Forestry, Guangzhou, China, [3]School of Geography, South China Normal University, Guangzhou, China

OPEN ACCESS

Edited by:
Mingfu Guan,
The University of Hong Kong, Hong Kong

Reviewed by:
An Liu,
Shenzhen University, China
James David Shucksmith,
The University of Sheffield, United Kingdom
Jiahong Liu,
China Institute of Water Resources and Hydropower Research, China

***Correspondence:**
Chuanfu Zang
chuanfuzang@163.com

Specialty section:
This article was submitted to Hydrosphere, a section of the journal Frontiers in Earth Science

Received: *22 April 2020*
Accepted: *08 February 2021*
Published: *14 April 2021*

Citation:
Pan Y, Li Z, Gao Y, Xiong Y, Qiao Y, Tao Y, Wu Q, Lin W, Qi Y, Long J, Ruan L, Dai S and Zang C (2021) Analysis of the Migration Characteristics of Stormwater Runoff Pollutants on Different Underlying Surfaces in Guangzhou, China. Front. Earth Sci. 9:554588. doi: 10.3389/feart.2021.554588

Stormwater runoff is identified as urban nonpoint source pollution that increasingly introduces contaminants to urban water bodies and impedes sustainable development. The pollution load of runoff varies due to the interception of different land cover types during the urban hydrological process. During the rainy season (June–August) in 2018, five different underlying surfaces (green roof, parking lot, urban road, parkway, and grassland) were selected in Guangzhou to analyze the migration characteristics of stormwater runoff pollutants. The concentrations of heavy metals, such as chromium (Cr), cadmium (Cd), lead (Pb), and mercury (Hg), as well as total nitrogen (TN), total phosphorus (TP), and polycyclic aromatic hydrocarbons (PAHs) were collected and analyzed on different underlying surfaces with the rainfall data at the beginning of a stormwater runoff event. The results showed that PAHs, heavy metals, and TP existed mainly in the form of particles; nitrogen was mainly present as ammonia and nitrate; and the TN, TP, PAHs, and heavy metal were significantly different in the stormwater runoff on each underlying surface. The pollutant concentration in urban road runoff was the highest, accounting for 40–70% of the total pollutant concentration in the stormwater runoff, and the pollutant concentration in green roof runoff was the lowest, accounting for 10–40% of the total pollutant concentration in the runoff. An obvious effect of initial rainfall erosion was observed during stormwater runoff from urban roads and parking lots, and the scouring effect on grasslands and green roofs was mainly due to the many factors affecting the underlying surface during the middle and late stages. The rates of reduction of heavy metals were the most significant. The effect of water purification was positively correlated with stormwater runoff duration. The rates of reduction of TN, heavy metals (Cr, Cd, and Hg), and PAHs in the grassland areas were 35.20 ± 26.28, 0.24 ± 10.13, 71.77 ± 10.97,32.62 ± 110.48, and 41.30 ± 8.78%, respectively. This study could provide a theoretical basis for preventing and managing pollutants in urban stormwater runoff.

Keywords: urban rainstorm runoff, Guangzhou city, urban pollutant migration, urban hydrology and hydraulics, polycyclic aromatic hydrocarbons

INTRODUCTION

Population growth, industrial development, land use, waste emissions, and automobile exhaust have significantly increased the urban environmental load with the development of urbanization (Gimeno et al., 2014). Environmental problems have become a major issue that we must face, and urban water pollution is serious (Xu and Haung, 2004; Wu, 2018; Iuliana et al., 2020; Zeng et al., 2020). Urban stormwater has been identified as a major nonpoint source of pollution containing heavy metals, polycyclic aromatic hydrocarbons (PAHs), and nutrients (nitrogen and phosphorus) that cause urban flooding, accelerate the migration of pollutants, and introduce secondary pollution into water and have toxic effects on human health. Urban underlying surfaces conditions are key drivers of urban runoff quality. Numerous studies on stormwater management strategies have focused on the characteristics of stormwater runoff occurring on different urban underlying surfaces (Gilbert and clausen, 2006; Ou et al., 2011; Ouyang et al., 2010), including the initial runoff erosion effect (Soller et al., 2005; Ouyang et al., 2010; Zeng et al., 2019) and runoff models and other aspects (Deletic, 1998; Yu et al., 2016; Andrzejc et al., 2020).

The US Environment Protection (EPA) reported that approximately 90% of surface pollutants are carried by the first 2.5–4 cm of rainfall (Shang and Sun 2019), and there are significant cumulative toxic effects of various stormwater contaminants that threaten public health. Therefore, mitigating contaminants from stormwater runoff has attracted attention. Stormwater can be managed by green infrastructures, such as green roofs, wells, or bioswales (Walaszek et al., 2018). Previous studies have concluded that the initial scour of different underlying surfaces was different, the initial scour of pavement is less than that of roofs, and the pollutant characteristics of runoff from roofs and pavement are different. The degree of pollution in pavement runoff is higher than that from roofs. Different types of land cover generally have different functional areas and pollution sources (Buytaert et al., 2014). However, the effects of different land cover types on runoff pollution in the same environment are not well understood.

Most scholars believe that the sources of water pollution can be divided into point sources and areal sources (Diebel et al., 2009; Shi, 2011). As national and local governments have paid more attention to the control of pointsource, pollution has basically been controlled. (Guo et al., 2006). However, the features of areal sources, such as fuzzy temporal and spatial distributions and complex influencing factors, are difficult to control, and areal source pollution is relatively serious (Donigian and Huber, 1991; Wang and wang, 2002). Urban areal source pollution, also known as urban stormwater runoff pollution, refers to precipitation and runoff in different cities, such as industrial areas, residential areas (Lusk et al., 2020), commercial areas, roofs, parking lots, green belts, and roads. The process of leaching and scouring of the pollutants deposited on the underlying surface allows the pollutants to be collected in the runoff and discharged into the receiving body of water, which pollutes the aquatic environment (Camorani et al., 2005; Chang et al., 2006; Huang and Nie, 2012; Ren et al., 2013).

Urban areal source pollution includes both impermeable ground leaching and erosion from parking lots, roofs, and roads, as well as permeable ground leaching of green belts, grasslands, and other permeable grounds (Ou et al., 2011; Bao, 2016). Areal source pollution caused by erosion includes a wide range of pollutant sources and complex components (Gupta and Saul, 1996; Sansalone and Cristina, 2004; Jair et al., 2020). One of the main effects of urban green infrastructure on runoff water quality is the overall reduction in runoff quantity, thereby reducing the quantity of pollutants reaching urban waterways and the sewer infrastructure (Gooré Bi et al., 2015). Research on urban rainfall and runoff pollution mainly includes the following aspects: the spatial and temporal distribution of urban stormwater runoff pollutants (Brezonik and Stadlemann, 2002; Jeffrey et al., 2005; Geonha et al., 2007); the pollution characteristics of stormwater runoff produced by different underlying surfaces such as urban asphalt pavement (Ellis, 2000) and green pavement (Huang et al., 2006); the controlling effect of urban greening on pollutants (Ren et al., 2005; Chen et al., 2009; Ren et al., 2020; Xu et al., 2020); and the erosive effect of stormwater runoff and the development on urban rainfall-runoff models (Murakami et al., 2008; Ouyang et al., 2010;; Jaiswal et al., 2020). Among them, studying the characteristics of urban rainfall and runoff products is the basis for in-depth research on urban areal source pollution.

Guangzhou is located in the south subtropical zone of China, with sufficient light and heat resources and abundant rainfall. This region has the fastest urbanization and economic developmental rate in China. The Guangdong-Hong Kong-Macao Greater Bay Area, where Guangzhou is located, is one of China's three regional economic centers and one of the most dynamic economic zones in China and the world (Ye et al., 2017). The surface vegetation structure in Guangzhou is undergoing major changes with economic development, rapid population growth, and construction leading to local environmental disturbances in land development (Zhu et al., 2016). The status of hydrology and water resources is also becoming increasingly severe. At the same time, chemical, power, mineral, printing, and other industries are developing rapidly in Guangzhou, with many factories and enterprises beginning production. Rainfall carries pollutants into the river system and pollutes the water (Gong et al., 2017). Therefore, comprehensive water pollution treatment is necessary in Guangzhou to control the pollutant output of precipitation, particularly the transport of pollutants on different underlying surfaces.

Low Impact Development (LID) had been imposed for increasing rainwater infiltration into the soil or vegetation in urban areas in Guangzhou (Zeng et al., 2019). LID infrastructure was widely used, mainly by ecological tree pools, green roofs, rain gardens, grasslands, and permeable pavements (Tang et al., 2021). Many of the traditional roofs and green spaces were transformed based on the corresponding LID designing (Zeng et al., 2019). The main aim of LID was to reduce initial rainwater pollution caused by the quick wash-off of pollutants accumulated on the watershed surfaces. Deep tunnel drainage systems had been

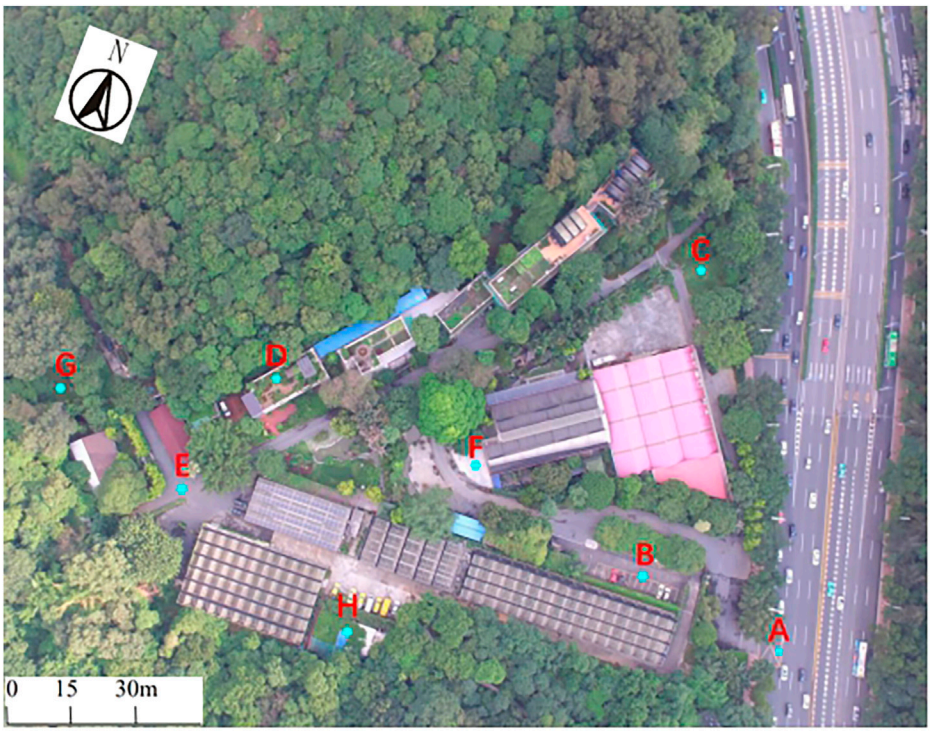

FIGURE 1 | Sampling site locations for the three sampling programs. **(A)** Urban road, **(B)** parking lot, **(C)** grassland, **(D)** green roof, **(E)** parkway, **(F)** CK, **(G)** weather station, **(H)** Guangzhou urban field station.

constructed at the final step among the measures that reduced combined sewer overflow (Wu et al., 2016). To investigate the effects of LID practices on purifying water quality, it is quite important to study the characteristics of pollutant concentrations in urban rainfall-runoff from different surfaces.

The objectives of this study were to develop an accurate understanding of pollutants loads of urban surface types and to investigate the pollutant hydrologic dynamics processes that occur during rain events. The study encompasses untreated stormwater runoff quality from five surfaces during three heavy rain events in different catchments within LuHu, Guangzhou. This research focused on heavy metals and PAHs primarily originating from automobile exhaust gases, which are the most common toxic chemical compounds present in urban stormwater. The filtration and storage efficiency of stormwater runoff pollutants under the different underlying surfaces were estimated based on the temporal and spatial patterns of the output of stormwater runoff pollution. The results elaborated the water quality characteristic for surface-specific runoff within a single climatic location to ensure an appropriate treatment solution is selected in urban water management.

METHODOLOGY

Study Area

This study was carried out in Guangzhou, located in southern China in central and southern Guangdong Province and on the north-central border of the Pearl River Delta. The study area included the confluence of the Xijiang, Beijiang, and Dongjiang Rivers. The southern subtropical monsoon climate is characterized by warm and rainy conditions, sufficient light and heat, long summers, and short frost periods. With an annual average temperature of 21.9°C, Guangzhou is one of the largest cities in China with the smallest annual average temperature difference. The hottest month of the year is July, with an average monthly temperature of 28.7°C. The coldest month is January, with an average monthly temperature of 13.5°C. The average relative humidity is 77%, and the annual rainfall is approximately 1,800 mm, which is mostly concentrated in April–September. Rainfall during the rainy season accounts for more than 70% of the annual rainfall.

Monitoring Point Selection and Sampling

The sampling area was a unit compound (Guangzhou Institute of Forestry and Landscape Architecture, GIFLA) located in LuHu, Guangzhou urban area (23°9′46.25″N, 113°17′22.4″E), also in the Guangzhou National Field Station for Scientific Observation and Research of Urban Ecosystem established in 2017 (**Figure 1**). It covers a total area of 8.9 × 104 m^2 and is primarily used for green space with some land set aside for construction and parkway. The drainage system uses a rainwater and sewage separation system.

Five underlying surfaces' runoff samples were collected from the grassland catchment, urban road water collection wellhead, parkway water collection wellhead, parking lot drain, green roof rainwater vertical drain, and precipitation (as control, CK) during

TABLE 1 | Parameters of typical rainfall events.

Event date	Total rainfall (mm)	Rainfall duration (min)	Maximum rainfall intensity (mm/min)	Average rain intensity (mm/min)	Antecedent dry days (h)
2018-06-01	48.2	90	1.4	0.355	>24
2018-08-02	34.7	150	1.5	0.475	>24
2018-08-28	102.5	420	2.0	0.486	>24

three rainfall events from June to August in 2018. Water collection wellhead is formed by a rainspout connecting urban stormwater drainage system when runoff occurs on the road. These sampling points were distributed within a range of 100 m and exposed to the same single climatic conditions.

For each effective stormwater runoff event, surface runoff samples were collected manually with a time interval of 5 min, that is, at 5, 10, 15, 20, 25, 30, 35, and 40 min from the start of runoff. Each water sampling was repeated three times and water samples were stored in 1 L brown glass bottles. The presence and characteristics of the first flush effect were detected by samples collected at 5 and 10 min after the first runoff outflow. The second stage of samples is followed by the first stage. All sampling was completed after approximately 45 min of rainfall event. All the samples were held at 4°C and delivered to the laboratory within 24 h of collection (HJ 494, 2009).

Rainfall data were recorded by a Campbell weather station at the neighboring Guangzhou National Field Station for Scientific Observation and Research of Urban Ecosystem at a frequency of 1 min. The annual rainfall is 1,723.9 mm, of which 21 rainfall events greater than 50 mm occurred within 24 h. However, for the sake of ensuring the safety of the experimental process, water samples were collected during the daytime, without lightning strikes, and the required rainfall time exceeded 1 h. Three effective stormwater events were finally successfully sampled on 1st June and 2nd and 28th August in 2018 (**Table 1**). The total rainfall was between 34.7 and 102.5 mm, the rainfall duration was from 90 to 420 min, the maximum rainfall intensity was 1.4–2.0 mm/min, the average rainfall intensity was from 0.355 to 0.486 mm/min, and the number of antecedent dry days was more than 24 h.

Laboratory Analysis

Seven water quality indexes were selected for analysis, including TN, TP, heavy metals involving Cr, Cd, Hg, and Pb, and 16 PAHs, including naphthalene (NAP), acenaphthene (ACE), acenaphthylene (ACY), fluorene (FLU), phenanthrene (PHE), anthracene (ANT), fluoranthene (FLa), pyrene (Pyr), benzo[a] anthracene (BaA), chrysene (Chr), benzo[b]fluoranthene (BbF), benzo[k]fluoranthene (BkF), benzo[a]pyrene (BaP), indeno[1, 2, 3-cd]pyrene (IcdP), dibenzo[a, h]anthracene (DahA), and benzo [g, h, i]perylene (BghiP) (Environmental Protection Agency and USEPA, 1983). Water quality measurements followed the standard methods (environmental quality standards for surface water, GB3838-2002) specified by the national standards of the P.R.C.

PAHs were determined by the EPA3510C-1996 and EPA8270D-2007 methods, and gas chromatography-mass spectrometry (GM-MS, QP2010plus) was used for the analysis with the selective ion detection method (SIM) to measure the samples. A DB5-MS GC-MS column (30 m × 0.25 mm × 0.25 μm) was used.

Pollutant Loads of the Stormwater and Runoff Events

Pollutant loading was estimated using the event mean concentration (EMC), which is used to represent the average concentration of a pollutant discharged during an entire stormwater event (Chow et al., 2013). In this study, the EMC was expressed as follows:

$$\mathrm{EMC} = \frac{M}{V} = \frac{\int_0^t C_t Q_t d_t}{\int_0^t Q_t d_t} = \frac{\sum C_t Q_t \Delta t}{\sum Q_t \Delta t},$$

where M is the total content of a certain pollutant (g) during the entire rainfall event; V is the corresponding total net flow (m^3); t is total runoff time (min); C_t is the pollutant content that changes with time (μg/L); Q_t is the runoff rate (m^3/min) that changes with time; and $\triangle t$ is the discontinuous time interval. Because the continuous concentration data of a pollutant cannot be monitored with actual measurements, the concentration of the pollutant at a certain point in the actual calculation process was used to replace the concentration in the time period.

RESULTS AND ANALYSIS

The Output of Pollutants on Different Underlying Surfaces

The Output of Heavy Metal Pollutants on Different Underlying Surfaces

As shown in **Figure 2**, the heavy metal Cd concentration at the beginning of the stormwater runoff ranked as the parking lot, urban road, grassland, parkway, and green roof. The concentrations of grassland and green roof were higher than those of other surface runoff at the end of the stormwater lasting 40 min. This result shows that the heavy metal Cd content collected by stormwater runoff on the impermeable surface was higher. According to the national environmental quality standards for surface water (The Ministry of Environmental Protection of the People's Republic of China, 2002), the Cd concentration in the stormwater runoff from 40 min rainfall event on urban roads and parkways is beyond the Class II standards. During the

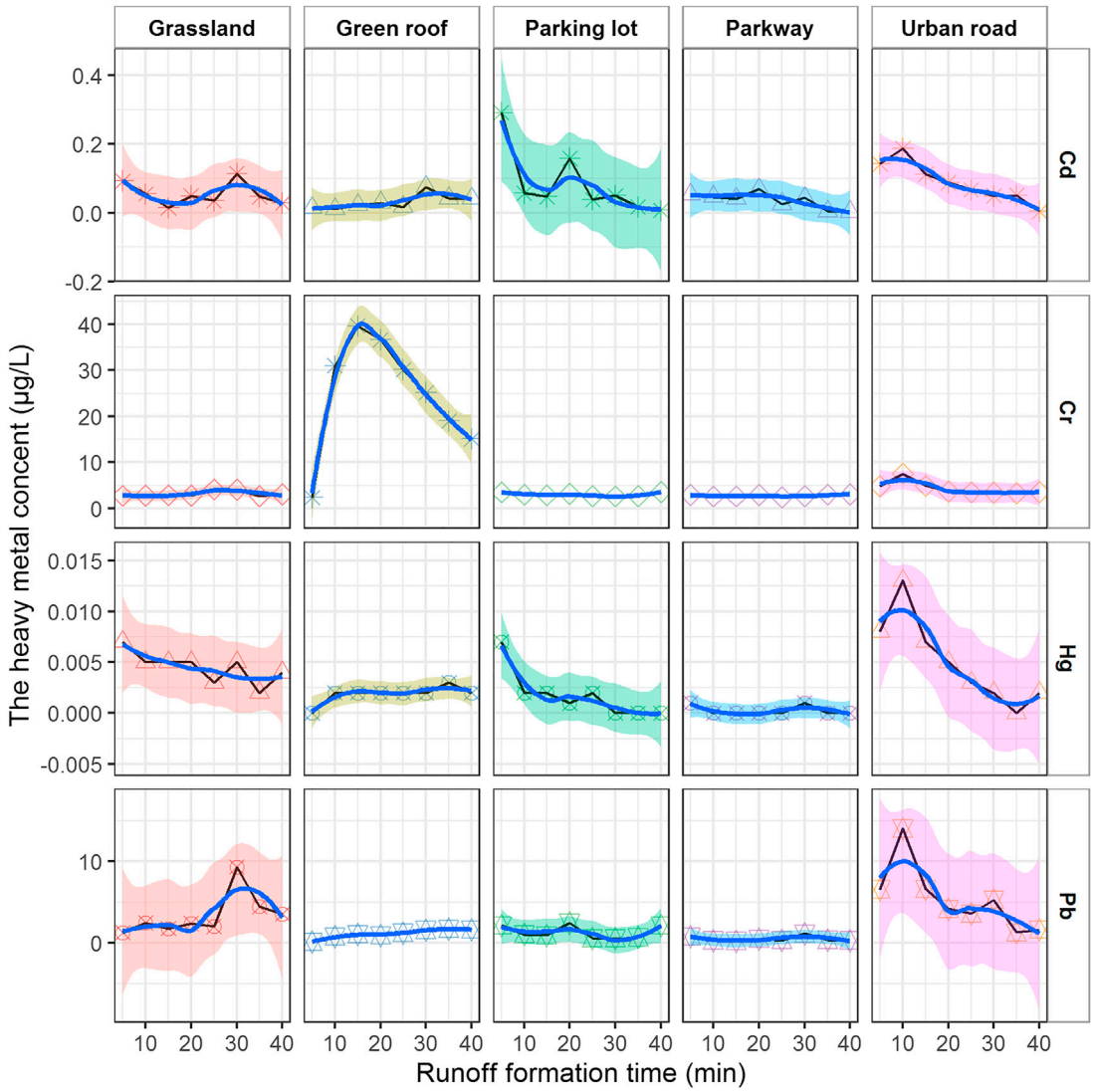

FIGURE 2 | The change in the heavy metal average concentration index over time. The smoothing blue curve was obtained by loess method, and the corresponding color shadow part was its 95% confidence interval.

40 min rainfall event, the average Cd concentrations of roads, parkways, and green roofs met the minimum emission standard V.

The higher Cr concentration was also detected on the urban road first flush and the lower in grassland. Unexpectedly, high levels of Cr were produced on the green roof runoff at the end of the storm lasting 40 min. The green roof runoff produced Cr concentrations up to 28.1 μg/L. During the 40 min rainfall, the average Cr concentrations on the grasslands, urban roads, parkways, and green roofs met the minimum emission standard V.

The Hg concentrations in the parking lot and parkway were very low later during the rain event and could not be detected. During the 40 min rainfall, the average Hg concentrations in grassland, urban road, parkway, and green roof runoff met the Class I emission standards.

The Pb concentration was substantially higher in the urban road runoff than other underlying surfaces at the beginning of the rain event. The higher concentrations were seen from higher trafficked urban roads in comparison with the lower trafficked roads. The average Pb concentration in the grassland, urban road, parkway, and green roof runoff reached Class I emission standards. The Pb concentrations due to the natural crude oil sources were excessive in the road and grassland runoff compared with that of the other land cover types.

Output of TP and TN Pollutants in the Different Underlying Surfaces

During the 40 min stormwater runoff, the average concentration of TN ranged from 1160.8 μg/L in the parkways runoff to 4989.6 μg/L in the urban road runoff (**Figure 3**). The average TN concentration in grassland, urban road, parkway, and green

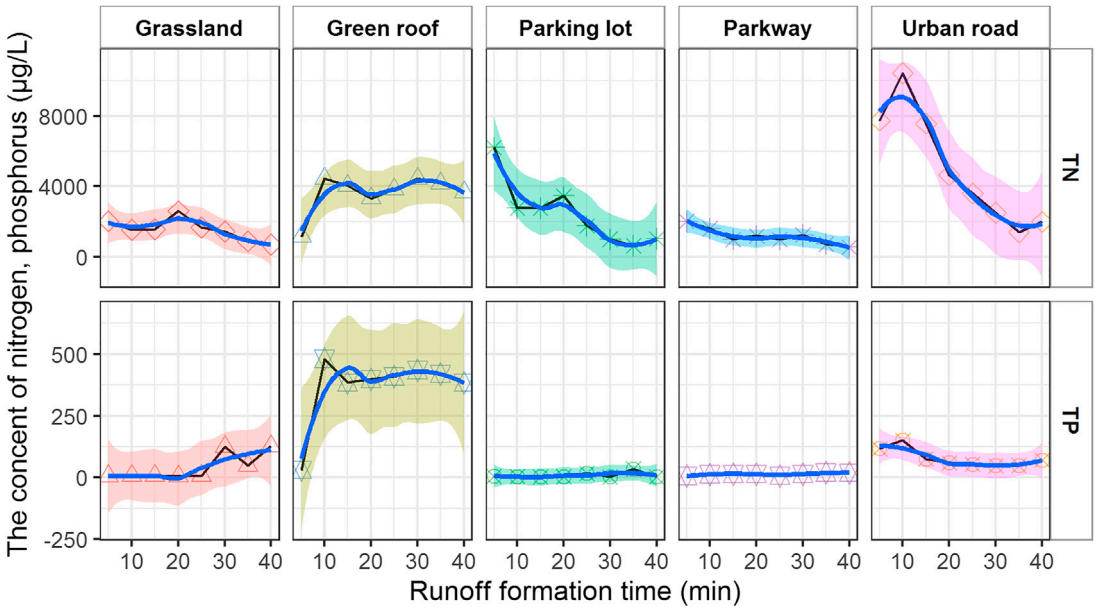

FIGURE 3 | The TP and TN average concentration index changes over time.

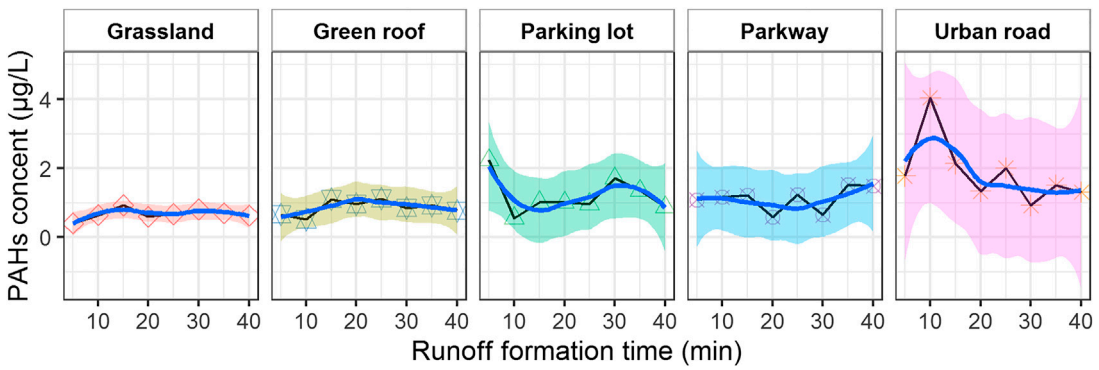

FIGURE 4 | PAH average concentration index changes over time in stormwater and runoff events. The smoothing blue curve was obtained by loess method, and the corresponding color shadow part was its 95% confidence interval.

roof runoff exceeded China's surface water Class V standard in the environmental quality standards. Among them, the concentration on the urban road reached a maximum of 10,460 μg/L and exceeded the Class V standard by four times during the 10 min stormwater runoff, but the concentration decreased by 86.63% after 35 min, which is within the Class IV standard.

The average concentration of TP in the urban road and green roof runoff fluctuated with stormwater duration. TP concentration in green roof runoff during the whole rainfall process was much greater than that in the parking lots, grasslands, and parkways (**Figure3**). TP concentration in green roofs was 40.78 times that on parking lots. At the beginning of the stormwater runoff, TP concentration was highest in the runoff water samples collected from urban road, followed by green roof, and the lowest in parking lot. TP concentration was highest in the green roof at the end of the stormwater runoff lasting 40 min. TP concentration almost met the Class IV standard except in the green roof runoff.

PAH Output in the Different Underlying Surfaces

The mean concentration of PAHs ranged from 0.67 μg/L in the grassland runoff to 1.88 μg/L in the urban road runoff (**Figure 4**). The urban road has a peak of 4.039 μg/L at 10 min of stormwater runoff and a minimum concentration of 0.927 μg/L at 30 min. The ranking of the concentrations of the PAHs at the beginning of the stormwater runoff was parking lot, followed by urban road, parkway, green roof, and grassland. The PAH concentration was the highest in the parkway and the lowest in grassland runoff at the end of the stormwater runoff lasting 40 min.

TABLE 2 | EMC values of storm runoff on different underlying surfaces (units: μg/L).

Sampling point	Underlying surface	TN	TP	Cr	Cd	Hg	Pb	PAHs
Grassland	Grassland	1672.730* ±122.425	29.220 ±9.286	3.086 ±0.331	0.060 ±0.011	0.005 ±0.0004	3.248 ±0.235	0.653 ±0.016
Urban road	Asphalt road	4988.311 ±249.345	69.961 ±14.252	4.147 ±0.204	0.088 ±0.011	0.005 ±0.0003	4.982 ±0.092	1.766 ±0.276
Parking lot	Asphalt road	3105.614 ±484.073	8.180 ±0.734	3.001 ±0.099	0.115 ±0.037	0.003 ±0.0009	1.324 ±0.600	1.327 ±0.108
Parkway	Asphalt road	1271.947 ±68.742	12.624 ±1.107	2.653 ±0.475	0.044 ±0.006	0.000 ±0.000	0.437 ±0.167	1.037 ±0.117
Green roof	Planted roof	3243.221 ±691.225	318.206 ±43.242	23.227 ±2.848	0.028 ±0.004	0.002 ±0.0004	0.931 ±0.724	0.852 ±0.096
CK	Precipitation	2870.500 ±1075.991	8.921 ±3.482	3.318 ±0.676	0.227 ±0.061	0.005 ±0.0026	1.324 ±1.171	1.130 ±0.183

**Data are shown as mean ± SD in the table.*

Urban land cover type and spatial pattern are the key factors affecting urban stormwater runoff contaminants. The average concentration index of pollutants in the runoff events changed over time. The contribution rates of the five types of underlying pollutants to the same pollutant and the changes in pollutant concentrations with time are quite different, but the overall initial pollutant concentration is relatively high after the erosion effect, and the concentration later decreased. Urban road runoff produced higher heavy metal concentrations (Cd, Pb, and Hg) than any other sampled surface except the higher Cr concentrations in green roof during the stormwater runoff process.

The smoothing blue curve was obtained by the loess method, and the corresponding color shadow part was its 95% confidence interval.

Analysis of the Pollution Load Caused by Stormwater Runoff

Asphalt pavement has higher pollution intensity, among which the main urban roads are the most polluted. The EMCs of TN and TP increased up to 4988.3 ± 249.3 and 318.2 ± 43.2 μg/L, respectively (**Table 2**). The TP concentration exceeds 1.5 times higher than the Class V standard in China's environmental quality standards for surface water. TN of the parking lot and green roof is lower than that of the urban road but still does not meet the Class V standard. The concentrations of Hg and Cd were mostly on the order of 0.002~0.005 and 0.028~0.115 μg/L. The EMC values of the heavy metals were not greater than the standard V.

The pollutant EMC values of the various underlying surfaces were different. The higher loads of TN, Pb, and PAHs were detected in urban road runoff. The higher loads of TP and Cr were tested in green roof runoff (**Table 2**). Asphalt pavement was most polluted by TN and TP, the most prominent heavy metals were Cr and Pb, and the EMC values of Cd and Hg pollutants were lower than the concentrations of PAHs.

The same pollutant showed differences on the various underlying surfaces. The TN, Hg, Pb, and PAHs pollution loads were higher in urban road runoff. Heavy metals and PAHs can easily enter surface runoff and drainage system and pollute urban water during rainfall events. The highest TP and Cr pollution loads occurred in the green roof runoff (**Table 2**).

Principal Component Analysis of the Stormwater Runoff Pollutants

The results of the principal component analysis of the pollutants in the storm runoff are shown in **Table 3**. The results divided the pollutants into three main components. The cumulative contribution rate of the first and second principal components reached 80.118%, which accounted for the largest proportion. These two main components contained more than 80% of the information content of the entire pollutant index, which met the requirement of main component extraction.

The pollutants in the Guangzhou stormwater runoff were divided into two groups. The first group included Pb, Cd, Hg, and PAHs which had a large positive correlation with the first principal component, TN had a weak positive correlation with the first principal component, and TP and Cr and the first principal component were weakly negatively correlated, so principal component 1 mainly represented the principal component of heavy metal pollution in the stormwater runoff. The second group of TN, TP, and Cr had a large positive correlation with the second principal component, while Pb, Cd, Hg, and PAHs were poorly correlated. Principal component 2 was the principal

TABLE 3 | Principal component load matrix of the pollutants in the stormwater runoff.

Pollutants	Principal component	
	1	2
Z-score (TN)	0.575	0.776
Z-score (TP)	–0.588	0.806
Z-score (Cr)	–0.658	0.738
Z-score (Cd)	0.834	–0.179
Z-score (Hg)	0.723	0.258
Z-score (Pb)	0.796	0.343
Z-score (∑PAHs)	0.75	0.271

TABLE 4 | The rates of decrease in the seven pollutants in stormwater runoff on the underlying surfaces.

Pollutants	Grassland (%)	Urban road (%)	Parking lot (%)	Parkway (%)	Green roof (%)
TN	−35.20 ± 26.28*	92.54 ± 75.64	23.36 ± 61.22	−51.76 ± 16.22	17.92 ± 19.97
TP	283.81 ± 205.52	778.45 ± 347.92	5.27 ± 47.54	67.72 ± 91.27	4070.58 ± 2105.70
Cr	−0.24 ± 10.13	35.10 ± 20.65	−1.71 ± 18.55	−10.99 ± 31.37	650.23 ± 80.52
Cd	−71.77 ± 10.97	−59.77 ± 10.00	−43.10 ± 36.15	−78.94 ± 9.53	−87.50 ± 1.36
Hg	−32.62 ± 110.48	−19.44 ± 78.53	−18.57 ± 81.69	−97.30 ± 1.99	−60.48 ± 22.14
Pb	530.19 ± 751.34	905.55 ± 1220.23	248.54 ± 507.35	−26.91 ± 81.29	49.45 ± 177.49
PAHs	−41.30 ± 8.78	56.40 ± 1.58	19.21 ± 19.15	−7.80 ± 4.38	−22.50 ± 19.71

**Data are shown as mean ± SD in the table.*
Note: positive values represent increased efficiency, and negative values represent decreased efficiency.

component that described the nutrients in Guangzhou stormwater runoff. The main component scores of the seven pollutants in the storm runoff were Cd (0.237)> Pb (0.226)> PAHs (0.213)> Hg (0.205)> Cr (−0.187)> TP (-0.167)> TN (0.163), suggesting that Pb, Cd, Hg, and the PAHs may have originated from the same pollution source. TN, TP, and Cr came from the same pollution source and played an important role in the concentrations of the stormwater runoff pollutants.

Filtration and Storage Characteristics of Pollutants in Stormwater Runoff on the Different Underlying Surfaces

Table 4 shows the differences in the reduced rate of pollutants in stormwater runoff between the different underlying surfaces. When the reduction rate is negative, the underlying surface plays a "sink" role in releasing pollutants; otherwise, the surface plays a "source" role.

The grassland played a role in purifying the seven kinds of pollutants, except TP and Pb, and its rank for the rate of reduction was Cd > PAHs > TN > Hg > Cr (**Table 4**). After the rain event, the rate of increase in TP was greater than that of Pb in the grassland runoff; the urban road was the main "source" for pollutants, and the ranking for the rate of increase in runoff pollutants was TP > Pb > TN > PAHs > Cr. The rate of reduction in Cd was greater than that of Hg. The parkway had a purifying effect on the seven pollutants, except TP. The ranking in the rates of reduction was Hg > Cd > Pb > TN > Cr > PAHs. The rate of increase in TP was 67.72%. The green roof played a role in purifying the heavy metals and PAHs, and the ranking of the rate of decrease was Cd > Hg > Pb > PAHs. The green roof increased nutrients in the stormwater runoff; in particular, TP increased 4070.58%.

DISCUSSION AND CONCLUSION

Discussion

The water quality of urban stormwater runoff varies by orders of magnitude between different land surfaces, and stormwater monitoring is important to design reasonable treatments to protect urban bodies of water. Heavy metals, PAHs, and pesticides were the main pollutants of concern in stormwater runoff and of concern in the urban catchment. However, Pb, Cr, Cd, and Hg were detected in all stormwater runoff sampling points, and their concentrations met the EPA worst-case-based water quality criteria. The Hg concentrations in urban stormwater runoff were too low to be detected. These results indicate that heavy metals in urban residential areas and road stormwater runoff are present in nontoxic forms to aquatic life in urban bodies of water.

Urban stormwater runoff contains elevated concentrations of various nutrients, such as nitrogen and phosphorus compounds, which can lead to eutrophication of urban water. It has been reported that the algae available P in urban stormwater runoff, grassland, and green roof areas is derived from the leaching of tree leaves and flowers (Lee and Jones-Lee 2005). The pollution from the urban road was the most serious. The TN and TP concentrations exceeded the Class V standard stipulated by the national surface water environmental quality standard by 1.5 times. The TN concentrations in green roof and parking lot runoff were lower than that in the urban road runoff but still failed to meet the standard V.

PAHs are adsorbed on particles with small aerodynamic diameters in the molecular state in the atmosphere, and some fall to the ground or water surfaces in raindrops. Stormwater runoff has become the main source of urban nonpoint source pollution. PAHs are persistent toxic organic pollutants of potential concern in urban stormwater runoff (Pilcher et al., 2018). China stipulates that the discharge standard for benzo[a] pyrene (BaP) in sewage is 30 ng/L (GB 18918-2002), but no regulations exist for discharge of other monomers or total PAHs. The BaP geometric means for the grassland, main road, parking

TABLE 5 | Feature ratios and source types of PAHs.

PAHs	The ratio range	Source type
Fla/(Fla + Pyr)	<0.4	The oil source
	0.4~0.5	Source of petroleum combustion
	>0.5	Coal/biomass fuel combustion
BaA/(BaA + Chr)	<0.2	The oil source
	0.2~0.35	Source of petroleum combustion
	>0.35	Coal/biomass fuel combustion
IcdP/(IcdP + BghiP)	<0.2	The oil source
	0.2~0.5	Source of petroleum combustion
	>0.5	Coal/biomass fuel combustion

TABLE 6 | Feature ratios of PAHs on the different underlying surfaces.

Underlying surfaces	Fla/(Fla + Pyr)	BaA/(BaA + Chr)	IcdP/(IcdP + BghiP)
Grassland	0.28	0.54	0.22
Urban road	0.98	0.66	0.99
Parking lot	0.92	0.57	0.99
Green roof	0.93	0.60	0.98
Parkway	0.94	0.71	0.99

lot, green roof, and parkway were 11.69, 339.57, 253.04, 99.75, and 237.61 ng/L, respectively. These results show that the grassland runoff met the national emission standard. Urban roads, parking lots, and parkways exceeded the standard by 11.32, 8.43, and 7.92 times, respectively, which should be taken seriously by relevant departments.

The feature ratio method is a commonly used method to analyze the source of PAHs. The principle is to judge the main source according to the ratio of the PAH concentrations of each isomer, and it is mostly used for qualitative analysis. The feature ratio method often uses the Fla/(Fla + Pyr), BaA/(BaA + Chr), and IcdP/(IcdP + BghiP) ratios to explain the possible sources of PAHs (Wu et al., 2019) (**Table 5**). We calculated the characteristic ratios of PAHs in the different underlying surfaces (**Table 6**), to show that the typical PAHs in Guangzhou mainly originated from coal/biomass fuel combustion and the petroleum sources originated from PAHs in the grassland, petroleum combustion source, and coal/biomass fuel combustion.

This study found that TN, Cd, Hg, Pb, and the PAHs exhibited first flush effects in the urban road stormwater runoff, while the P elements were adsorbed on the surface by dry sedimentation. Urban road surfaces are important impervious surfaces and an essential platform for PAHs and heavy metal ions during antecedent dry days (Ma et al., 2017). When stormwater runoff was generated, PAHs and heavy metals were washed away and dissolved. After the TP concentration increased, it remained flat, and Cr and TP changed in similar ways. The green roof Cr and TP concentrations exhibited the same pattern as that of the urban road runoff, and the other pollutants decreased-increased and then decreased again.

The pollutant concentrations after filtration through the soil and vegetation decrease, the soil and vegetation pollutants leach into the runoff, the concentration increases, and then the pollutant concentrations decrease due to dissolution by stormwater runoff. The TP, Cd, and Hg concentrations in the grassland runoff suddenly increased, mainly because grassland absorbs each element into the soil through dry deposition, and after long-term runoff leaching, each element reenter the water, causing secondary pollution (Wu, 2018). There were obvious initial erosive effects on the urban road and parking lot, whereas the grassland and green roof mitigated runoff. The initial erosion effects were not obvious on residential areas and roads, which agrees with the results of Huang and Nie (2012).

The underlying surfaces of parkways and urban roads are asphalt, but the pollutant EMC value of the parkways runoff was much lower than that of urban roads, mainly because litter and dust are cleaned up on parkways, and the roads are washed. When pollutants are adsorbed on dust and ground, they enter other areas. Thus, the total amount of pollutants can be effectively controlled by urban environmental sanitation, intercepting, precipitating, and filtering stormwater runoff, which is similar to the report by Ren et al. (2005).

The TN and TP EMC values of the green roof were much larger than those of the other underlying surfaces and had also been detected in Shengzhen (Tang et al., 2021). This result may be attributed to the fact that the artificial application of compound fertilizers causes an abnormal increase in the concentrations of TN and TP in the runoff. Especially during storm events, stormwater runoff transports massive amounts of P from urban greening soil to the surrounding water systems. The Cr content also increased, indicating that the green roof substrate may have a certain concentration of Cr. Their green roof design and maintenance may neglect nutrient pollution.

The parking lot had a high TN content, mainly because the exhaust gas of motor vehicles contains a large amount of incomplete combustion products and combustion reaction intermediate products such as NO_X. After a rain event, NO_X dissolves in the water resulting in high TN content (Ren et al., 2013).

The five underlying surfaces had different effects on reducing/increasing pollutants. Among them, the rates of reduction by grassland and green roof were higher, and the reduction in heavy metals was the most significant. Grassland and green roof play a blocking role and reduce rain intensity so that the soil structure is not damaged. When rainwater enters the soil, some pollutants are adsorbed on the soil, the nutrient elements are absorbed by plants at a later stage, and most of the heavy metals form complexes. The five underlying surfaces all played roles in reducing Cd concentrations because Cd is a water-soluble heavy metal, which is leached in large amounts during the stormwater runoff (Chen and Duan, 2013). The different underlying surfaces in cities intercept the rainfall at different rates and change the pollution load of the runoff.

Urban surface runoff emissions affect the quality of the receiving water, and heavy metals and PAHs are the main pollutants in urban runoff pollution and play a major toxic role (Zhao et al., 2015). Many nonpoint sources of heavy metals are detectable in the urban environment, particularly the traffic pollution caused by motor vehicles. The heavy metal pollution load is detected in the main roads and parking lots runoff (Yu et al., 2016). PAHs adhere to the surface of particulate matter, and it becomes the main persistent organic pollutant in the urban water environment as rainwater enters the surface runoff, which is mainly caused by asphalt roads and gasoline combustion (Chen and Adams, 2006). Therefore, PAHs and heavy metal pollution loads are high in urban road stormwater runoff and become an important source of urban

water pollution. Strengthening the diversion of rain and sewage urban runoff is an important way to alleviate urban water environmental pollution.

The LID design in Guangzhou was required to develop stormwater runoff water pollution control programs to control pollution to the maximum extent practicable using the best ecologically designed stormwater management practices. Ponds, grassy swales, etc., cannot be considered sufficient to treat urban stormwater runoff to achieve compliance with water quality standards.

This study had some limitations. The rainfall spatial heterogeneity in Guangzhou is high, industrial development in each region is different, and the composition of the rainfall pollutants differed. The sampling point for this study was in Baiyun District, so the sampling range was relatively small. In the future, sampling points should be set up in each administrative area to expand the scope of the study. For the variability in accumulative and wash effect in the hydrological processes, we should make it accurate that the flush amount of pollutants is only a partial indication of the buildup. However, the relationship was far too complex to ignore. Sampling points can be set up in each administrative area to expand the scope in future study. The characteristics of heavy rain in Guangzhou are that the rain duration is short and the rain intensity is strong. Therefore, the research results represent the load of pollutants due to short-term heavy rainfall. On the other hand, pollutants cannot be tracked for long-term rainfall loads, and there was uncertainty associated with the temporal resolution of rainfall. However, the influence of rainfall intensity and runoff cannot be neglected. More factors can be considered in future including the impacts from land use in each catchment, dry deposition pollutant concentration, and the seasonal variations of rainfall. As basic research, we should also strengthen the research on the impact of surface runoff on urban water bodies and provide a theoretical and practical basis for risk assessment by specific pollutants in urban surface runoff.

Conclusion

In this study, the stormwater pollution mitigation performance of five urban underlying surfaces was quantitatively characterized with natural stormwater runoff event-based field monitoring. Some key findings are in the following:

1) The first flush effect of impermeable pavement system was most prone, while urban grasslands and green roofs reduced the pollutions because the first flush contributed to rainwater purification.
2) The pollutant abatement of green roofs is not significant or even storage effects. The substrate material, nutrient pollution, and dry deposition cannot be neglected in green roof and green spaces design.
3) The grassland purified the seven pollutants, except TP and Pb. The urban road was the main "source" of pollutants. The parking lot had a purifying effect on TP, Cd, Hg, and Pb and the parkway had a purifying effect on the seven pollutants except TP, whereas the green roof purified the heavy metals and PAHs.
4) The preliminary treatment of stormwater runoff should be strengthened due to the integration of ecological concerns and urban green infrastructures, such as green spaces, green roofs, vertical greening, grasslands, and forestry.

DATA AVAILABILITY STATEMENT

The original contributions presented in the study are included in the article/Supplementary Material; further inquiries can be directed to the corresponding author.

AUTHOR CONTRIBUTIONS

YP, YG, YT, and CZ conceptualized the study and were responsible for resources; YP, ZL, YG, and YX were responsible for methodology; YQ and QW were responsible for software; YP, YG, LR, SD and CZ validated the study, prepared the original draft, reviewed and edited the manuscript, and supervised the study; WL, YQ, and JL performed formal analysis; YP, ZL, YG, YX, YQ, and QW investigated the study; YP, YG, CZ, ZL, YT, and YX were responsible for data curation; LR, SD, XL, and CZ were responsible for visualization; YP and CZ involved in project administration.

FUNDING

This research was supported by the Guangdong Natural Science Foundation Project (2019A1515011627), National Natural Science Foundation of China (31660233; 31770492), and the project of Guangdong provincial innovation platform of forestry science and technology "Construction of network platform for forestry and ecological monitoring" (No. 2020-KYXM-09). The authors acknowledge the financial special project of Guangzhou City in 2020: the long-term scientific research base operation fee project, Guangzhou urban ecosystem national field station, for our support.

REFERENCES

Andrzej, W., Devendra, A., Peter, C., Dan, M., and Sudhanshu, P. (2020). Assessment of storm direct runoff and peak flow rates using improved SCS-CN models for selected forested watersheds in the Southeastern United States. *J. Hydrol. Reg. Stud.* 27. doi:10.1016/j.ejrh.2019.100645

Bao, X. (2016). *Characteristics analysis and load calculation of urban storm runoff pollution for harbin city example*. Harbin, China: Harbin Normal University.

Brezonik, P. L., and Stadelmann, T. H. (2002). Analysis and predictive models of stormwater runoff volumes, loads, and pollutant concentrations from watersheds in the Twin Cities metropolitan area, Minnesota, USA. *Water Res.* 36 (7), 1743–1757. doi:10.1016/s0043-1354(01)00375-x

Buytaert, W., Zulkafli, Z., Grainger, S., and Acosta, L., AlemieAlemie, T. C., Bastiaensen, J., et al. (2014). Citizen science in hydrology and water resources: opportunities for knowledge generation, ecosystem service management, and sustainable development. *Front. Earth Sci.* 2, 26. doi:10.3389/feart.2014.00026

Camorani, G., Castellarin, A., and Brath, A. (2005). Effects of landuse changes on the hydrologic response of reclamation systems. *Phys. Chem. Earth* 30 (8/10), 561–574. doi:10.1016/j.pce.2005.07.010

Chang, J., Liu, M., Xu, S., Hou, L., and Wang, H. (2006). Temporal-spatial distribution and first flush effect of urban stormwater runoff pollution in Shanghai City. *Geographical Res.* 25 (6), 994–1002. doi:10.11821/yj2006060006

Chen, J., and Adams, B. J. (2006). Analytical urban storm water quality models based on pollutant buildup and washoff processes. *J. Environ. Eng.* 132 (10), 1314–1330. doi:10.1061/(asce)0733-9372(2006)132:10(1314)

Chen, T., Tie, B., Duan, Z., Yang, Y., and Deng, G. (2013). Impact of rainfall and micro-fertilizers on the leaching migration of heavy metals under planting rape condition. *J. Soil Water Conservation* 1 (27), 142–145. doi:10.13870/j.cnki.stbcxb.2013.01.003

Chen, Z., Yang, K., Huang, M., Xie, B., and Li, X. (2009). Reduction effect of sunken green space on urban rainfall-runoff pollution. *China Environ. Sci.* 29 (6), 611–616. doi:10.CNKI:SUN:ZGHJ.0.2009-06-014

Chow, M. F., Yusop, Z., and Shirazi, S. M. (2013). Storm runoff quality and pollutant loading from commercial, residential, and industrial catchments in the tropic. *Environ. Monit. Assess.* 185, 8321–8331. doi:10.1007/s10661-013-3175-6

Deletic, A. (1998). The first flush load of urban surface runoff. *Water Res.* 32 (8), 2462–2470. doi:10.1016/S0043-1354(97)00470-3

Diebel, M. W., Maxted, J. T., Robertson, D. M., Han, S., and Vander Zanden, M. J. (2009). Land-scape planning for agricultural nonpoint source pollution reduction III: assessing phosphorus and sediment reduction potential. *Environ. Manage.* 43 (1), 69–83. doi:10.1007/s00267-008-9139-x

Donigian, A. S., and Huber, W. C. (1991). *Modeling of nonpoint source water quality in urban and non-urban areas*. United States: EPA600/3-91/039.

Ellis, J. B. (2000). Risk assessment approaches for ecosystem responses to transient pollution events in urban receiving waters. *Chemosphere* 40, 85–91. doi:10.1016/S0045-6535(99)00393-8

Environmental Protection Agency; (USEPA) (1983). *Results of the nationwide urban runoff program*. Washington, DC: Water Planning Division.

Geonha, K., Joonghyun, Y., and Jeongkon, K. (2007). Diffuse pollution loading from urban stormwater runoff in Daejeon City, Korea. *J. Environ. Manage.* 85, 9–16. doi:10.1016/j.jenvman.2006.07.009

Gilbert, J. K., and Clausen, J. C. (2006). Stormwater runoff quality and quantity from asphalt, paver, and crushed stone driveways in Connecticut. *Water Res.* 40, 826–832. doi:10.1016/j.watres.2005.12.006

Gimeno, L., Nieto, R., Vázquez, M., and Lavers, D. A. (2014). Atmospheric rivers: a mini-review. *Front. Earth Sci.* 2, 2. doi:10.3389/feart.2014.00002

Gong, J., Li, Y., and Huang, J. (2017). Heavy metal pollution and its spatial distribution in the Guangzhou-Dongguan reach of the Pearl River. *J. Guangzhou Univ. (Nat. Sci. Edition)* 4 (16), 78–81.

Gooré Bi, E., Monette, F., and Gasperi, J. (2015). Analysis of the influence of rainfall variables on urban effluents concentrations and fluxes in wet weather. *J. Hydrol.* 523, 320–332. doi:10.1016/j.jhydrol.2015.01.017

Guo, Q., Ma, K., and Yang, L. (2006). Main sources of urban non-point source pollution and control measures for classified catchments. *Environ. Sci.* 27 (11), 2170–2175. doi:10.13227/j.hjkx.2006.11.006

Gupta, K., and Saul, A. J. (1996). Specific relationships for the first flush load in combined sewer flows. *Water Res.* 30 (5), 1244–1252. doi:10.1016/0043-1354(95)00282-0

HJ 494 (2009). *Water quality–Guidance on sampling techniques [S]*. Beijing.

Huang, G., and Nie, T. (2012). Characteristics and load of non-point source pollution of urban rainfall runoff in Guangzhou China. *J. South China Univ. Tech. (Natural Sci. Edition)* 40 (2), 142–147. doi:10.3969/j.issn.1000-565X.2012.02.025

Huang, J., Du, P., AO, C. T., Lei, M. H., Zhao, D. Q., Ho, M. H., et al. (2006). Characterization of urban roadway runoff in Macau. *China Environ. Sci.* 26 (4), 469–473. doi:10.CNKI:SUN:ZGHJ.0.2006-04-019

Jair, A., Nerilde, F., Jeferson, D., and Gabriel, B. (2020). Manure application at long-term in no-till: effects on runoff, sediment and nutrients losses in high rainfall events. *Agric. Water Management* 228, 105908. doi:10.1016/j.agwat.2019.105908

Jaiswal, R., Ali, S., and Bharti, B. (2020). Comparative evaluation of conceptual and physical rainfall–runoff models. *Appl. Water Sci.* doi:10.1007/s13201-019-1122-6

Jeffrey, S., Julie, S., Kendra, O., James, D., and Adam, W. O. (2005). Evaluation of seasonal scale first flush pollutant loading and implications for urban runoff management. *J. Environ. Manage.* 76, 309–318. doi:10.1016/j.jenvman.2004.12.007

Lee, G. F., and Jones-Lee, A. (2005). "Urban stormwater runoff water quality issues," in *Water encyclopedia: surface and agricultual water*. Hoboken, NJ: Wiley, 432–437. doi:10.1002/047147844X.sw1602

Iuliana, C., Alexandru, C., Felicia, I., and Silviu, G. (2020). City water pollution by soot-surface-active agents revealed by FTIR spectroscopy. *Appl. Surf. Sci.* 499, 142487. doi:10.1016/j.apsusc.2019.04.179

Lusk, M. G., Toor, G. S., and Inglett, P. W. (2020). Organic nitrogen in residential stormwater runoff: implications for stormwater management in urban watersheds. *Sci. total Environ.* 707, 135962. doi:10.1016/j.scitotenv.2019.135962

Ma, Y., McGree, J., and Liu, A., DeilamiDeilami, K., EgodawattaEgodawatta, P., and GoonetillekeGoonetilleke, A. (2017). Catchment scale assessment of risk posed by traffic generated heavy metals and polycyclic aromatic hydrocarbons. *Ecotoxicol Environ. Saf.* 144, 593–600. doi:10.1016/j.ecoenv.2017.06.073

Murakami, M., Nakajima, F., and Furumai, H. (2008). The sorption of heavy metal species by sediments in soakaways receiving urban road runoff. *Chemosphere* 70, 2099–2109. doi:10.1016/j.chemosphere.2007.08.073

Ou, L., Hu, D., and Huang, Y., CuiCui, S., GuoGuo, T., ZhangZhang, W., et al. (2011). First flush analysis of PAHs in roof runoff in beijing. *Environ. Sci.* 32 (10), 2896–2902. doi:10.13227/j.hjkx.2011.10.043

Ouyang, W., Wang, W., Hao, F., Song, K. Y., and Wang, Y. H. (2010). Pollution characterization of urban stormwater runoff on different underlying surface conditions. *China Environ. Sci.* 30 (9), 1249–1256.

Pilcher, D. J., Siedlecki, S. A., Hermann, A. J., Coyle, K. O., Mathis, J. T., and Evans, W. (2018). Simulated impact of glacial runoff on CO2 uptake in the Gulf of Alaska. *Geophys. Res. Lett.* 45 (7), 880–890. doi:10.1002/2017GL075910

Ren, X., Hong, N., Li, L., Kang, J., and Li, J. (2020). Effect of infiltration rate changes in urban soils on stormwater runoff process. *Geoderma* 363. doi:10.1016/j.geoderma.2019.114158

Ren, Y., Wang, X., Han, B., Ouyang, Z., and Miao, H. (2005). Chemical analysis on stormwater-runoff pollution of different underlying urban Surfaces. *Acta Ecologica sinica* 25 (12), 3225–3230.

Ren, Y., Wang, X., Ouyang, Z., and Hou, P. Q. (2013). Analysis of first flush effect of typical underlying surface runoff in beijing urban city. *Environ. Sci.* 34 (1), 373–377. doi:10.13227/j.hjkx.2013.01.046

Sansalone, J. J., and Cristina, C. M. (2004). First flush impervious concepts for suspended and dissolved solids in small watershed. *Jouranal Environ. Eng. ASCE* 130 (11), 1301–1314. doi:10.1061/(ASCE)0733-9372(2004)130:11(1301)

Shang, H., and Sun, Z. (2019). PAHs (naphthalene) removal from stormwater runoff by organoclay amended pervious concrete. *Construction Building Mater.* 200, 170–180. doi:10.1016/j.conbuildmat.2018.12.096

Shi, R. (2011). Ecological environment problems of the three gorges reservoir area and countermeasures. *Proced. Environ. Sci.* 10, 1431–1434. doi:10.1016/j.proenv.2011.09.228

Soller, J., Stephenson, J., Olivieri, K., Downing, J., and Olivieri, A. W. (2005). Evaluation of seasonal scale first flush pollutant loading and implications for urban runoff management. *J. Environ. Manage.* 76, 309–318. doi:10.1016/j.jenvman.2004.12.007

Tang, S., Jiang, J., Zheng, Y., Hong, Y., Chung, E. S., Shamseldine, A. Y., et al. (2021). Robustness analysis of storm water quality modelling with LID infrastructures from natural event-based field monitoring. *Science of the Total Environment* (753), 142007. doi:10.1016/j.scitotenv.2020.142007

The Ministry of Environmental Protection of the People's Republic of China (2002). *Environmental quality standards for surface water, GB3838-2002*, Beijing (in Chinese).

Walaszek, M., Bois, P., Laurent, J. E., and Wanko, A. (2018). Micropollutants removal and storage efficiencies in urban stormwater constructed wetland. *Sci. Total Environ.* 645, 854–864. doi:10.1016/j.scitotenv.2018.07.156

Wang, X., and Wang, X. (2002). Recent progress of diffuse pollution on loading, control and management. *J. capital normal Univ.* 023 (001), 91–96. doi:10.19789/j.1004-9398.2002.01.020.101

Wu, H., Huang, G., Meng, Q., Zhang, M., and Li, L. (2016). Deep tunnel for regulating combined sewer overflow pollution and flood disaster: a case study in Guangzhou city, China. *Water* (8), 329. doi:10.3390/w8080329

Wu, J., Xiong, L., Wu, J., Sha, C. Y., Tang, H., Lin, K. F., et al. (2019). Comparison and source apportionment of PAHs pollution of runoff from roads in suburb and urban areas of shanghai. *Environ. Sci.* 05 (40), 2240–2248. doi:10.13227/j.hjkx.201810055

Wu, Q. (2018). *The phyto immobilizing characteristics of the polycyclic aromatic hydrocarbons (PAHs) contents of rainstorm runoff from forest and different surfaces in Guangzhou city*. Beijing, China: Chinese Academy of Forestry.

Xu, D., Lee, L., Lim, F., Lyu, Z., Zhu, H., Ong, S. L., et al. (2020). Water treatment residual: a critical review of its applications on pollutant removal from stormwater runoff and future perspectives. *J. Environ. Manage.* 259. doi:10.1016/j.jenvman.2019.109649

Xu, S., and Huang, Y. (2004). *Study of atlas of shanghai urban physical geography*. Beijing: China Cartographic Publishing House.

Ye, Y., Li, S., Zhang, H., Su, Y., Wu, Q., and Wang, C. (2017). Spatial-temporal dynamics of the economic efficiency of construction land in the Pearl River delta megalopolis from 1998 to 2012. *Sustainability* 10 (1), 63. doi:10.3390/su10010063

Yu, G., Choi, J., Kang, H, M., and Kim, L. H. (2016). Evaluation of the volume and pollutant reduction in an infiltration and filtration facility with varying rainfall conditions. *J. Korean Soc. Water Environ.* 32 (1), 30–35. doi:10.15681/KSWE.2016.32.1.30

Zeng, J., Huang, G., Luo, H., Mai, Y., and Wu, H. (2019). First flush of non-point source pollution and hydrological effects of LID in a Guangzhou community. *Scientific Rep.* 9, 13865. doi:10.1038/s41598-019-50467-8

Zeng, Y., Cai, Y., Tan, Q., and Dai, C. (2020). An integrated modeling approach for identifying cost-effective strategies in controlling water pollution of urban watersheds. *J. Hydrol.* 581, 124373. doi:10.1016/j.jhydrol.2019.124373

Zhao, D., Tan, C., and Peng, X. (2015). Preliminary study on the pollution of rainwater in the initial stage of shijing river basin in Guangzhou. *J. Guangdong Tech. Coll. Water Resour. Electric Eng.* 3 (17), 5–8.

Zhu, Z., Fu, Y., Woodcock, C. E., Olofsson, P., Vogelmann, J. E., Holden, C., et al. (2016). Including land cover change in analysis of greenness trends using all available Landsat 5, 7, and 8 images: a case study from Guangzhou, China (2000–2014). *Remote Sensing Environ. S0034425716301407* 185, 243–257. doi:10.1016/j.rse.2016.03.036

Conflict of Interest: The authors declare that the research was conducted in the absence of any commercial or financial relationships that could be construed as a potential conflict of interest.

Advantages of publishing in Frontiers

OPEN ACCESS
Articles are free to read for greatest visibility and readership

FAST PUBLICATION
Around 90 days from submission to decision

HIGH QUALITY PEER-REVIEW
Rigorous, collaborative, and constructive peer-review

TRANSPARENT PEER-REVIEW
Editors and reviewers acknowledged by name on published articles

Frontiers
Avenue du Tribunal-Fédéral 34
1005 Lausanne | Switzerland

Visit us: www.frontiersin.org
Contact us: frontiersin.org/about/contact

REPRODUCIBILITY OF RESEARCH
Support open data and methods to enhance research reproducibility

DIGITAL PUBLISHING
Articles designed for optimal readership across devices

FOLLOW US
@frontiersin

IMPACT METRICS
Advanced article metrics track visibility across digital media

EXTENSIVE PROMOTION
Marketing and promotion of impactful research

LOOP RESEARCH NETWORK
Our network increases your article's readership